INFORMATION TO USERS

This manuscript has been reproduced from the microfilm master. UMI films the text directly from the original or copy submitted. Thus, some thesis and dissertation copies are in typewriter face, while others may be from any type of computer printer.

The quality of this reproduction is dependent upon the quality of the copy submitted. Broken or indistinct print, colored or poor quality illustrations and photographs, print bleedthrough, substandard margins, and improper alignment can adversely affect reproduction.

In the unlikely event that the author did not send UMI a complete manuscript and there are missing pages, these will be noted. Also, if unauthorized copyright material had to be removed, a note will indicate the deletion.

Oversize materials (e.g., maps, drawings, charts) are reproduced by sectioning the original, beginning at the upper left-hand corner and continuing from left to right in equal sections with small overlaps. Each original is also photographed in one exposure and is included in reduced form at the back of the book.

Photographs included in the original manuscript have been reproduced xerographically in this copy. Higher quality 6" x 9" black and white photographic prints are available for any photographs or illustrations appearing in this copy for an additional charge. Contact UMI directly to order.

UMI®

Bell & Howell Information and Learning
300 North Zeeb Road, Ann Arbor, MI 48106-1346 USA
800-521-0600

ST. LAWRENCE ISLAND POLYNYA:
ICE CIRCULATION and DENSE WATER PRODUCTION

A

THESIS

Presented to the Faculty

of the University of Alaska Fairbanks

in Partial Fulfillment of the Requirements

for the Degree of

DOCTOR OF PHILOSOPHY

By

Mary Frances Milkovich Glueck, B.S., M.S.

Fairbanks, Alaska

August 1999

ST. LAWRENCE ISLAND POLYNYA:

ICE CIRCULATION and DENSE WATER PRODUCTION

By

Mary Frances Milkovich Glueck

RECOMMENDED:

Advisory Committee Chair

Department Head

APPROVED:

Dean, School of Fisheries and Ocean Sciences

Dean of the Graduate School

6-28-99

Date

ABSTRACT

The St. Lawrence Island polynya (SLIP) opens every winter off the coast of St. Lawrence Island as winds move ice away from the shore. The SLIP is an important site for production of the dense water that flows northward through the Bering Strait to help maintain the Arctic Ocean halocline. Winter 1991/1992 ERS-1 SAR, thermal infrared, and passive microwave imagery are analyzed in combination with regional climate system and analytical simulations to investigate SLIP ice circulation, heat fluxes, and dense water production. Emphasis is on the February 1992 southern SLIP event. Satellite-based measurements show this polynya extended ~165km offshore and ~100km along shore at maximum extent. ERS-1 SAR GPS-derived ice motion indicated maximum ice speeds of ~30km day^{-1} during polynya expansion. Ice along the polynya boundary drifted parallel to the wind at 3-4% of the wind speed during north/northeasterly winds >7m s^{-1}. Heat fluxes associated with the SLIP varied depending on method of calculation, but indicated increasing trends during polynya development. Associated ice production rates of 4.2-18.9cm day^{-1} were computed via different models. Dense water production, derived from ice production rates and polynya size, ranged from 0.011-0.017Sv, suggesting that the SLIP could account for 19-27% of the Bering Sea's contribution and 1-2% of the total Arctic contribution to Arctic Ocean halocline maintenance.

Although the regional climate system model generated the SLIP on the same time scales as observed, a larger polynya resulted. The simulated polynya's heat and moisture impact was observed to at least 800mb, reaching 50km downstream. During periods of sustained winds, ice circulation was similar to that observed. Incorporation of a "barotropic" ocean component suggested that ocean circulation may be an important ice circulation forcing mechanism at the SLIP, especially during periods of weak winds, as inclusion greatly improved the simulated ice circulation. The "barotropic" ocean also improved polynya shape and extent.

If regional climate changes alter the existence of polynyas like the SLIP, changes in the Arctic Ocean halocline might occur. Additional *in situ* observations and better fully-coupled atmosphere-ice-ocean models are needed to further ascertain the impact of polynyas on the overall Arctic climate system.

TABLE OF CONTENTS

LIST OF FIGURES

LIST OF TABLES

ACKNOWLEDGMENTS

I would like to acknowledge and thank the following people for making it possible for me to successfully complete this dissertation:

My dissertation advisory committee consisting of Drs. T. J. Weingartner (Chairman), H. J. Niebauer, T. C. Royer, B. L. Norcross, G. E. Weller

Dr. Ron Kwok and colleagues at the Jet Propulsion Lab

Dr. Amanda H. Lynch and David Bailey, ARCSyM SLIP Project: My collaborative work with the ARCSyM model group resulted in the ARCSyM simulation of the SLIP presented here. My original contributions to this joint project, and to "Satellite Observation and Climate System Model Simulation of the St. Lawrence Island Polynya by Amanda H. Lynch, Mary F. Glueck, William L. Chapman, David A. Bailey, and John E. Walsh", Tellus, 1997 include SLIP project design initiation, observational analyses, observation-simulation comparison/discussion, collaborative writing of the Tellus article, and all responses to Tellus peer review comments relevant to the science content and non-model technique aspects of the project. Dr. Lynch was responsible for overall project management (ARCSyM Principle Investigator; the SLIP was an "experiment on the side" and far from being the main emphasis of the overall ARCSyM project), actual model algorithm changes as needed (in collaboration with me, Bailey, Chapman, and Walsh), financial & computer resources, collaborative writing of the Tellus paper (in collaboration with me), and model technique-specific peer review comments. Many figures shown here in my dissertation in association with my SLIP results may be similar to those in my Tellus paper, although all captions and some figures will differ herein to the extent necessary to reflect discussion/presentation of results in my dissertation. The SLIP experiments were made possible as a much appreciated favor to me and to satisfy the curiosity of all of us – "Could the model predict a polynya and if so, how well ?".

Rick Guritz and Joanne Groves, Alaska SAR Facility

John R. Glueck, Daniel J. Glueck, Piper Cat, and my parents

My dissertation research was funded by NASA Grants NAGW-2829. NAGW-2637 and NAGW-2517. ERS-1 SAR imagery in this dissertation are © ESA 1992 or 1994.

CHAPTER 1: OBJECTIVES AND BACKGROUND

1.1 What is a polynya ?

I refer to a polynya or a "polynya region" as being an area of open water, or a mix of open water and thin ice, surrounded by seasonal or perennial pack ice. Smith et al. (1990) define polynyas as follows: "At predictable, recurring locations throughout the polar regions, there are oceanic areas (polynyas) which remain partially or totally ice free at times and under climatological conditions where we would expect waters to be ice covered." Polynyas are typically separated into two classifications: sensible heat polynyas and latent heat or wind-driven polynyas. A sensible heat polynya is created by warm ocean water melting the local ice cover. A latent heat (or wind-driven) polynya (Figure 1.1) is created when wind or ocean currents remove ice from a region, often in the lee of land, resulting in open water with ocean temperatures at the freezing point and new ice formation. [1] Polynyas may display characteristics of either or both types at various developmental stages, and so not all polynyas are well-described by this simple classification. A polynya event is defined here in terms of polynya development and ice circulation, beginning with the initial observation of open water and ending with the last observation of a distinct polynya boundary within the seasonal ice field.

1.2 Objectives

The polynyas that form on the leeward side of coastlines (Figure 1.2) are sensitive and dramatic indicators of sea ice motion and interaction with the atmosphere-ocean

---

[1] This "latent heat" label refers to polynyas at which the heat transfer to the atmosphere from the open ocean within the polynya is compensated for by the latent heat of fusion of the continuously forming ice. (Smith et al., 1990).

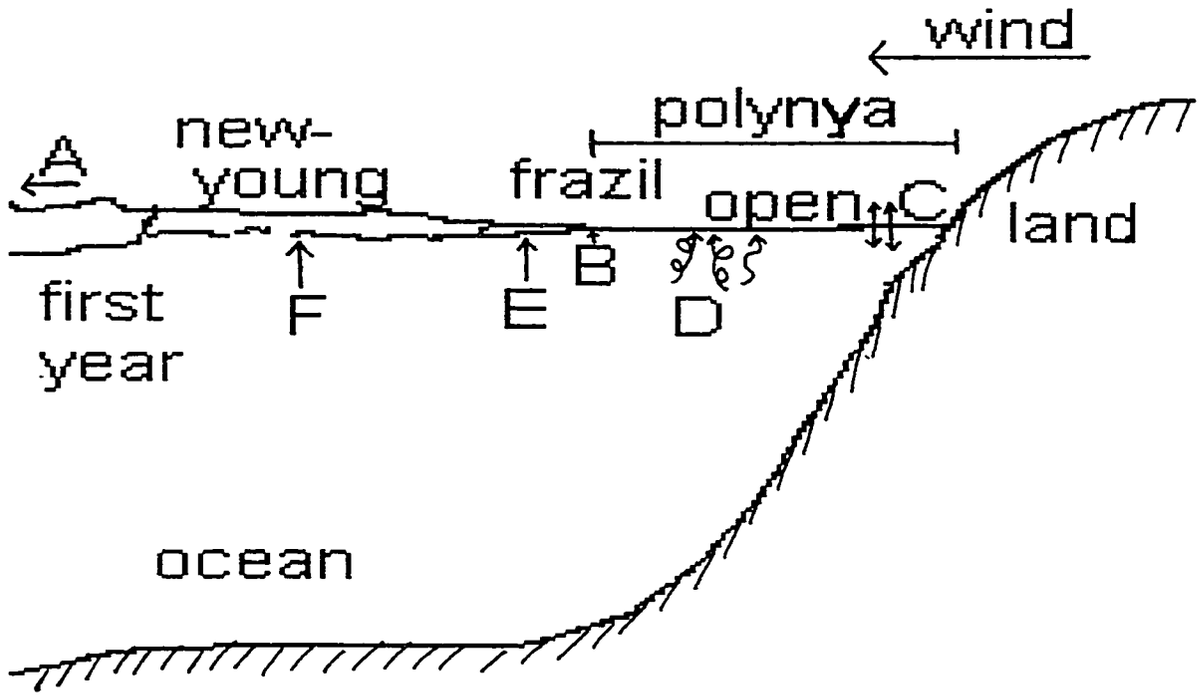

Figure 1.1: Wind-driven (Latent Heat) Polynya Formation. The atmosphere-ice-ocean processes associated with latent heat polynya development and growth are (After Pease, 1980): A) first year ice is blown offshore by "offshore" winds to create open water along the shoreline; B) polynya continues to expand offshore until new ice production matches offshore ice velocity; C) vigorous exchanges of heat and moisture between atmosphere-ocean-ice take place at the open water region; D) frazil is produced in the "turbulent boundary layer" of the open water and rises to the surface; E) newly-formed frazil is blown downwind to collect along already existing ice floes moving downwind; F) frazil gathers and solidifies at the farthest downwind portion of the polynya along the first year ice boundary where it too thickens into first year ice over time.

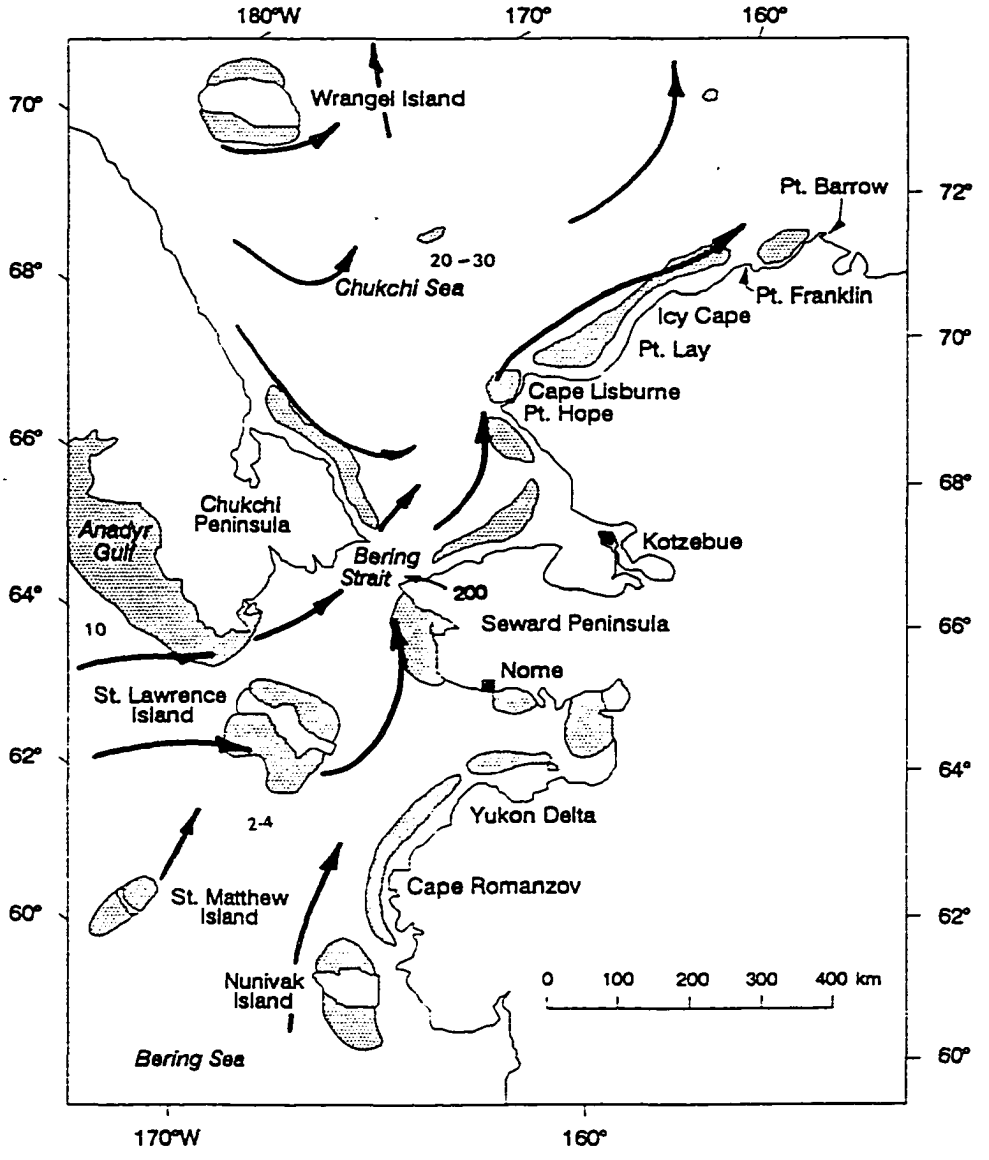

Figure 1.2: Polynyas of the Bering and Chukchi Seas. Recurrent wind-driven polynyas are represented as shaded areas along coastlines. Arrows represent ocean circulation direction. Numbers represent current speed (units: cm s^{-1}). (After Stringer et al., 1982 and Niebauer & Schell, 1993).

system of the Bering Sea. Many research efforts (Pease, 1980 and 1987; Schumacher, 1983: Overland and Pease, 1982; and Cavalieri and Martin, 1994) have provided descriptions of the St. Lawrence Island polynya (SLIP), one of the largest and most active wind-driven polynyas in the Bering Sea region (Figure 1.2), but more detailed studies of the SLIP's kinematics, dynamics, and thermodynamics are needed before polynyas can be realistically included in climate models to better understand and predict the effects of polynyas on regional climate. Other such wind-driven polynyas are observed within the Bering Sea along the coasts of St. Matthew Island. the Pribilof Islands, western Alaska, and eastern Russia (Figure 1.2).

Polynyas such as the SLIP are important to the regional climate system, and perhaps, on a broader scale, to the global climate system. As polynyas are sites of open water and rapid ice formation, they reflect heat flux characteristics of both open water and ice. The presence of ice and snow within a polynya region leads to insulation of oceanic heat and reflection of incoming radiation, while the presence of open water within a polynya leads to large "ocean to atmosphere" fluxes of heat and moisture. Turbulent losses of latent and sensible heat from open leads and polynyas can average over 600Wm^{-2} in winter (Andreas and Murphy, 1986). By comparison, the solar constant is 1376Wm^{-2}, of which less than 20% enters the ocean surface. Net heat loss from a small percentage of open water and thin ice greatly exceeds that associated with the surrounding ice pack. In fact, annual turbulent heat exchange between ice and atmosphere is approximately double the magnitude when winter leads and polynyas are taken into account, even though these openings only account for 1% of the area (Smith et al, 1990). Net heat loss over ice of 0.5m thickness is an order of magnitude larger than that over 1m of ice (Maykut, 1978). Ice growth rates are likewise considerably higher over leads and polynyas than over the main pack ice (Massom and Comiso, 1994). Smith et al. (1990) estimate that almost half of the

ice in the Bering Sea is formed in its coastal polynyas. Air temperature is also known to influence ice growth and heat transfer fluxes from ice or open water to the atmosphere in that it has a large role in determining the extent of open water within a polynya region.

During its initial stages of formation, sea ice rejects approximately 2/3 of the salt originally present in the sea water (Weeks and Ackley, 1986). The polynyas, located over the shelves adjacent to the Arctic Ocean, provide mechanisms for growth of large amounts of ice in a small regional area and thus contribute relatively large amounts of brine to source waters for the halocline layer. Arctic polynyas annually produce around 800km^3 of new ice and 2 x10^{13}kg of salt that is released to the ocean (Cavalieri and Martin, 1994). The SLIP region, although not in the Arctic Ocean proper, is one known site of rapid ice formation; thus, it is also considered to be a site of significant brine production. In the case of the SLIP, the cold, salty water is considered to be entrained into the northward regional flow and advected into the Arctic Ocean (Aagaard et al., 1981), where it contributes to the Arctic Ocean halocline.

My hypotheses are:

- St. Lawrence Island polynya is a site of significant brine production.
- The SLIP is a wind-driven feature, but the ocean also plays an important role in determining ice circulation associated with the SLIP.
- Ice speed/direction:wind speed/direction ratio associated with SLIP events varies according to wind speed/direction, but does not always follow the free drift theory for ice.
- The SLIP is a site of high sensible and latent heat flux affecting the local atmosphere as well as the surrounding area.
- A SLIP event can be resolved and predicted using a regional climate system model- a first step in investigating the SLIP's effects on multiple spatial scales of climate.

The objectives of this dissertation are to combine satellite observations with ice-atmosphere-ocean models to describe and quantify ice circulation at the SLIP; to describe and quantify ice and brine (i.e. cold, salty water rejected from the ice) production associated with the SLIP; and to validate and analyze results from the first high resolution coupled atmosphere-ice-ocean regional climate system model simulation of a SLIP polynya event.

1.3 Background: Bering Sea and the SLIP

Most of the seasonal sea ice pack within the Bering Sea is first year ice of 0.01 to 1.0m thickness that forms at polynya sites (Muench, 1989) on the leeward side of coastlines. The ice drifts southward under the predominantly northerly or northeasterly winds towards the warmer water off the shelf break in a manner that has been compared to a conveyor belt (Pease, 1980). The rate of the ice's southward motion is dependent on wind speed and direction (Pease, 1980). Although ice speeds may be several tens of km day^{-1} as will be shown in Chapter 3, the typical large-scale ice advance and retreat over the Bering Sea is slower.

The Bering Sea sea ice extends from the Bering Strait in October southward to the Bering Sea shelf break in April - a distance of ~1000km. Ice usually extends to St. Lawrence Island and beyond by late December. Once the maximum ice extent has been reached in April, most of the ice begins to melt *in situ* (a small amount retreats northward as well) until no ice remains south of the Bering Strait after mid-June.

In general, polynyas tend to form within the ice cover of the northern Bering Sea shelf along the leeward side of coastlines from November to March during periods of sustained northerly winds. Climatologically, these winds are most prevalent during this

period due to the strength and position of the Aleutian Low and/or Siberian High. Winds may fluctuate locally, however, depending on the position, intensity, and track of individual storm systems. As a direct result of the orientation of Bering Sea coastlines and the varying wind directions, many of these coastal polynyas open, close and then redevelop several times throughout the winter season. Although the recurrent, wind-driven SLIP may open on either the north or the south side of the island (dependent on wind direction), a northern polynya is generally much smaller and shorter-lived than a southern polynya.

Coastal polynyas such as the SLIP are important to the Bering Sea's regional climate, in part, because they are among the primary ice generation sites for the seasonal Bering Sea ice cover. One reason for the importance of ice production in polynyas is that although, thicker ice is associated with a lower oceanic-atmosphere heat flux than thin ice, the greatest decrease in oceanic heat flux to the atmosphere occurs during the initial growth stages of an ice cover (Maykut, 1978). The turbulent heat fluxes (sensible and latent) at the ocean surface are reduced by 5-20% (Shuchman and Onstott, 1990) when open water is covered by ice. Once an ice cover thickness reaches a meter, there is little difference between heat loss through it and that lost through even thicker ice.

New ice production and subsequent growth at the SLIP also leads to enhanced levels of cold, salty water (brine) production at the polynya. Brine produced during new ice formation within the SLIP might remain within the polynya for a period of time because, although regional currents are ~5-20cm s^{-1} (Muench et al., 1988), mean nearshore currents are weak. The mean speed of the water immediately south of St. Lawrence Island is 1 to 4cm s^{-1} with a variable heading (Salo et al., 1982). This residence time could result in greater salt enhancement of the local seawater through mixing processes, as the dense water is not being flushed out of the polynya region by currents as rapidly as the brine is being produced. Eventually, the strong northward ocean currents (shown earlier in Figure

1.2) in the vicinity of St. Lawrence Island (Muench et al., 1988; Salo et al., 1982) transport the dense water produced at the SLIP and other Bering Sea polynyas through the Bering Strait (Schumacher et al., 1983; Overland and Roach, 1987) where they contribute to the maintenance of the Arctic Ocean halocline (Aagaard et al., 1981; Coachman and Barnes, 1961).

The Arctic Ocean halocline lies between 50m and 200m depth. It is characterized by water temperatures less than -1°C, and salinities of 30.4 to 34.4 (Carmack, 1990; Figure 1.3a). The halocline water characteristics (i.e., temperatures near freezing, salinity increasing with depth) are not likely to be attained solely through vertical mixing of water masses above or below the halocline layer, due to stability constraints (Aagaard et al., 1981). However, the layer is thought to be maintained, in part, by advection of salinity-enhanced shelf water created (Figure 1.3b) during winter ice formation at polynyas and other open water sites (i.e., areas of highly divergent ice floes) on the broad, shallow shelves surrounding the Arctic Ocean. Measurements of salinity and biogeochemical tracers (Jones and Anderson, 1986) within the halocline suggest the presence of waters from the broad (~500km), shallow (<100m depth) Bering Sea shelf, and thus, from polynyas such as the SLIP.

The Arctic halocline is a "climatically-important" insulating layer of water that separates the low salinity, cold surface mixed layer of the Arctic Ocean above it from the warmer, but saltier, Atlantic layer observed directly below the halocline layer (Figure 1.3). The halocline layer prevents much of the Atlantic layer's heat from reaching the ocean's surface layer, thus helping preserve the Arctic Ocean ice cover. If the halocline layer were to weaken significantly, this heat flux from the Atlantic layer would likely lead to a reduced Arctic Ocean ice cover and a resultant increase in the ocean to atmosphere heat transfer, thereby changing the climate of the region. It is this involvement in the maintenance of the

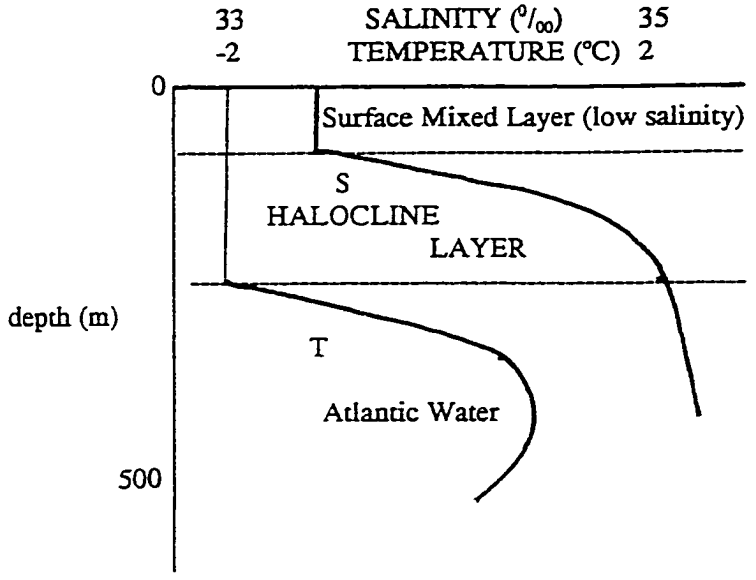

(a)

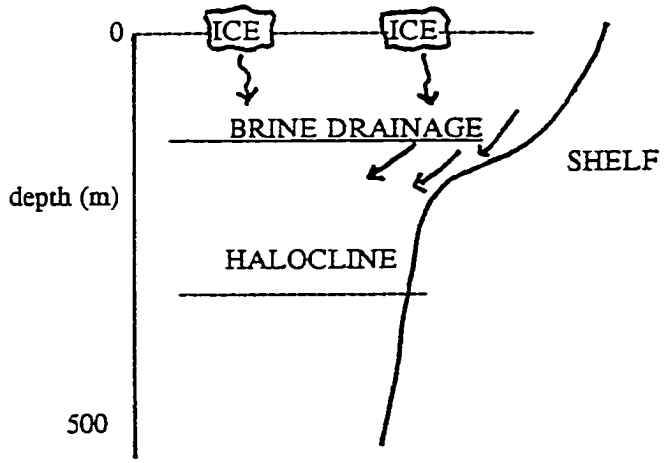

(b)

Figure 1.3: Arctic Ocean halocline. (a) This schematic profile of the upper Arctic Ocean temperature and salinity illustrates the characteristics of cold temperature and high salinity that define the halocline layer. This layer is located between 50 and 150 m depth (After Aagaard et al., 1981), beneath the surface mixed layer and above the Atlantic water. (b) A schematic diagram of the shelf drainage mechanism thought to be responsible for halocline maintenance is shown (After Aagaard et al., 1981). Ice forms on the surface of the ocean. As it forms, it releases brine to the ocean. These brines drain down the shelf bathymetry to help maintain the halocline layer found in the Arctic Ocean.

heat balance of the Arctic climate system that causes some to consider the halocline to be one of the most significant features of the Arctic Ocean (Aagaard et al., 1981; Carmack, 1990).

1.4 Organization

I have chosen to focus my research on the 1992 SLIP events because of the good European Remote Sensing Satellite-1 synthetic aperture radar (ERS-1 SAR) regional coverage of these events (see satellite track in Figure 1.4), and the availability of potentially useful SAR-based Geophysical Processor System (GPS) techniques (Kwok et al., 1991) for tracking ice motion. The winter 1992 SLIP events are discussed in terms of stages of polynya development and ice circulation (Chapter 3). Chapter 2 presents the basic "theory and methodology" relating to research presented in later chapters. In my work, I use ice motion products, satellite-based measurements of polynya size, and meteorological data to estimate the heat fluxes. ice production, and brine production associated with the SLIP to assess it's relative contribution to the Arctic Ocean halocline and regional energy budget (Chapters 3-5). Models incorporated into this project include the Arctic Climate System Model (ARCSyM) atmosphere-ice-ocean model (Lynch et al., 1995; Lynch et al., 1997), the Cox-Weeks-Wade (CW2 model) ice growth model (Wade, 1993), a 2-d barotropic circulation model (Proshutinsky. 1988), the Pease (1987) model of polynya size, and a heat flux-ice production-brine production model (Cavalieri and Martin, 1994). The ARCSyM high resolution, fully-coupled atmospheric-sea ice-ocean model was incorporated into my research to determine if it was possible to simulate a realistic SLIP using both model-derived atmospheric circulation and model-derived ice field, to investigate the potential role of ocean circulation in polynya development and to further investigate heat fluxes at the polynya. The other models were used to estimate polynya size and/or ice and brine

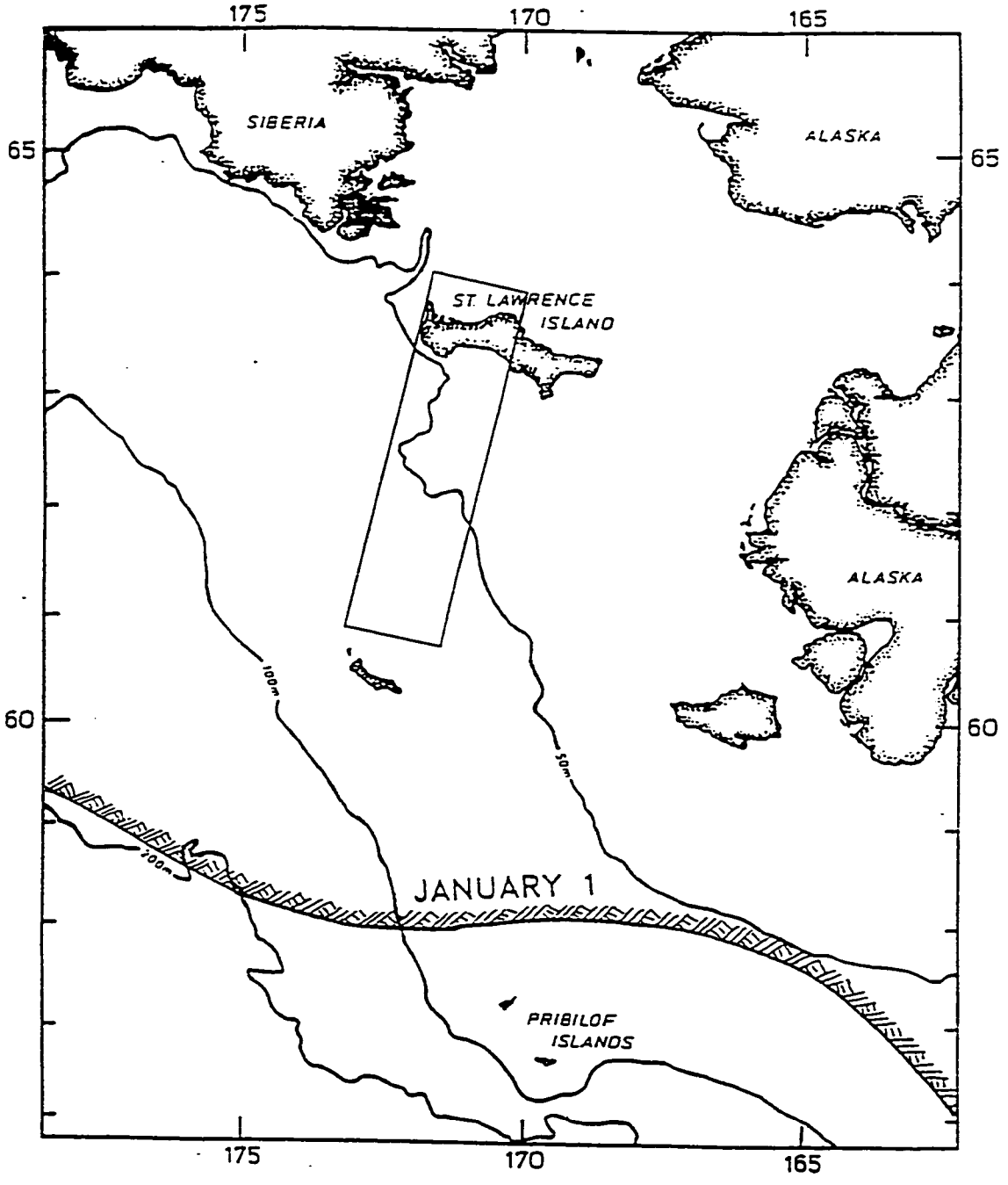

Figure 1.4: ERS-1 satellite track over St. Lawrence Island. The primary ERS-1 satellite track over St. Lawrence Island during the ice phase orbit of 1991/2 is depicted by the extended rectangle drawn across the island. Although the actual track is, in reality, much longer in north-south extent, the rectangle indicates the portion of the track that this project's imagery was drawn from. The mean January ice edge position is denoted by the hatched line extending across this diagram. Bathymetry is also shown to illustrate the shallow ocean offshore of St. Lawrence Island on the broad Bering Sea shelf.

production rates. Remotely-sensed data were used to validate model simulation results. Chapter 6 concludes this dissertation with some final thoughts on my work as well as ideas for expanding on my efforts and suggestions for future research.

CHAPTER 2: THEORY and METHODOLOGY

2.1 Introduction

The purposes of this chapter are:

- to introduce the ERS-1 SAR imagery of the SLIP region;
- to discuss the method I used to obtain the SLIP ERS-1 SAR GPS ice motion products;
- to review the AVHRR thermal infrared data and SSM/I ice concentration data;
- to discuss the ERS-1 SAR/AVHRR combined image products;
- to describe the DMSP-based SSM/I ice concentration data;
- and to introduce the models that I will be using in later chapters.

This chapter is divided into two parts: satellite observation and model simulation. It is not, however, meant to be an exhaustive presentation of sea ice remote sensing or analytic/numerical modeling theory. ERS-1 SAR, AVHRR, and DMSP SSM/I satellite data all are useful for sea ice research. However, the combination of imagery has proven to be an even more powerful tool in my studies of the ice/open water characteristics of the SLIP region. Analytic and numerical models such as those incorporated into my research promise to provide additional spatial and physical information leading to better understanding and perhaps, ultimately, prediction of the effects of air-sea-ice interactions in the data-sparse region encompassing the SLIP.

2.2 Satellite Observation: Theory, Background, Methodology

2.2.1 ERS-1 SAR Theory and Background: Detailed descriptions of basic synthetic aperture radar theory and image processing procedures applicable to sea ice SAR analyses can be found in Ulaby et al. (1981, 1982, and 1986), McCandless and Mango (1990), Curlander et al. (1985), and in the contributions of the many authors represented in Microwave Remote Sensing of Sea Ice (Carsey, 1992). Initial data validation reports for ice classification algorithms (Holt et al., 1993) and ice motion products (Stern et al., 1993) associated with the ERS-1 SAR were released in July 1993 and are contained in the *ASF GPS Data User's Handbook* (Kwok and Cunningham, 1993). A collection of the initial ERS-1 SAR studies may be found in the Alaska SAR Facility special section of the *Journal of Geophysical Research, volume 99 C11, 1994.* Finally, the Alaska SAR Facility has created

an extensive Internet homepage (http://www.asf.alaska.edu/) detailing the entire ERS-1 SAR project and its many scientific applications.

The combination of the SAR imagery's high spatial and temporal resolution allows good description of the winter ice conditions and ice circulation associated with the Bering Sea polynyas as the microwave sensor is relatively unaffected by darkness or weather/cloud conditions. SAR is an active microwave radar system that sends out a calibrated electromagnetic pulse. measures the strength of the return signal or backscatter (waves scattered back to the antenna from the surface), and presents these results in a map-like format (usually a gray-scale image) reconstructed from phase histories stored in the return signal. The expression "Synthetic Aperture" refers to the way the radar achieves its along-track spatial resolution through the motion of its real antenna in relation to a target. In contrast, a real aperture radar's spatial resolution is a function of the real antenna's size. The result is that a real aperture antenna would have to be so large as to prevent deployment from a spacecraft in order to obtain the high spatial resolution that is possible to obtain through SAR.

SAR uses a large number of low resolution returns obtained by a small antenna aboard a moving platform to numerically "synthesize" the equivalent of a high resolution return obtained from a very large antenna (McCandless and Mango, 1990). The SAR system saves the Doppler shifts or phase histories of the radar returns from each position along the instrument's track as the radar pulse moves through an area. The moving antenna and Doppler principles allow the spatial resolution of SAR to be nearly independent of wavelength and target length (McCandless and Mango, 1990).

The backscatter from different materials along the satellite's orbital path is the primary source of geophysical data used in creating SAR imagery. This backscatter is a function of radar frequency, incidence angle, and polarization. As such, it is an absolute measure of scattering behavior. The strength of the backscatter is determined by the degree of surface roughness (related to surface scattering) and spatial variations in the dielectric properties (related to volume scattering) within the material being targeted.

One of the most crucial parameters affecting radar backscatter signatures for sea ice and ocean water is the penetration depth, also called the skin depth, of the surface material. This depth is a measure of how far the radiation may penetrate into the ice or open ocean and still give a detectable signal. Strictly speaking, this is the depth at which the transmitted power falls to 1/e or ~37% (also called "e-folding" depth) of the power at the material's surface. Once this penetration depth is known, the relative importance of

surface and volume scattering can be determined for the material. The properties of the ice or open water throughout this depth determine the volume scattering component of the radar backscatter. Figure 2.1 illustrates volume and surface scattering characteristics for different types of ice and open water.

The complex dielectric constant of sea ice affecting the penetration depth of the radar signal is dependent on the distribution of liquid brine and gas within the ice which, in turn, is a function of ice salinity, density, and crystal structure (Weeks and Ackley, 1986). Scattering loss is caused by particles of different composition embedded within the ice. The dielectric constant of a material can be estimated as a function of the ice's brine volume. As a means of comparison, open (ice-free) ocean has an extremely high dielectric constant value. New ice (and in fact, all first year ice) also has a high brine content, and a high dielectric constant value (Weeks and Ackley, 1986) although neither is as high as that of the ice-free ocean. Thicker ice and multi-year ice, in particular, contain much less brine than the younger ice due to brine drainage over time. This results in the much lower dielectric constant value characteristic of multi-year ice.

High brine content also results in a material being classified as a "lossy" material into which radar transmission penetrates only a short distance (a few cm). Because of its high dielectric constant, the ice-free ocean has an insignificant penetration depth. The penetration depth of first year ice falls between that of the ice- free ocean and that of thicker, multi-year ice. The region within a polynya will have characteristics of open water, initially, followed by those of new ice and first year ice as ice formation and subsequent thickness growth occurs. The lower dielectric constant of the older ice outside the polynya leads to the larger penetration depths associated with the seasonal pack ice surrounding the polynya.

Surface scattering from sea ice is a function of the surface roughness of ice, which can be attributed to the environment in which the ice was formed and continues to grow. Sea ice that exists in turbulent atmosphere-ocean environments is characterized by sharp edges, ice streaks, ridging, and rafting which make this ice "appear" considerably rougher to the microwave sensor than ice forming in a calm environment. Additionally, a mix of new ice crystals, frazil, and wind-blown open water will appear rough until the ice has formed a continuous layer damping out the ocean's wave field and creating a smooth surface. The SLIP region exhibits many different degrees of surface roughness characteristics as it goes through its cycle of changes from first year ice to open water and then new ice formation.

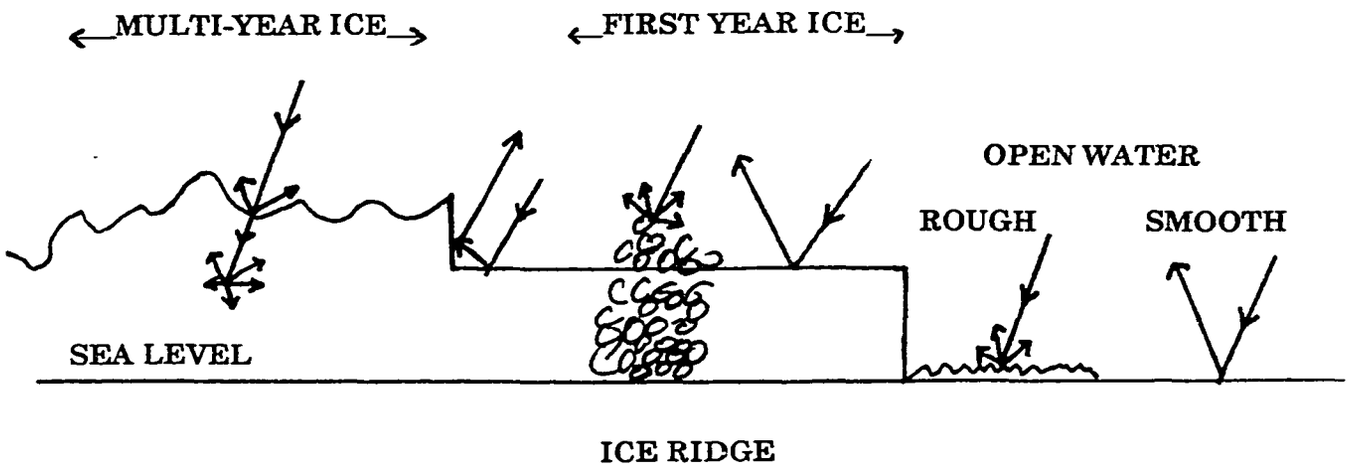

Figure 2.1: Surface and Volume Scattering. Microwave scattering characteristics for different types of ice and open water surfaces (after NASA, 1986) are illustrated. Scattering within the ice is referred to as volume scattering. Scattering from the ice or water surface is called surface scattering. Surface scattering is dominant for open water and younger ice. Scattering attributed to multi-year ice is a combination of volume scattering and surface scattering. The differences in scattering characteristics observed for types of sea ice, and between sea ice and open water, result from differences in surface roughness, penetration depth, and the dielectric constant.

In terms of SAR backscatter signal, a rougher surface results in a stronger backscatter (surface scattering component) or return signal than does a smooth surface. This might seem contrary to common sense, but can be explained as shown in Figure 2.2. Remember that the SAR antenna is moving relative to the material. A smooth surface acts as a "specular" reflector of the radar pulse. However, the antenna will never receive this return because the signal is reflected away from the receiver and because the receiver has moved beyond the incident location. A rough surface scatters the transmitted pulse in many directions so that, in theory, a portion of the energy will be received by the antenna. This rough surface may be thought of as a "diffuse" reflector as it reflects or scatters energy in many directions. Although most ice surfaces can be classified as somewhat "rough" to the ERS-1 SAR sensor, due to the differences in scale between ice surface variations and the C-band wavelength of the SAR sensor, surface scattering is larger for multi-year ice and wind-blown open water than for first year ice.

The total radar backscatter coefficient (referred to as σ^{o}) for sea ice obtained from the radar is a combination of the volume scattering component and the surface scattering component. For ice and open water, the total radar backscatter coefficient can be expressed (Kim et al., 1985) in terms of surface scattering plus a constant value added to account for volume scattering (Soulis et al., 1989).

2.2.2 ERS-1 SAR Imagery: The launch of the ERS-1 satellite in 1991 by the European Space Agency (ESA) resulted in the acquisition of new synthetic aperture radar (SAR) products and new approaches to sea ice research. This SAR system is characterized by an active C-band microwave (wavelength = 5.6cm) single channel radar with a vertical transmit and receive (VV) polarization; a frequency of 5.3 GHz +/- 0.05 MHz; a 23° incidence angle; and a radiometric resolution of 2.5dB (Massom, 1991). The low resolution (LoRes) image swath is 100km. During the winter of 1991/2 and 1994, the satellite was in a sun-synchronous, exact three day repeat orbit cycle, dubbed "the ice phase orbit" (ESA, 1992), from December through March. This means that the satellite crossed the same place at the same time during the day, just three days apart. It is the 1991/2 ERS-1 SAR data set that I will be using throughout the following chapters.

Synthetic aperture radar (SAR) products such as imagery and geophysical processor system (GPS) output are derived from a SAR system that includes a transmitter, a receiver coupler, an antenna, and a processor to make images (McCandless and Mango, 1990) out of calibrated radar returns. The SAR signal processor at the Alaska SAR Facility produces

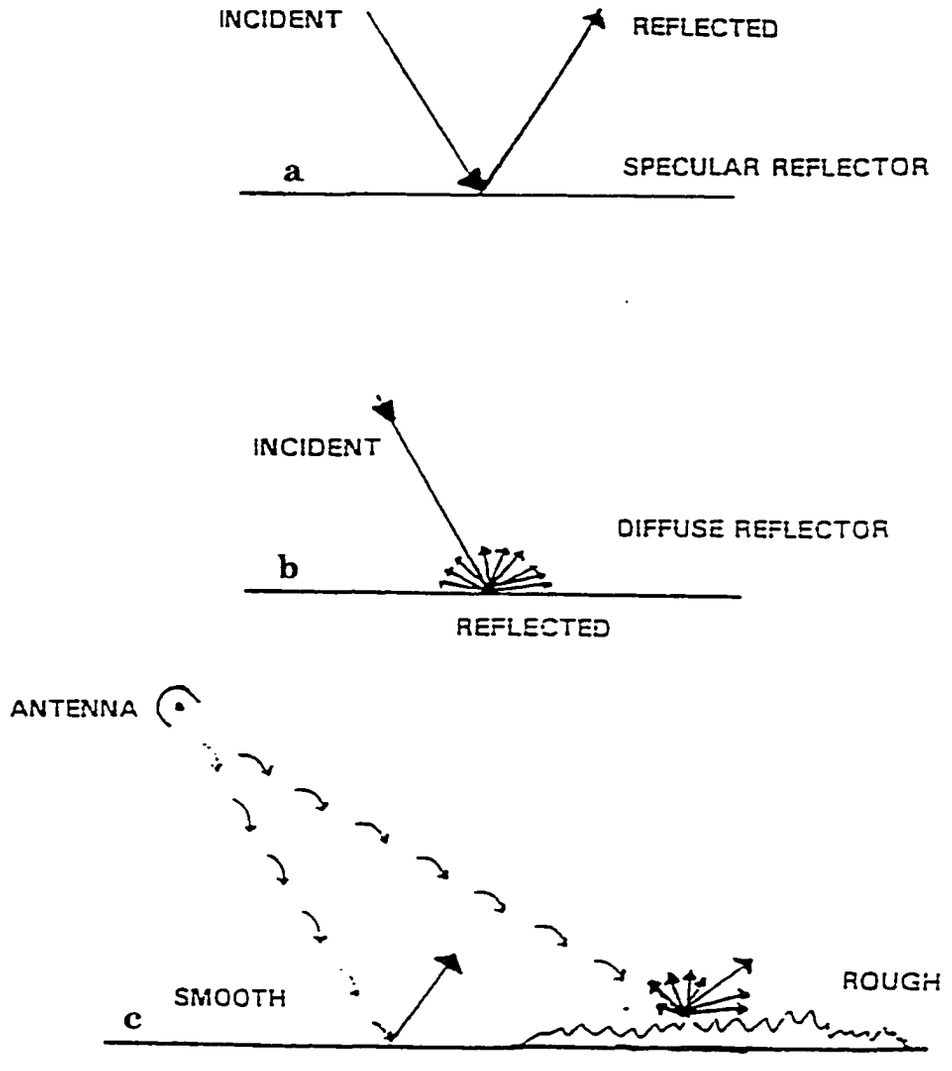

Figure 2.2: Specular vs. Diffuse Reflection. Radar reflection characteristics for:(a) specular reflector and (b) diffuse reflector. Radar backscatter intensity is a measure of how much energy is reflected back (i.e. backscattered) to AND received by the radar antenna. In a specular reflection case (similar to a mirror), none of the transmitted radar pulse is reflected back to the antenna. Diffuse reflection scatters the transmitted pulse in all directions so that some of the energy will return back to the antenna. A smooth surface acts as a specular reflector and thus, will have no surface-based backscatter signature. Rough surfaces act as diffuse reflectors and are characterized by a varying intensities of surface-based backscatter depending on their surface characteristics.

SAR images by using the Doppler information (relative shift of every targets' position in the antenna field of view) stored in the data returned by targets moving relative to the radar. Image formation is based on the principle that the instantaneous Doppler frequency of fixed objects on the earth's surface can be related to the object's position relative to the radar antenna (McCandless and Mango, 1990). The images that I used were produced at the Alaska SAR Facility by converting a histogram of "predicted waveform to radar data correlations" (McCandless and Mango, 1990) to a gray-scale, and assigning gray-scale values representing calibrated radar backscatter coefficients to each pixel of an image (DeSoto, 1991; Kwok et al., 1991; Curlander et al., 1985; Hilland et al., 1991). The grey-scale images for the area shown in Figure 2.3 are archived at the Alaska SAR Facility for distribution to those requesting them for geophysical research.

The low resolution images used in this project are produced by ASF through an 8 x 8 averaging of full resolution images. The result is a 1024 x 1024 pixel image with 8 bit precision, 100m pixels, and 240m spatial resolution (DeSoto, 1991). Geocoded ERS-1 SAR images can be ordered from ASF in a specific map registration, or as in my case, the user can map the standard imagery to a specific registration. I chose to register my imagery to a polar stereographic (tangent plane at 70°N to minimize distortion at lower latitudes) map projection that would correspond to that used for the SAR ice motion products.

When SAR image data is received from the archives, the images may include detrimental effects related to the SAR system, range, and area of illumination. Any gain variations occurring during reception and processing of data will also be included in the calibrated backscatter data. As a result, the grey scale backscatter values are usually converted, also called "radiometrically-corrected", to a set scale of "σ_o values" or "sigma-naught values" (σ_o(dB)= 0 to -25.5) which eliminates or lessens the effect of the above factors, and allows for image to image comparisons (Wade, personal communication). I have converted all of the SAR imagery presented in following chapters to this σ_o scale using a conversion routine resident on the Interactive Image Analysis System at ASF.

Once I radiometrically corrected the imagery to this specific σ_o scale (0 to -25.5dB), I began my geophysical interpretation of the imagery. The key to distinction between open ocean, first year ice, and multi-year ice in the SAR imagery is the strength, or range of their respective backscatter values. Two of the actual SAR mosaics that I created from an ERS-1 satellite pass over St. Lawrence Island are shown in Figure 2.4. Calm open ocean has a very weak backscatter and thus will appear dark (black or nearly so in Figure 2.4) in these grey-scale images. Rough open ocean within the polynya region and in leads opening

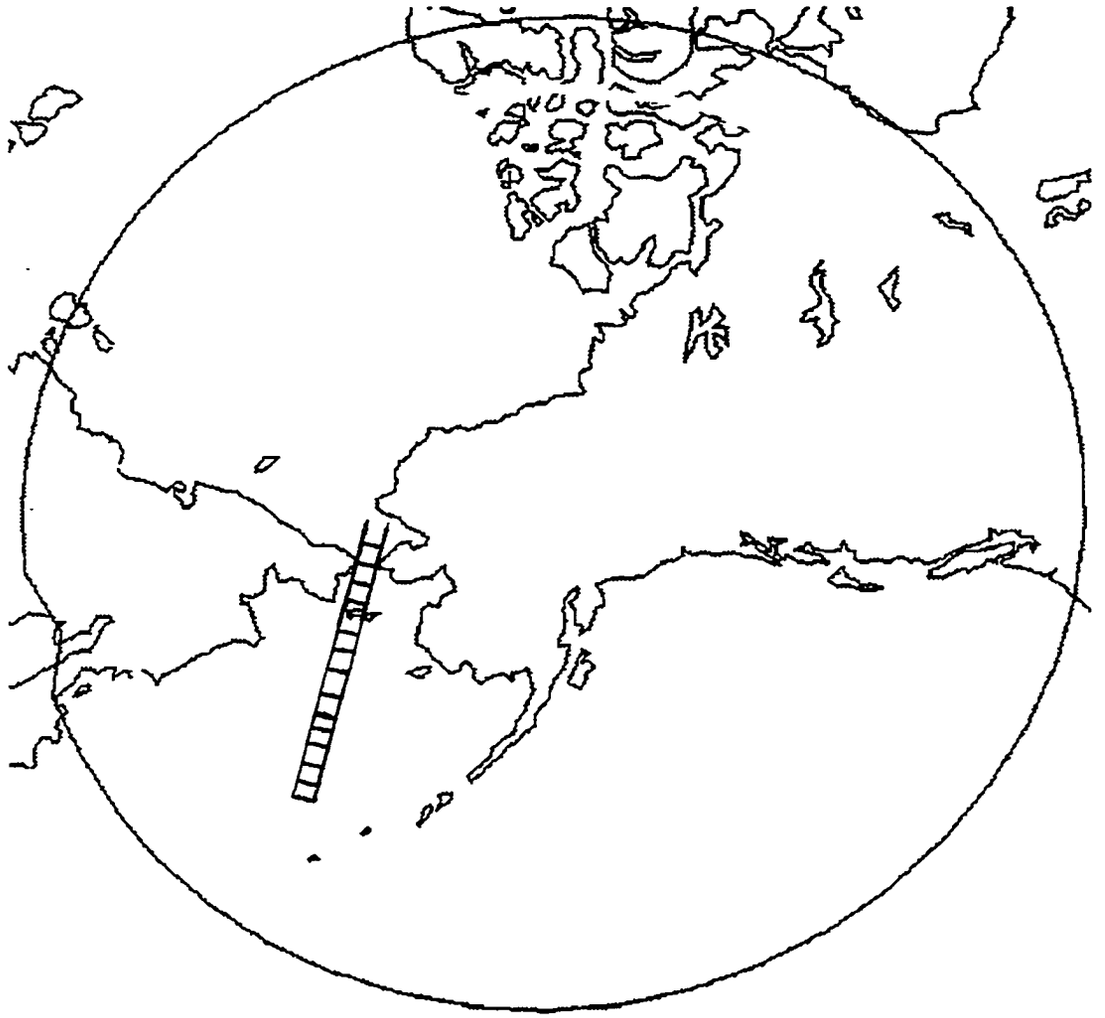

Figure 2.3: ERS-1 SAR station mask for the Alaska Synthetic Aperture Radar Facility. The large circle denotes the "nadir locations corresponding to the limit of reliable tracking for ERS-1" (Alaska SAR Facility Homepage, 1997). The gridded track within the mask represents the February 24,1992 radar coverage of St. Lawrence Island acquired by the ERS-1 SAR for ASF processing (ESA, 1992). The track's repeated coverage of the island is the primary source of the ERS-1 SAR data used in this study of the St. Lawrence Island polynya. (Source of mask: Alaska SAR Facility Homepage, 1997)

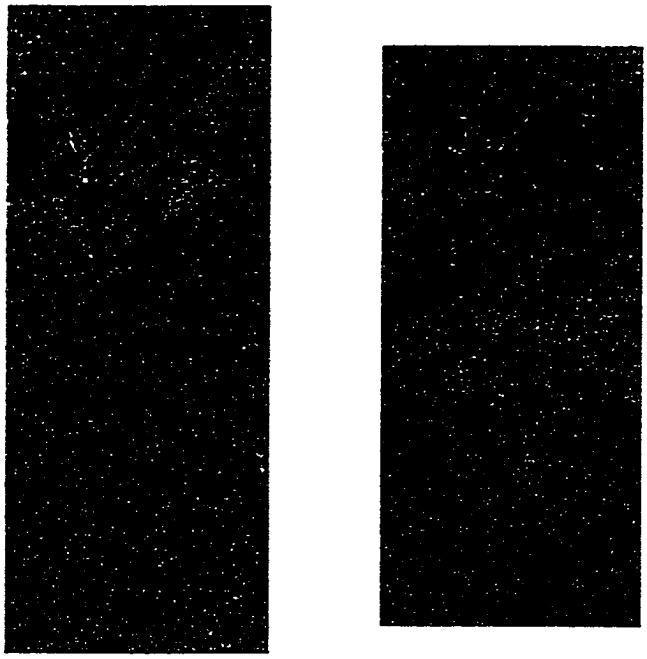

Figure 2.4: ERS-1 SAR LoRes image mosaics. These mosaics are of the 1992 St. Lawrence Island polynya. St. Lawrence Island is visible in the upper portion of the image. The polynya region extends downward from the island. The polynya region visible in the left image is larger and older than that in the right image. The right mosaic's polynya region appears to have more potentially open water (black off southwest coast) than the left mosaic's polynya region. Different stages of open water/ice formation are denoted by the variations in grey-scale (grey-scale represents backscatter) throughout the imagery. The streaks within the polynya are wind-driven bands of frazil ice on wind-roughened open water. The ice outside the distinct polynya region boundary is the seasonal ice cover of first year ice. Pixel size is 100 m and spatial resolution is 240 m.

in the seasonal ice pack will appear brighter (whiter in Figure 2.4) due to the water surface's relatively higher backscatter attributable to stronger surface scattering. Weak backscatter is characteristic of newly formed ice, frazil, and young ice, although the backscatter is larger (appears whiter) than that of the calm open water. The dark band visible along the island's south-central coast in Figure 2.4 is smooth shorefast ice. In general, ice may range from the "dark" of open water to a high "brightness" in a grey-scale image. The absolute backscatter range for each type of ice is highly dependent on differences in ice composition and texture within an ice type category, and external environmental factors such as wind and temperature. As a result of these uncertainties, SAR-ice classification is a topic of extensive research within the sea ice and remote sensing community.

2.2.3 GPS Ice Motion Products: The standard procedures for creating ice motion vectors using the ERS-1 SAR imagery and the ASF Geophysical System Processor have been fully described in the Alaska SAR Facility's Geophysical Processor System DATA USER'S HANDBOOK version 2.0 (Kwok and Cunningham, 1993; Kwok et al., 1990). The Geophysical Processor System algorithm associated with the ERS-1 SAR project attempted to track ice floes from one satellite pass to the next using a combination of feature tracking and area-based methods to determine ice displacement during the time separation between subsequent imagery (in this case, a time separation of three days). The GPS algorithm used geostrophic wind-ice motion relationships (Thorndike and Colony, 1982) to obtain an initial estimate of ice motion and to aid in locating ice feature matches. Next, for each pair of images, ice motion was computed on a grid (SSMI grid, Bonbright, 1984) fixed in space using cross-correlation and ice feature edge detection (concept of feature recognition and tracking), so that regularly-spaced grid points defined in one image were followed to their new location in a second image of the same area acquired three days later. This resulted in Eulerian fields of ice motion. As a side note, the next generation GPS, RADARSAT GPS or RGPS (Kwok et al., 1995), has been designed to be capable of this Eulerian method as well as a Lagrangian-based (travel with parcel) technique in which individual ice features can be followed over a period of time without the grid component.

Prior to December 1994, the Geophysical Processor System (GPS) (Kwok et al., 1990 and 1991; Kwok and Cunningham, 1993) at the Alaska SAR Facility processed the SAR imagery into ice type (classification) products and ice motion products for areas north of 73°N within the Alaska SAR Facility station mask. Because the geographic domain of the Geophysical Processor algorithm had not yet been successfully extended southward of 73°N

for routine ice motion processing by the ERS-1 GPS at ASF, I was unable to readily obtain SLIP ice motion products through routine processing efforts. In addition, the ASF processor was known to have problems locating, and tracking ice features when ice was undergoing major deformation, and when ice motion was very rapid (Kwok and Cunningham, personal communication). These conditions are quite characteristic of the SLIP. For example, my visual examination of 1991/2 SAR imagery mosaic strips revealed that during major polynya growth stages the SLIP ice was driven more than 100km southward during the three day period between successive images. The SLIP region is considered to be a highly dynamic (divergent, large shear) area while the region encompassing the Arctic basin ice pack is more quiescent (Rothrock and Stern, 1992). Because of the problems in using the standard means of creating ice motion products from these SAR images, special processing was necessary to create ice motion data for the SLIP region. As a result, all of the SLIP ice motion products described in this dissertation were obtained through special request processing using the Jet Propulsion Lab's GPS. I was able to assist with the actual ice motion processing phase, working directly with Ron Kwok, Shirley Pang, Amy Pang, and Glenn Cunningham of the Jet Propulsion Lab to obtain these SLIP ice motion products. I had the opportunity to visually examine the ice motion products as soon as they were produced and to collaborate with JPL staff in fine-tuning the GPS algorithm used for my products.

In order to create the SLIP ice motion products, I first selected approximately 50 SAR image pairs (Note: these are pairs of individual images separated in time by three days, rather than multi-image mosaic strips) from the ASF archives of ERS-1 satellite passes over the SLIP region to be processed into ice motion products. The image pairings were chosen manually based on their coverage of the SLIP, the amount of geographic overlap between scenes, and the presence of readily identifiable features common to both images. This selection process resulted in my choosing some image pairs which overlapped completely in terms of spatial domain, and others which overlapped as little as 10%. As a general rule, this overlap should be 20% or more to insure enough points for GPS tracking and to insure good quality results (Kwok and Cunningham, 1993). However, the ice displacement at the SLIP was often too great for this image overlap requirement to be realistic. The selected images were then sent to the Jet Propulsion Lab (JPL) in Pasadena to be geocoded (i.e., mapped to a polar stereographic map projection), and radiometrically-corrected. This was necessary to avoid any possible format incompatibility with the JPL Geophysical Processor that was going to attempt to create the ice motion products.

To determine data quality, I inspected each of the tiepoint (ice motion vector endpoints) grids, and the vector fields associated with each SAR image pair (see Figure 2.5 for an example), point-by-point after GPS processing attempts. In addition to my visual inspection of data results, three out of four possible pre-existing filters built into the JPL GPS algorithm were applied at intermediate stages in the vector creation procedure to automatically check GPS tracking results and to insure quality motion products before a motion product was generated. The three original filters used were standard processing filters that proved to be applicable to this SLIP imagery processing once their thresholds were adjusted to accommodate the region's motion characteristics. (See Kwok and Cunningham (1993) for a complete description of algorithm and filters; filter 2 did not apply to the SLIP environment). A new filter, filter 5, was added to the algorithm during this SLIP project to remove erroneous ice crossings (i.e., endpoints that tracked across land) from the products.

The final SLIP vector products used in this study were acquired through a series of four different JPL GPS processing attempts. My initial GPS run attempted to create motion products for all 50 SAR image pairs that I had selected prior to my arrival at JPL. The "supervised" GPS basin algorithm for this first GPS run, (Kwok, personal communication) was set up with the F1 filter turned "off", an area or "patch" size of 32 pixels, and the 5km SSM/I (Special Sensor Microwave Imager, DMSP satellite) sampling grid used for ice position determination. The basin algorithm was chosen for use. as it is generally employed to track ice within an ice pack (i.e., middle of the Bering Sea ice pack) rather than at an ice edge (i.e., marginal ice zone). The F1 filter determines whether ice feature matching results meet acceptable processor thresholds, based on how well a mathematical representation of an ice feature correlates with a potentially matching ice feature in a subsequent image. This filter was initially thought to be too large a constraint on feature matching within the SLIP imagery as it might cause potentially real matches to be thrown out. Gridpoint motion (representing ice motion) was estimated by the GPS by checking all possible feature matches within a "pre-specified" area or patch (generally 3-5km). The closest, best algorithm-based matches were determined through the use of FFT and cross-correlation techniques built into the algorithm. According to the GPS, acceptable ice motion products were all individual ice displacement vectors that met standard deviation and quality threshold criteria for acceptable data, as specified within the GPS algorithm filters.

The first processing run resulted in production of 24 vector products (i.e., a product

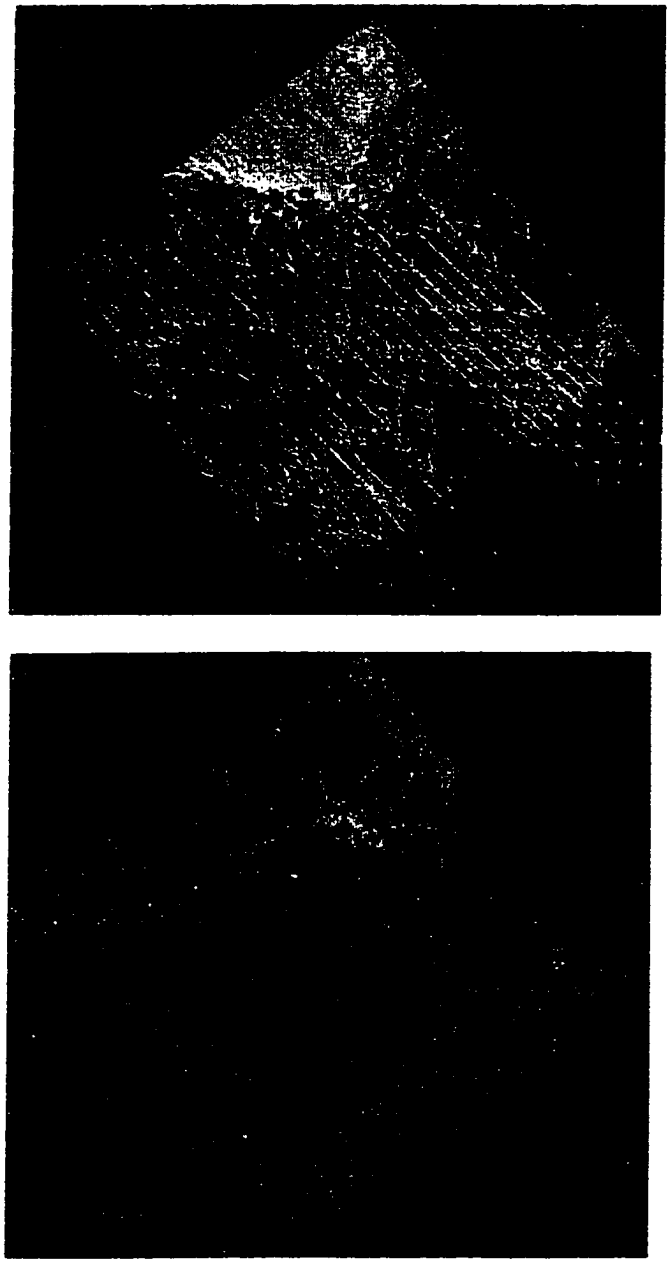

Figure 2.5: An example of a geo-coded SAR image pair. The source image (top) and the target image (bottom) are separated in time by three days and in this case, only a small overlap in geographic domain. Vectors represent ice motion and a 5 km grid is used for vector tiepoints. Deformation in the grid represents divergent motion within the ice field if resolvable at the 5 km grid scale. (PV-Wave software for viewing imagery and GPS products in this format is courtesy of H. Stern, personal communication).

is a set or field of ice motion vectors representing the displacement of ice floes located within the domain of a specific image pair) of varying quality and vector quantity, about a 50% success rate in production of products from image pairs. Errors in GPS processing that were visually apparent in these 24 products included missed manually trackable features, bad vectors along the edges of the imagery, an occasional long vector within a short vector field, and butterfly-like overlaps in the grids of the most rapidly moving ice fields.

In an effort to remove some of the undesirable aspects of the first processing results, the entire SAR image set (50 pairs) was then processed a second time with algorithm adjustments. During this second run, the F1 filter was turned "on" for all but two of the images, and a slight adjustment was made to the contrast thresholds. One new vector product (in addition to recreating the 24 products from the first run) was created during this run. While this run resulted in virtually the same success rate in terms of number of vector products, there were far fewer vectors (30-50% less trackable matches) within the products. The changes in the algorithm set-up eliminated some of the bad vectors, but also eliminated the good vectors on the south side of St. Lawrence Island in many of the products. As a result, even products with very heavily populated fields south of the island had their vector fields significantly reduced. In addition, all of the vectors within the polynya region itself were eliminated. This loss of polynya vectors was not desirable as vectors within the polynya, if correct, would have been quite valuable to my study. Finally, the remaining vectors' magnitudes in three products were actually larger than those determined for those products by the first processing attempt.

A third processing run was then undertaken with the F1 filter "on" and a new patch size of 64 to see how the patch size affected the feature tracking/area matching process. This larger patch size led to a reduction in the motion grid distortion in many cases. Although many of the "disappearing" vectors were restored near the actual polynya, the vectors were still sparse on the south side of the island and vector magnitudes were small. Additionally, the tracking results were still questionable in a number of the products. In one case, vectors indicated that ice flowed directly across St. Lawrence Island. Other products simply had bad matches that I could identify by visual inspection of the ice features.

The fourth and final processing attempt was set-up with the F1 filter turned "off", the original patch size of 32, and a new filter for removing the butterfly or "criss-cross" ice motion overlap seen on the vector product grids in a number of cases. This algorithm set-up resulted in the return of tiepoints or vector endpoints south of the island and clean (i.e.

no overlaps) grids.

In the end, I was successful in obtaining 25 vector products from the original 50 SAR image pairings using the JPL GPS. The final products I used were drawn from results from all four processing attempts. These 25 final ice motion products were distributed in time throughout my study period, although the highest concentration of products corresponded to the main polynya event of the winter (February-March 1992). The resulting ice motion products are discussed in Chapter 3 with respect to the SLIP events of Winter 1991/1992.

2.2.4 AVHRR: AVHRR are multispectral (multi-band) passive radiometers that collect and discriminate radiated and reflected electromagnetic energy from the earth's surface (Massom, 1991). Energy detected by the radiometer in the thermal infrared band (Band 4; used extensively in Chapter 4) is that emitted from the surface or "close to the surface" of an object in the wavelength range of 10.3 to 11.3μm. Brightness temperatures within the sensor's field of view can be related to actual surface temperature differences of materials. In the case of sea ice, these temperatures will include the presence of sea ice as well as any open water within the field of view.

All AVHRR imagery data presented here were acquired from the National Weather Service Forecast Office, Anchorage, and from the GeoData Center archives of the Geophysical Institute, University of Alaska Fairbanks. The AVHRR HRPT (high resolution picture transmission) image pixel size is 1.1km near the center of the image, but degrades to 6km at the swath edge. Image size is 100km x 100km. HRPT images include 2048 samples per scan line. The calibrated imagery has 1024 digital levels (10 bit precision).

The raw HRPT data were also calibrated and mapped to represent fields of actual surface temperatures such as cloud top temperatures, sea surface temperatures and ice surface temperatures. I calibrated and mapped all of the AVHRR imagery presented here using LAS (Land Analysis System, an image analysis package) Autoregistration modules based on NOAA's calibration coefficients (Kidwell, 1991). I also geo-registered the imagery to a polar stereographic projection identical to that of the SAR imagery by using LAS auto-registration modules. Then I mapped (and color-coded) all of the AVHRR Band 4 imagery used in my study to a temperature range of -47°C to 3.8°C based on the HRPT data's Digital Number (DN) range of 0 to 1024.

The AVHRR imagery discussed in the following chapters represent only Band 4 data as the images are winter dark period scenes chosen for their minimal cloud cover and

close correspondence to the time of SAR data acquisition. Typical methods of surface temperature determinations from AVHRR use daytime imagery and a regression formula including thermal infrared data from two channels and station air temperature (assumed to approximate snow and ice skin temperature). Massom and Comiso (1995) found that the standard deviation of their regression results when compared with in situ data was about 0.5°C over leads and polynyas. Although many cloud masking, atmospheric filtering, and "sea ice extraction" methods exist (Ebert, 1987; Key, 1990; Haefliger, et al., 1993; Maslanik and Key, 1993; Massom and Comiso, 1995), there are no established procedures for filtering clouds and atmospheric effects in thermal IR (TIR) data acquired during dark winter periods. According to Massom (personal communication), when only one AVHRR band can be used in AVHRR temperature analyses, Band 4 data should be used as atmospheric transmission is greater at this band. Although generally quite "noisy", Band 5 was another potentially useful TIR option in some cases, but since it is more sensitive to water vapor (McMillan and Crosby, 1984) than Band 4, I did not attempt to use it. In addition, Band 4 data generally contain more signal from the earth's surface and less from the atmosphere (McMillan and Crosby, 1984). Therefore, I decided that the use of unfiltered Band 4 data was an acceptable method of determining ice surface temperature. As Yu and Rothrock (1995) showed that multi-band regression and single-band technique temperature estimates had essentially negligible differences. I assume that my single band temperature mapping standard deviation is on the order of that of Massom and Comiso (1995).

A formal review of AVHRR theory and initial sea ice applications can be found in *Satellite Remote Sensing of Polar Regions* by Massom (1991). An additional collection of papers on AVHRR applications research, and a formal statement on "where do we go from here", as compiled by the scientific user community, can be found in the *Annals of Glaciology, Proceedings of the Symposium on Remote Sensing of Snow and Ice, Volume 17* (1993).

2.2.5 SAR/AVHRR Analysis Technique: In order to draw on the strengths of both ERS-1 SAR (high spatial resolution and "all weather capability") and NOAA AVHRR satellite data (daily repeat cycle and temperature mapping), I combined the different imagery using a technique known as the Hue-Lightness-Saturation (HLS) color model (Harris et al., 1990) to create a three-banded red-green-blue (RGB) graphic product (Glueck and Groves, 1994). The HLS color model is based on the concept that color may be represented as a three dimensional solid: hue, lightness, and saturation. Hue is defined as being within the range

of visible spectra. Lightness is light intensity expressed as a gray scale ranging from black to white. Saturation refers to the purity of the color. i.e., how much white is mixed with the color.

The two most critical aspects of this HLS to RGB procedure were the image autoregistration and calibration procedures used to ensure geographic co-registration between the two types of satellite imagery. Joanne Groves (UAF Geophysical Institute) and I developed an automated procedure to take the imagery from its initial form through registration and calibration stages and then through the HLS model using LAS (Land Analysis System) software developed for AVHRR at the EROS Data Center, software for ERS-1 SAR imagery written at the Alaska SAR Facility (ASF) Interactive Image Analysis System Lab (IIAS), and ephemeral data (i.e., satellite position, data acquisition time, navigational data) provided with the imagery.

For the SLIP regional analyses, I assigned the temperature range from the AVHRR TIR band (Band 4) to the hue component of the HLS model. The thermal IR band data of individual AVHRR images for February 21, 24, 27 and March 1, 1992 were calibrated, geo-registered to the same map projection as the SAR data. and mapped to represent surface temperatures. The lightness component of the HLS model was represented by the backscatter range of the corresponding (in time and space) SAR imagery. (Note: In this procedure I used SAR image mosaic strips made from individual images, NOT the individual SAR image frames independently). The final HLS component, saturation, was represented by a uniform saturation value. Thus, my combined HLS product yielded a three-banded graphic product with temperatures distributed from blue (cold; -47°C) to red (warm; +3.8°C) and a spatial detail distributed as a grey scale from black (dB=-25.5) to white (dB=0) when converted to an red-green-blue (RGB) format.

These HLS products provided my first look at variations in temperature across the polynya regions in the highly detailed SAR imagery, and allowed me to determine. in a broad sense, potential areas of open water as well as ice at different stages of growth. In my work, I determined sections of open water, active ice formation (distinguished as areas with a mix of open water and frazil. i.e., areas -9°C and warmer), and older ice by using the SAR and AVHRR imagery (independently as well as in combination) for the February 1992 southern SLIP event. Once I determined basic ice-water boundaries. I used LAS to measure the length, width, and surface area for each distinct section. As the eastern portion of the SLIP extended past the SAR image boundary, I was forced to count "eastern portion" AVHRR pixels guided by the "western" temperature/ice correspondences to

determine the eastern areas of ice or open water. Results from these SAR/AVHRR procedures will be presented in Chapter 4.

2.2.6 DMSP SSM/I Ice Concentration: SSM/I data is another currently available remote sensing product useful for examining ice field characteristics. It is used here primarily as an additional validation tool. SSM/I is a passive microwave sensor as opposed to the active SAR sensor. Daily brightness temperature data were obtained for the study period from NSIDC (National Snow and Ice Data Center, Boulder; NSIDC, 1992). These brightness temperatures were derived from the DMSP F11 satellite SSM/I data. The NASA Team algorithm (Cavalieri et al., 1984 and 1991; Gloersen and Cavalieri, 1986) was applied to the brightness data to create daily ice concentration fields. Daily ice concentration fields were obtained for first year ice, then multi-year ice, and finally a composite field. Only the first year ice field was used in my work as the Bering Sea rarely contains multi-year ice. Although ice concentration derived using this algorithm is known to be in error by at least 10%, it was the most reliable ice concentration data for this region during the time period of study.

2.3 Analytical and Numerical Models: Simulation of the SLIP

Modeling a SLIP is a challenging task due to the spatial and temporal scale of the polynya event (the opening and closing of the polynya), and the scale of interactions between the polynya and the ocean/atmosphere system. Global climate models such as the Geophysical Fluid Dynamics Laboratory Model (GFDL; Manabe and Wetherald, 1987; Wetherald and Manabe, 1988) and the Goddard Institute for Space Studies Model (GISS; Hansen et al., 1983; Rind, 1988) typically have grid sizes in excess of 400km, much larger than the SLIP. Further, the scales and scopes of the interactions involving the atmosphere, ocean, and sea ice requires a model capable of incorporating all of these components in an "interactive" or "coupled" manner. Although others have developed 1-D analytic models for the SLIP, these models do not necessarily allow for the complex feedbacks that take place between the ice, the atmosphere, and the ocean. I have used four different approaches to modeling or predicting the SLIP's development, ice circulation, and potential dense water production. Two of these models, the Pease Model (Pease, 1980) and the two-part CMI/CMD Model (Cavalieri and Martin, 1994) are simple analytical thermodynamic models. One model, the CW2 (Wade, 1993) is a one-dimensional numerical model based on energy balance computations. These three models will be presented in later chapters.

2.3.1 ARCSyM Structure: The fourth and final model used in my research is the ARCSyM (Lynch et al., 1995), a numerical regional climate system model of the Arctic atmosphere-ice-ocean system. My work represents the first application of such a model to predict and investigate a polynya. The ARCSyM (Lynch et al., 1997) has the potential to more realistically simulate the SLIP with minimum external forcing of the model, because of the model's high temporal (as high as 25 seconds) and spatial resolution (7km) in comparison to other climate models. Due to the complexity of the ARCSyM and the fact that this model is used throughout the next chapters, I have chosen to present a description of the model and basic experiment scheme here rather than in later chapters.

The ARCSyM model domain (Figure 2.6) chosen for this simulation is a region centered south of the Bering Strait covering much of the eastern Bering Sea shelf as well as coastal Alaska and Siberia. The southern boundary of the domain corresponds loosely to the shelf break. The 7km horizontal grid spacing used here is small for a regional climate system model (regional climate system model resolution typically ~60km resolution; standard GCM grid spacing is > 400km). The grid, centered on 62°N, 168°W, includes 106 points in the X-direction (west to east) and 82 points in the Y-direction (north to south). The model contains 23 vertical levels with the highest vertical spatial resolution located in the lower boundary layer. The top layer of the model represents a 50mb atmospheric level. The atmospheric model's time step is 25 seconds while the ice model's time step is five minutes.

The atmospheric model component of the ARCSyM is based on the NCAR RegCM2 (Regional Climate Model, Version 2; Giorgi et al., 1993a), a hydrostatic, primitive equation model with a terrain-following vertical coordinate and a staggered "Arakawa B" horizontal grid. The atmospheric dynamics component of the model is based on the MM4 (NCAR/Penn State Mesoscale Model Version 4) (Anthes et al., 1987). The MM4 incorporates the land surface exchange and vegetation model, Biosphere-Atmosphere Transfer Scheme Version 1E, or BATS1E (Dickinson et al., 1993), and the CCM2 radiative transfer scheme (Briegleb 1992a, 1992b). The BATS1E scheme includes a vegetation/canopy layer, a multiple-layer soil scheme, and a snow cover distributed uniformly across a grid cell.

European Center for Medium Range Weather Forecasting (ECMWF) analyses (Trenberth, 1992) provided the initial and boundary conditions for my ARCSyM model experiments. The gridded ECMWF archive, obtained from National Center for Atmospheric Research (NCAR), consists of six-hourly analyses on 14 pressure levels, using

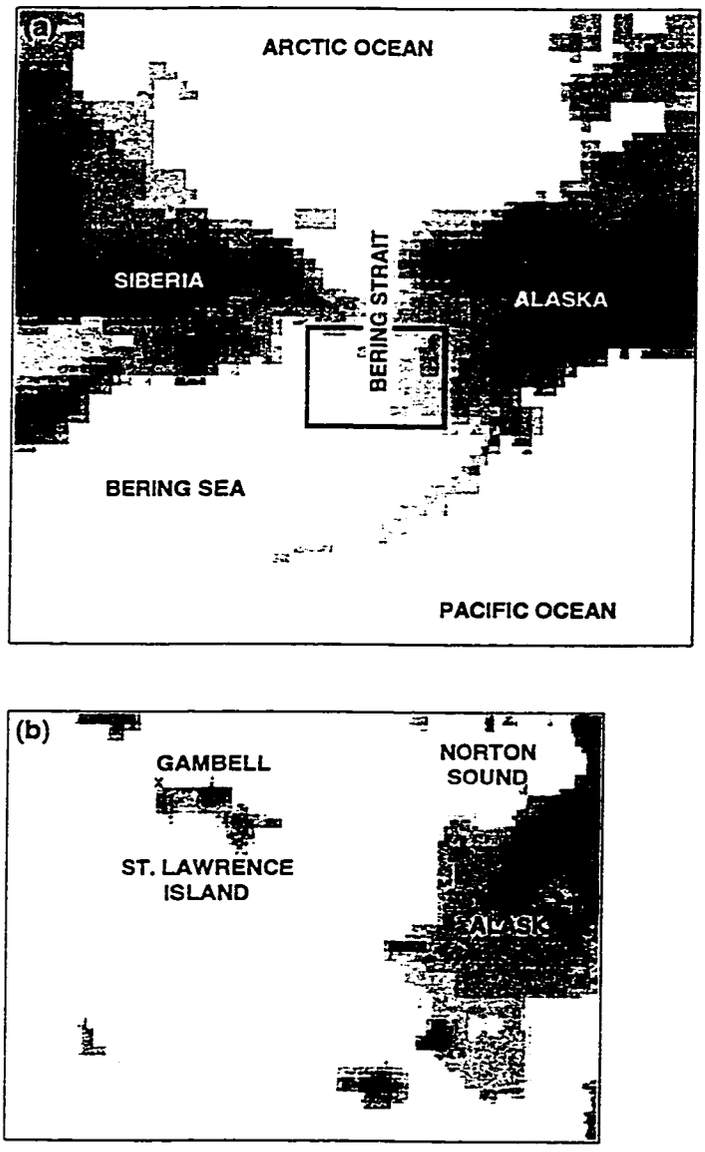

Figure 2.6: ARCSyM Model Domain for all SLIP Simulations: (a) Overview map of the Bering Sea. Alaska. and Siberia. The highlight box indicates the model domain used in the SLIP project. (b) The model domain showing Gambell. St. Lawrence Island. The simulated SLIP. February 1992 southern event. develops off the southern coast of St. Lawrence Island.

a T42 truncation from the ECMWF T106 spherical harmonics (Lynch, personal communication). The archived fields used as input for the model's atmospheric component include geopotential heights, temperature, wind, humidity, surface pressure and orography. The wind and pressure fields used to "drive" the model are allowed to change over time according to the atmospheric model's determinations during the simulation period. This atmospheric model is coupled to a dynamic-thermodynamic sea ice model (Lynch and Chapman, personal communication). The physical parameterizations used in the ARCSyM atmospheric component are discussed in Lynch et al. (1995 and 1997).

The sea ice model for the ARCSyM has been incorporated (Lynch and Chapman, personal communication) to resolve the small features required in the SLIP simulation. The dynamics portion of the sea ice model is based on a momentum balance for a mass of ice within a grid cell, and the cavitating fluid ice dynamics scheme of Flato and Hibler (1992; also Hibler, 1979) with the anti-diffusion option. The cavitating fluid rheology parameterizes the internal ice stresses in a computationally efficient and stable manner at higher resolutions (Flato and Hibler, 1992). In such a cavitating scheme, the ice is considered to be an ideal fluid free to diverge or shear, i.e. to flow freely, and to open up as much as desired or to "cavitate" freely. However, although the ice is not considered completely incompressible, it is not "allowed" to converge unless the internal pressure is greater than a set "failure threshold" value (Hibler, personal communication; Flato and Hibler, 1992) or limiting compressive ice strength. The pack ice is assumed to be a two phase medium in which the ice phase is relatively rigid and the water phase has no strength at all. The composite resists compaction due to the ice phase and is free to diverge due to the water phase. As it is not completely rigid, the ice phase will compress and thicken until a limiting compressive strength is reached as determined by the ice thickness and the ice compactness (Lynch et al., 1997; Flato and Hibler, 1992).

The thermodynamics within the ice model are based on the scheme of Parkinson and Washington (1979). The ice model thermodynamic formulation (Parkinson and Washington, 1979) includes a simple two layer model that allows for ice, leads and snow cover. Thermodynamic changes in thickness of the ice and snow layers are based on energy balances at the various interfaces. Turbulent fluxes are calculated using the standard formulations. Bulk Richardson numbers are calculated separately over ice and open water surfaces following Curry and Ebert (1992).

The initial sea ice cover within the domain was set to be a uniform thickness of 1.5m to represent the seasonal ice cover of the Bering Sea. Although this thickness is at

the high end for the Bering Sea, it was thought to be an acceptable starting point given the uncertainty of the model's applicability to this region at this resolution. Ice concentration was set to be 99.5% within each grid cell. Initial ice edge data were obtained from the weekly ice concentration charts of the Navy/NOAA Joint Ice Center. The ice model does not allow for differing ice classification types. Snow cover over land and ice was initialized to 0.3m depth at all grid points within the domain.

In order to determine the role of ocean currents in periods of weak and strong atmospheric forcing, the model was run once with a "swamp" ocean, and once with a "barotropic" ocean component. The "swamp" ocean is prescribed in terms of thermodynamics and is without currents. The barotropic ocean includes currents for the period of February 18-March 2 derived from a simulation by a two-dimensional (vertically averaged) barotropic circulation model (a 21km resolution ice-ocean model; Proshutinsky, 1988). The ocean circulation was forced at the surface by winds obtained from the ARCSyM "swamp" simulation. Bilinear interpolation was used to interpolate the ocean data to the finer ARCSyM grid resolution of 7km. There was little temporal variance in the overall current field within the model domain during the ARCSyM simulation period, due to the persistence of northerly winds over the two week forecast period I examined. So, the current field was averaged in time and held constant in time. The simulated ocean currents were added to the ARCSyM as part of the forcing on the ice drift for the entire simulation period of the barotropic experiment (i.e., February 18-March 2). Ocean surface current strength and direction in the region surrounding St. Lawrence Island are known to be quite susceptible to variability in the prevailing wind direction and stage of polynya development (Schumacher et al., 1983; Muench, 1989). The simulated ocean circulation field I used in the ARCSyM is in agreement with the ocean circulation typically observed within the model domain boundaries in terms of flow direction (Schumacher et al., 1983; Overland and Roach (model data), 1987). However, the simulated ocean circulation tended to be stronger than previously observed (Schumacher et al, 1983) with current meters. Differences in observed and simulated ocean circulation may be due to many factors, including model parameterization of the currents, the assumption of a constant current field (temporally unvarying current field), and differences in atmospheric forcing of the ocean during this period. Fully coupling a varying ocean circulation model to ARCSyM was beyond the scope of my research, although this would have led to a more accurate representation.

For both the "swamp" ocean and the "barotropic" ocean cases, initial sea surface temperatures were derived from the data of Shea et al. (1992), with modifications for the

observed ice cover. Unmodified initial sea surface temperatures were only applicable outside the ice pack. Modifications for the ice-covered regions within the domain include a resetting of the sea surface temperatures to -1.8°C under the ice pack. This was necessary as the unmodified sea surface temperature data did not take ice cover into consideration and, thus, were too warm in areas of ice cover.

Model coupling (Lynch et al., 1997) consisted of passing air temperature, u and v components of the wind, specific humidity, snow cover, and radiative fluxes to the ice model every half hour. The ice/ocean model computes the energy balance and ice distribution over non-land grid points. The surface temperature, sensible and latent heat fluxes, and ice and snow distribution are then passed to the atmosphere/land model. The model allows snow to accumulate and/or melt over the land through the BATS1E scheme (Dickenson et al., 1993). Behavior of snow on ice is also determined by the surface energy balance. Overall, the use of vertically-varying exponential boundary conditions in this model minimized the forcing required at the surface level and, therefore, allowed the model to generate its own behavior from initial conditions as much as possible. Climate system models such as the ARCSyM, which operate at high resolutions, are in their early stages of development, and there are still no known existing models that "incorporate a completely coupled atmosphere-sea ice-ocean system of this type, with this many degrees of freedom" (Lynch, personal communication).

2.3.2 ARCSyM SLIP Experimental Design: In my research, I performed two separate primary experiments and a series of intermediate "tuning" experiments using the ARCSyM model to predict the SLIP. My first primary experiment consisted of using the ARCSyM model coupled to a "swamp" ocean. The model run was initialized at 00Z February 18, 1992 using ECMWF meteorological analyses and run until 00Z March 2, 1992. The first primary model run employed wind forcing of ice over a static or "swamp" ocean. Within the two week span of this experiment there was a period of strong wind forcing (February 24-27) and a period of weak wind forcing (February 27-March 1). Prior to my second primary experiment, the "swamp" model scheme was also used to perform a series of intermediate or secondary "tuning" experiments to determine a more realistic drag coefficient than originally used in the primary "swamp" ocean experiment (Lynch et al., 1997). In my second primary experiment, the ARCSyM model was coupled to a "barotropic" ocean, and run for the same two weeks as the "swamp" ocean experiment (February 18-March 2, 1992) so that the impact of ocean circulation forcing on polynya development (i.e., ice circulation)

could be better assessed during the weak and strong wind forcing regimes encountered in the "swamp" ocean experiment. This second primary run also employed wind forcing of the ice but over a dynamic or "barotropic" ocean. It also included the more realistic drag coefficient between wind and ice. Results from these experiments will be discussed throughout the next three chapters in relation to my observations and results of the three other models employed.

Chapter 3: ICE CIRCULATION AT THE SLIP

3.1 Introduction

In this chapter, SAR imagery (December 1991- March 1992) and ARCSyM simulation results are analyzed in conjunction with regional weather observations to document SLIP events. "Special request" ice motion products created from ERS-1 SAR imagery via the Jet Propulsion Lab's GPS (Kwok et al., 1990 and 1993; Vesecky et al., 1988) are used to illustrate the ice circulation associated with the SLIP during Winter 1991/1992. Simulated ice circulation fields from my ARCSyM SLIP experiments are presented for the southern SLIP event periods of February 24-27 and February 27-March 1, 1992.

3.2 Observed Data: Imagery, Meteorological Observations, and GPS Products

Imagery for this project was selected from a descending (southward) orbital pass over the western 2/3 of St. Lawrence Island. Data acquisition included 164 individual images (five to eight images per pass) for the three-day passes of December 29, 1991 to March 28, 1992. The SAR imagery were combined into mosaic strips for each satellite pass over St. Lawrence Island for preliminary visual analysis purposes. This resulted in 29 strips, each of which extends from ~50 km north of St. Lawrence Island south to the ice edge.

Meteorological data for my SLIP analyses included surface wind observations and air temperatures for the period of December 1991 to March 1992 (source: National Weather Service). Data from Gambell, Alaska (situated on the north side of St. Lawrence Island) were the primary station observations used. Additional data included six-hourly (0000, 0600, 1200, 1800Z) sea level pressure grid data (2.5° x 2.5° grid spacing) obtained from the Fleet Numerical Oceanography Center (FNOC). Geostrophic winds derived from the pressure fields were reduced by 30% and rotated by -15° to create a third wind data set, RRWIND. The reduced-rotated wind usage was suggested by Schumacher et al. (1983) to approximate surface winds, which was necessary because surface data from the south side of the island did not exist. I found that the computed RRWIND at 62.5°N, 171°W was more coherent with the observed Gambell data, and more closely located to the primary polynya activity, than RRWIND at 65°N, 171°W, or 60°N, 171°N. All three sets of "observation-based" wind data, i.e., RRWIND at 62.5° N, 171°W, geostrophic wind at 62.5°N, 171°W, and Gambell station wind, were applied in the SLIP analyses.

In addition, the 0000Z gridded sea level pressure data were plotted as 0000Z sea

level pressure charts to illustrate the synoptic situation occurring over the study region at the closest time possible to the satellite passes. For example, the 0000Z February 22 sea level pressure chart was used to represent the synoptic-scale atmospheric circulation over the SLIP region during the 2239Z February 21 ERS-1 SAR pass over the polynya.

The ice motion products presented in this chapter are unique in that they are the only ERS-1 SAR-based ice motion products successfully produced by a GPS for the SLIP region. The 25 vector products obtained from my original 50 SAR image pairings (100 images) are described Tables 3.1 and 3.2. Because of their uniqueness. the products created for this project were also used by JPL to assist in development of the proper filter tunings and algorithms for highly dynamic regions in hopes of making this processing routine in a later generation GPS (Kwok and Pang. personal communication). In fact, the RADARSAT program has drawn from experiences with the ERS-1 GPS and is now creating new ice motion products for the Arctic Region using a "next generation" RGPS or RADARSAT GPS.

3.3 The SLIP Events of Winter 1991/1992

The SLIP is not a constant or continuous area of open water in the ice pack. Rather. it undergoes definite opening and closing events. A polynya event is defined here as an episode that begins with wind moving ice away from St. Lawrence Island and the initial appearance of open water. The polynya expands to a maximal open water extent. with associated formation of new ice. The end of a polynya event occurs when a distinct weakening of winds or a shift in the winds takes place, causing the open water to freeze or the ice to move back toward the island (or both), closing the polynya. The outline of the polynya may, however. remain visible in the ice pack for a period of time, even though there is no open water present.

The SAR imagery for December 1991-March 1992 showed three or, perhaps, four distinct wind-driven polynya events: three occurred off the southern coast of St. Lawrence Island. and one occurred off the northern coast of the island. The first south coast event reached a peak in mid-January and early February. The second south coast event began in mid-February (between the 18th and 21st) peaked in late February-early March. and ended soon after. These two southern events were separated in time by a brief wind-driven polynya event off the northern coast that occurred between February 6 and 15. The third and final southern polynya event visible in the SAR imagery began in mid-March and ended in late March/early April.

Although the polynyas were well-defined in the SAR imagery. the length of time

Table 3.1: ERS-1 SAR GPS Ice Motion Products. Products created during this study are listed here by "source" image (contains vector start points) date, "source" image ID, "source" image geographic center, and corresponding "target" image (contains vector endpoints) detail. Also listed is the number of vector tiepoints (or ice motion vectors) obtained from each image pair. Letters next to each source image ID indicates the processing run (a= first run; b= second attempt; c= third attempt; d= fourth attempt) that produced the associated vector product. A vector product is composed of the ice motion vectors (ice features' displacements over the three day image time separation) created from a specific image pair. A "*" indicates an image pair time separation of six days. Breaks in table indicate approximate grouping by SLIP event (see text).

SOURCE IMAGE DATE	IMAGE ID & PROCESS	IMAGE CENTER LAT,LONG	TARGET IMAGE DATE	TARGET IMAGE ID	IMAGE CENTER LAT,LONG	NUMBER OF ICE VECTORS
Dec 29,1991	8754 c	63.2N, 171.4W	Jan 1, 1992	9287	62.7N, 171.6W	21
Jan 1, 1992	9287 d	62.7, 171.6	Jan 4	9454	62.3,171.8	20
Jan 4	9453 c	63.1,171.4	Jan 7	8609	62.8,171.5	8
Jan 25	10229 b	62.8,171.5	Jan 28	8902	61.9,172.0	65
Jan 28	8900 a	63.5,171.1	Jan 31	10716	63.6,171.0	72
Jan 28	8901 d	62.7,171.6	Jan 31	10717	62.8,171.5	122
Jan 31	10716 a	63.6,171.0	Feb 6 *	10428	63.5,171.1	69
Feb 12	10589 b	63.5,171.1	Feb 15	11702	63.5,171.1	51
Feb 15	11702 a	63.5,171.1	Feb 18	10759	63.5,171.1	14
Feb 18	10759 a	63.5,171.1	Feb 21	10911	63.5,171.1	15
Feb 21	10911 d	63.5,171.1	Feb 24	10987	63.5,171.1	75
Feb 24	10988 d	62.7,171.5	Feb 27	11744	61.9,172.0	71
Feb 24	10989 b	61.9,172.0	Feb 27	11745	61.2,172.4	73
Feb 27	11743 d	62.7,171.5	Mar 1	11443	62.2,171.8	27
Feb 27	11745 b	61.2,172.4	Mar 1	11444	61.5,172.3	40
Feb 27	11745 a	61.2,172.4	Mar 1	11445	60.7,172.7	31
Mar 1	11442 d	63.0,171.4	Mar 4	16570	62.7,171.6	162
Mar 1	11443 a	62.2,171.8	Mar 4	16571	61.9,172.1	187
Mar 10	16668 d	63.3,171.3	Mar 13	16734	63.6,171.0	20
Mar 13	16734 d	63.6,171.0	Mar 16	16778	63.3,171.2	27
Mar 13	16735 d	62.8,171.5	Mar 16	16779	62.5,171.7	31
Mar 16	16778 d	63.3,171.2	Mar 19	16818	63.5,171.1	45
Mar 19	16818 a	63.5,171.1	Mar 22	16862	63.6,171.1	75
Mar 19	16820 a	61.9,172.1	Mar 22	16864	62.0,172.0	71
Mar 19	16821 a	61.2,172.5	Mar 22	16865	61.3,172.4	156
Mar 22	16862 a	63.5,171.1	Mar 28 *	13284	63.5,171.2	53

Table 3.2: ERS-1 SAR GPS Ice Motion Products and Ice Motion/Wind Relationships (Part 1). Multiple entries for the same date indicate multiple SAR image pairings. A "*" indicates imagery six days apart. The term "Island Coast" refers to the geographic location of the ice vector start/ endpoints in relation to St. Lawrence Island, and does *not* indicate the direction of ice motion. GWIND is Gambell station wind. RRWIND is the rotated, reduced geostrophic wind at 62.5°N, 171°W.

SAR IMAGERY DATE	NUMBER OF ICE VECTORS	ISLAND COAST (N,S,Mix)	GAMBELL AIR T (°C)	ICE MOTION cm s^{-1} ; To (°)	GWIND m s^{-1} To (°)	ICE:GWIND SPEED %	RRWIND m s^{-1} To (°)	ICE:RRWIND SPEED %
Southern SLIP								
Dec 29-Jan 1	21	S	missing	26.8 SW (217)	8.9 SW (228)	3.0	missing	missing
Jan 1-4	20	S	-17.6	4.9 E (088)	7.3 SW (220)	0.6	3.6 SW (217)	1.3
Jan 4-7	8	S	-12.5	13.1 NW (319)	7.7 SW (238)	1.7	6.4 W (266)	2.0
Jan 25-28	65	S	-17.8	22.8 SW (219)	7.6 SW (213)	3.0	10.1 SW (211)	2.3
Jan 28-31	122	S	-18.3	6.4 S (178)	3.1 SW (226)	2.1	4.0 S (185)	1.6
Jan 28-31	72	N	-18.3	0.4 NE (032)	3.1 SW (226)	0.1	4.0 S (185)	0.1
Northern SLIP								
Jan 31-Feb 6*	69	Mix	-18.6	0.2 S (178)	4.5 SW (240)	0.04	3.6 WSW(255)	0.05
Feb 12-15	51	Mix	-8.7	0.1 ESE (107)	5.9 W (267)	0.02	1.7 NW (314)	0.1
Feb 15-18	14	Mix	-13.5	0.2 SSE (166)	9.2 W (267)	0.02	8.7 NW (299)	0.02
Southern SLIP								
Feb 18-21	15	N	-12.2	0.03 NW (314)	7.3WNW(279)	0.0	5.3WNW(275)	0.01
Feb 21-24	75	Mix	-16.1	0.2 SSW(193)	8.7 SSW(191)	0.02	11.1 S (183)	0.02
Feb 24-27	71	S	-15.5	34.2 S (189)	10.8 S (188)	3.2	11.5 S (181)	3.0
Feb 24-27	73	S	-15.5	31.4 S (187)	10.8 S (188)	2.9	11.5 S (181)	2.7
Feb 27-Mar 1	27	S	-20.7	20.7 SSE(168)	6.8 SSE (170)	3.0	8.2 SSE (160)	2.5
Feb 27-Mar 1	40	S	-20.7	11.0 SSW(196)	6.8 SSE (170)	1.4	8.2 SSE (160)	1.4
Feb 27-Mar 1	31	S	-20.7	11.0 SSW(196)	6.8 SSE (170)	1.4	8.2 SSE (160)	1.3
Mar 1-4	162	S	-21.5	5.8 SW (235)	2.9 S (186)	2.0	2.2 SSW(199)	2.6
Mar 1-4	187	S	-21.5	8.4 WSW(253)	2.9 S (186)	2.9	2.2 SSW(199)	3.8
Southern SLIP								
Mar 10-13	20	N	-17.7	0.02 NW (323)	4.3 SW (204)	0.0	1.8 ESE(126)	0.01
Mar 13-16	31	S	-21.1	28.9 SW (211)	6.2 SW (202)	4.7	7.8 SW(202)	3.7
Mar 13-16	27	N	-21.1	0.1 WSW(252)	6.2 SW (202)	0.02	7.8 SW(202)	0.01
Mar 16-19	45	Mix	-19.4	0.04 SSW(197)	12.3 SW (209)	0.0	13.4 SW (217)	0.00
Mar 19-22	71	N	-16.2	0.2 ENE (070)	7.8 SW (207)	0.03	10.0 S (181)	0.02
Mar 19-22	75	S	-16.2	13.6 SE (139)	7.8 SW (207)	1.7	10.0 S (181)	1.3
Mar 19-22	156	S	-16.2	12.6 SE (156)	7.8 SW (207)	1.6	10.0 S (181)	1.3
Mar 22-28*	53	Mix	-15.1	0.2 WSW(258)	3.4 WSW(240)	0.1	6.1 S (182)	0.03

that completely ice-free, open water existed was short and the actual area of completely open water was small. This was because atmospheric and oceanic conditions strongly favored new ice formation as soon as water was exposed. It was difficult to determine the actual amount of open water from the SAR imagery, as the very new ice and wind-roughened open water have similar radar backscatter characteristics during windy conditions.

3.3.1 South Coast Polynya Event of December 1991-January 1992: The south coast polynya event of December 1991-January 1992 can best be described in three parts. Part 1 is December 29, 1991 (date of the first ERS-1 SAR imagery available for this region) to January 7, 1992. This was a transitional period between "unknown" ice activity in December and the main polynya event of January 1992. Part 2 includes January 7 to January 22, 1992, the main southern polynya event of the month. Part 3 includes January 22 to January 31, 1992, the last brief appearance of polynya activity prior to the demise of polynya.

3.3.1.1 December 29, 1991-January 7, 1992: The first 1991/2 ice phase SAR imagery for the SLIP area (Figure 3.1) depicted a definite boundary line across the ice pack extending from east to west south of St. Lawrence Island on December 29, 1991. This line separated regions of the ice field with notable backscatter differences. By January 1, this boundary line had moved considerably southward to form the southern edge of a fan-shaped ice feature.

Ice motion vectors for the period between December 29 and January 1 shown in Figure 3.2 (also Tables 3.1 and 3.2) indicate displacement at 0.27m s^{-1} towards the southwest. Winds during this period averaged 8.9m s^{-1} from the north/northeast. Northeasterly winds such as those observed throughout January 1992 resulted from the strong Aleutian Low (Figure 3.3) and are typical of the Bering Sea winter atmospheric circulation.

From January 1-4, ice motion (Figure 3.2) was slower than that initially observed with speeds of 0.05m s^{-1} (0.6-1.3% of the wind speed), directed towards the east rather than the southwest. This change in ice motion was reflected in the SAR imagery (Figure 3.1) by the eastward progression of the fan feature and the separation of the fan's extension from the island.

Ice motion vectors depicted in Figure 3.2 for the January 4-7 SAR image pair

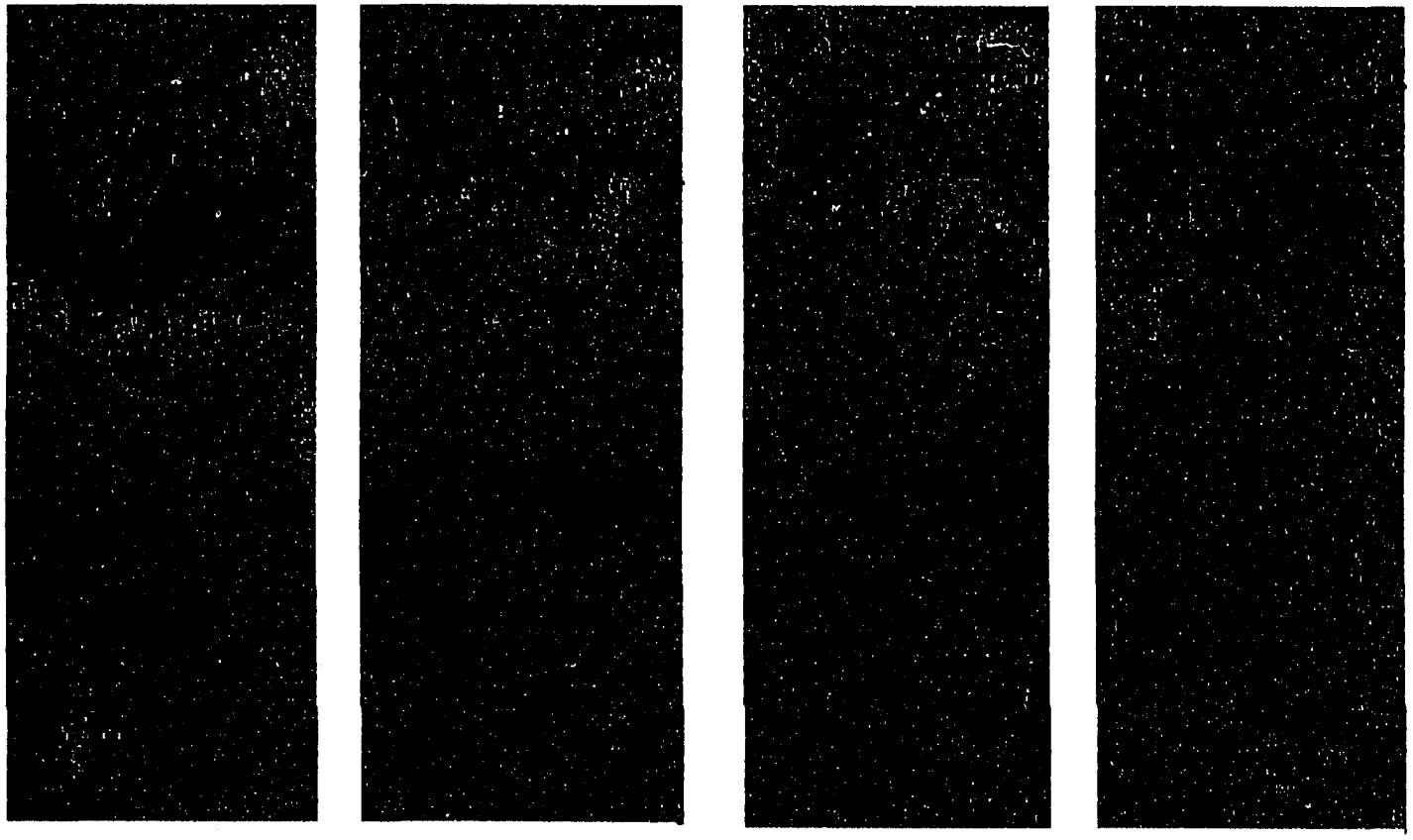

Figure 3.1: LoRes ERS-1 SAR image mosaics of the SLIP-December 29, 1991-January 7, 1992. Shown above are mosaics for (left to right): December 29, 1991, January 1, 1992, January 4, 1992, and January 7, 1992. Distinctive features within the ice field are indicated by outlines drawn on the mosaics. St. Lawrence Island is the main land feature outlined in the top 1/3 of the mosaic. Only the western 2/3 of the island will be evident in the SAR imagery discussed here due to the swath width of the imagery itself. Letters on the imagery indicate readily apparent features common to consecutive mosaics (3-day time separation) as a means of depicting ice motion. In this case, ice feature A29 and B29 shown on the December 29th mosaic have moved to their new positions, A1 and B1, respectively, on the January 1 mosaic over a period of three days. Also, the southern portion of the "fan" moves eastward in the time between January 1 (C1) and January 4 (C4), but disappears by January 7. This method of indicating motion of individual ice features (letter and date specific to a common feature) will be used whenever possible for all SAR imagery and GPS ice motion product maps presented here.

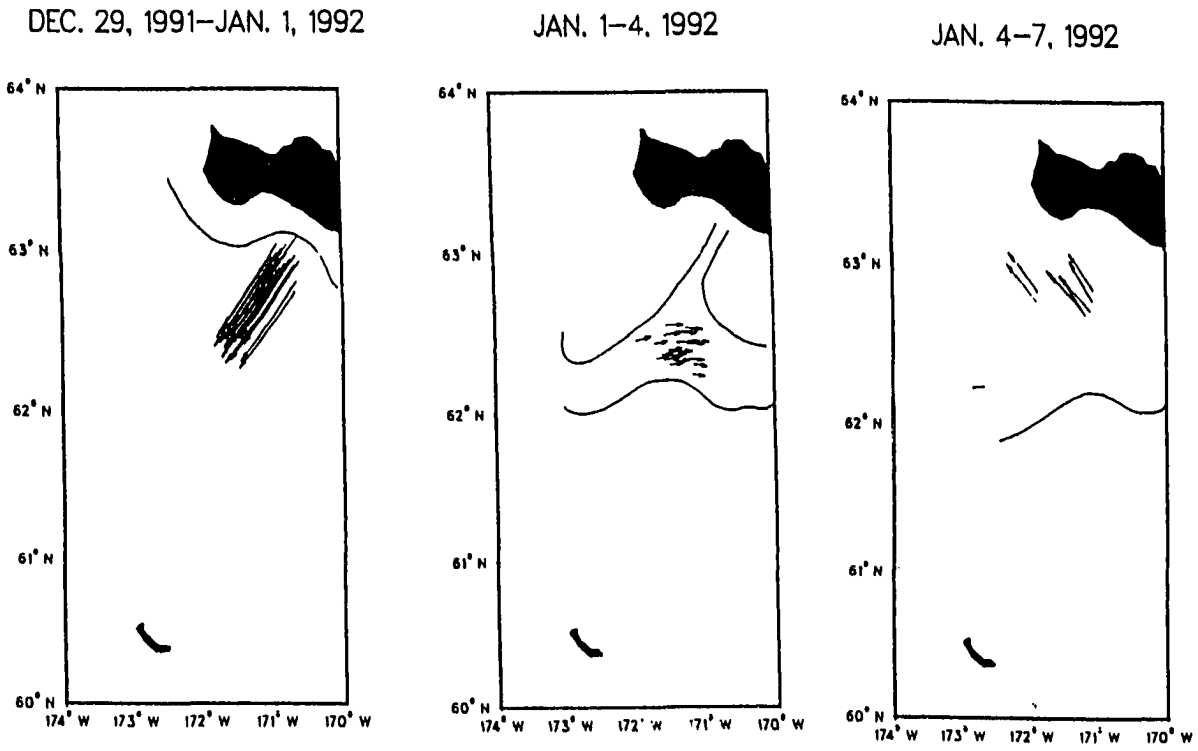

Figure 3.2: ERS-1 SAR GPS ice motion-December 29, 1991-January 7, 1992. Polynya development is indicated by outlines extending southward from St. Lawrence Island (solid black; St. Matthew Island is at the bottom of the diagram). Dates refer to dates of SAR imagery used to create the vectors. Polynya depiction is that observed in the earliest (source image) SAR image, i.e., for January 4-7, polynya is depicted as observed on January 4. (See also Tables 3.1 & 3.2 and Figure 3.1; Refer to Chapter 2 for ice motion methodology).

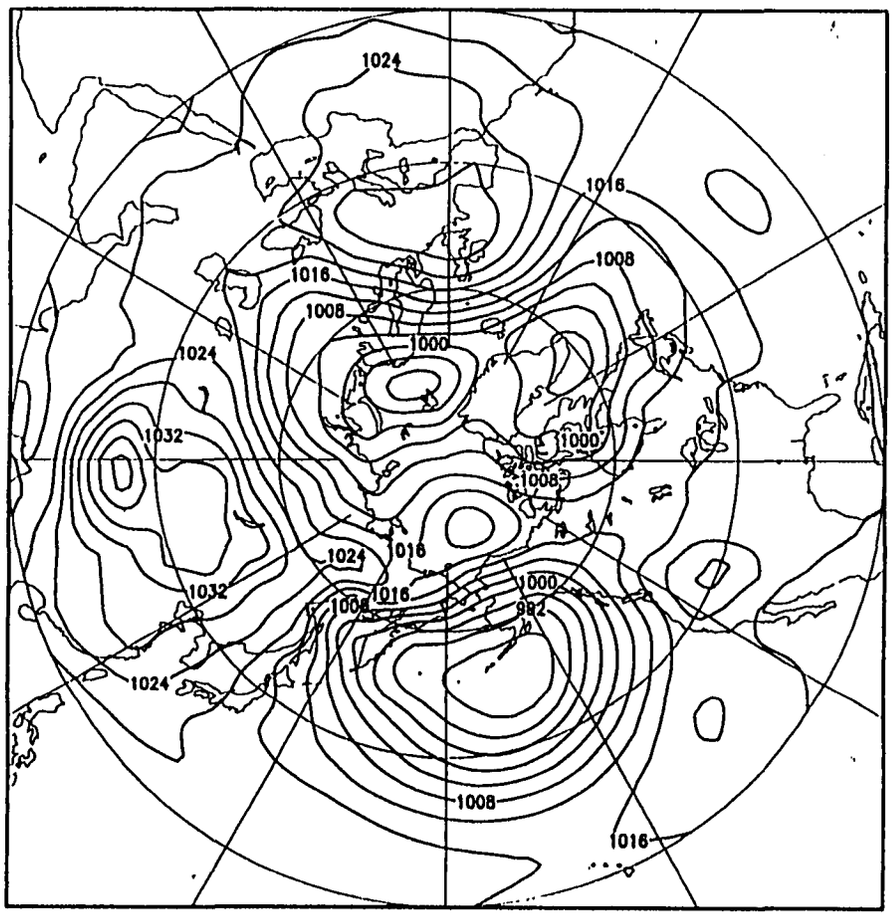

Figure 3.3: Monthly Mean Sea Level Pressure Map-January 1992. Note the position and intensity of the single Aleutian Low feature.

indicated a northwestward ice velocity of 0.13m s^{-1} in response to winds of 6.4-7.7m s^{-1} from the east/northeast. In other words, ice drifted at about 1.7-2% of the wind speed, and 50°-80° to the right of the wind direction. Again the ice's response to the shift in wind direction was evident in the SAR imagery of Figure 3.1 as the ice feature visible in the January 4th imagery was now positioned much farther north, just off the coast of the island.

3.3.1.2 January 7-January 22, 1992: The SLIP opened between January 7 and January 10, along the southern coast of St. Lawrence Island, marking the beginning of the January southern polynya event as shown in Figures 3.1 and 3.4. The darker area south of the island is the newly-forming polynya composed of a mixture of open water and new/thin ice. No ice motion products were successfully produced for the period from January 7 to January 25. I was only able to describe the ice motion associated with this polynya in a qualitative sense or by manually tracking features common to pairs of images as this turned out to be a very active period of ice circulation with very few recognizable features in common from image to image.

The January polynya extended along the entire south coast of the island by the time of the January 10 satellite passage (Figure 3.4), and it had taken on a shape resembling two lobes similar to the shape of the coastline. The lobes were separated by a north-south extension of older ice rubble. The arch-like features visible in the January 7 SAR (Figure 3.4) were now positioned farther south and on January 10 they formed part of the polynya's southern boundary (Figure 3.4). Between January 13 and 16, the polynya reached its greatest areal extent and by January 19, only broad areas of younger ice remained evident in the imagery of Figure 3.4.

3.3.1.3 January 22-31: Between January 22 and January 25, the polynya made a brief renewed appearance. SAR imagery for January 25 (Figure 3.5) showed not only two active polynyas along the island's south coast, but also a fan-shaped region of older ice resulting from earlier polynya activity. By January 28 (Figure 3.5), the areas of active ice formation had been completely filled in with ice, and the fan-shaped (narrow stem towards St. Lawrence Island) feature had drifted ~50km southward. Between January 25 and January 28, ice south of the island drifted at 0.23m s^{-1} (19.7km day^{-1}) towards the southwest (Table 3.1 & 3.2: Figure 3.6). The ice was traveling at a rate of 2-3% of the wind speed, but less than 10° to the right of the wind.

For the period of January 28-31, there were two sets of ice vectors for two pairs of

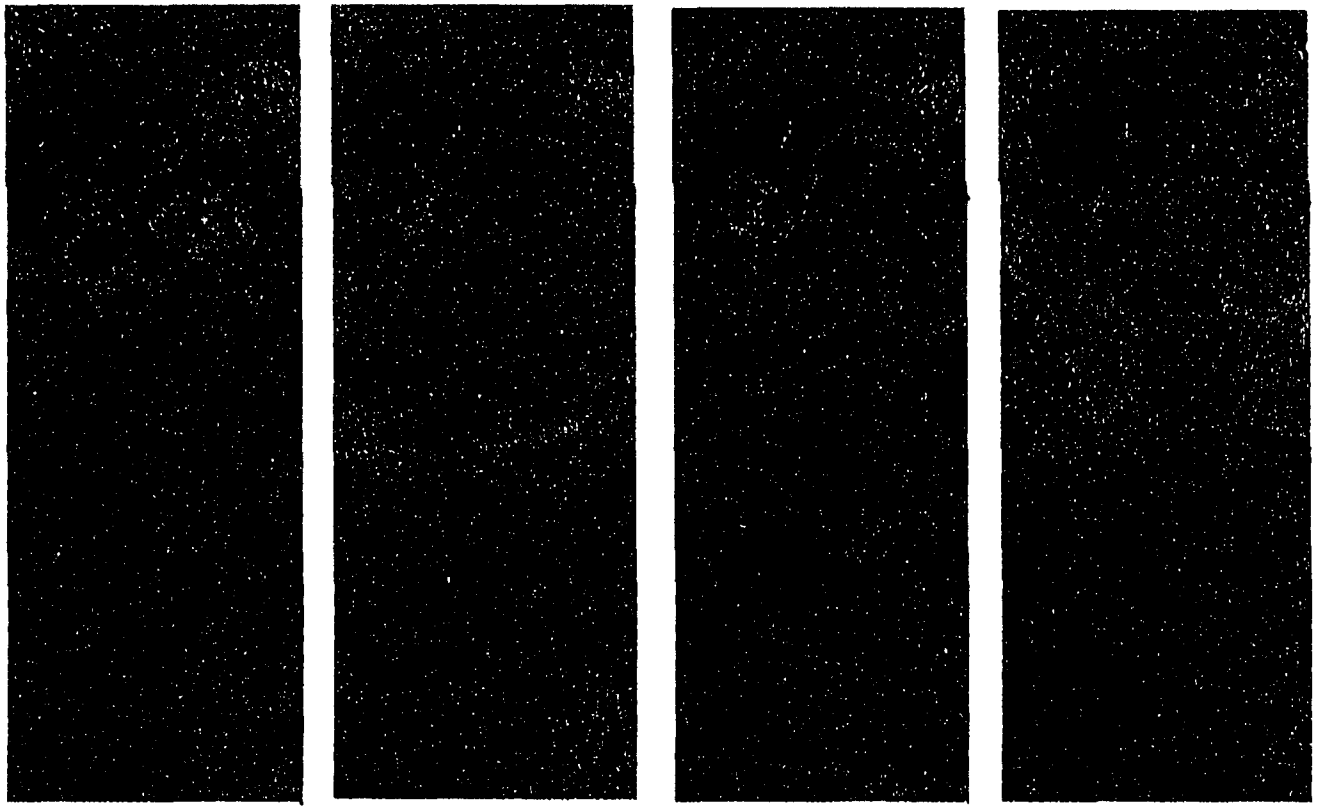

Figure 3.4: LoRes ERS-1 SAR image mosaics of the SLIP-January 10-19, 1992. As in Figure 3.1 except that imagery is for (left to right): January 10, 1992, January 13, 1992, January 16, 1992, and January 19, 1992. The SLIP becomes apparent during this period as the ice along the southern coast of St. Lawrence Island has been pushed offshore by the wind. The polynya region of January 10th is visible directly south of the island between the island and the dashed black line drawn across the January 10th panel. This polynya consists of open water, remnant ice blocks left when the seasonal ice pack was blown offshore, and newly-formed frazil ice. The thin band of ice (appears black in the imagery) located along the southcentral coast of the island is shorefast ice.

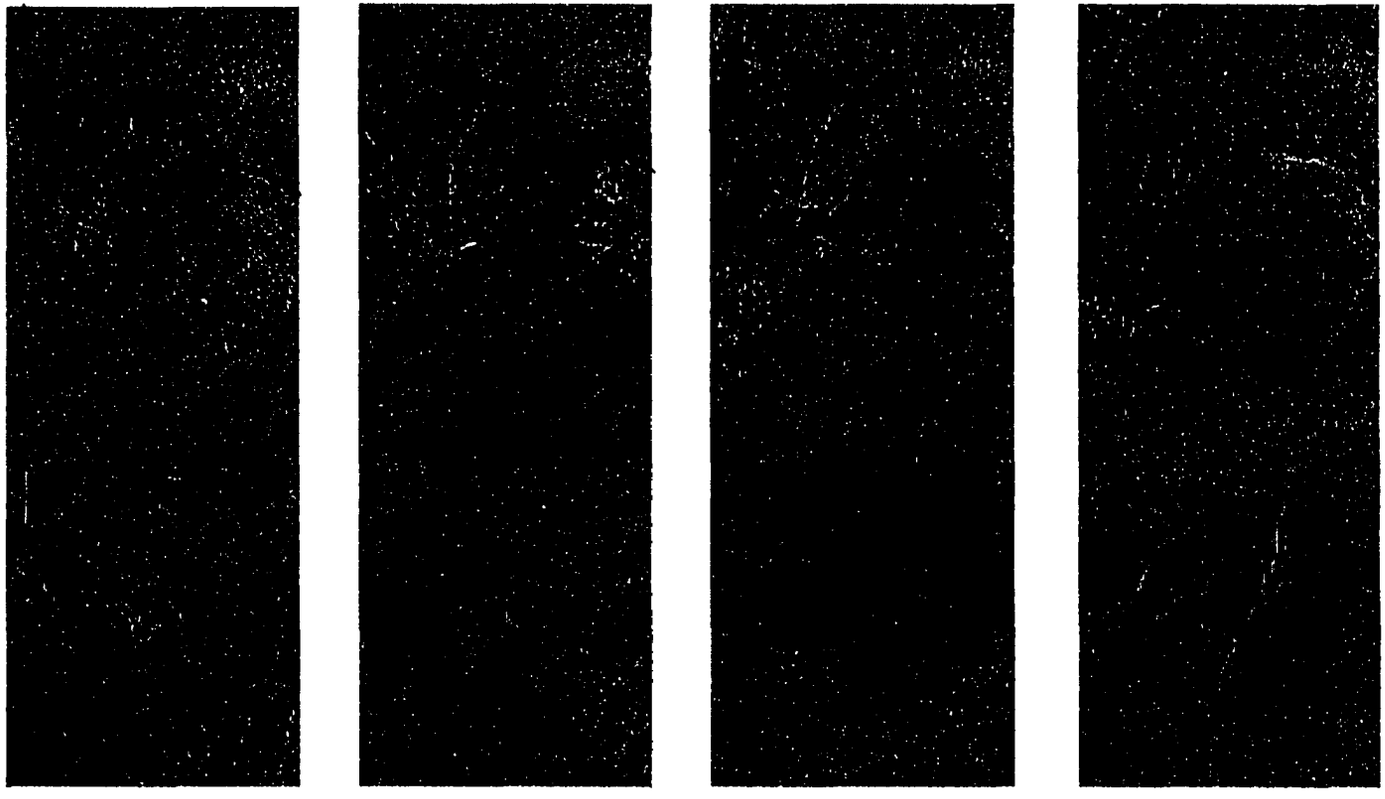

Figure 3.5: LoRes ERS-1 SAR image mosaics of the SLIP-January 22-31, 1992. As in Figure 3.1 except that imagery is for (left to right): January 22, 1992, January 25, 1992, January 28, 1992, and January 31, 1992. During this time period, the large fan-shaped region extending off the coast of St. Lawrence Island moves towards the southwest and expands to fill the width of the imagery strip (100km). The most active region of the SLIP becomes filled in completely with ice by January 28. By the 31st, only the southern-most edge of the fan remains visible. Ice activity around St. Lawrence Island in the latter images indicates ice motion offshore along all shorelines. The large white region in the mid-section of the January 31 strip is a feature of unknown identity and composition. Suggestions as to its identity have ranged from a processing anomaly to an intense snowstorm. The letters D and E followed by numbers on the imagery denote changing positions of two specific ice floes as they appear on January 25 (D25, E25), January 28 (D28, E 28), and January 31 (D31, E31).

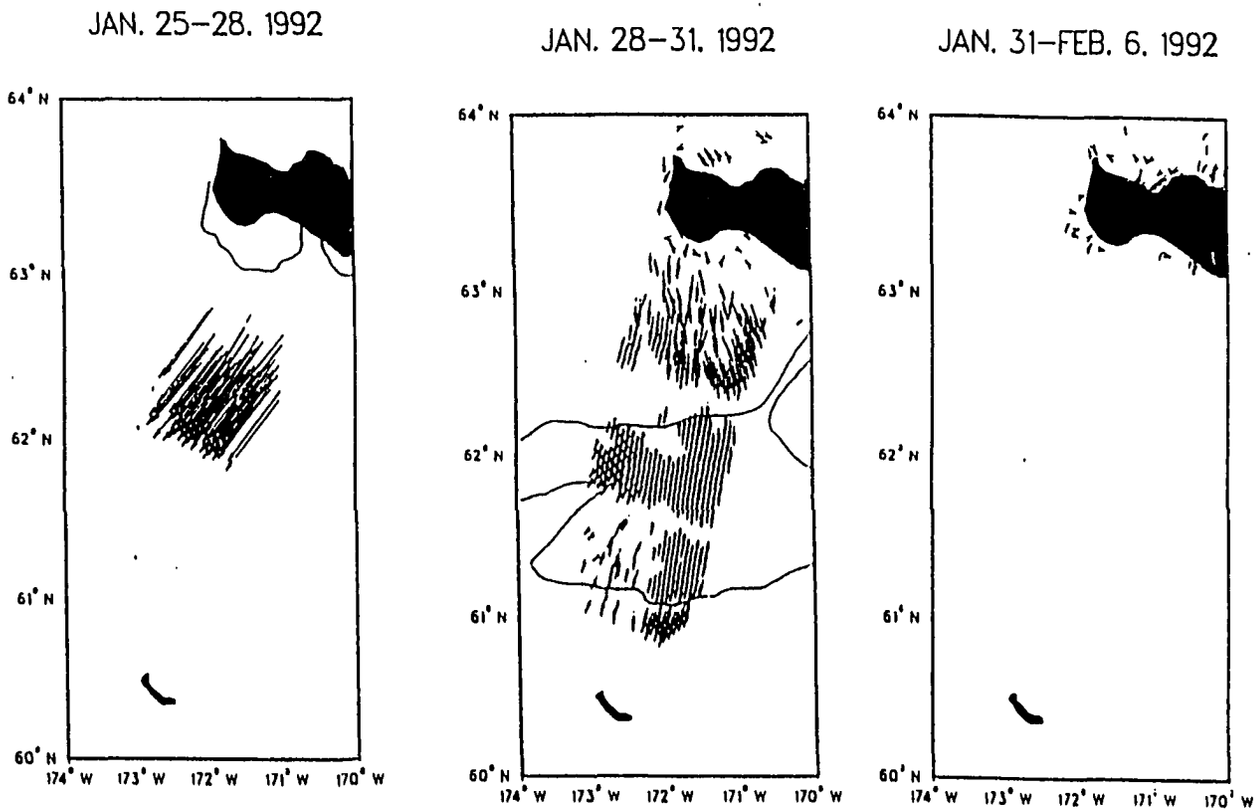

Figure 3.6: ERS-1 SAR GPS ice motion-January 25-February 6, 1992. As in Figure 3.2 except that the maps are for the image date pairings noted in the individual panels shown on this page. (See also Tables 3.1 & 3.2 and Figure 3.5)

SAR images: one motion product each for the north and south sides of St. Lawrence Island (Table 3.1 & 3.2 and Figures 3.5-6). Winds between January 28 and 31 were 3.1-4.0m s^{-1} from the north and northeast. Ice vectors on the south side of the island were 0.06m s^{-1} (5.5km day^{-1}) toward the south. This resulted in ice motion of 1.6-2.1% of the wind speed, directed 7° to 48° to the left of the wind. However, the north side ice motion was very slow at 0.004m s^{-1} (0.3km day^{-1}) toward the north-northeast and bears little relation to the wind. One reason for this is that the ice on the north coast was trapped against the island by winds blowing onshore. There are nearshore currents on the north side of the island, but the nature of the interaction with ice is non-linear and sub-grid scale; thus, discussion of it is beyond the scope of this study.

Although the ice vectors and ice features indicated that the ice was still moving southward between January 28 and 31, ice coverage south of the island appeared rather solid except for a few large leads extending northward near the bottom of the imagery (Figure 3.5). By January 31, the only indications of polynya activity were the polynya's western edge and the south edge of the fan-shaped feature as indicated by the lines drawn along the island in Figure 3.5. In addition, there were no remaining areas of new ice formation visible along the southern coast and the ice positioned along the southern coast had aged enough to develop visible cracks.

Although the polynyas were well-defined during mid-late January, the actual ice concentration was quite variable. The actual ice concentration was impossible to obtain from SAR alone, but by using a combination of SAR and passive microwave data, Cavalieri and Onstott (1992) were able to obtain an estimate of ~ 50% ice concentration within the southern polynya during the most active stage of this southern polynya event. Cavalieri and Onstott (1992) considered the polynya visible in the SAR imagery during this event to be a mix of young and new ice extending over 100km south of St. Lawrence Island. My results shown, shown in Chapter 4, concur.

3.3.2 North Coast Polynya Event of February 1992: Between the end of January and mid-February, the Aleutian Low split into two centers of low pressure as depicted in Figure 3.7. One center developed to the west of the SLIP, in the vicinity of Kamchatka, resulting in southerly winds and high pressure over the eastern Bering Sea. The second center was located over the Gulf of Alaska. As a result, the southern SLIP shown in the January SAR imagery was no longer visible in the early February SAR imagery (Figure 3.8), as the ice was forced back toward the south shore by the southerly winds. As hinted at by the late

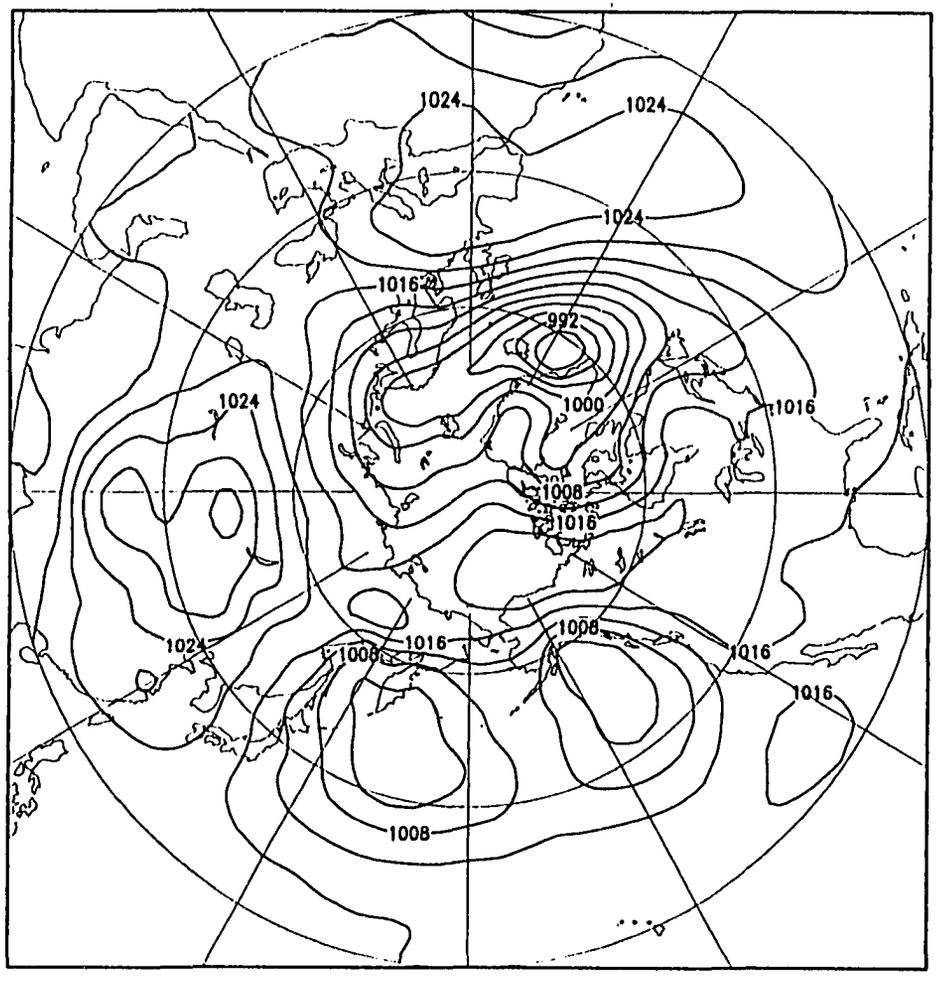

Figure 3.7: Monthly Mean Sea Level Pressure Map-February 1992. In a major departure from the January map, the Aleutian Low has split in to a "two center" feature. The effect is a change in the atmospheric circulation over the northeastern Bering Sea. Persistent northerly/northwesterly/northeasterly winds did not exist in the region of St. Lawrence Island during the first half of February.

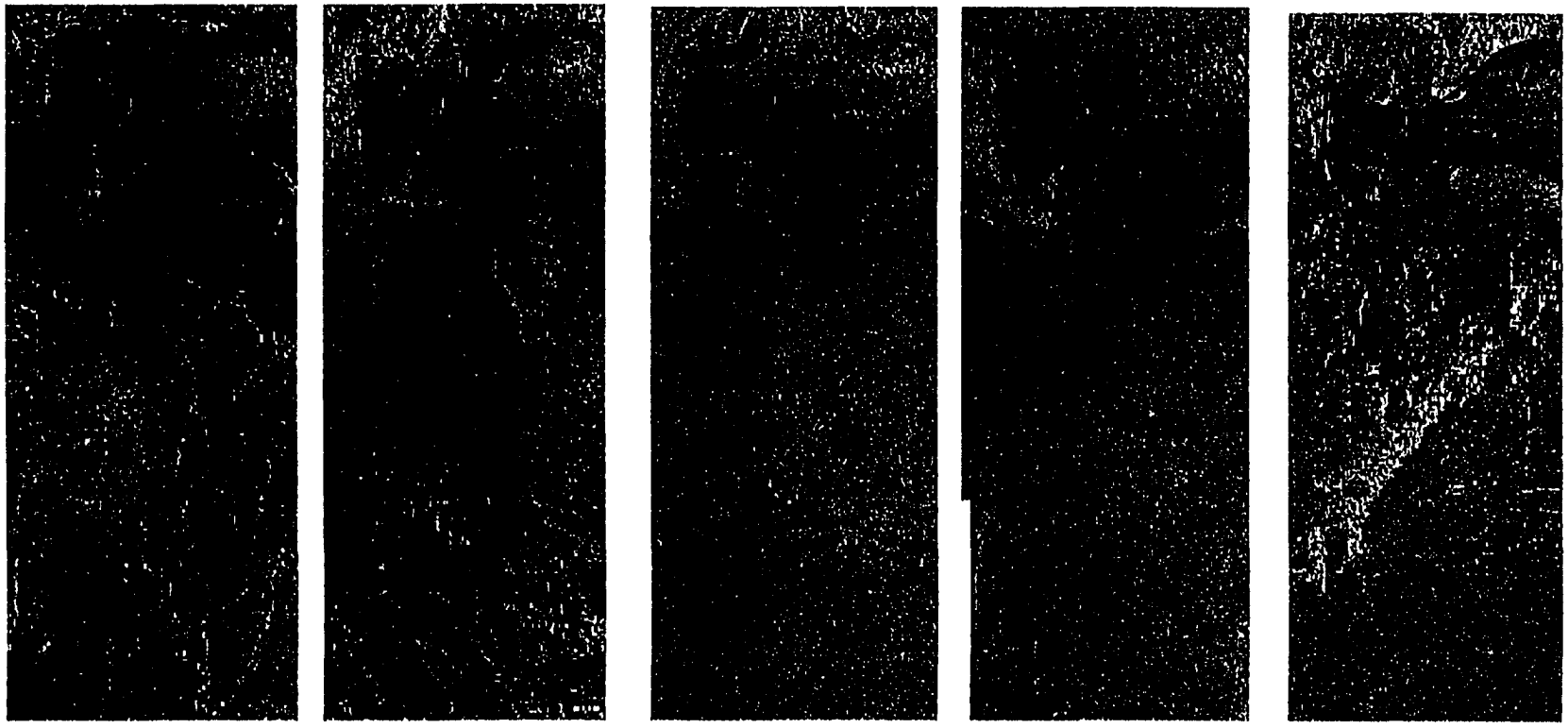

Figure 3.8: LoRes ERS-1 SAR image mosaics of the SLIP-February 6-18, 1992. As in Figure 3.1 except that imagery is for (left to right): February 6, 1992, February 9, 1992, February 12, 1992, February 15, 1992, and February 18, 1992. There is no evidence of a southern SLIP in the earlier images shown here. Instead, a northern polynya region has started to form on the north and west sides of the island. The polynya region is denoted by the bright wind-roughened areas along the island's coasts. By the 12th, the SLIP is quite visible along the west/northwest coast of the island. However, by the 15th the SLIP region has closed on the northern coast although open water is still observed along the western coast. In addition, initial development of a new southern polynya can be observed in the ice pack on the 15th and 18th.

January SAR imagery (Figure 3.5), the ice west and north of the island was broken up and displaced northward away from the island between early and mid-February (Figure 3.8). Pools of open water and several stages of frazil and grease ice were apparent along the western and northern coasts of the island. Although no GPS ice motion products were successfully produced for February 6-12, due to the lack of "processor-trackable" ice features, overall ice activity visible in the imagery (Figure 3.8) suggested that a small northern polynya opened.

Between February 15 and 23, observed winds shifted once again from southerly and easterly back to northerly. A strong low pressure system, part of the Aleutian Low system, moved over the Gulf of Alaska, pushing the area of high pressure already present over the eastern Bering Sea toward the northwest (Figure 3.9). These changes resulted in cooling at St. Lawrence Island (Table 3.2), and in ice being pushed onshore along the northern and western coasts of the island. The new atmospheric pattern led to the beginning of a new south coast SLIP event.

3.3.3 South Coast Polynya Event of February/Early March 1992: This is the best-documented SLIP event of my study. At the beginning of the event, during the period from February 15-18, ice vectors shown in Figure 3.10 indicated little net ice drift (speeds of much less than 1km day^{-1}), as winds were quite variable in terms of both speed and direction (Table 3.2). In fact, the entire period from February 12-21 should be thought of as a transitional period. Similarly variable winds and variable ice motion have also been noted throughout the northeastern Bering Sea region during mid-late February in previous years (Niebauer, 1980). In the case presented here, ice vectors for February 15-18 indicated ice drift of 0.0018m s^{-1} towards the southeast. As shown in Figure 3.8, SAR imagery for February 15 revealed an area of ice/water mix along the western coast of the island and the beginnings of a polynya along the southern coast. By February 18 (Figure 3.8), however, these areas had become completely ice- covered again, and an area of younger ice had developed along the south-central island coast. Further, a large lead had opened in the seasonal ice pack as shown in the central section of the February 18 SAR image (Figure 3.8). This lead closed by February 21 as it was not visible in the ice field for that date (Figure 3.11). Ice had also returned along the western and northern sides of the island by February 21, and no open water was evident in these areas.

Despite average northeasterly winds of 8.7-9.2m s^{-1} between February 15-21, it was not possible to obtain realistic ice vectors from the SAR imagery for February 18-21. The

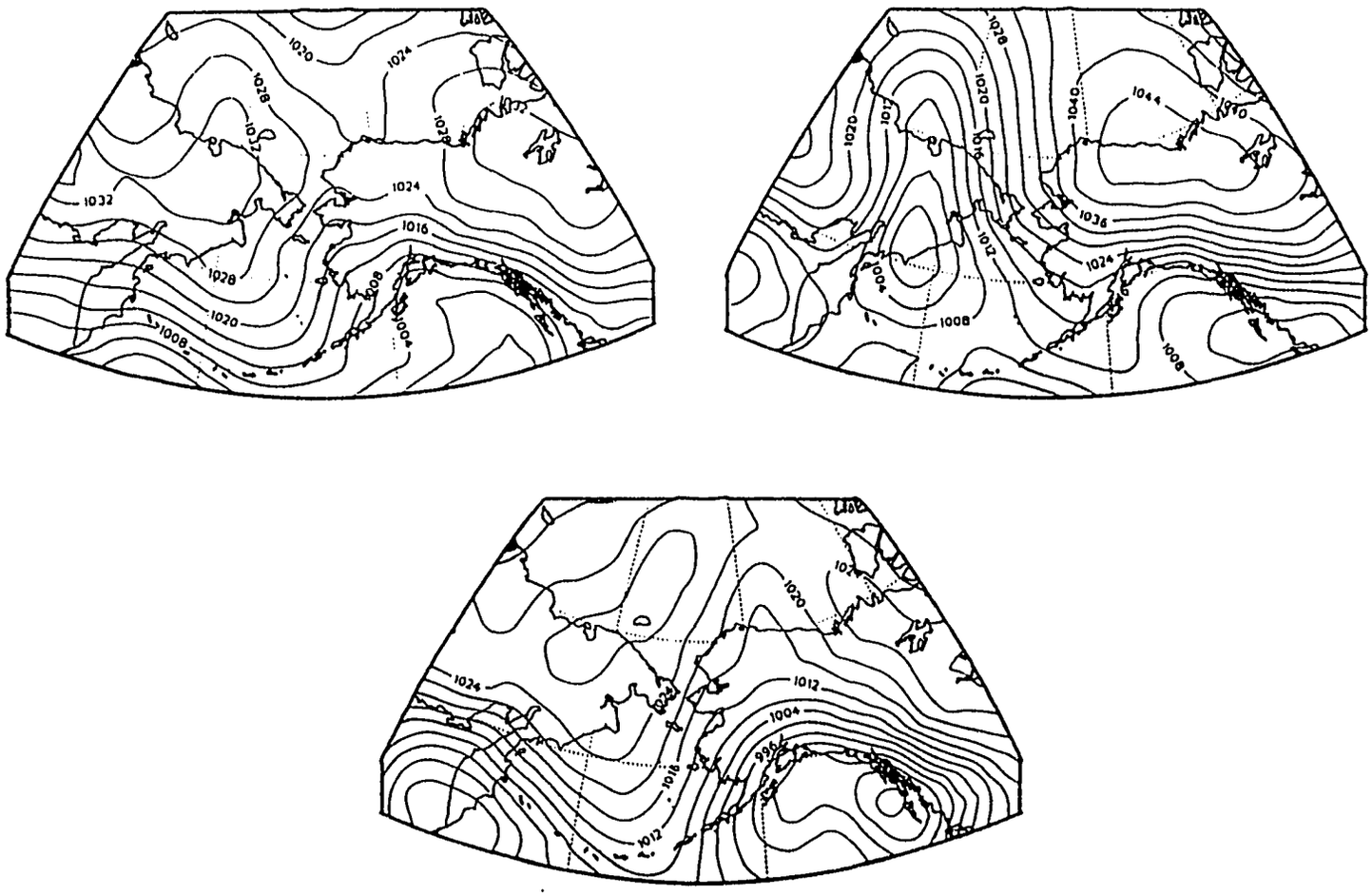

Figure 3.9: Daily Sea Level Pressure Maps (00 Z)-February 13, 19, and 22, 1992. Contour interval is 4 mb. Note the variation in gradient intensity across St. Lawrence Island as well as the shifts in position of the primary low pressure systems throughout the period. Top (left to right): February 13 and February 19. Lower: February 22.

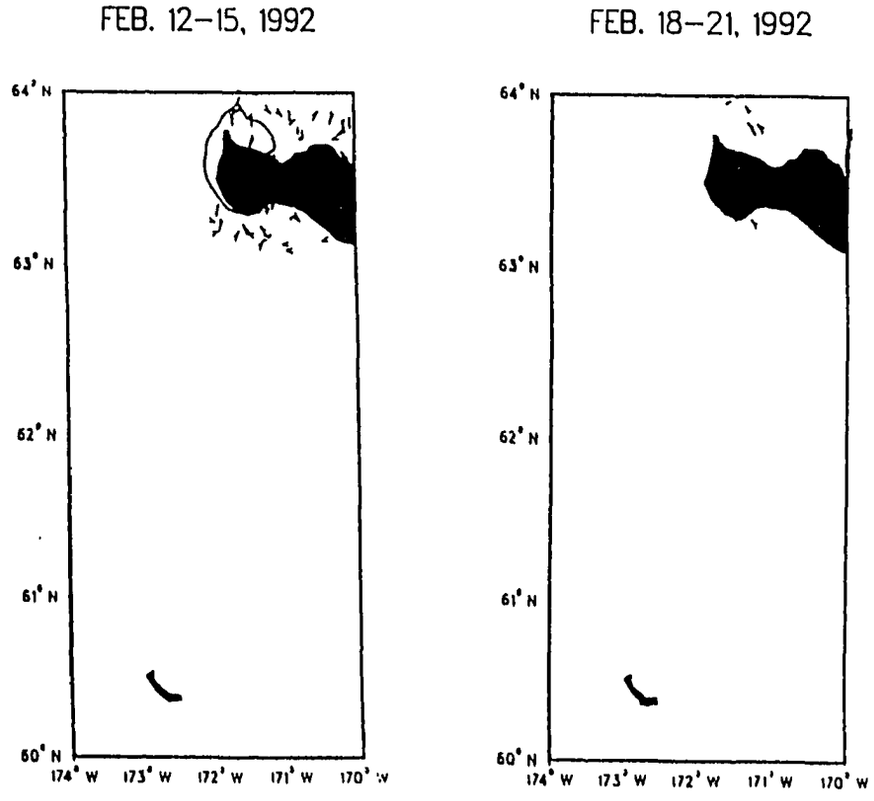

Figure 3.10: ERS-1 SAR GPS ice motion-February 12-21, 1992. As in Figure 3.2 except that the maps are for the image date pairings noted in the individual panels shown on this page. (See also Tables 3.1 & 3.2 and Figure 3.8)

GPS tracker was unable to track features common to both images correctly because of: failure to geographically locate trackable features; failure to distinguish properly between too many potential matches (i.e., the wrong target feature was matched with a source feature); or the predominance of sub-grid scale (i.e., < 5km over 3 days) ice motion. I estimated the ice motion to be at least 0.02m s^{-1} (>5km over 3 days), based on features I could identify as common to both images by visual inspection.

The longer-lived, more extensive southern polynya developed along the southern coast of St. Lawrence Island between February 18 and February 21. The polynya was readily observable south of the island in the February 21 SAR imagery (Figure 3.11). As SAR imagery were not available between 2239Z on February 18 and 2239Z on February 21, and the AVHRR data for this time period were not usable, it was hard to determine when this polynya opening occurred. Weather records did show persistent northerly winds after February 19. Also "open water" was evident in the SAR imagery of February 21 (Figure 3.11) immediately adjacent to the coast, indicating that the ice had just recently been blown offshore. Based on the wind forcing, and this presence of open water, the major opening activity most likely took place on February 20 or early on February 21 (also see Chapter 4).

The polynya evident in the SAR imagery of February 21 had expanded significantly by February 24 (Figure 3.11). The entire bowl-shaped region extending south from the island is part of the polynya, reflecting an expansion offshore of > 50km. In contrast, ice vectors for February 21-24 (Figure 3.12) suggest speeds of only 0.002m s^{-1} directed towards the southwest. The slow average ice speeds were completely misleading as they did not reflect the large expansion. This was in part due to the fact that ~ 50% of the acceptable ice vectors were located within the area of nearly negligible ice motion north of the island. The magnitudes of the south side vectors were also somewhat small, but the southwesterly direction of motion indicated by the vectors was confirmed by the SAR imagery for the period. The GPS was also unable to detect any potentially trackable features within the polynya due to their fine scale and rapid transformation. However, based on my measurements of the polynya offshore extent on February 21 and February 24 (Figure 3.11), the southern edge of the polynya moved offshore at a rate of 55-60km in 3 days (0.23m s^{-1} or 20km day^{-1}), which corresponds to 2.5% of the wind speed for that time period.

The strongest sustained ice motion in my data set occurred over the week of February 24 to March 1, when southward ice vectors driven by northeasterly winds averaged 0.29m s^{-1} (25km day^{-1}; Table 3.2 and Figure 3.12). From February 24 to March 1, the average wind direction was toward the south and the average ice drift was slightly to

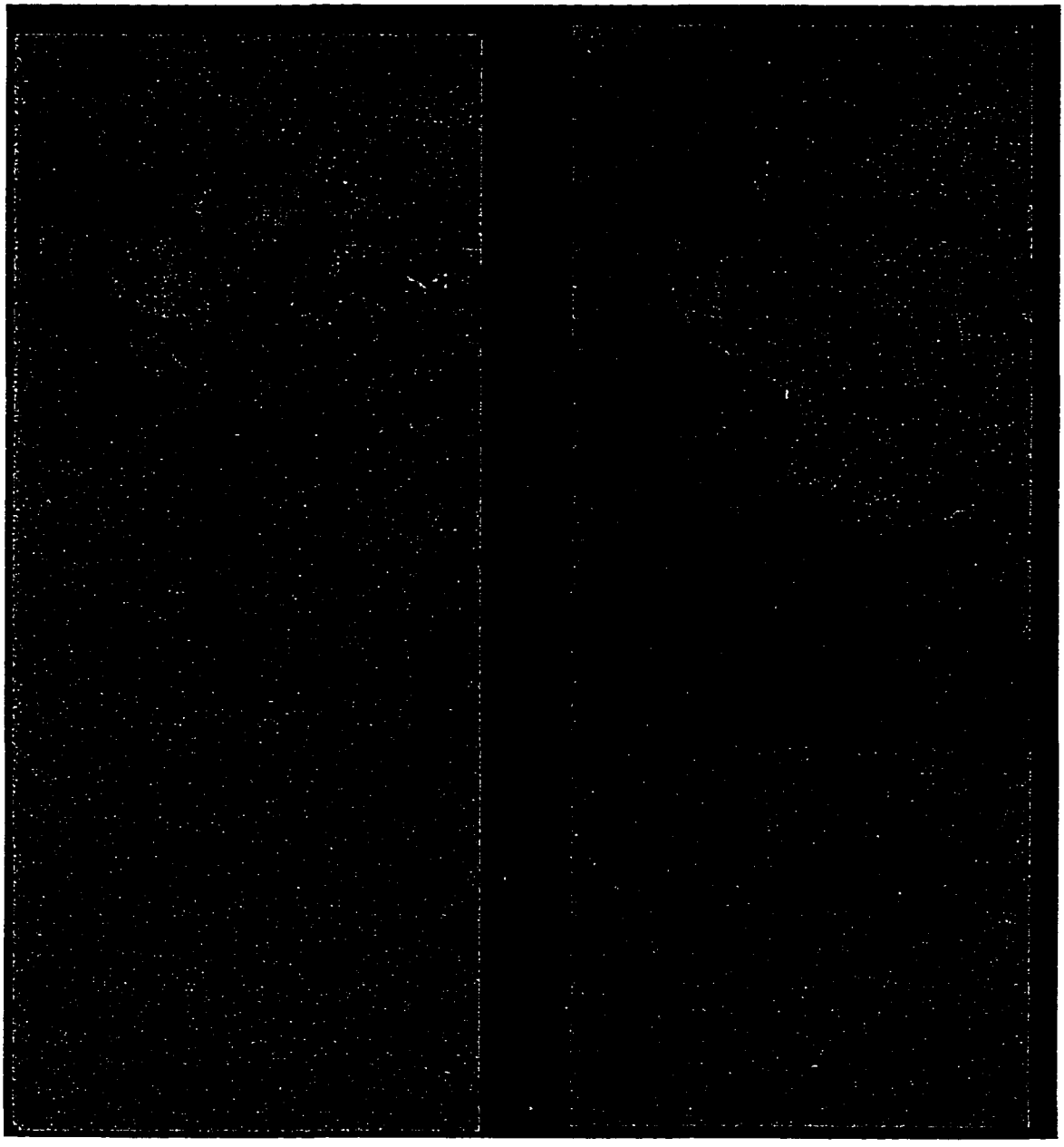

Figure 3.11: LoRes ERS-1 SAR image mosaics of the SLIP-February 21-February 24, 1992. As in Figure 3.1 except that imagery is for (left to right): February 21, 1992 and February 24, 1992. The polynya region expands southward from the island considerably (~50 km) between February 21 and February 24 in response to persistent northerly winds. As before, letters (feature identification) and numbers (date of location) drawn on the imagery represent changes in position of distinct ice features as observed in consecutive image mosaics.

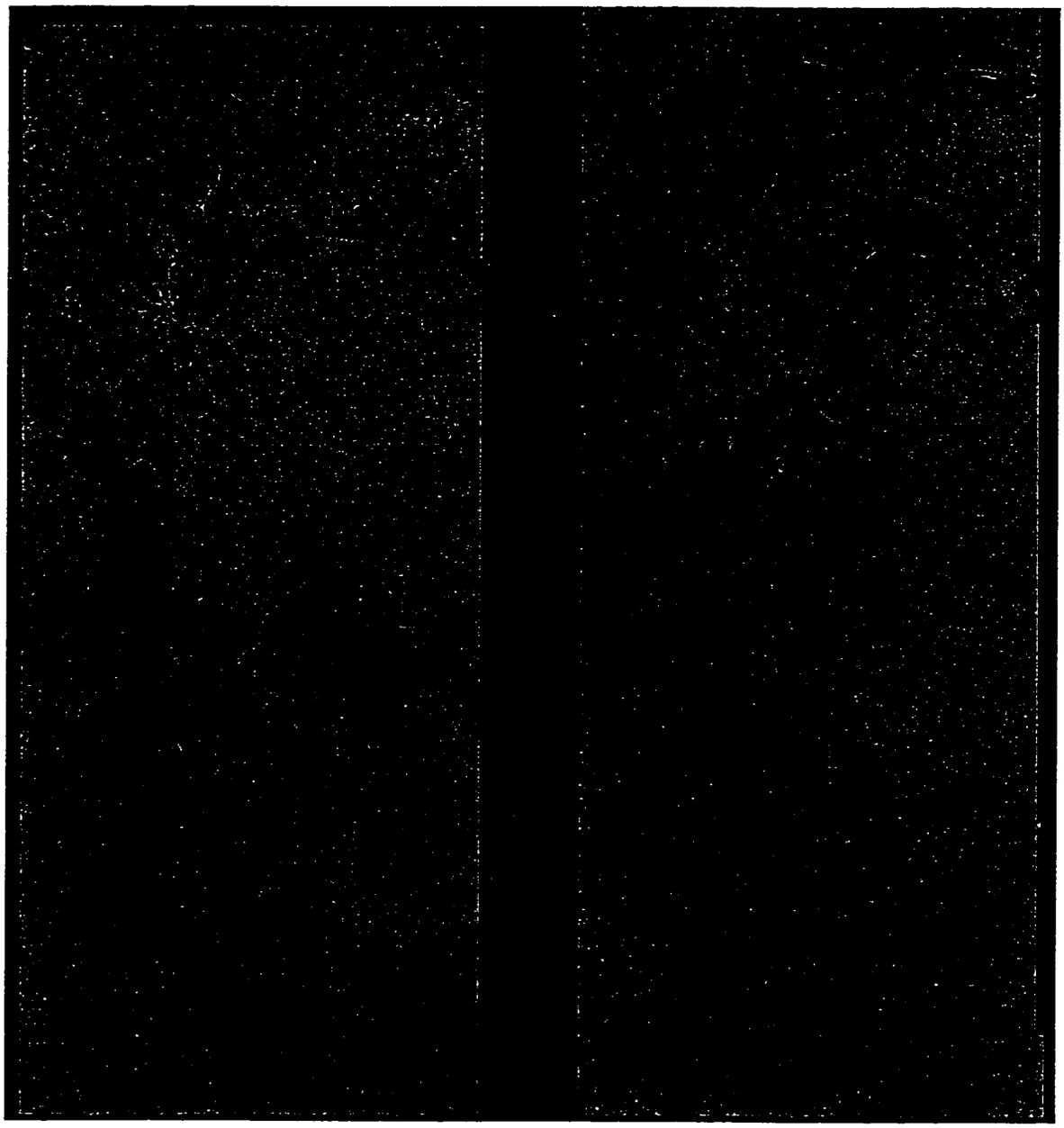

Figure 3.11 (continued): LoRes ERS-1 SAR image mosaics of the SLIP-February 27-March 1, 1992. The polynya region extends ~169 km south from the island by February 27 (left image). The banding within the polynya region on February 27 suggests that the SLIP expansion occurred as a series of growth pulses (possible on a diurnal scale) rather than as a continuous southward progression. Note that the March 1 polynya region (shown in right image) is narrower than that on February 27 and that the March 1 SLIP region appears to be more solidified (more compacted). Cracks and leads have begun to develop in the ice on March 1 and no pulse bands are apparent in the polynya region.

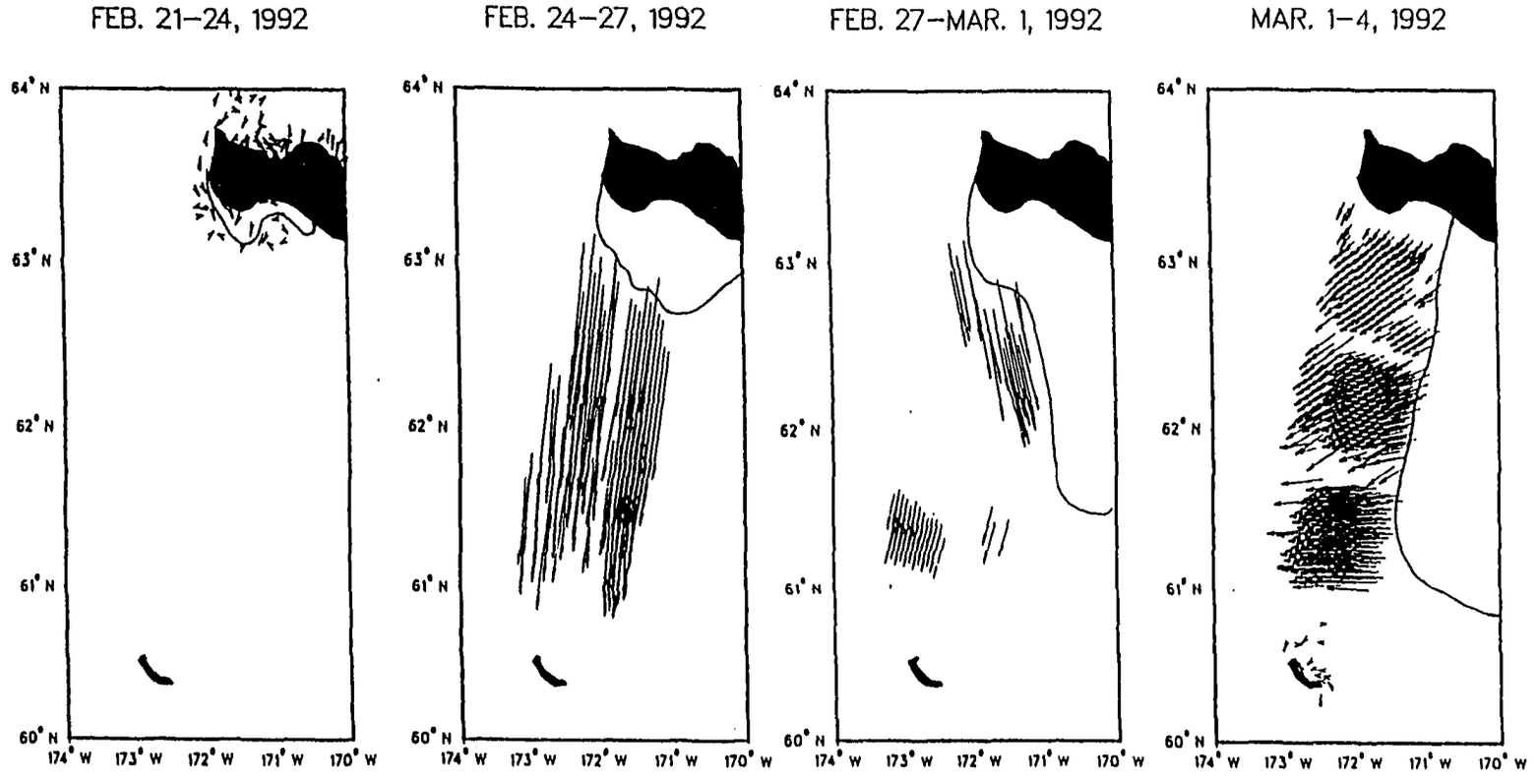

Figure 3.12: ERS-1 SAR GPS ice motion-February 21-March 4, 1992. As in Figure 3.2 except that the maps are for the image date pairings noted in the individual panels shown on this page. (See also Tables 3.1 & 3.2 and Figure 3.11)

the right of the wind. The ice speeds for this entire period averaged 2.3- 2.9% of the wind speed. quite similar to the free drift "rule of thumb" relationship between ice and wind of 2%.

The maximum three day ice speeds in my entire data set were obtained for the period of February 24-27 (Table 3.2 and Figure 3.12) at 0.34m s^{-1} (29km day^{-1}). Winds for this period averaged 10.8-11.5m s^{-1} in response to the strong low pressure system centered over the northern Gulf of Alaska (Figure 3.13). This ice:wind relationship compares remarkably well with wind-driven free-drift ice observations of Pease and Overland (1984) that suggested ice speeds of 0.37m s^{-1} would be observed when winds averaged 10.4m s^{-1}.

The February 1992 SLIP region (open water as well as new and young ice) depicted in the SAR imagery expanded to its greatest size between February 24 and February 27 (Figure 3.11). By February 27. the polynya extended 165km south of the coastline and across the entire length of the southern coastline. If this polynya event started on February 21 or late on February 20. this indicates ice motion of ~165km in ~6 days, or 0.33m s^{-1} which agrees with the GPS estimates of ice motion at 0.31-0.34m s^{-1}. The earlier SAR imagery from February 24 hinted at this large expansion. as a faint outline of the polynya was visible extending from the southern limit of the bowl-shaped region (Figure 3.11). This imagery also shows some banding in the polynya tail region. Indeed. the February 27 SAR imagery of Figure 3.11 revealed that the large "wind-sock" or "plume"-shaped polynya consisted of graduated zones ranging from the newly formed ice nearest St. Lawrence Island, to young ice and floes of thin first year ice farther away. This banding was evidence of pulses in the wind, and also perhaps evidence of forcing by diurnal factors such as tides. It was evident from the lack of large areas of open water and the abundance of frazil and grease ice in the polynya that open water froze almost as soon as it was exposed to the air (see also Chapter 4). Based on SAR and SSM/I imagery, Cavalieri and Onstott (1992), estimated the ice concentration within the most active sector of the February 27 polynya to be a minimum of 80% (i.e., 20% open water and 80% ice of variable thickness).

Between February 27 and March 1 (Figure 3.12), ice drift closest to the island was 0.20m s^{-1} (18km day^{-1}) while drift farther south away from the island was slower at 0.11m s^{-1} (9.5km day^{-1}). The shape of the island may have caused an intensification of the wind closer to the shore that was not felt farther offshore. Also, ice farther away from the shore was older than the newly formed ice and more "compacted" (higher concentration), so that it provided greater resistance to wind forcing. Whatever the ultimate cause, this ice

motion suggests a convergence in the ice, which probably resulted from convergence in the wind and/or ocean flow field.

The low pressure system driving the strong northerly winds from February 24-27 decayed over the Alaskan Interior after February 27, and a second low pressure system quickly took its place over the Gulf of Alaska (Figure 3.13). This second low weakened as it moved north/northwestward to its position directly north of St. Lawrence Island by February 29. It was this second low that accounted for the relatively weak and variable winds observed at the SLIP from February 29 to March 1.

SAR imagery in Figure 3.11 showed a reduced polynya by March 1. The older pack ice outside the polynya responded to the onset of weak, variable winds by compressing the polynya from the west, rather than moving rapidly southward as it did in response to the preceding extended period of northerly winds.

Although the ice within the polynya appeared older and more continuous throughout the region on March 1, the huge polynya south of St. Lawrence Island was still well defined for over 150km offshore south of the island (Figure 3.11). However, by this time, the east-west length of the polynya had been reduced by ~50%. The western edge of the polynya extended southward from the island's south-central coast by March 1, rather than from the southwestern coast as shown for February 27 (Figure 3.11). From March 1 onward, cracks and leads were capable of forming within the polynya as well as outside, indicating that the ice was getting thicker in place rather than being blown continually toward the polynya's southern boundary.

The "filling in" of the polynya with ice from the west between February 27 and March 1 (Figure 3.11) may have been due to a combination of a weakened wind field and the strong ocean current to the west of St. Lawrence Island. Once the atmospheric forcing was reduced, only oceanic forcing and internal ice stresses remained to move the ice. This concept of the increased role of oceanic forcing is examined in Chapter 5 using a regional climate system model. The thinner ice within the polynya appeared to offer only weak resistance to the forcing along the boundary of the region and, as a result, the SLIP became narrower as observed in the early March imagery. By March 4 (Figure 3.14), the polynya had "detached" itself from its earlier zones of ice formation along the southern coastline and expanded slightly in east-west extent. The ice feature appeared to be moving southward within the seasonal ice pack rather than remaining as unconsolidated floes within a frazil/water mix.

The sets of ice vectors from the March 1-4 (Figure 3.12) and March 4-7 SAR

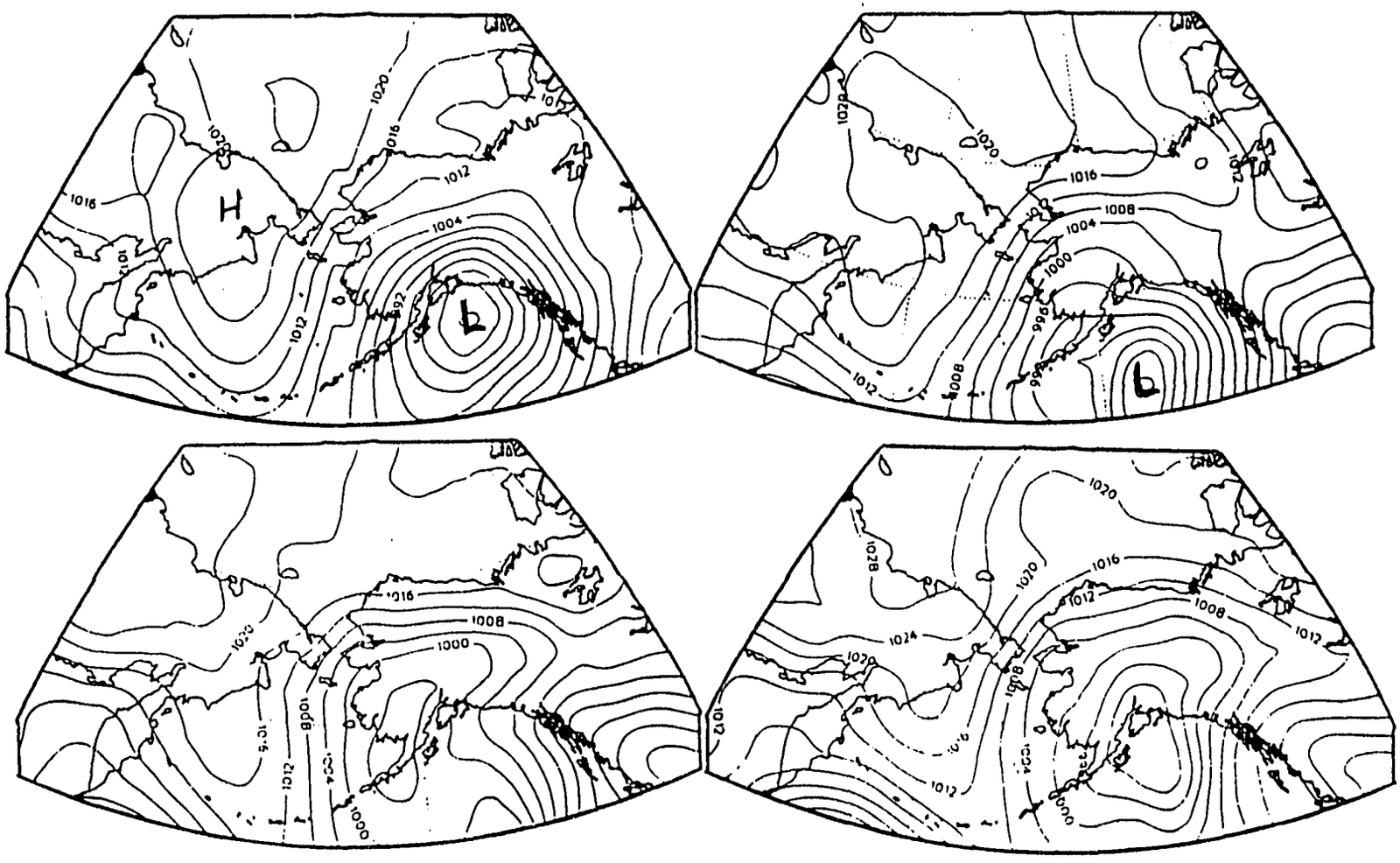

Figure 3.13: Daily Sea Level Pressure Maps (00 Z)-February 24-March 2, 1992. Contour interval is 4 mb. Note the variation in gradient intensity across St. Lawrence Island as well as the shifts in position of the primary low pressure systems throughout the period. Top (left to right): February 24 and 25. Bottom (l to r): February 26 and 27.

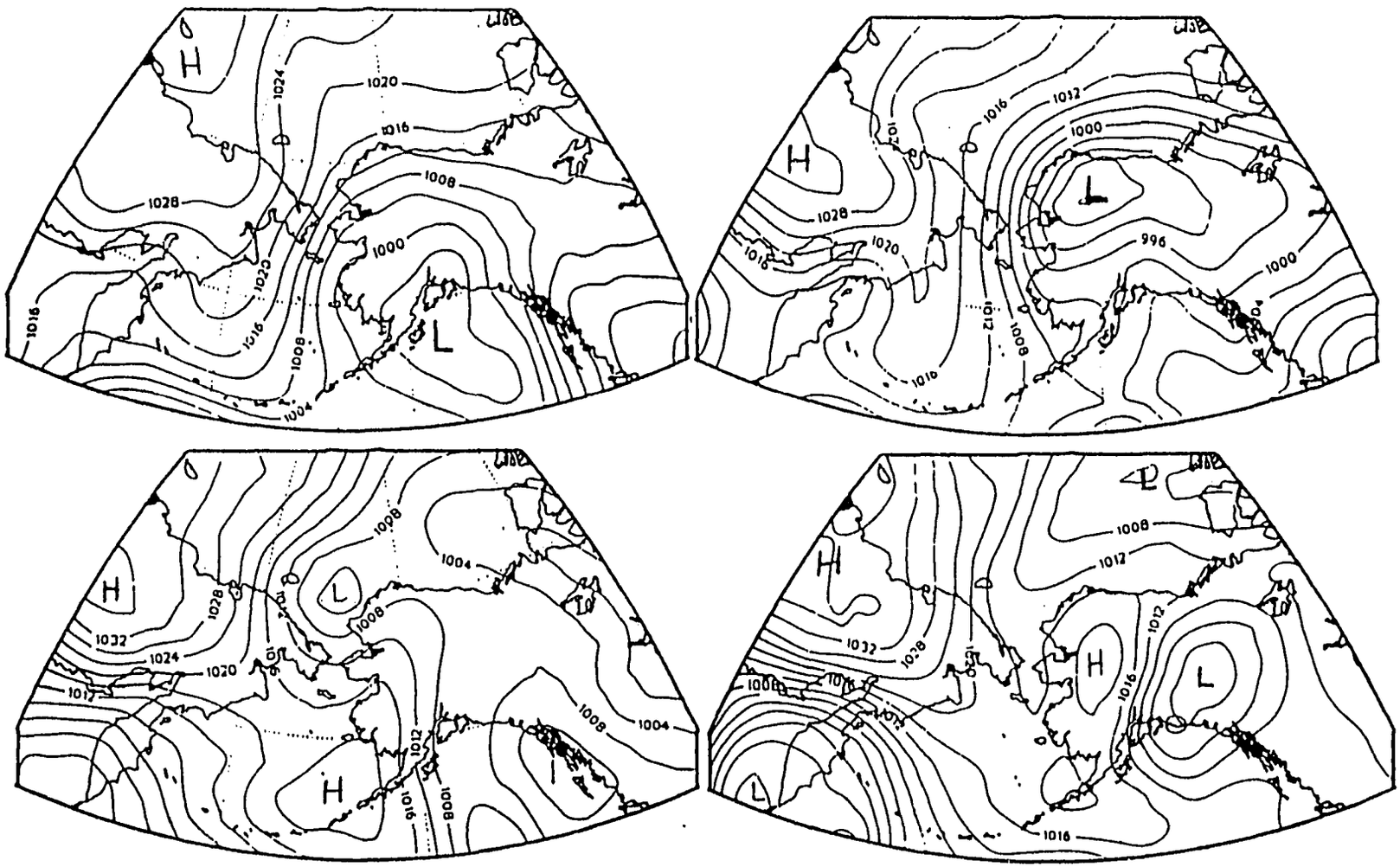

Figure 3.13 (continued): Sea Level Pressure Maps. Top (l to r): February 28 and 29. Bottom (l to r): March 1 and 2.

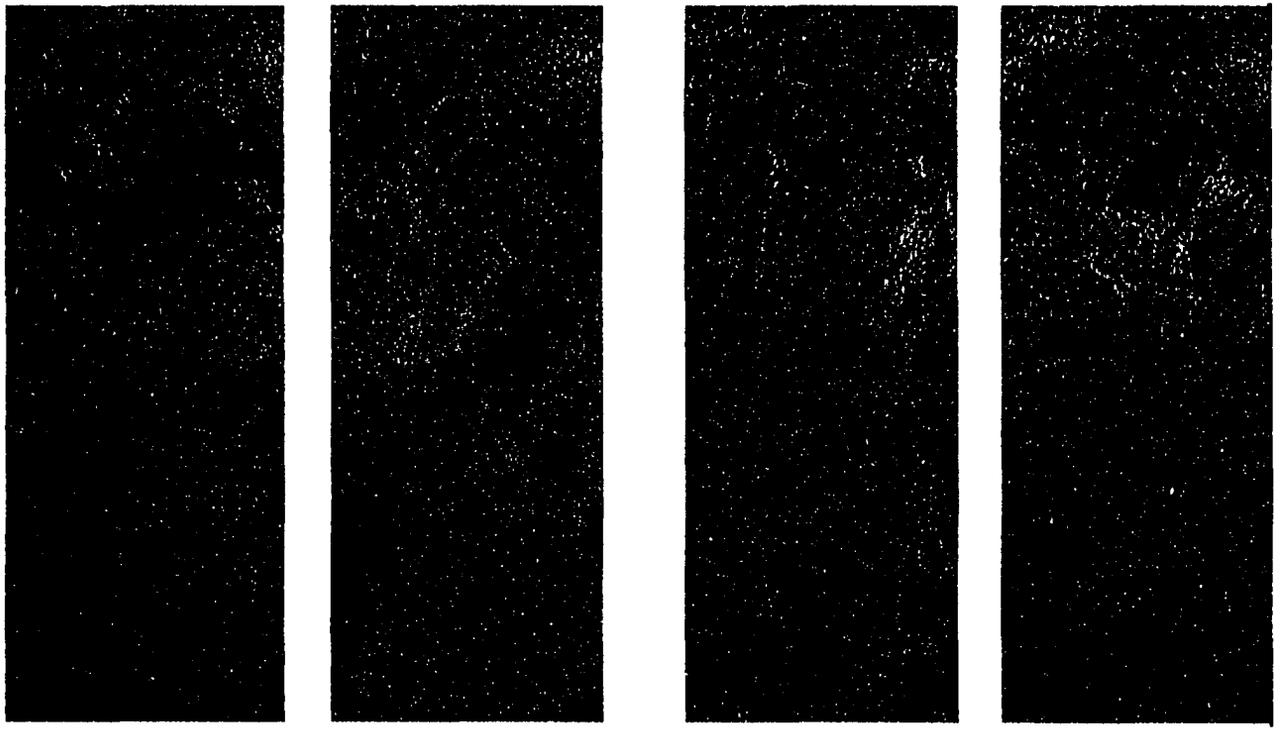

Figure 3.14: LoRes ERS-1 SAR image mosaics of the SLIP-March 4-13, 1992. As in Figure 3.1 except that imagery is for (left to right): March 4, 1992, March 7, 1992, March 10, 1992, and March 13, 1992. The polynya region has now become an offshore "ice feature" and part of the seasonal ice pack. It moves south/southwestward with the rest of the surrounding pack ice. However, on March 10th, long plume-like features extend southward from the island once again, suggesting offshore ice motion in addition to the background pack motion. A new southern polynya was beginning to form as ice along the southern coast of the island was being driven offshore by strong northerly winds. By March 13, a new southern SLIP is evident. As before, the letter (feature identification) and number (date of location) drawn on the imagery represents changes in position of a distinct ice feature as observed in consecutive image mosaics.

pairings (Tables 3.1 and 3.2) indicated ice motion at a rate of 0.06-0.08m s^{-1} (5.2-7.0km day^{-1}), directed toward the southwest and west/southwest, in response to northerly winds of 2.2-2.9m s^{-1}. The ice drifted at 2-4% of the wind speed and 36°-67° to the right of the wind. The period from March 4-7 marked the end of this southern polynya event.

Ice motion products were not created for March 7-10 due to lack of "processor-trackable features" common to successive images and the vectors obtained for March 10-13 (Figure 3.15) only reflected the ice motion on the north side of the island. As such, the March 10-13 vectors indicated nearly negligible (see Table 3.2) displacement. This was unfortunate as the SAR images for March 10 and 13 (Figure 3.14) indicated a large amount of activity in the ice field south of the island. Manual calculation of ice displacement using Figure 3.14 indicated ice motion of 0.07m s^{-1} (6km day^{-1}) toward the south/southeast, which is 1.8 to 3.9% of the associated wind speed over this three-day period. The backscatter differences across the March 10 image (Figure 3.14) reveal two large plumes of younger ice extending southward from the island, and a well-defined area of ice along the northern coast of the island. The long plumes reflect the strengthening of the winds from the northern quadrant.

The two plume pattern visible in the imagery of Figure 3.14 was quite curious as it was similar to the January polynya features (Figure 3.5). The strip of older ice between the lobes was located in approximately the same position as the "handle" (narrowest portion) of the "fan-shaped" features in the January imagery (Figure 3.5). This band location was also similar to the location of a slight variance in backscatter running north-south in the middle of the polynya, found in the February 24th imagery (Figure 3.11). The location of the band was in the vicinity of the string of ice blocks extending from, or toward the coast shown in the February 27 imagery (Figure 3.11). The recurrence of the feature in a similar location throughout the winter suggests that it is due to a variation in the prevailing localized wind field downwind of the Kookooligit Mountains, caused by island topography. Or perhaps, the feature is due to a persistent anomalous ocean circulation ("dead ocean"; Carsey, personal communication) in this area. As curious as these features (i.e., the plumes and the dividing band) were, they were short-lived. The only evidence of them in the March 13 imagery is a broad lobe well off the coast. Instead, the main feature visible in the March 13 SAR strip was a new polynya opening (Figure 3.14).

3.3.4 South Coast Polynya Event of March 1992: SAR imagery for March 13 shown in Figure 3.14 did indeed indicate the opening of a new polynya along the south coast of St.

Lawrence Island in response to another storm passing through the northeast Bering Sea. As some ice structure is apparent within the polynya, it appears that either the winds were not as persistent (or as strong) as they were during the February southern event, or that the polynya opened closer to March 10 so that ice within the region had time to consolidate. In fact, as Table 3.2 shows, wind speeds ranged from 8.7 to 11.1m s^{-1} during the period of February 21-27, while wind speeds ranged from 1.8 to 4.3m s^{-1} during the period of March 10-13. This southern polynya expanded considerably over the next three days as shown in Figures 3.15-3.16. However, unlike for the February event, SAR imagery showed two separate lobes with each lobe was oriented towards the southwest rather than the southeast. This change in polynya shape and ice direction was probably due to the fact that the prevailing winds shifted from northerly (southward) in late February to northeasterly or westerly/northwesterly in March. Further, no open water was evident in the March 16 imagery. Finally, neither of the two lobes shown in the March 16th imagery was as extensive as the polynya observed on February 27.

Between March 13 and 16, ice north of the island drifted 0.001m s^{-1} (0.1km day^{-1}) towards the southwest, while the ice motion south of the island was 0.29m s^{-1} (25km day^{-1}) towards the south (Figure 3.15). South of the island, ice drift was 3.7-4.7% of the wind speed (Table 3.2). However, ice motion north of the island appeared to be unrelated to the winds. This dramatic difference in ice drift speed again reflects the fact that ice north of the island was trapped by the "pack" ice, with no open ocean northward to allow for expansion, and the island acting as a southern boundary, while ice south of the island was free to expand over the open Bering Sea.

Between March 16 and March 19, the polynya remained apparent on the south side of the island as shown in Figure 3.16. The lobes continued to remain separate entities, although both had expanded in width by March 19. The southern edge of the western lobe was no longer visible along the left edge of the imagery (Figure 3.16) as this lobe also continued to expand along a northeast to southwest axis. No banding is evident within the polynyas or lobes, although the ice appeared to have some structure that would indicate grease ice matting. SAR imagery indicated only slight evidence of wind roughened surfaces near the island associated with a very active ice formation sector. Furthermore, despite the large expansion of the plumes, either small cracks or leads had become apparent within the plumes by March 19 (Figure 3.16), which indicated the presence of more consolidated ice.

Vectors for March 16-19 (Figure 3.17 and Table 3.1 & 3.2) indicated very slight ice motion on the north side of the island. Vectors were not successfully processed on the south

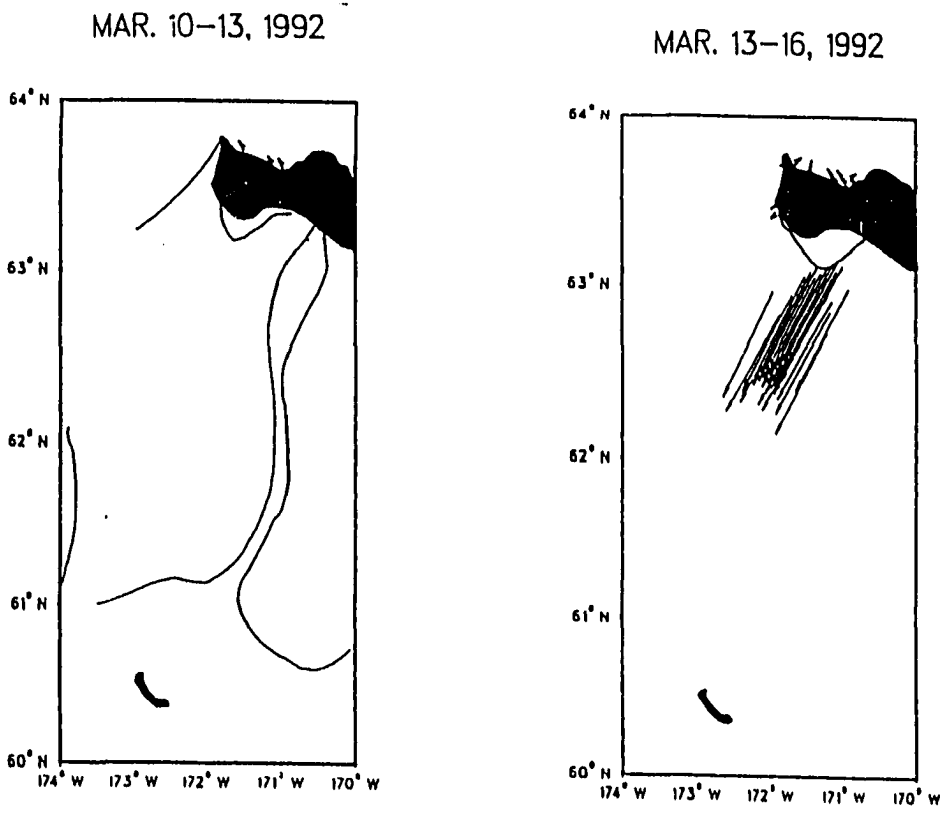

Figure 3.15: ERS-1 SAR GPS ice motion-March 10-16, 1992. As in Figure 3.2 except that the maps are for the image date pairings noted in the individual panels shown on this page. (See also Tables 3.1 & 3.2 and Figure 3.14)

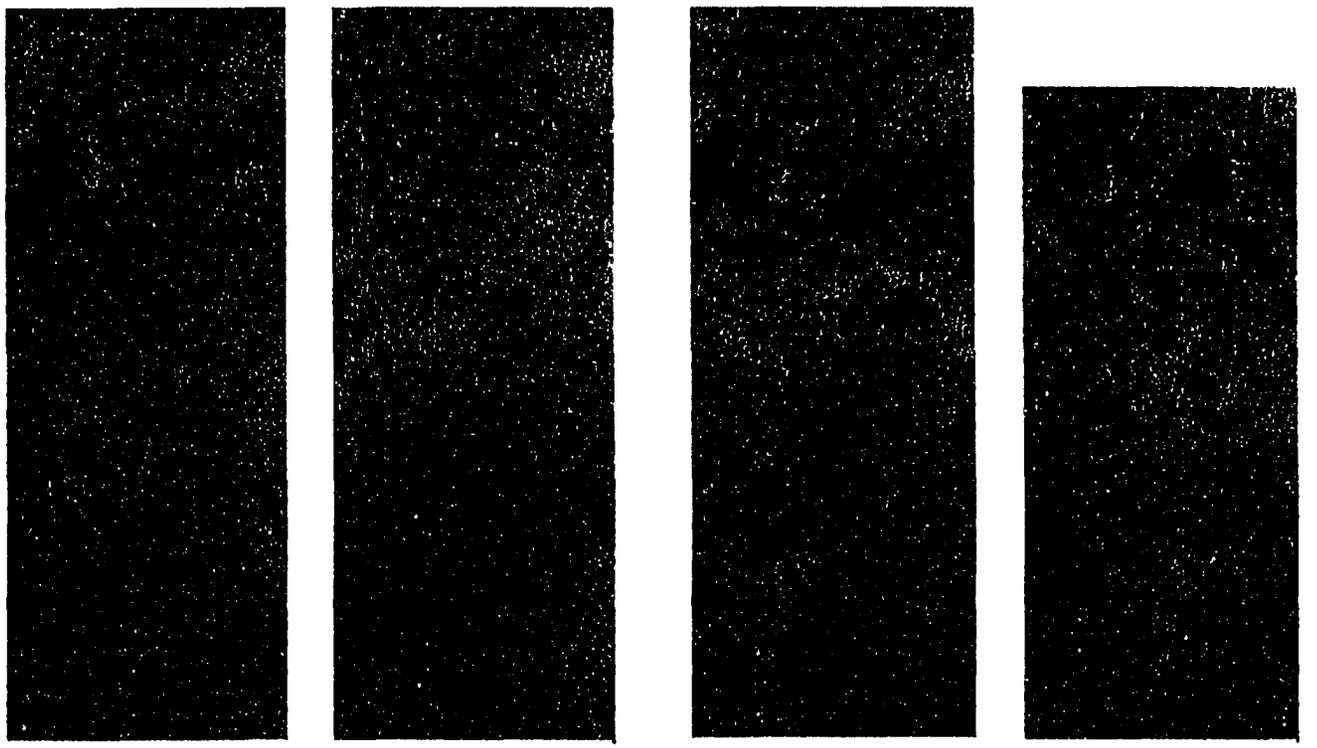

Figure 3.16: LoRes ERS-1 SAR image mosaics of the SLIP-March 16-28, 1992. As in Figure 3.1 except that imagery is for (left to right): March 16, 1992, March 19, 1992, March 22, 1992, and March 28, 1992. The southern SLIP is still apparent in the imagery from the 16th, but takes on a much more diffuse appearance by the 19th. The polynya region appears as large bands or plumes of wind-swept frazil extending offshore from the island. The plumes nearly double in size from the 16th to the 19th. By the 22nd, there is very little evidence of the polynya activity three days earlier. The small area of open water/ice-water mix visible off the southern coast in the March 28th strip is either the last of the earlier SLIP or the initial stages of another SLIP event, beyond the time span of the ERS-1 SAR 1992 ice phase imagery. As before, the letter (feature identification) and number (date of location) drawn on the imagery represents changes in position of a distinct ice feature as observed in consecutive image mosaics.

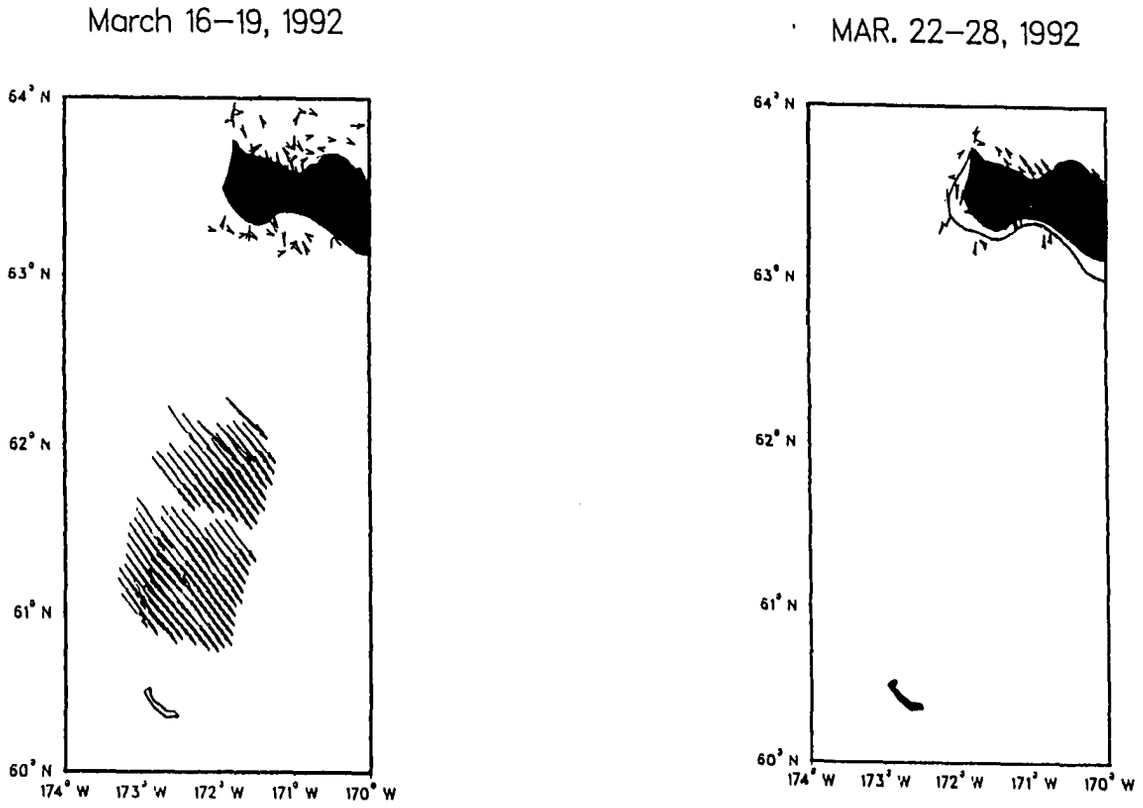

Figure 3.17: ERS-1 SAR GPS ice motion-March 16-28, 1992. As in Figure 3.2 except that the maps are for the image date pairings noted in the individual panels shown on this page. (See also Tables 3.1 & 3.2 and Figure 3.15)

side of the island due to lack of trackable features remaining within the SAR swath over the three-day period. Using SAR imagery for these dates and manual tracking, I estimated the ice motion to be on the order of 0.10 to 0.12m s^{-1} (25 to 30km over three days) toward the southwest.

Between March 19 and March 22, the polynya closed as the ice returned to the southern shore of the island. As can be seen in the imagery for March 22 (Figure 3.16), the ice pack south of the island was not completely solid. Instead, there were leads, cracks, and small blocks of ice (rubble) within the ice cover. The prominent plumes of the earlier imagery were only hinted at by variations in backscatter at the bottom of this image strip far south of the island. Interestingly, there was some evidence of pulse-like behavior in the ice motion, as denoted by the arch-like markings along the southern island coast (Figure 3.16).

Ice motion products for the period of March 19-22 shown in Figure 3.17 indicated that ice drift on the south side of the island was 0.12 to 0.13m s^{-1} towards the south/south-east, 1.3 to 1.6% of the associated north/northwesterly wind speeds of 7.8 to 10m s^{-1}. Although this southward ice motion indicates a period of polynya expansion, the imagery presented in Figure 3.16 showed just the opposite. Because of this, it is assumed that the demise of the polynya visible on March 22 (Figure 3.16) took place during a short period of time between March 19 and March 22 (Figure 3.16), during which the northward ice motion was not picked up by the GPS algorithm.

Between March 22 and March 28, winds at the island became more easterly in response to the changing larger-scale atmospheric circulation. Vectors indicated that the ice drift north of the island remained negligible (Table 3.2 and Figure 3.17). It was not possible to create many realistic vectors south of the island for this image pairing. This is not surprising as the time separation between image mosaics for these dates (Figure 3.16) is six days, due to the lack of data acquisition on March 25. As shown in Figure 3.16, the imagery from March 22 and 28 suggested that ice was starting to break away from the southern shore again by March 28. Polynya-like features in the imagery of Figure 3.16 appear to "trend" toward the southeast like those of the late February southern polynya event. It was hard to tell if this was the beginning of a new polynya event as the SAR ice phase orbit ended after March 28.

3.4 ARCSyM Ice Circulation-February 1992 Southern SLIP Event: Due to limited resources, my two primary ARCSyM simulation experiments considered only one SLIP

event, the southern event in February 1992. I have divided my results into four categories to reflect the two types of simulated oceans incorporated into the model experiments, and also the observation-based strong wind forcing/weak wind forcing episodes that occurred during the SLIP event from February 24-March 1, 1992. Discrepancies are most notable in comparisons of observed fields and the swamp model output, as the "swamp" model version of the ARCSyM does not respond accurately to varying or weak forcing. The model ice motion responds more quickly to the changed atmospheric forcing than the observed ice does. The low temporal resolution of the observed ice drift (i.e., based on images three days apart), in comparison with the continually changing atmospheric forcing, made it difficult to assess more than just the three-day average simulated ice motion. However, the differences between the averaged simulated ice motion fields obtained during the weak forcing period and the strong forcing period, and the ice motion changes resulting from the different ocean parameterization, are noteworthy. The discrepancy between observed ice motion and simulated ice motion also points to a potentially important role for the ocean circulation, especially during periods of weak atmospheric forcing.

3.4.1 Ice Motion: Swamp Ocean-Strong Atmospheric Forcing: February 24-27: Simulated and observed sea level pressure fields for start and end dates of this period are shown in Figure 3.18. Agreement between observed and simulated pressure fields is quite good. For this experiment, the ocean was specified only in terms of thermodynamics, i.e., no ocean circulation field was incorporated into the ARCSyM model. Figure 3.19 shows the ARCSyM simulated ice drift field for February 24-27. Simulated ice drift results indicated ice drift to be 0.35m s^{-1} (i.e., 3.3% of the simulated wind speed). The average simulated wind speed over the island was 10.6m s^{-1} directed towards the southwest. Observed ice speeds were as much as 0.34m s^{-1} during this period, so the model and observations are in good agreement. The simulated ice circulation was directed about 20 degrees more to the southwest than observed in the GPS fields. The good agreement here indicates that the ice motion was predominantly wind-driven.

3.4.2 Ice Motion: Barotropic Ocean-Strong Atmospheric Forcing: February 24-27: The simulated ice motion fields produced by this barotropic ocean run are shown in Figure 3.20. The currents, shown in Figure 3.20, are averaged over the time of the entire experiment (February 18-March 1) and held constant in time. During this period of strong persistent winds (February 24-27), the simulated ice displacement was reduced by nearly

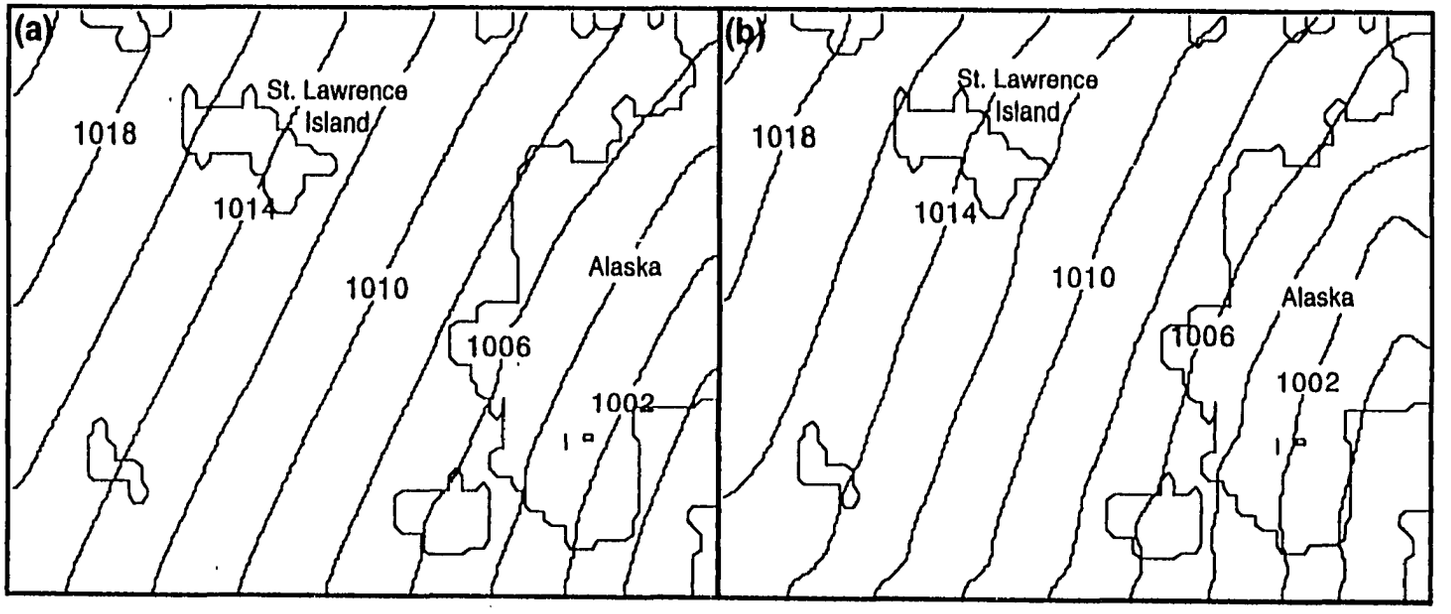

Figure 3.18: A Comparison of Sea Level Pressure Maps-February 24, 1992 (00Z): (a) European Center for Medium-Range Weather Forecasting (ECMWF) analysis and (b) Arctic Region Climate System Model (ARCSyM) "swamp" ocean simulation results. Contour interval is 1 mb.

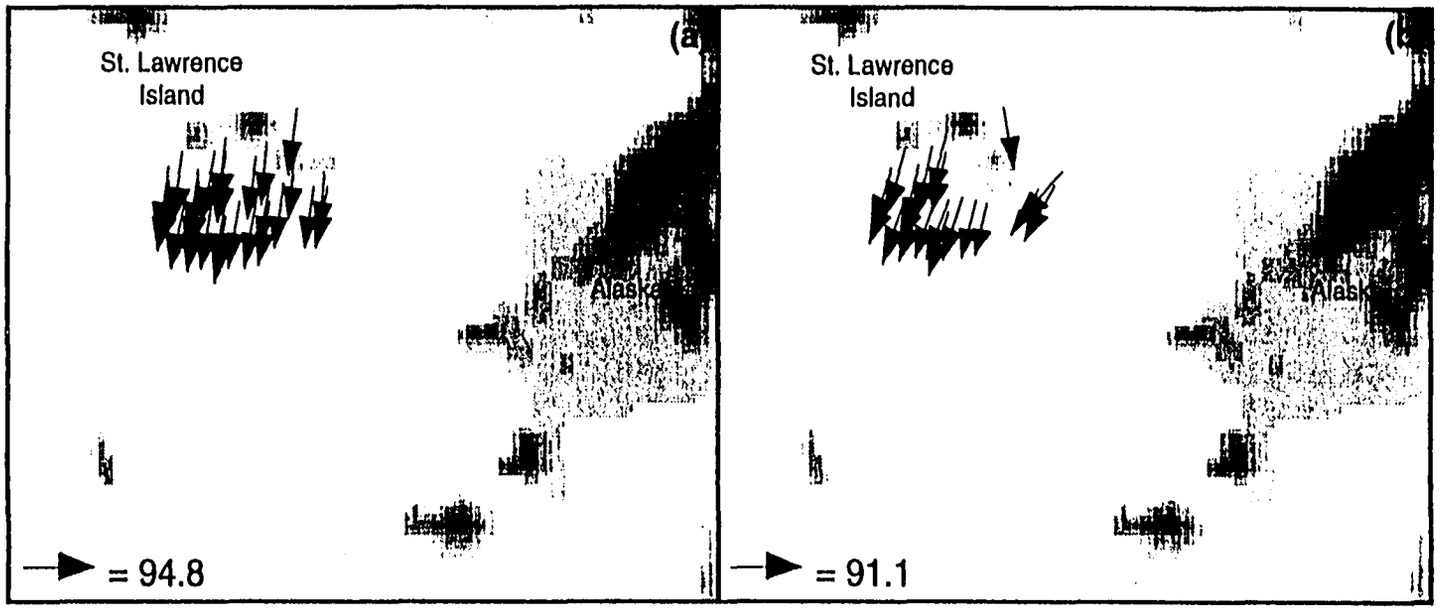

Figure 3.19: A Comparison of Observed and Simulated Ice Motion-February 24-27, 1992. (a) Observed ERS-1 SAR GPS ice motion and (b) ARCSyM "swamp" ocean experiment ice motion results. Maximum ice vector for each map is as shown. Note: vectors are overlaid on the model generated topography and thus, may appear to go through land due to the model's resolution constraints. In order to reflect the ice displacement as it was observed in consecutive SAR passes, units for ice motion are given here as "km per three days".

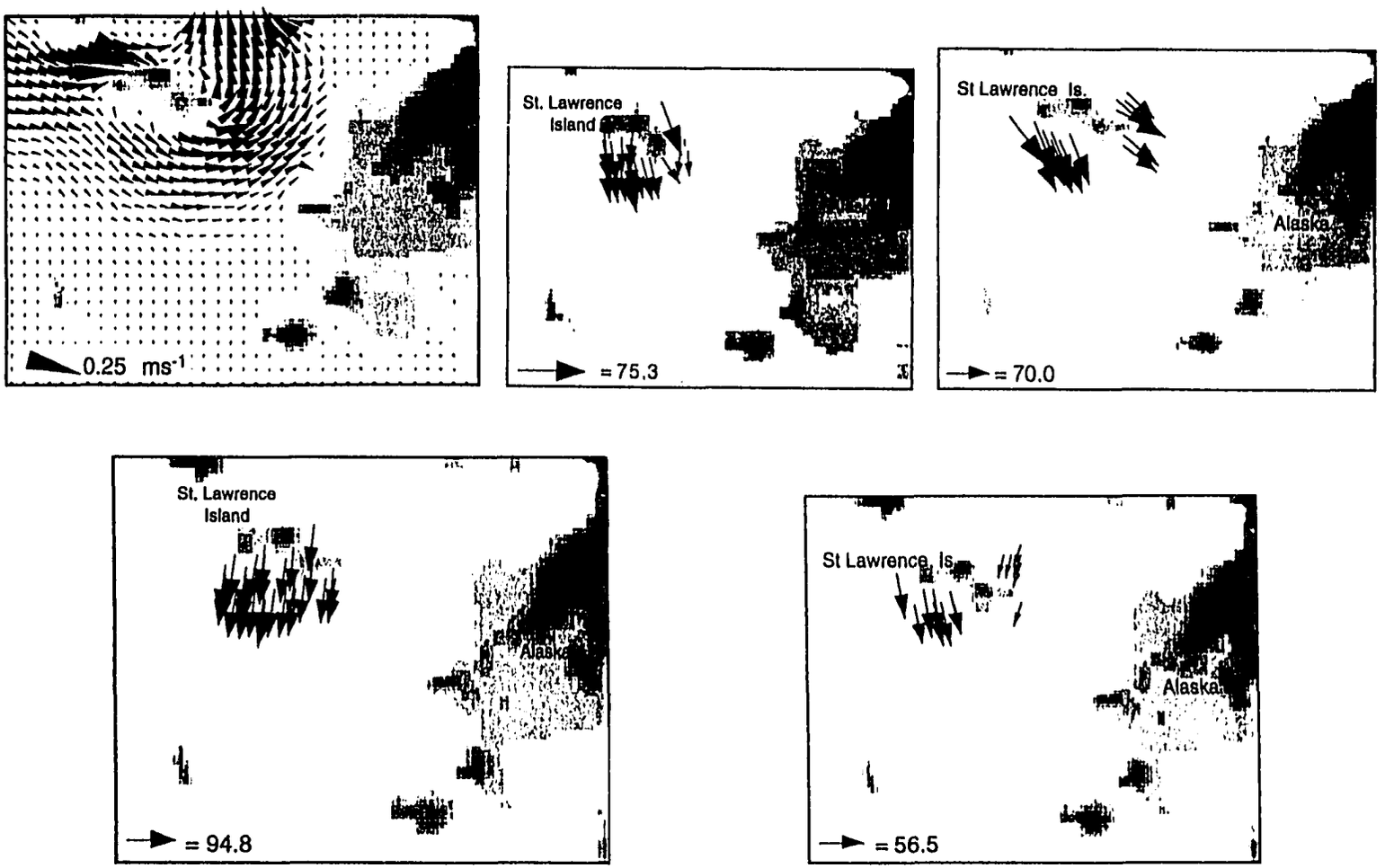

Figure 3.20: "Barotropic" Ocean Circulation Field & Comparison of Model and Observed Ice Motion : February 24-27 and February 27-March 1, 1992. Top (l to r): Ocean currents as calculated for the region from output of a barotropic model (see Chapter 2 for details); ARCSyM "barotropic ocean experiment ice motion for February 24-27 and for February 27-March 1, 1992. Bottom (l to r): ERS-1 SAR GPS ice motion for February 24-27 and for February 27-March 1, 1992. As in Figure 3.19, units are "km per three days".

30%, from 91.1km over the three day period of February 24-27 (30km day^{-1}) as simulated by the "swamp" model to 75.3km over the same period (25km day^{-1}) as shown in Figures 3.19 and 3.20. For comparison, the GPS ice motion for February 24-27 was 29km day^{-1} or 87km over three days. The simulated ice motion from this "barotropic" experiment was directed more southward at the polynya than it was in the "swamp" ocean experiment. This addition of oceanic forcing brings the simulated ice motion closer to the observed ice circulation in terms of direction, but the combined effect of the simulated oceanic and strong northerly wind forcing is evidently not reproduced accurately, as the simulated ice motion for this period is smaller than that observed. This erroneously small drift reduction may indicate that the ratio of oceanic to atmospheric drag is too high (Lynch et al., 1997), despite the attempts made to fine tune the drag coefficient.

3.4.3 Ice Motion: Swamp Ocean-Weak Atmospheric Forcing: February 27-March 1: The simulated and observed sea level pressure fields for this period are shown in Figure 3.21. Discrepancies between observed and simulated fields are apparent, especially in the contours along the domain boundaries. The model also moves the low pressure feature through the domain faster and more intensely than observed. The observed ice drift was much smaller during this period, and the simulated ice drift field (Figure 3.22) also indicates a great reduction in speed. The maximum simulated ice drift is 13.1km or 0.05m s^{-1} to the east-southeast. The simulated ice drift suggests that the simulated ice motion is not directly responding to the wind forcing during this period. The fact that the simulated ice is still moving at all, given the lack of simulated ocean circulation, seems to indicate a time-lag in the ice's response to atmospheric forcing in the model. The SAR-based ice motion suggests a more predominant influence of ocean circulation during this weak wind period, or, perhaps, a combination of a forcing-response time lag and increased ocean influence. Only the ocean contribution was investigated further in my research.

3.4.4 Ice Motion: Barotropic Ocean-Weak Atmospheric Forcing: February 27-March 1: As shown in Figure 3.20, the addition of a barotropic ocean current field increases the simulated maximum ice displacement by more than 5 times the "swamp" ocean simulated value of 13km, to a new value of 70km over the same three day period. This 70km ice displacement exceeds the GPS ice displacement of 56km for that same three day period. The simulated ice motion farther away from the island's south coast is now directed more southward than in the "swamp" simulation. Close to the polynya, though,

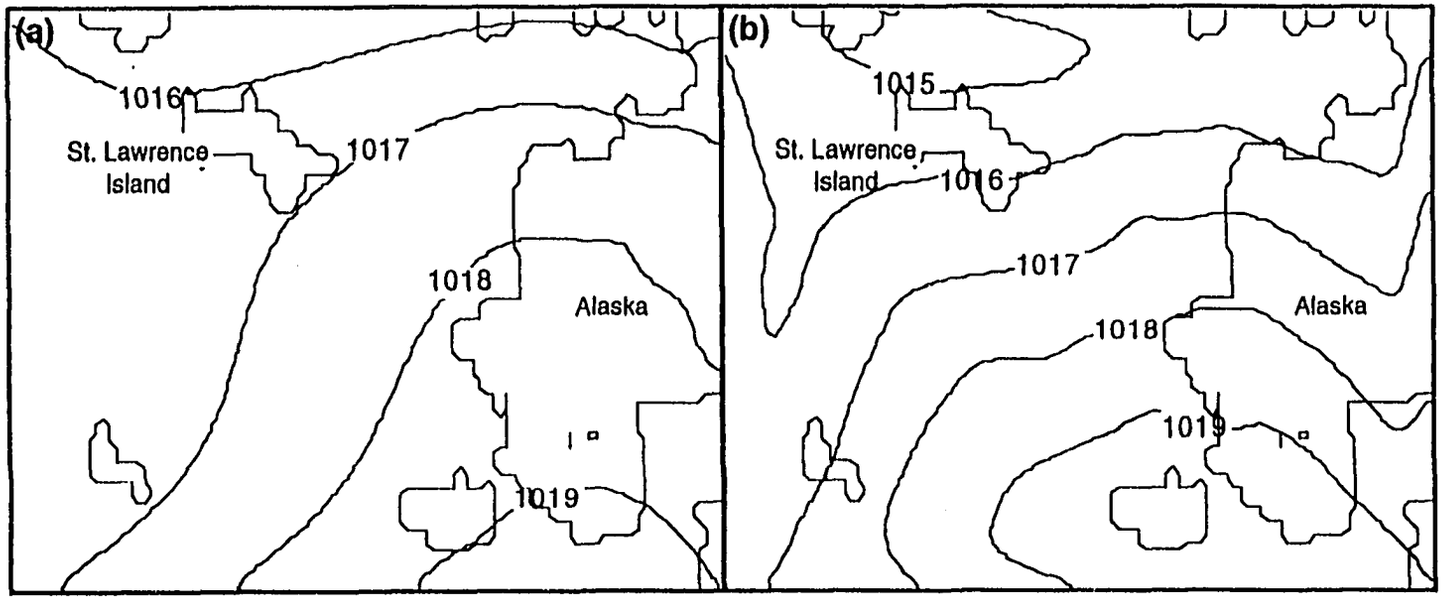

Figure 3.21: A Comparison of Sea Level Pressure Maps-February 27, 1992 (00Z): As in Figure 3.18, but for February 27, 1992. (a) ECMWF Analysis and (b) ARCSyM "swamp" ocean experiment simulated pressure field. Contour interval is 1 mb.

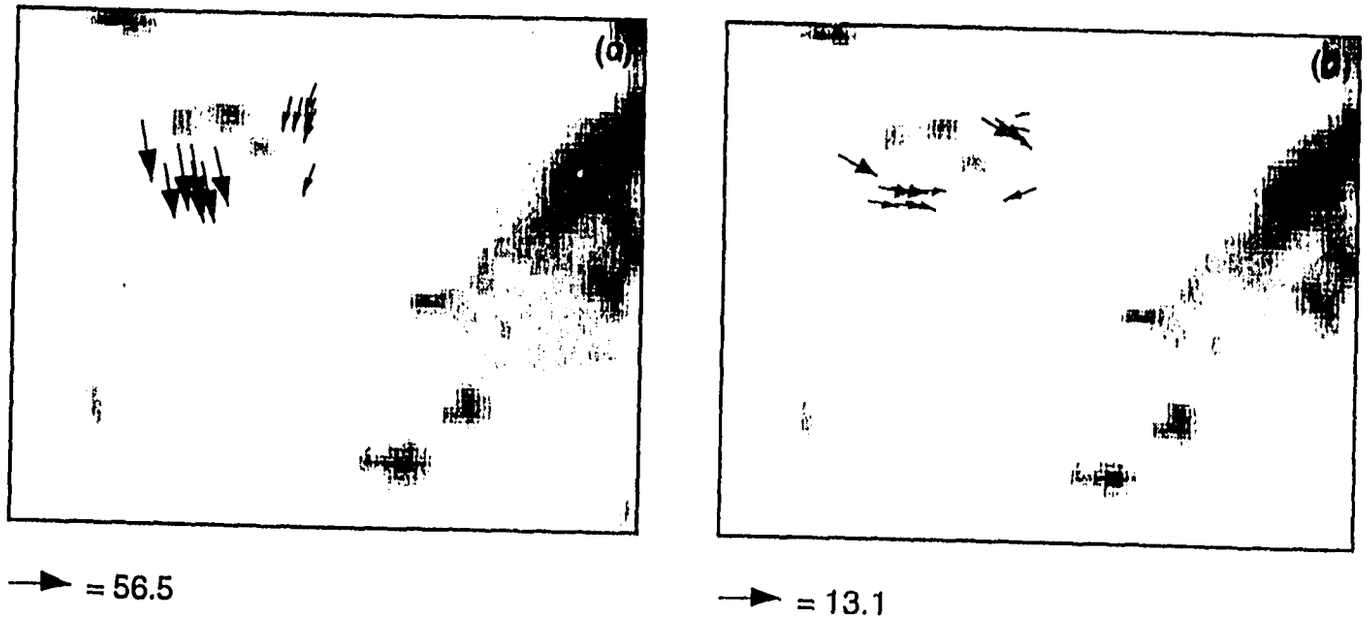

Figure 3.22: A Comparison of Observed and Simulated Ice Motion-February 27-March 1, 1992: As in Figure 3.19, but for February 27-March 1, 1992. (a) Observed ERS-1 SAR GPS ice motion and (b) ARCSyM "swamp" ocean experiment ice motion results. Maximum vector for each map is as shown. As before, units are "km per three days".

the simulated ice drift is still directed eastward of the southward direction indicated by SAR-derived vectors. Also, northeast of the island, the simulated ice drift is still directed eastward (90° deflection) of the observed SAR ice motion. However, the simulated ice motion is essentially parallel to the simulated ocean currents along the southern and southeastern island coasts, suggesting that the ice motion and ocean circulation are more strongly related under weak wind conditions. The eastward overall tendency of the simulated ice motion south of the island (Figure 3.20) is reflected in the narrowing of the polynya from the west by March 1. As the ice motion still has a bit of a southward component as well, the polynya retains areas of low ice concentration areas immediately off the island's southern coast to the end of the simulation experiments.

3.5 Discussion

Changes in ice displacement and the occurrence of polynya events are shown to be closely-related to shifts in local wind direction resulting from the passing storm systems. In light of these results, it is not surprising that synoptic-scale storms are considered to play the largest role in SLIP events (Overland and Pease, 1982; Schumacher et al., 1983; Kozo et al., 1990). However, the ocean circulation also appears to be important to SLIP ice circulation; it seemed to play its largest role during the weak wind forcing episode (February 27-March 1). The potential impacts of the oceanic forcing on the ice motion were plainly visible during this period of weak wind as the oceanic forcing was no longer overwhelmed by the effects of strong, sustained wind.

In the southern polynya events discussed above, polynya development began with the onset of northerly winds over the island, causing the ice along the southern coast to be driven southward. In fact, the three southern SLIP events that occurred were quite dynamic in terms of southward ice motion and variation in regional ice cover extent. For example, ice speeds of up to 0.34m s^{-1} were observed, yet very little open water was observed. The extent of downwind expansion of the polynya was directly related to the speed and direction of persistent offshore winds. The January and March southern polynya events both resulted in ice motion that created polynyas with two lobes visible in the SAR imagery, both tilted toward the southwest, while the February southern polynya event resulted in a one-lobed polynya extending towards the southeast. The February polynya was probably also a two-lobed feature, but it was too extensive a polynya to be observed completely in a single image-wide SAR imagery strip. The difference in the tilt of the lobes in January-March can be traced to the difference in prevailing wind direction and the

persistence of that direction. The prevailing wind direction throughout most of January and March was towards the southwest, while the prevailing wind direction during the southern February event was towards the south/southeast. The only northern polynya event in February occurred during the winter's only extensive period of southeasterly (towards the northwest) or easterly winds.

This atmospheric-ice circulation connection can be traced one step further in that the monthly mean sea level pressure map for both January and March (Figure 3.23) indicated a single Aleutian Low. In contrast, the same type of map for February indicated two low pressure centers along the Aleutian Island chain. As a result, northerly winds were not prevalent over the northeastern Bering Sea and did not have a large effect on the SLIP region during the first 18-20 days of February. The retrograding behavior of the Aleutian Low in mid-late February is not unusual (Niebauer, 1980), although the split Aleutian Low pattern shown in the mean sea level pressure field for February (Figure 3.23) is less commonly observed. The timing, orientation, and type of polynya (southern or northern) events is thus directly related to the intensity and position of the Aleutian Low.

The polynya events ended when the onshore winds became persistent enough to close the polynya completely, or the open water froze, so that the polynya became indistinguishable from the first year ice field, as on February 6. As expected, polynya expansion slowed considerably or stopped when the winds weakened, or wind direction became onshore or along shore. However, the southern polynyas did remain distinct even when wind speeds were reduced to as low as 1.8-2.2m s^{-1}. The fact that ice was moving even when winds were negligible suggests again that ocean forcing on the ice is important in this region.

The balance between wind-ice stress, ice-water stress, and Coriolis force, known as "free-drift", provides a reasonably good estimate of sea ice motion away from coastal boundaries, and also during periods when ice is divergent (i.e.. no ice-ice stress). Zubov (1943) observed that the Arctic ice drifted parallel to the sea level isobars, approximately 20° to the right of the surface wind at a speed of 2% of the geostrophic wind. Similarly, Thorndike and Colony (1982) found that more than 70% of the variance of the ice velocity in the central Arctic Ocean was attributable to the geostrophic wind. However, the free-drift concept does not include ice-ice stress contributions, which become important in areas near the shore, as well as in other areas of ice convergence where ice motion is obstructed by land or other ice. An obvious example would be the motion of the ice trapped along the north coast of St. Lawrence Island during periods of sustained northerly winds.

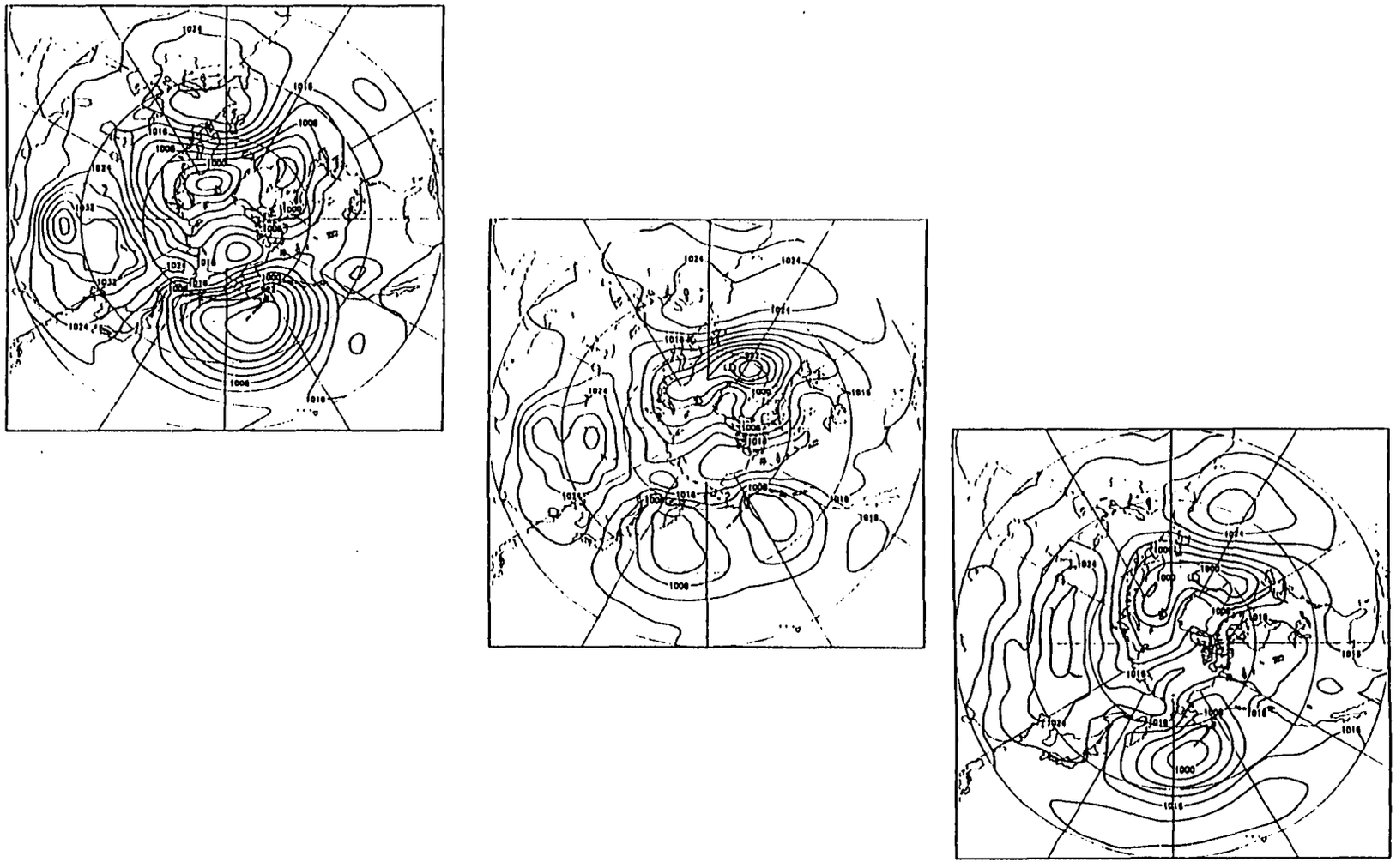

Figure 3.23: Monthly Mean Sea Level Pressure Maps-Winter (JFM) 1992. Maps are for (top) January 1992; (mid) February 1992; (lower) March 1992. Contour interval is 4 mb. Note the variations in position and intensity of the Aleutian Low throughout the period.

During the period of observation, the largest ice velocities were located on the southern side of the island. During periods of northeasterly or northerly winds below 7m s^{-1}, ice drift magnitudes were approximately 2-4% of the wind speed with positive drift angles relative to the wind direction as shown in Figure 3.24. The drift angle of the ice relative to the wind direction (Table 3.3) ranged from 48° to the left of the wind (negative angle) to 53° to the right of the wind (positive angle).

Stronger northeasterly and northerly winds of speeds greater than 7m s^{-1} were associated with ice drifting nearly parallel to wind direction, resulting in the smallest turning angles observed for ice motion associated with the winter 1992 SLIP events. The turning angle or drift angle of the ice relative to the wind direction ranged from 1° to 10° to the right of the wind (Table 3.3). In fact, the drift angles less than 18° were always directed to the right of the wind. The smallest drift angle of the study period was 1° to the right of the wind: it occurred between February 24 and February 27 in association with 10.8m s^{-1} station winds directed almost due south. Ice motion during that episode was the largest observed from the SAR imagery at 0.34m s^{-1}, or 3.2% of the station wind speed. In general, ice motion during these periods of stronger winds were 3-4% of the wind speed, the highest ice-wind speed ratios of the study period (Figure 3.24).

The mean drift angle for ice located on the south side of the island during northerly/northeasterly winds was 7°, with a range of 132° to the left of the wind through 67° to the right of the wind. The large positive angles of 20° or more occurred during north-northwesterly winds of 2-7m s^{-1}, while a large negative angle was only observed once during northeasterly winds (January 1-4).

It is important to note that, although the purely geostrophic-type forcing relationships of the GPS ice motion algorithm applied during the vector creation procedure may be marginally suitable for "south side" SLIP ice motion, the relationships are not applicable to the "north side" SLIP ice motion. This departure is reflected in north-side ice motion, and in ice motion during weak/variable or easterly winds listed in Table 3.3 and Figure 3.24. Ice motion vectors on the north-central side of the island show very little relationship to wind characteristics, since this ice is trapped by topography and by the overall motion of the first year ice pack. Ice drift angles relative to the wind for this trapped ice are as much as 180° different from the wind (Figure 3.24).

In summary, as shown in Figure 3.24, an increase in the wind led to an increase in the speed of the ice drift. The majority of the south side ice motion was at 2-4% of the ice speed, especially for Gambell station winds near 7m s^{-1} or greater. The overall range of

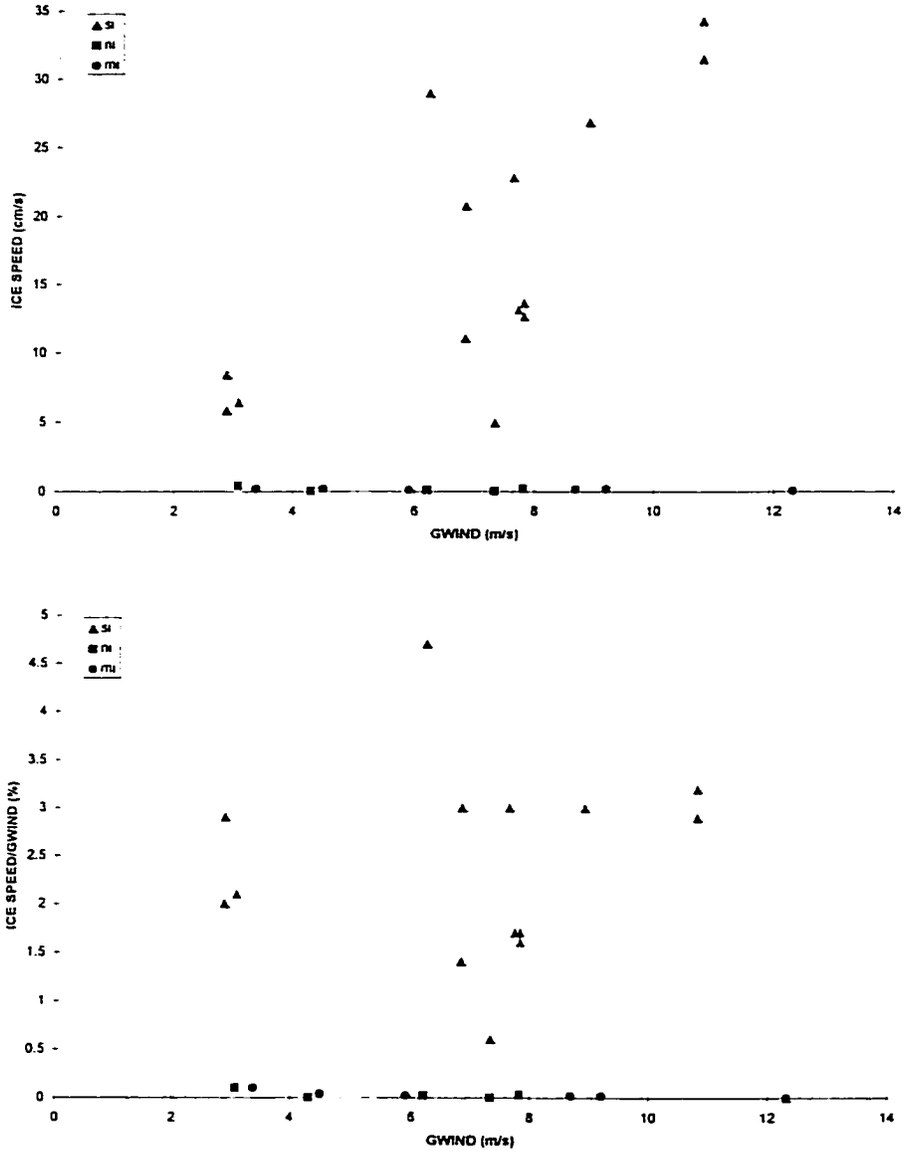

Figure 3.24: Ice Motion-Wind Relationships. Shown here are plots of: (top) GWIND vs. ICE SPEED; GWIND vs. ICE SPEED/GWIND. Units for GWIND are m s^{-1}. The unit for ICE SPEED is cm s^{-1}. SI (triangle)= vector products with vectors on south side of the island only; NI (square)=north side of island only; MI (circle)=mix of north side and south side of island. See also Tables 3.1-3.3 for additional detail.

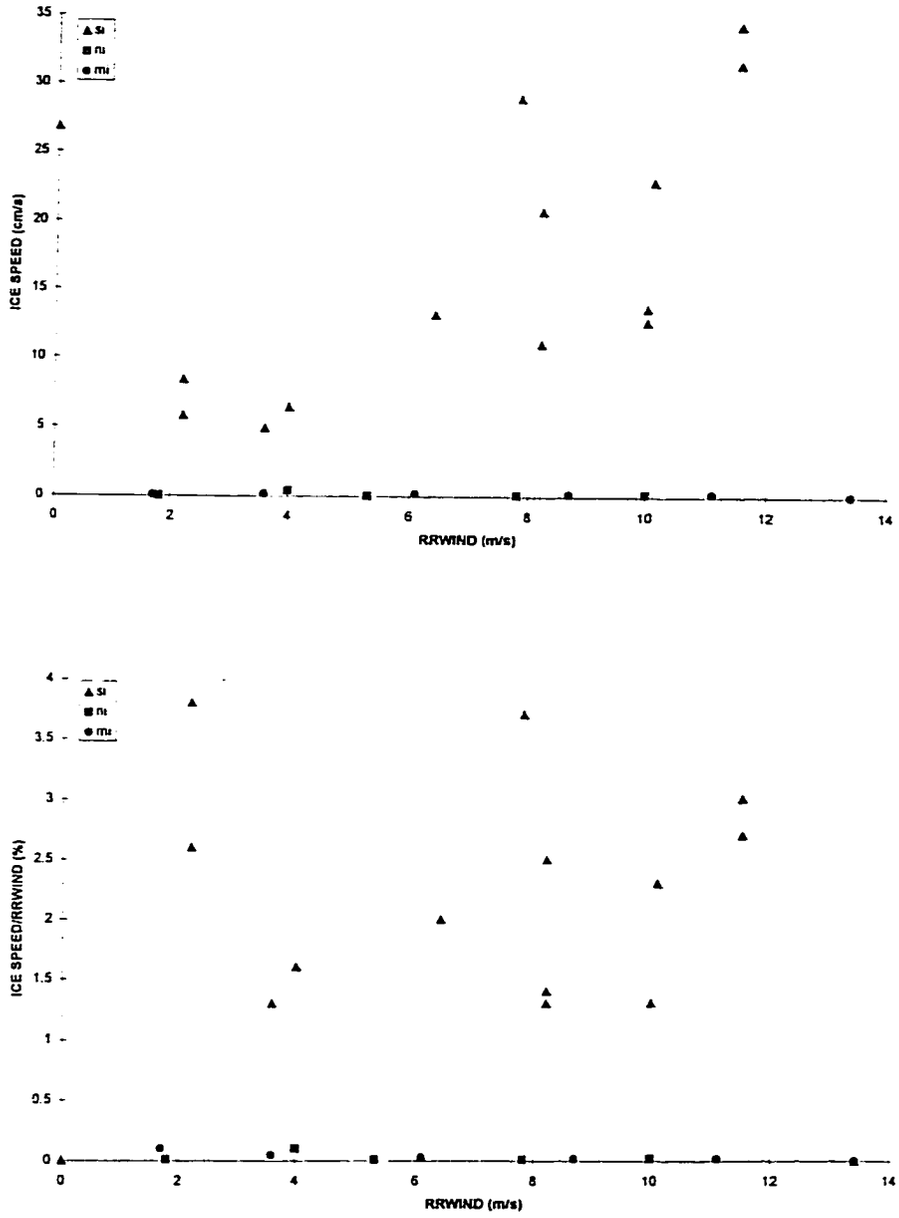

Figure 3.24 (continued): Ice Motion-Wind Relationships. Shown here are plots of: (top) RRWIND vs. ICE SPEED; (bottom) RRWIND vs. ICE SPEED/RRWIND. Units for RRWIND are m s^{-1}. The unit for ICE SPEED is cm s^{-1}. SI (triangle)= vector products with vectors on south side of the island only; NI (square)=north side of island only; MI (circle)=mix of north side and south side of island. See also Tables 3.1-3.3 for additional detail.

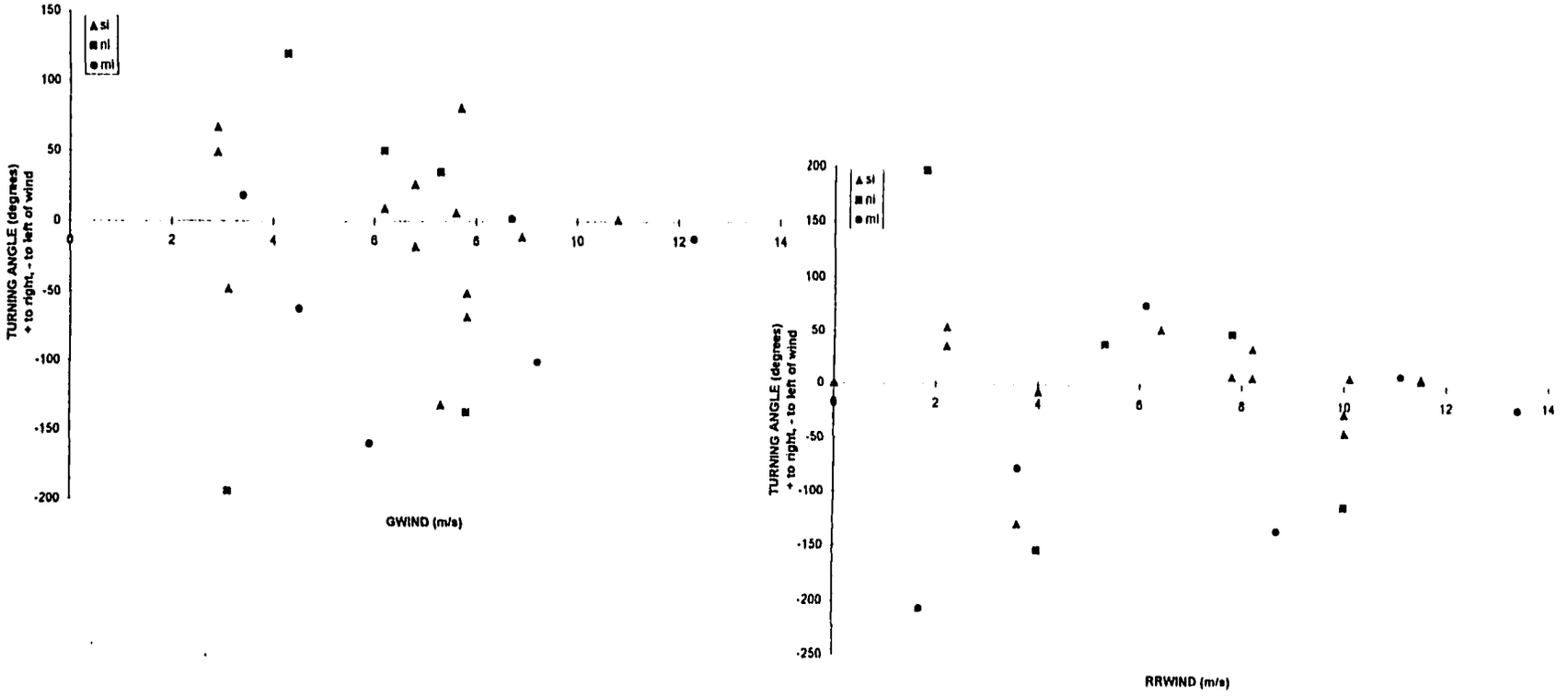

Figure 3.24 (continued): Ice Motion-Wind Relationships. Shown here are plots of: (left) GWIND vs. ICE TURNING ANGLE; (right) RRWIND vs. ICE TURNING ANGLE. TURNING ANGLE is defined as the drift angle between the ice motion direction and the wind direction with "+" representing ice motion to the right of the wind and "-" representing ice motion to the left of the wind. Units for GWIND and RRWIND are m s^{-1}. The unit for TURNING ANGLE is degrees. SI (triangle)= vector products with vectors on south side of the island only; NI (square)=north side of island only; MI (circle)=mix of north side and south side of island. See also Tables 3.1-3.3 for additional detail.

Table 3.3: ERS-1 SAR GPS Ice Motion Products and Ice Motion/Wind Relationships (Part 2). As in Table 3.2, except that ice turning angle in relationship to wind has been included here. Positive turning angle refers to ice motion "to the right" of the wind direction, negative turning angle refers to ice motion "to the left" of the wind. As before "*" indicates a six day time separation between imagery dates.

SAR IMAGERY DATE	ICE MOTION cm s^{-1} ; To (°)	GWIND m s^{-1} To (°)	ICE:GWIND SPEED %	ICE TURNING ANGLE (°)	RRWIND m s^{-1} To (°)	ICE:RRWIND SPEED %	ICE TURNING ANGLE (°)
Southern SLIP							
Dec 29-Jan 1	26.8 SW (217)	8.9 SW (228)	3.0	-11	missing	missing	missing
Jan 1-4	4.9 E (088)	7.3 SW (220)	0.6	-132	3.6 SW (217)	1.3	-129
Jan 4-7	13.1 NW (319)	7.7 SW (238)	1.7	81	6.4 W (266)	2.0	53
Jan 25-28	22.8 SW (219)	7.6 SW (213)	3.0	6	10.1 SW (211)	2.3	8
Jan 28-31	6.4 S (178)	3.1 SW (226)	2.1	-48	4.0 S (185)	1.6	-7
Jan 28-31	0.4 NE (032)	3.1 SW (226)	0.1	-194	4.0 S (185)	0.1	-153
Northern SLIP							
Jan 31-Feb 6*	0.2 S (178)	4.5 SW (240)	0.04	-62	3.6 WSW(255)	0.05	-77
Feb 12-15	0.1 ESE (107)	5.9 W (267)	0.02	-160	1.7 NW (314)	0.1	-207
Feb 15-18	0.2 SSE (166)	9.2 W (267)	0.02	-101	8.7 NW (299)	0.02	-133
Southern SLIP							
Feb 18-21	0.03 NW (314)	7.3WNW(279)	0.0	35	5.3WNW(275)	0.01	39
Feb 21-24	0.2 SSW(193)	8.7 SSW(191)	0.02	2	11.1 S (183)	0.02	10
Feb 24-27	34.2 S (189)	10.8 S (188)	3.2	1	11.5 S (181)	3.0	8
Feb 24-27	31.4 S (187)	10.8 S (188)	2.9	1	11.5 S (181)	2.7	6
Feb 27-Mar 1	20.7 SSE(168)	6.8 SSE (170)	3.0	-18	8.2 SSE (160)	2.5	8
Feb 27-Mar 1	11.0 SSW(196)	6.8 SSE (170)	1.4	26	8.2 SSE (160)	1.4	36
Feb 27-Mar 1	11.0 SSW(196)	6.8 SSE (170)	1.4	26	8.2 SSE (160)	1.3	36
Mar 1-4	5.8 SW (235)	2.9 S (186)	2.0	49	2.2 SSW(199)	2.6	36
Mar 1-4	8.4 WSW(253)	2.9 S (186)	2.9	67	2.2 SSW(199)	3.8	54
Southern SLIP							
Mar 10-13	0.02 NW (323)	4.3 SW (204)	0.0	119	1.8 ESE(126)	0.01	197
Mar 13-16	28.9 SW (211)	6.2 SW (202)	4.7	9	7.8 SW(202)	3.7	9
Mar 13-16	0.1 WSW(252)	6.2 SW (202)	0.02	50	7.8 SW(202)	0.01	50
Mar 16-19	0.04 SSW(197)	12.3 SW (209)	0.0	-12	13.4 SW (217)	0.00	-20
Mar 19-22	0.2 ENE (070)	7.8 SW (207)	0.03	-137	10.0 S (181)	0.02	-111
Mar 19-22	13.6 SE (139)	7.8 SW (207)	1.7	-68	10.0 S (181)	1.3	-42
Mar 19-22	12.6 SE (156)	7.8 SW (207)	1.6	-51	10.0 S (181)	1.3	-25
Mar 22-28*	0.2 WSW(258)	3.4 WSW(240)	0.1	18	6.1 S (182)	0.03	76

ice:wind varied from as little as 0.5% to as much as 4.5%. Turning angle or drift angle results indicated that wind speeds of 7m s^{-1} or more resulted in ice motion south of the island being nearly parallel to the wind. The turning angles of ice south of the island decreased from 50° or more to almost zero as wind speeds increased (Figure 3.24). Finally, no ice motion was detected by the GPS algorithm when wind speeds were less than 1.7m s^{-1}.

Although the SAR GPS vectors were acceptable for observing the basic ice circulation associated with the SLIP, it was evident that the GPS has limitations. These problems included: (a) poor detection and tracking of features where ice was forming or very thin and was drifting rapidly within the polynya itself; (b) inability to detect many of the features available for tracking that were easily detectable by visual examination of sequential (time-wise) image pairs; and (c) large differences in the number of individual points (also referred to as tie points or vector endpoints) in subsequent image pairs (or any image pairs from different dates).

Problem (a) led to virtually a complete lack of ice motion vectors within the polynya itself, where all the ice formation and associated small-scale motion was taking place. The ice floes within the region were well below the 5km grid scale so they were not resolvable by the processor. Further, the ice within the polynya itself was undergoing extremely turbulent motion due to the large energy transfers taking place at the most active sectors within the polynya, in addition to the persistent offshore wind forcing. The newly forming ice was also undergoing developmental changes, from frazil crystals to pancakes and/or grease ice mats, at such a rapid pace that it undoubtedly changed shape, composition, and size numerous times between the 3-day satellite passes.

Problem (b) proved to be the most curious, and the most likely root of the other problems. Why couldn't the GPS tracker see and track features correctly that were obvious upon inspection? An example is shown in the February 21-24 image pairing (Figure 3.11) which indicated the large expansion of the southern SLIP. Ice speeds determined from my measurements of the position of the southern edge of the polynya on February 21 and February 24 indicated 0.23m s^{-1} or 20km day^{-1} which corresponds to 2.5% of the wind speed. The GPS average ice motion for that pairing of images was 0.002m s^{-1}, much too low. In fact, the GPS algorithm missed 50km of southward motion. There are other examples, such as March 10-13 (Figures 3.14 and 3.15).

Problem (c) resulted in vectors within GPS products ranging from 8 in the January 4-7 pairing to 187 in the March 1-4 pairing (Table 3.3). The more populous products resulted when winds had prevailed from the north quadrant for several days, or when there

were very obvious ice features such as the polynya boundary or large leads in the first year ice pack to use for tracking. As no time series of dense motion grids (ice motion fields) similar to those produced for the Arctic Ocean (Colony and Kwok, personal communication) resulted from this GPS processing, I was unable to calculate any quantitative terms such as ice divergence over time between image pairs. The lack of completed motion grids was largely due to the lack of persistent features to track from one image to the next and to the fact that potentially trackable features were no longer within the swath width of the imagery by the time of the next image acquisition three to six days later. Melting or new ice feature formation would definitely lead to such a problem. The GPS cannot be blamed for missing features that disappear within the three-day repeat. However, the user needs to be aware of the potential for this type of error when analyzing GPS results.

The missed features and missed tracking can potentially be attributed to other things. One is that the algorithm attempts to match features using techniques including a mathematical representation of the feature shape. If after three days, the feature in question was no longer similar enough to the "target" image, or if it had moved out of range as judged by the geostrophic wind relationships invoked, a match would not be made by the algorithm. Perhaps in the future, GPS algorithms including ice texture, and/or ice type classification guidelines could be developed as a means of ice identification, cross-check, and elimination. Another reason for missing features may be due to the use of a single wind point at the centerpoint of an image to estimate the wind forcing on the ice and the ice's potential range of motion. It may be that the use of a wind data grid or wind fields from the satellite's own instrumentation would be more appropriate for these more dynamic regions such as the SLIP. The use of climatological ocean currents or regional current meter data in conjunction with a wind data grid would aid in estimating potential ice motion. Tracking features using image strips or "image mosaics" rather than individual image frames would also reduce the number of features that drift out of an image domain over the three-day period. Although I have presented the SAR imagery here in mosaic form for ease in observation, all GPS processing was done on pairs of single frame images as the GPS was not capable of handling the larger strip format. Decreasing the time period between images would greatly enhance ice motion tracking ability at the SLIP and within the northeastern Bering Sea as this would allow the algorithm to match and track individual features that disappear or transform in periods of less than three days. RADARSAT GPS (Kwok et al., 1995) has been designed to have the additional ability to track individual ice features in a Lagrangian fashion as they move through the Arctic.

Finally, perhaps models like the ARCSyM could be used to simulate a "first guess" field to aid the GPS in tracking ice motion outside its designed geographical range, so that study of the marginal ice areas outside of the Arctic could also benefit from this newer technology on a more routine basis.

Validation error statistics for Arctic-based GPS ice motion products, in general, show uncertainty in the geolocation of common features to be between 100m and 200m due to errors resulting from the geographic registration of the imagery (Stern et al., 1993; Kwok and Cunningham, 1993). Including all possible sources of error led to an overall estimate of ice movement errors in the range of 300m (Stern et al., 1993) for the Arctic region. GPS ice motion errors around the SLIP are likely to be higher than those for the Arctic due to the highly dynamic nature of the ice motion in the region, the limited number of trackable features present in the SLIP SAR imagery, and the greater chance of incorrect or non-existent feature matching in the SLIP SAR GPS processing. As a result, errors in GPS ice displacements or speeds associated with a suite of SLIP ice motion products will also be more variable than those from the Arctic. Unfortunately, it was not possible to develop any formal error statistics for the SLIP ice motion products as the products were so variable in content (number of individual vectors within a field), and areal coverage (within field distribution and field geographic location).

The GPS processor and the ARCSyM model were successful in producing the SLIP ice motion products regardless of darkness, storms, and clouds. While the GPS products were not representative of the entire region surrounding St. Lawrence Island, or even the SLIP expansion at times, the GPS produced a qualitatively and quantitatively useful set of ice motion data for a region well beyond its intended domain (i.e., the SLIP is well south of the accepted "north of 73°N" GPS domain). These ice motion products represent the first ERS-1 SAR-based ice motion products for the SLIP region and for the Bering Sea as a whole. ERS-1 imagery is crucial to studying the ice circulation associated with the SLIP as it provides the high resolution, remotely acquired, "unimpeded by weather" image data needed to produce ice circulation vectors. Although some additional tuning and adjustment is obviously needed, the ARCSyM has the first ever successful regional climate system model view of simulated ice circulation associated with the SLIP. As our understanding of SAR-sea ice relationships improves, and our ability to define (GPS algorithm tuning) and simulate parameters at this scale increases, so will our ability to remotely observe, model, and predict the ice circulation associated with polynyas under all conditions.

CHAPTER 4: POLYNYA SIZE

4.1 Introduction

In this chapter, I determine the areal extent of the February 1992 southern SLIP event for the purpose of establishing a polynya area to use in the energy balance computations of ice production and dense water production discussed in Chapter 5. Calculations of polynya size are accomplished here by using satellite observations, an analytic model of polynya growth (hereafter, PM model; Pease, 1987), and a regional climate system model (ARCSyM; Lynch et al., 1995 and 1997). The satellite observations used in this chapter are the low resolution (100m pixels) SAR images of the SLIP for February 18-March 1, 1992, the corresponding (time and space) AVHRR thermal IR images (1km pixels) for February 18-March 1, 1992, and the SSM/I-based brightness temperatures (converted to first-year ice concentration; 25km pixels) for February 25 and February 28, 1992. I chose to focus here and in the following chapter on this particular SLIP event of the 1991-1992 winter as this SLIP event had the most comprehensive coverage in terms of satellite imagery, ice vectors and meteorological data.

Identification of open water and ice in the SLIP is crucial for the measurement of the polynya's size as accurate measurement of these characteristics' extents leads to more accurate estimates of the extent of the heat fluxes, ice production and dense water production associated with the SLIP. Heat fluxes from open water to the atmosphere are an order of magnitude or more larger than those through a ice cover. This difference increases as ice cover grows thicker and more continuous over time. It is possible for the following ice categories to exist within a polynya like the SLIP (Massom and Comiso, 1995): open water, new ice, dark grease ice (thickness=0.05m), light grease ice (0.05 to 0.1m thick), and young ice (gray and gray-white ice 0.1- 0.3m thick). New ice (including frazil ice) may be swept into long streaks or rows within the polynya region by the wind. In optimum growing conditions, almost all new ice crystals can be transformed to grease ice within an hour of initial formation (Svensson and Omstedt, 1994). Grease ice (also referred to as "nilas" in the literature) appears as a film-like layer on the sea surface within a polynya. The grease ice is advected by wind (and wind-driven currents) to be piled against the downwind polynya region boundary becoming, in time, indistinguishable from first-year ice. The outer boundary of the SLIP region is, generally speaking, distinctly marked

by first year ice. A summary of representative results from earlier investigations of SLIP-related ice concentration and ice types is shown in Table 4.1.

4.2 Determination of Polynya Size

The distinction between open water and the newer forms of ice is difficult using SAR imagery alone, because of the similarities in backscatter characteristics between newly formed ice and open water during windy conditions. In addition, neither AVHRR nor SSM/I alone provides the resolution necessary to define boundaries within the polynya region. The accurate characterization of a polynya is made even more difficult by the many categories of ice present within the polynya region and the ever-changing ice thicknesses and surface temperatures. I attempted to estimate the size of the SLIP through a combination of different satellite image-based measurements, and also by using model simulations.

4.2.1 SAR/AVHRR-based Estimate of Polynya Size: As no routine SAR or AVHRR ice classification algorithms or products were available for the SLIP region, I was forced to devise other methods of determining just how big this SLIP was, how much open water existed in it, and how big the regions of water, frazil, and grease ice were. In doing so, I attempted to relate the sea ice surface temperature values (obtained from the thermal infrared band of AVHRR imagery) to the ice-water spatial details characteristic of LoRes SAR imagery through the use of "combination" SAR/AVHRR graphic products. These unique graphic products provided my first look at the variations in temperature distribution across the polynya regions visible in the highly detailed SAR imagery and allowed me to initially determine, in a broad sense, potential areas of open water as well as ice at different stages of growth. Details of procedures used to create these products were presented in Chapter 2. I then determined geographic locations of ice features distinctly visible in the SAR imagery so that the geographically-mapped AVHRR temperature fields could be related to the ice boundaries. AVHRR temperature values corresponding to these distinct SAR ice features guided my determination of open water, newly formed ice and older polynya ice on the basis that colder ice was older ice and therefore thicker ice.

The polynya opening along the island's southern coast on February 21 is denoted by the combination of ice features and variation in surface temperature as shown in Figure 4.1. The black lines visible within the seasonal ice pack are open leads or leads which have recently been covered with a thin layer of frazil or grease ice. The large black area just

Table 4.1: Ice Type and Temperature. Ice type-temperature relationships drawn from prior observational studies of the SLIP region. Walter (1989) involved aircraft reconnaissance of the February 1983 SLIP. Massom and Comiso (1994) is a satellite-based study of thin ice types.

REFERENCE	ICE TYPE	ICE TEMPERATURE (°C)	SLIP EVENT
Walter (1989)	a) white young ice b) frazil to grey young ice w/ open holes c) grey/white young ice w/ frozen holes	a) -7 to -11 b) -6 to -7; holes: near -2 c) -12 C; holes: near -8	February 1983
Massom and Comiso (1994)	a) newly-created open water b) shorefast ice c) open water-new ice d) ice-open water mix e) pack ice f) new ice g) light nilas, young ice h) first year ice	a) -2 b) -10 to -11 c) -2 to -3 d) -3 to -6 e) -9 to -13 f) -2 g) -4 to -7 h) colder than -7	March-April 1988

Figure 4.1: SAR/AVHRR (HLS to RGB) Image-February 21, 1992. Shown here (facing page) is the SAR/AVHRR image of the SLIP for February 21, 1992 (ERS-1 SAR date and AVHRR date). St. Lawrence Island has been masked out so that the temperature field emphasis is on the ice. The black outlines drawn on the image denote boundaries of backscatter differences or ice features reflecting SLIP development visible in the SAR imagery. The red areas along the southwestern coast of the island are the warmest areas of the polynya region shown here, and are most likely to contain a significant amount of open water. The black areas along the southern coast are either registration errors or, the shorefast ice was too cold to be distinguished properly using this temperature scale. The red/yellow stripes in the seasonal ice cover (green region) are the result of cloud contamination as the AVHRR image used here was not completely cloud-free to the north of the island or to the south of the polynya region. The black cracks in the seasonal pack are leads and cracks that developed as the ice moved and are visible here as a result of the high spatial resolution of the SAR imagery (here and Figure 4.3).

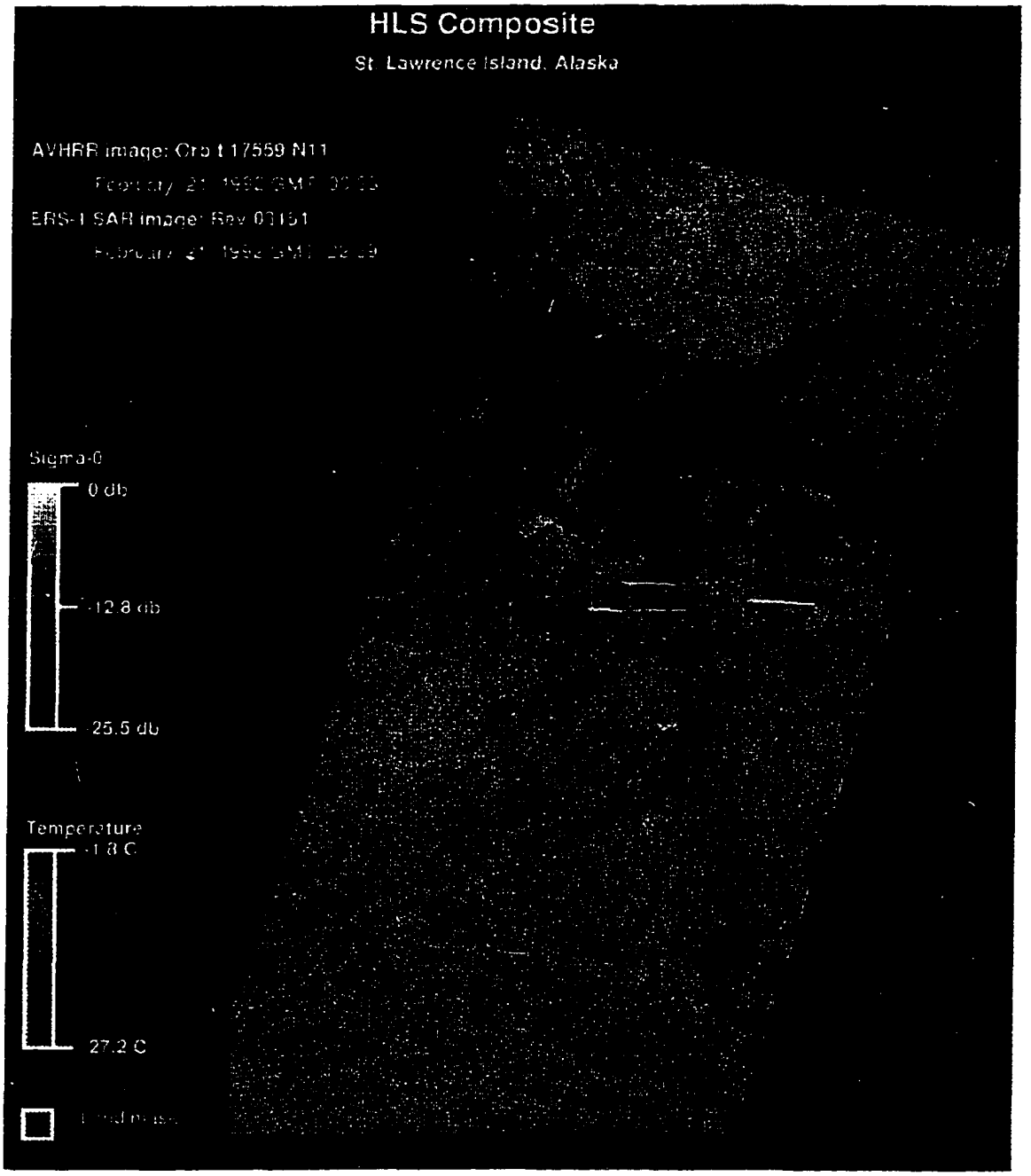

south of the eastern end of the island is an area of frazil or grease ice. The areas of green may not be truly representative of the ice surface temperatures as the corresponding AVHRR image (Figure 4.2) did have a thin cloud cover in it. This cloud cover would tend to result in a lower surface temperature being recorded by the mapping.

By noting latitude-longitude coordinates of ice and water features in the corresponding SAR mosaic of Figure 4.3, I determined that the most active areas of new ice formation on February 21 were along the southwest coast of St. Lawrence Island as denoted by the warm AVHRR temperatures. The white section in that location on the AVHRR image (Figure 4.2) is probably open water as it is near -3°C. Interestingly, Walter (1989) also noted that this southwestern coast area in the lee of the mountains tended to be the warmest location in the 1983 and 1985 SLIP events. The other large areas of warm temperature along the lower left border of the figure are leads that have recently attained a partial covering of frazil or grease ice. The areas of warm temperatures north of the island are left over from the northern polynya earlier in the month. From the imagery of Figures 4.1-4.3, I determined that there were two and possibly three bands of water-ice mix that could be considered as part of the polynya sector area[1] in the SLIP on February 21, 1992. The first extends approximately 3.4km offshore and 24.4km along shore. It is considered to be open water or low frazil concentration for flux calculation purposes. The second is 5.8km-11.8km wide and 38km along shore, and appears to be a mix of open water, frazil ice, and grease ice mat. The third, although considerably less distinct in the AVHRR temperature field, is 7.4 to 10.4km wide and 21.6km along shore, and it is all ice except for cracks and leads. This third band is also just barely suggested by the variation in backscatter across the SAR image (Figure 4.3).

SAR/AVHRR coverage of the SLIP indicates that only the western ~2/3 of the polynya is visible due to the SAR's limited swath width. To account for the "missing" coverage of the polynya in polynya size calculations, I applied the same temperature-ice associations used for the western 2/3 of the SLIP to the eastern 1/3. I obtained an eastern sector area of 283.1km^2 as distinguished by the white-yellow areas of the AVHRR (Figure 4.2) along the island coast. Thus, the total sector area (west and east combined) for February 21 to be used for heat budget analyses purposes is 809km^2 (i.e., total sector area

---

[1] Note that area of the polynya region defined as "polynya sector area" in my energy balance calculations (Chapter 5) is the area of newest ice or water/ice mix within the polynya, rather than the entire area of the polynya region. For example, only the first two divisions (band 1 area =171.5km^2 and band 2 area=354.3km^2) shown in the schematic of the February 21 SLIP (Figure 4.4) region are used to define the western sector area of the polynya for energy balance purposes in Chapter 5.

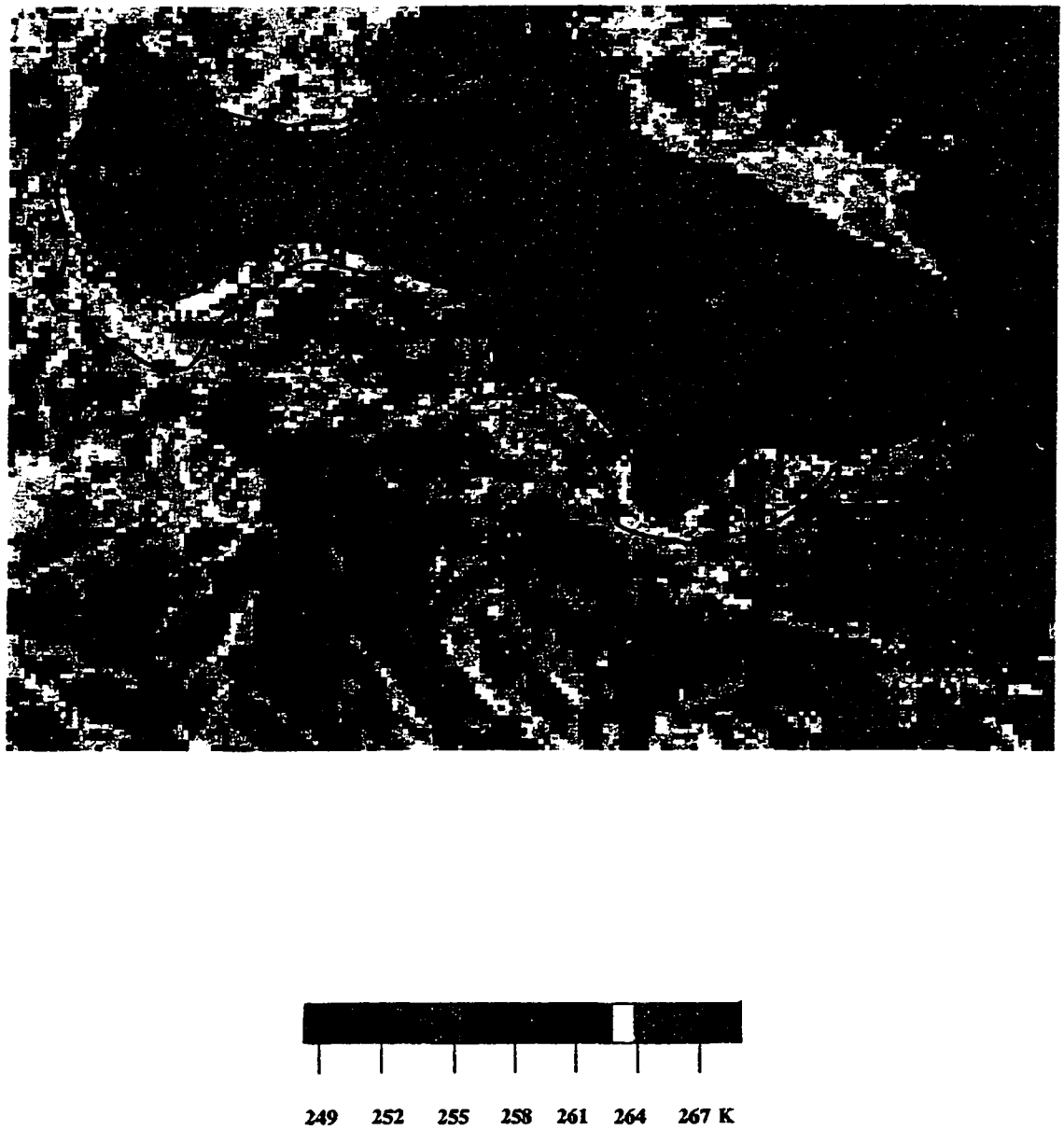

Figure 4.2: AVHRR Image-February 21, 1992. Here the AVHRR Thermal IR band (Band 4) has been color-mapped using the temperature scale shown. The divisions drawn on the graphic were defined based on ice/water temperature values and features visible in the SAR imagery for this date (Figure 4.3).

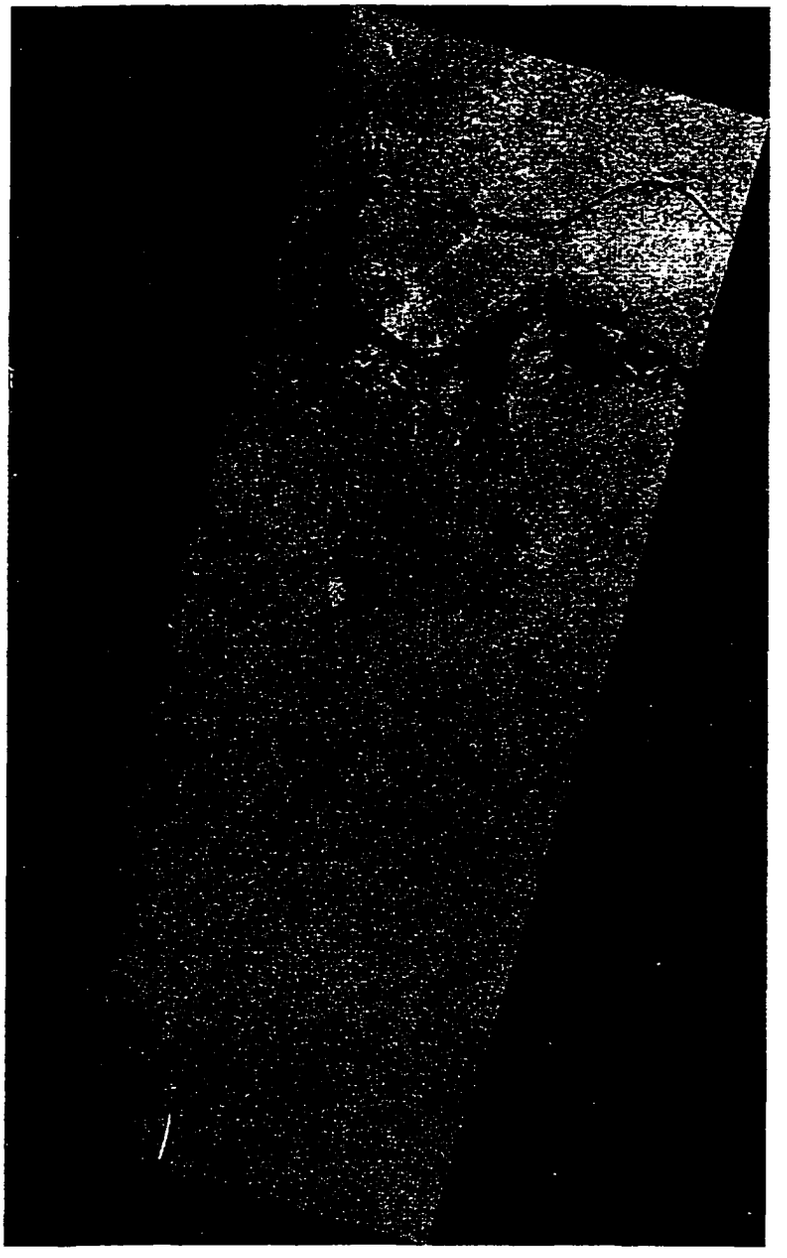

Figure 4.3: LoRes ERS-1 SAR Mosaic-February 21, 1992. This is the ERS-1 SAR image mosaic that was used to delineate the polynya region and associated sectors (see 4.4) indicating ice and open water on February 21, 1992. The sectors or divisions drawn on the imagery were defined by differences visible in the SAR backscatter (grey-scale) field, and by the temperature distributions shown in the corresponding AVHRR imagery (Figure 4.2).

= west sector area + east sector area). Figure 4.4 shows a schematic of the polynya sectors as visible in the SAR imagery. This figure also includes a table of sector measurements.

February 24 was determined to have three polygonal areas of ice-water mix as shown in Figures 4.5-8. These areas are denoted by the red and red-yellow coloring on the SAR/AVHRR graphic of Figure 4.5. They appear as areas of maroon to yellow in the AVHRR image (Figure 4.6) and as a portion of the light streaked "bowl" south of St. Lawrence Island in the SAR imagery (Figure 4.7). The region of the polynya visible in the SAR imagery had an area of 3,116.6km^2; however, the AVHRR imagery indicated that much of this area was colder than the -9°C (i.e., Sector 3, especially the yellow-green areas) cutoff specified for my "energy budget" sector area determinations. As a result, for energy budget purposes, the western sector area was measured to be 745km^2 (Figure 4.8). Using the same technique as for February 21, the eastern sector area was measured to be 448.8 km^2. The total sector area used for heat budget analysis was 1194km^2.

The SAR imagery for February 27 (Figure 4.9) showed the polynya region as a series of east-west oriented bands extending south from St. Lawrence Island. These bands range from 2 to 40km in north-south (offshore) extent and have well-defined boundaries. The five southernmost and oldest bands average about 30km in north-south extent. As mentioned in Chapter 3, this seems to indicate an episodic development that corresponds well to the observed ice velocities, whether wind-driven, tide-influenced, or a combination of both. However, here and in the next chapter, only measurements of the newest three bands will be used as these were the only areas to meet the temperature-ice feature criteria. These three bands make up the red to yellow area visible in the SAR/AVHRR graphic of Figure 4.10 and the maroon to yellow area visible off the island's southern coast as depicted in the AVHRR image (Figure 4.11). These three areas also have the lightest coloring in the SAR imagery shown in Figure 4.9, indicating the presence of open water and newer ice. The western sector was measured to be 940.5km^2 and the eastern sector was 774.4km^2. The total sector area to be used in my energy budget calculation was, then, 1,715km^2. A schematic of the sectors and a table of measurements is shown in Figure 4.12.

Although the polynya's outer defining boundary is still evident in the SAR/AVHRR graphic for March 1 (Figure 4.13), SAR imagery shown in Figure 4.14 indicates that the ice-water field within the boundaries is generally a continuous ice cover with scattered leads and cracks in it. As shown in Figure 4.15, AVHRR imagery concurs with this interpretation as surface temperatures are cooler throughout the polynya region than on

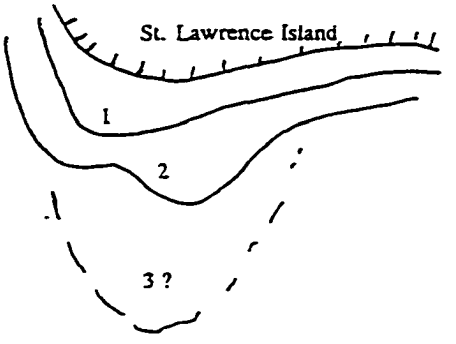

POLYNYA SECTOR	ALONG SHORE LENGTH OF POLYNYA SECTOR (km)	OFFSHORE WIDTH OF POLYNYA SECTOR (km)	SURFACE AREA OF POLYNYA SECTOR (km^2)
WEST SECTORS			
1 *	24.40	3.40	171.50
2 *	38.00	5.8 to 11.8	354.30
3 ?	21.6	7.4 to 10.4	~192
TOTAL SAR POLYNYA REGION (Sector 1+2)	38.0 (max) 31.2 (avg)	~3.40 to 11.80	~525.80
TOTAL WEST POLYNYA SECTOR *	38.00	~3.4 to 11.8	~525.80
TOTAL EAST POLYNYA SECTOR *	———	———	283.14
TOTAL E+W POLYNYA SECTOR *	———	———	808.94

Figure 4.4: Polynya Sector Schematic-February 21, 1992. This is a schematic of the sectors within the polynya region as visible in the SAR imagery swath (west sectors). The eastern sector is given as a surface area, only, due to the lack of SAR coverage (see text for further explanation: see also corresponding AVHRR and SAR/AVHRR images in this chapter). Sectors denoted by a "*" are those chosen for further use in the heat budget analyses presented here in Tables 4.5-4.10. All "*" regions are characterized by surface temperatures warmer than -9°C (white to yellow AVHRR categories). These areas include open water, frazil/water mix, and potentially grease ice mats with recently frozen holes. Note: Schematic not drawn to precise scale.

Figure 4.5: SAR/AVHRR (HLS to RGB) image-February 24, 1992. As in Figure 4.1, but for February 24, 1992. The large polynya region south of the island is denoted by the red and yellow areas which also comprise the "bowl-shaped" polynya region so evident in the SAR imagery (here and Figure 4.7). This "bowl" and later, "windsock" shape is due to the island's topography and the direction of the prevailing wind. The red areas of frazil ice and open water range from ~-6°C to ~-1.8°C with the warmest sector being off the island's southwestern coast. The yellow areas (warmer than -9°C) are most likely composed of grease ice mats and holes of open water. The green areas within the "yellow" indicate polynya ice whose temperature is probably being masked by steam fog that developed due to intense heat/moisture exchange between the open water and the cold atmosphere above the polynya. Streaks in the warmer areas are frazil rows or frazil streaks. The green band along the southern shore of the island is shorefast ice, while the green surrounding the polynya region is the seasonal pack ice. Future expansion of the polynya is hinted at by the thinning of ice south of the current polynya region.

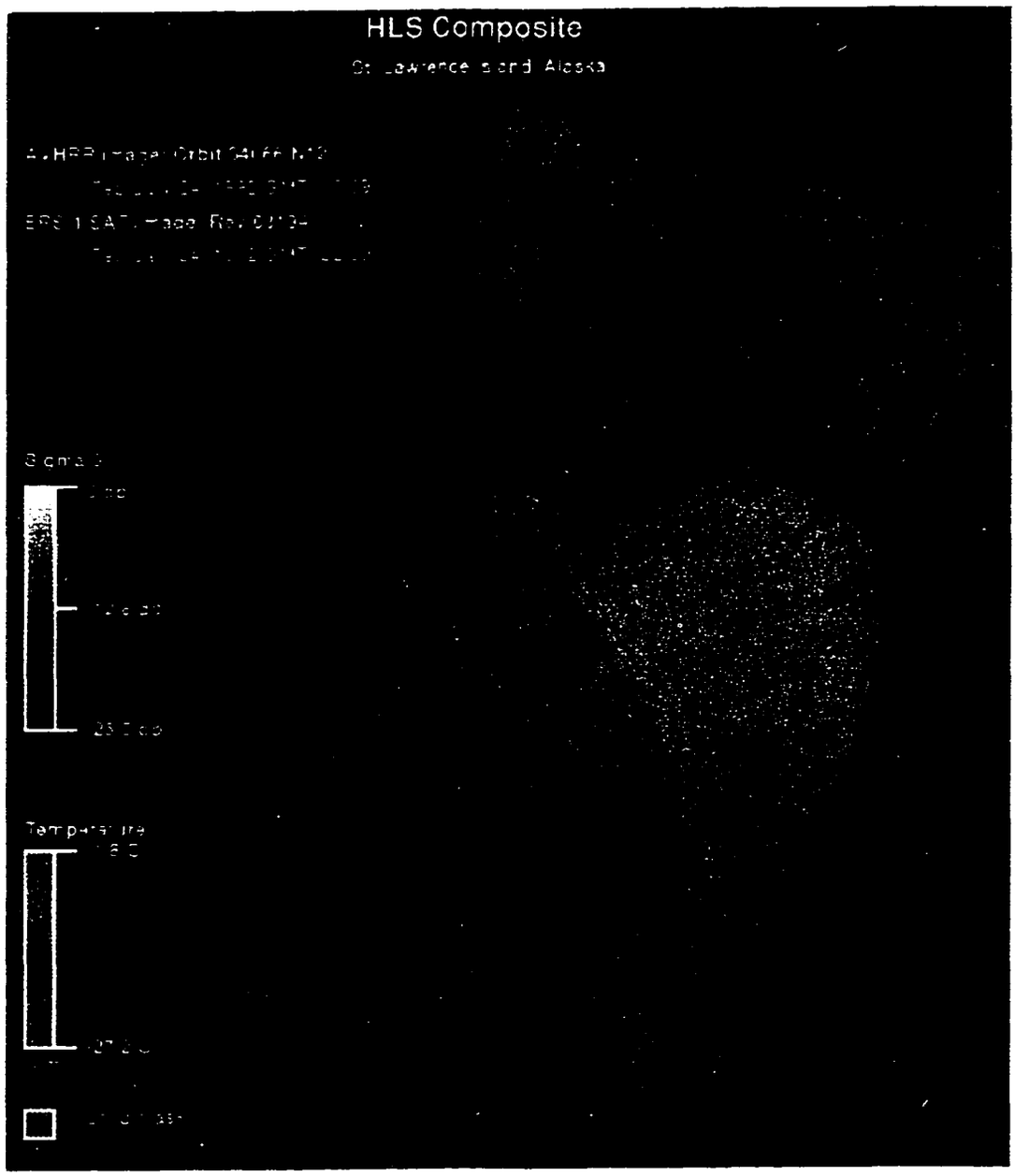

Figure 4.6: AVHRR Image-February 24, 1992. As in Figure 4.2, but for February 24, 1992.

Figure 4.7: LoRes ERS-1 SAR Mosaic -February 24, 1992. As in Figure 4.3, but for February 24, 1992

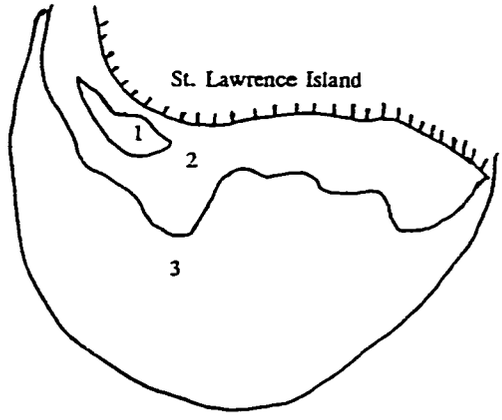

POLYNYA SECTOR	ALONG SHORE LENGTH OF POLYNYA SECTOR (km)	OFFSHORE WIDTH OF POLYNYA SECTOR (km)	SURFACE AREA OF POLYNYA SECTOR (km^2)
WEST SECTORS			
1 *	13.21	3.42	24.93
2 *	74.46	12.15	720.23
3 *	53.89	56.99	2,370.42
TOTAL SAR POLYNYA REGION (Sector 1+2+3)	74.46 (max) 53.89 (avg)	~69.14	~3,115.58
TOTAL WEST POLYNYA SECTOR *	74.46	~69.14	~3,115.58
TOTAL EAST POLYNYA SECTOR *	———	———	448.81
TOTAL E+W POLYNYA SECTOR *	———	———	1,193.97

Figure 4.8: Polynya Sector Schematic-February 24, 1992. As in Figure 4.4, but for February 24, 1992. Note: Schematic is not drawn to precise scale.

Figure 4.9: LoRes ERS-1 SAR Mosaic-February 27, 1992. As in Figure 4.3, but for February 27, 1992.

Figure 4.10: SAR/AVHRR (HLS to RGB) Image-February 27, 1992. As in Figure 4.1, but for February 27, 1992 (AVHRR date: February 26, 1992 due to cloud cover and poor image quality on February 27, 1992). The much expanded polynya has also developed a highly noticeable series of horizontal bands extending southward offshore. These bands are thought to be the result of pulses in the wind (see text) and/or diurnal tidal influences. The area of red is shown to be much narrower than in earlier images, indicating that the intense ice formation within the open water sector of the polynya is less extensive. The yellow plume-like feature at the center-right of the image is indicative of steam fog being blown down wind over the ice. The ice in the southern part of the polynya region is nearly as cold as the seasonal ice pack; however, it is still within the well-defined polynya region boundary visible in the SAR imagery (Figure 4.10). Corresponding AVHRR imagery is shown in Figure 4.11.

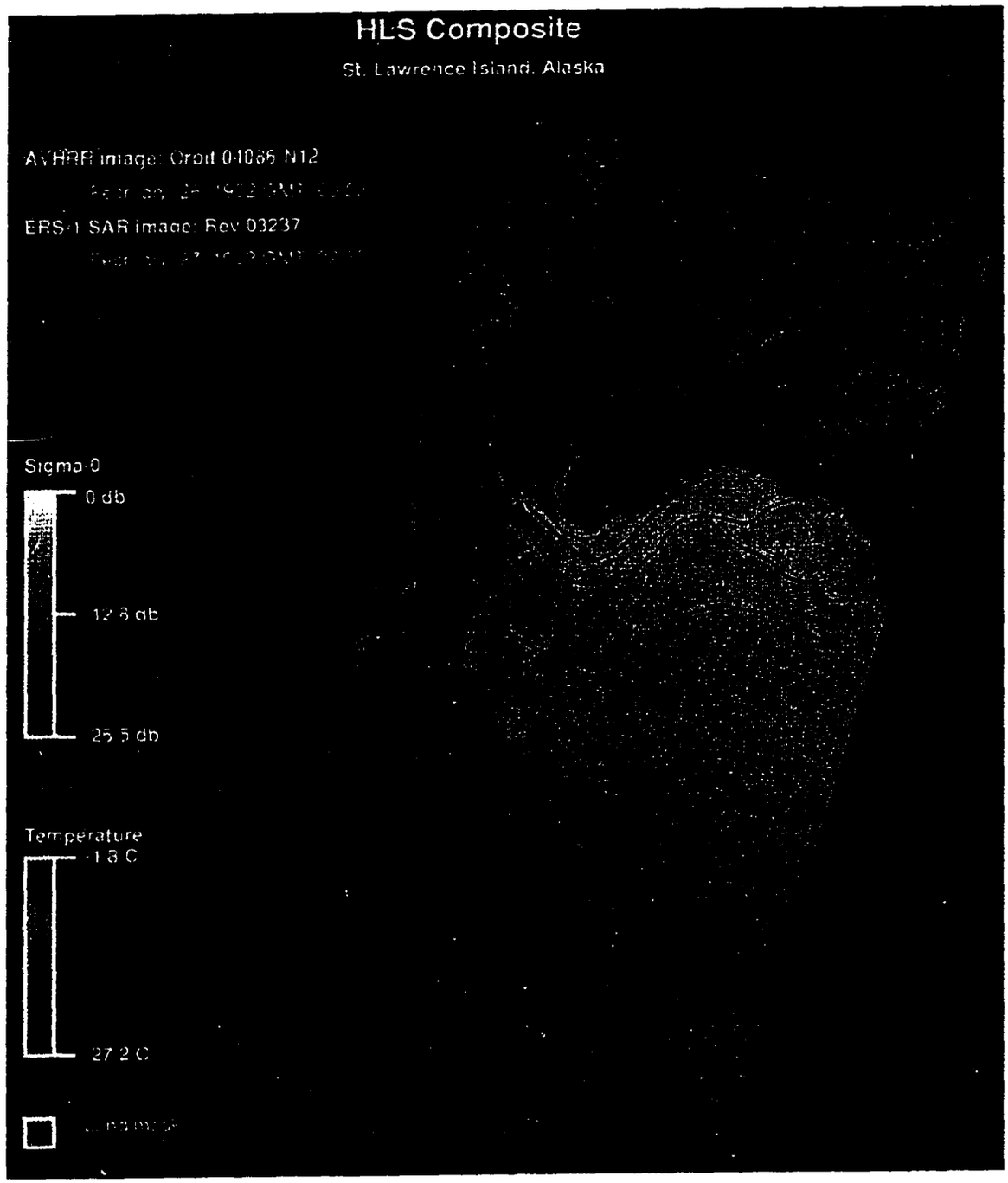

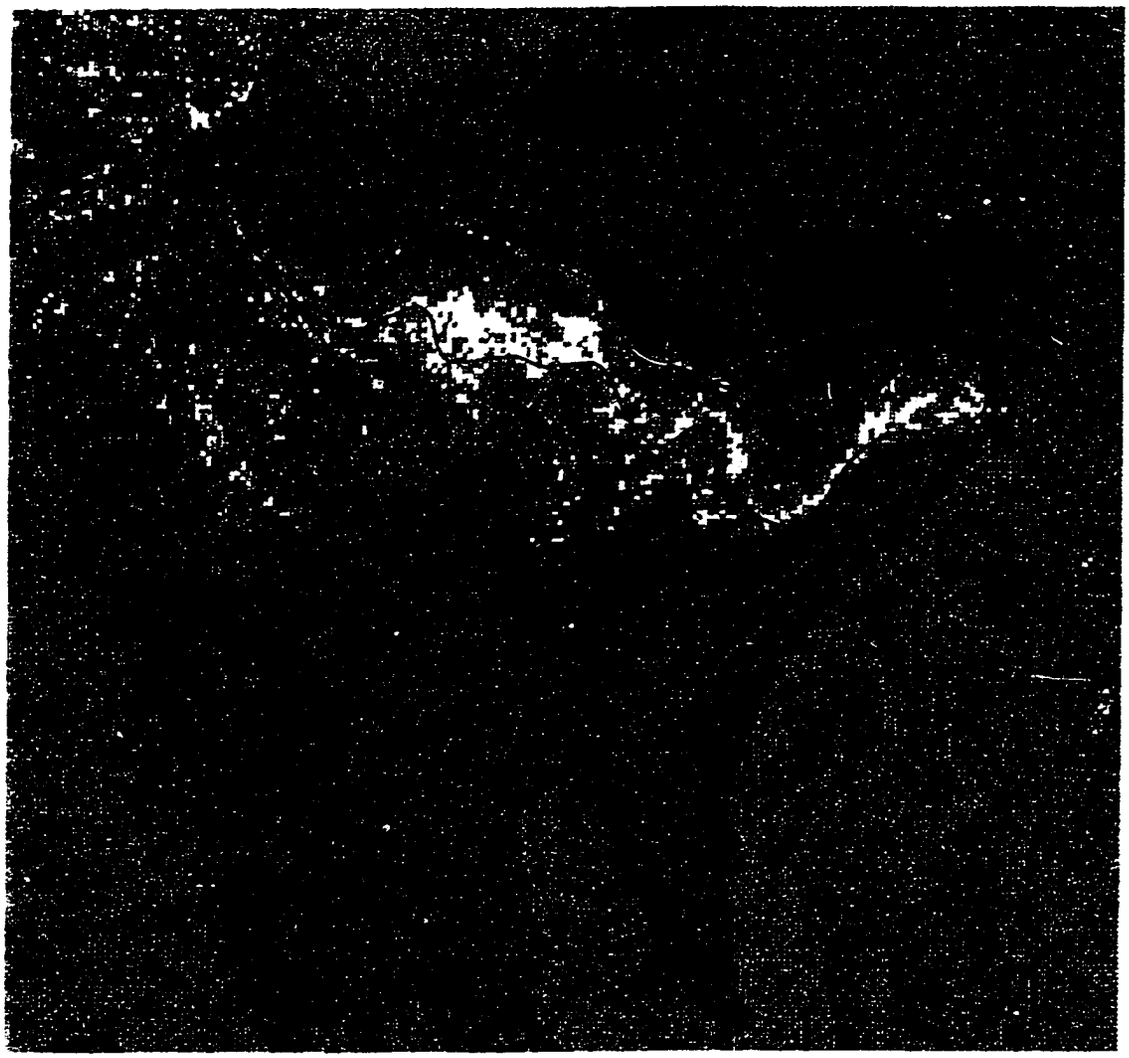

Figure 4.11: AVHRR Image-February 26, 1992. As in Figure 4.2, but for February 26, 1992. Cloud cover and image quality considerations did not allow me to use a February 27, 1992 image.

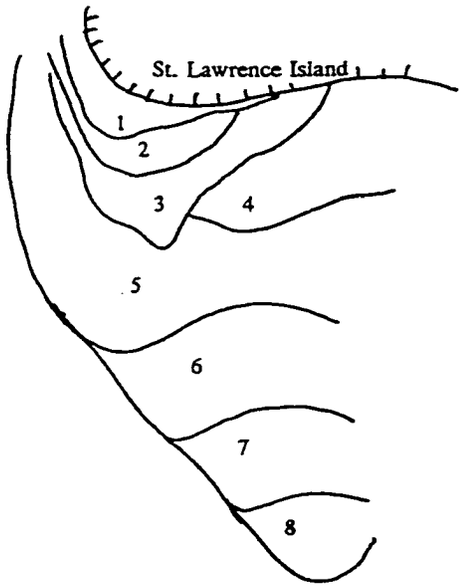

POLYNYA SECTOR	ALONG SHORE LENGTH OF POLYNYA SECTOR (km)	OFFSHORE WIDTH OF POLYNYA SECTOR (km)	SURFACE AREA OF POLYNYA SECTOR (km^2)
WEST SECTORS			
1 *	16.67	2.90	38.67
2 *	4.47	6.40	125.20
3 *	13.20 to 20.80	2.98 to 28.80	815.28
4	34.86	19.20	827.44
5	68.50	27.20	2,569.44
6	44.14	40.41	1,548.24
7	28.80	27.89	779.44
8	27.70	38.80	1,021.20
TOTAL SAR POLYNYA REGION (Sectors 1+2+ 3+4+5+6+7+8)	68.50 (max) 44.96 (avg)	~169	7,686.28
TOTAL WEST POLYNYA SECTOR * (Sectors 1+2+3)	**~20.80**	**~38.10**	**940.52**
TOTAL EAST POLYNYA SECTOR *	———	———	**774.20**
TOTAL E+W POLYNYA SECTOR *	———	———	**1,714.20**

Figure 4.12: Polynya Sector Schematic-February 27, 1992. As in Figure 4.34, but for February 27. 1992. Note: Schematic is not drawn to precise scale.

Figure 4.13: SAR/AVHRR (HLS to RGB) Image-March 1, 1992. As in Figure 4.1, but for March 1, 1992. The ice field has become much colder as is evidenced by the blue seasonal pack ice and the green polynya region. The only possible open water on this date would be found in leads and holes (see yellow south of island) that exist within the relatively solid ice cover of the polynya region. The polynya region has decreased considerably in east-west extent. The polynya region is only still classified as such because its boundary remains distinct in the SAR image (Figure 4.14). Note: The yellow-green band visible slightly north of the island is a band of clouds.

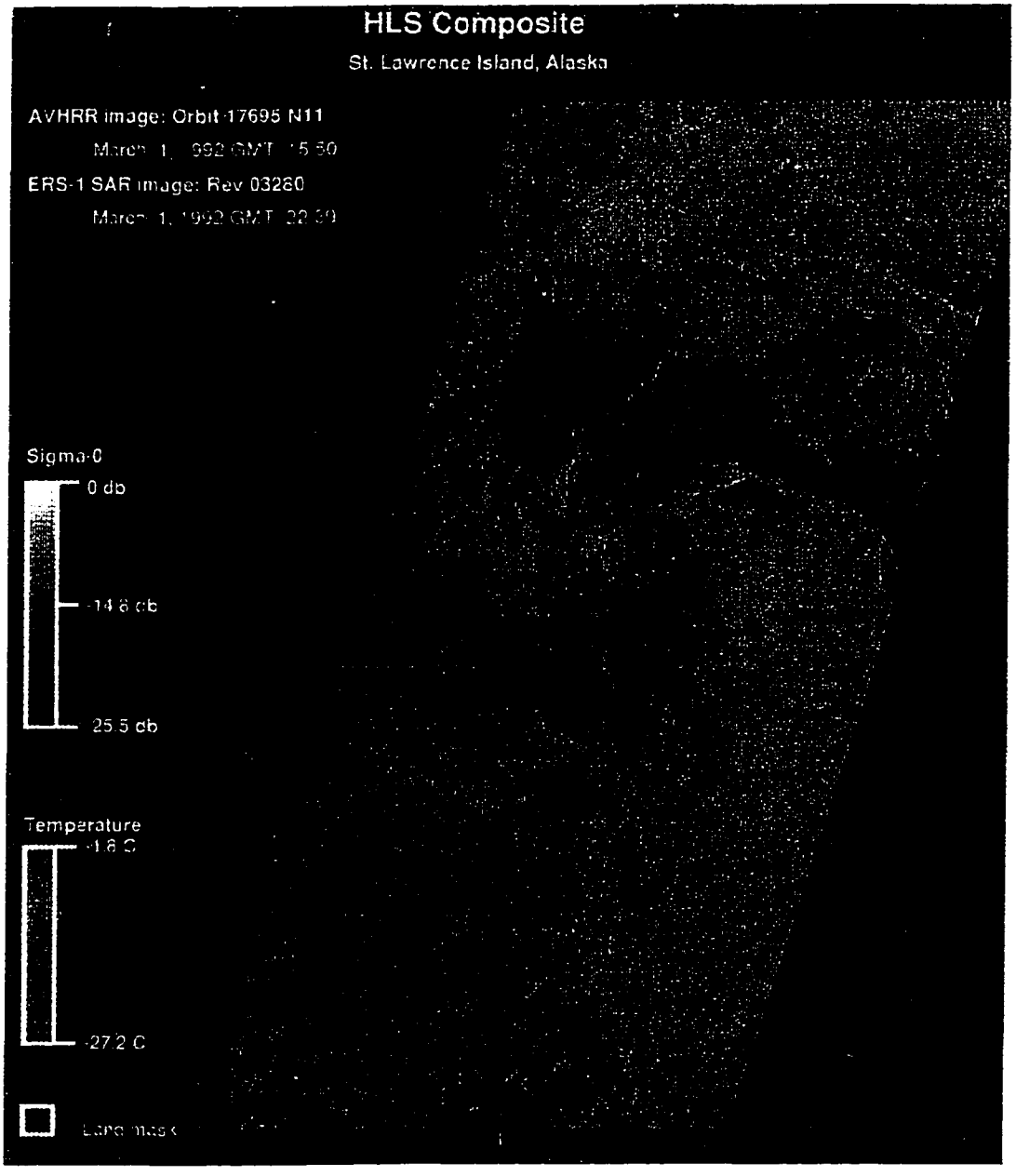

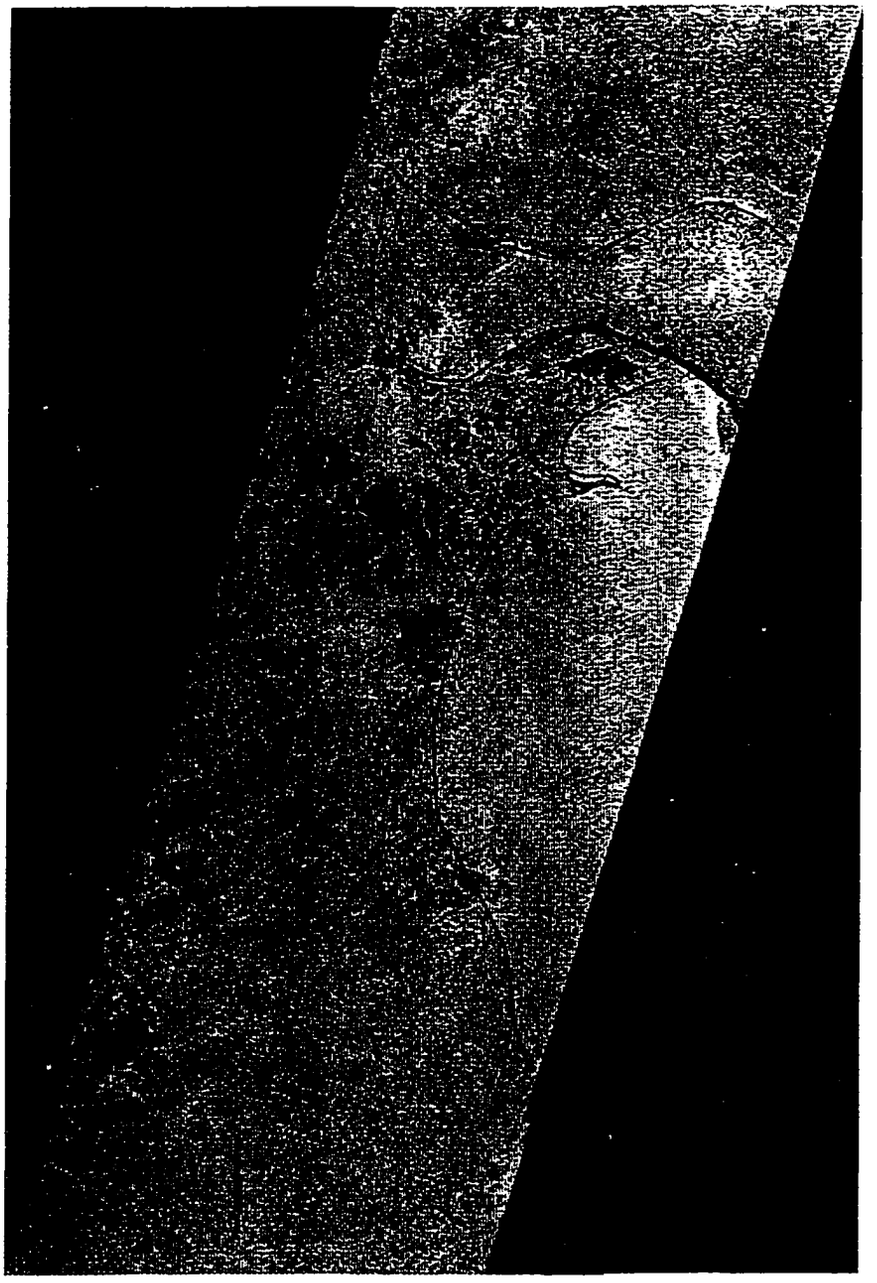

Figure 4.14: LoRes ERS-1 SAR Mosaic -March 1, 1992. As in Figure 4.3, but for March 1, 1992. Note: No sector schematic will be shown for this date as the entire polynya region was, with only a very few small sparsely distributed exceptions, colder than -9°C.

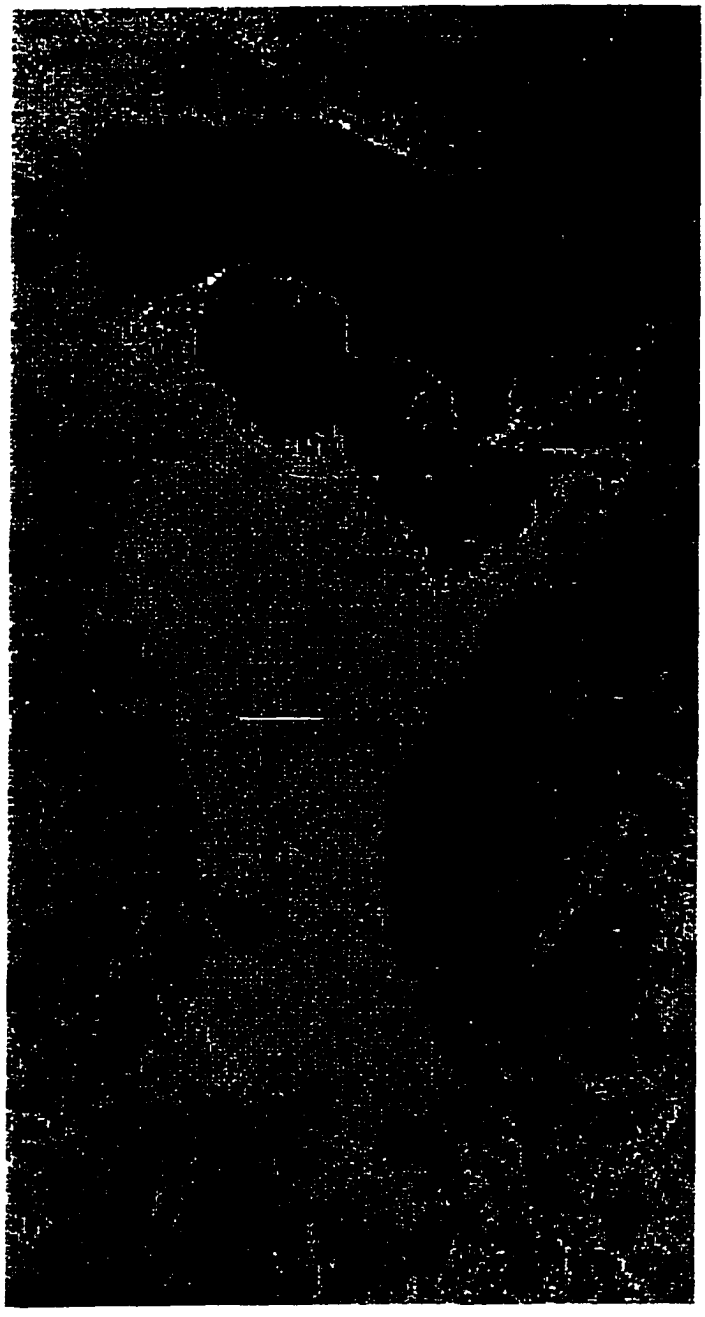

Figure 4.15: AVHRR Image-March 1, 1992. As in Figure 4.2, but for March 1, 1992.

February 24 and February 27. As a result of these observations, I assigned a value of 0 km^2 to the total sector area for March 1; therefore, no sector schematic is shown for this date.

As a means of comparison with the polynya sizes I measured, previously reported multi-year observations of the entire SLIP area (Stringer and Groves, 1991) suggested that the median size of the SLIP was in the range of 1,640km^2 to 2.480km^2. While my entire SLIP area measurements have a greater range than those of Stringer and Groves (1991). as the portion visible in the SAR imagery alone (2/3 of the polynya in February 1992) ranged from 526 to 7686km^2, my total sector area values (i.e., 809, 1194, and 1715km^2; average= ~1240km^2) were more similar to their entire SLIP measurements. My larger values of total polynya area are undoubtedly a result of different criteria for determining what constitutes a polynya, the higher resolution imagery that I have used, and their reporting an overall average size range rather than my single event sizes.

4.2.2 Model Estimate of Polynya Size

I used two different models to help determine the size of the SLIP, the PM model (Pease, 1987) and the ARCSyM (Lynch et al., 1995 and 1997).

4.2.2.1 Pease Model (PM model; Pease, 1987)- Polynya Extent: I used two different models to help determine the size of the SLIP, the PM model (Pease, 1987) and the ARCSyM (Lynch et al., 1995 and 1997). The first was an analytic model of polynya size developed by Pease (1987; PM model) which was used to determine how large a polynya might be predicted given certain weather conditions. I applied the model to the Gambell weather observations associated with the February 1992 southern SLIP event (see also Chapter 3). This model is only applicable to latent heat polynyas as it does not include a realistic oceanic heat source formulation, an important part of sensible heat polynya parameterization. PM develops polynyas based strictly on relationships between ice production rates. wind speed. and air temperatures. Temperature has been suggested to be the most size-limiting parameter of polynya development (Pease, 1987), but size is also a function of wind speed, especially for winds greater than 10m s^{-1}, since increasing the wind speed increases both the advection rate and the ice production rate. Further, Pease (1987) noted that increasing the wind speed above 5m s^{-1} does not increase the maximum size which the polynya can maintain, but does increase the speed at which the maximum size is attained. The actual time required for the polynya to reach near equilibrium size is

typically considered to be a half day to 4 days (Pease, 1987; McNutt, 1974; Smith et al., 1990).

The polynya size model formulation (Pease, 1987) consists of

$$\frac{dX_p}{dt} = V_i - X_p \frac{F_i}{H_i} \tag{4.1}$$

where dX_p/dt represents the change in polynya width over time; V_i=3% wind speed (the offshore ice velocity of the newly-formed ice being driven off the coast): F_i is the rate of ice production over the polynya width; and H_i is the collection depth of frazil ice. Collection depth is simply the thickness of ice that collects at the downwind boundary of the polynya. Polynya width, X_p, is then determined as

$$X_p = V_i \frac{H_i}{F_i} [\, 1 - \exp (- t \frac{F_i}{H_i}) \,] \tag{4.2}$$

with the boundary condition, X_p=0 at t=0. The depth of collection of frazil ice and grease or nilas ice (H_i) was chosen to be 0.1m as in Pease (1987).

I ran a number of cases of the model using daily average air temperatures and the northerly wind speeds observed over St. Lawrence Island for the period of February 18 to March 1, 1992. Averages of the columns in Table 4.2 indicate that, under conditions with winds of 9-10m s^{-1} and air temperatures of -17°C, the model polynya widths grow to 3.5km after 4 hours and 14km after 24 hours. These estimates are similar to my observed widths of the most active regions presented earlier in this chapter. i.e., the 2.9 to 3.4km (average width= 3.2km) regions of February 21-24 and February 24-27, as well as the frazil streak regions (average = 17km) of both three-day periods. The model average equilibrium width (T951 column in Table 4.2), defined by Pease (1987) to be 95% of the model's polynya width (MAXIMUM column in Table 4.2) at very long growth times, is 17.4km (MAXIMUM width average=20.8km). The time (t_{95}) required to come to this equilibrium width was 2.9 days,

Table 4.2: Polynya Size-PM model results. Model estimates of polynya size have been derived for the February 1992 southern SLIP event using the analytical Pease Model (Pease, 1987). Model results are compared to satellite observations of the SLIP's width for. February 21, 24, 27, and March 1, 1992. Model widths are shown for polynya growth 4 hours after the wind "starts', for 24 hour growth, for the polynya's T951 size, and for the polynya's maximum size. T951 is the time it takes the polynya to reach 95% of its maximum or "limiting size". Maximum or "limiting" size calculated as Xp=ViHi/Fi (e.g., Xp=polynya width, Vi=ice velocity, Hi=ice collection thickness, Fi=ice production rate) is the size attained after a long time period. The equation for Xp (see text) is bounded for a very large t (t=time). In all cases here, width refers to distance from shore to southernmost extent of the active polynya. Integrated ice speeds were calculated from my GPS ice motion products discussed in Chapter 3. Meteorological data are daily average values for Gambell. In Column 8: water%>ice% indicates more open water than ice in the sector.

DATE FEB/MAR 1992	AVERAGE DAILY WIND SPEED (cm s^{-1})	AVERAGE DAILY AIR TEMP (°C)	FOUR HOUR MODEL POLYNYA WIDTH (km)	24 HOUR MODEL POLYNYA WIDTH (km)	T951 MODEL POLYNYA WIDTH (km; # of days)	MAXIMUM MODEL POLYNYA WIDTH (km)	SAR AVHRR POLYNYA WIDTH (km) 1: water% > ice% 2+:ice% > water%	INTEGRATED ICE SPEED (km per 24hr)
18	15.9	-10.9	6.2	24.4	29.7; 2.6	35.7	0	0.2
19	12.8	-11.6	5.1	20.8	27; 2.9	32.4	-	-
20	5.2	-10.2	2.2	10.9	26; 7.0	31.4	-	-
21	8.0	-16.1	3.2	13.1	17.4; 3.0	20.9	1: 3.4 2: 5.8-11.8	-
22	8.9	-17.9	3.5	13.4	15.8; 2.5	18.9	-	0.2
23	8.8	-15.9	3.5	14.1	17.9; 2.8	21.5	-	0.2
24	10.1	-14.5	4.0	16.0	20.3; 2.8	24.3	1: 3.42 2: 12.15	0.2
25	8.5	-13.8	3.4	14.6	20.83; 3.4	25.0	-	28.3
26	11.2	-15.9	4.4	16.2	18.6; 2.3	22.3	-	28.3
27	13.7	-17.9	5.1	16.7	16.8; 1.7	20.1	1: 2.9 2: 6.4 3: 6.98	28.3
28	12.1	-21.1	4.5	14.1	13.8; 1.6	16.6	-	12.3
29	6.0	-22.8	2.4	9.3	11.4; 2.6	13.7	-	12.3
1	5.9	-21.2	2.3	9.5	12.2; 2.9	14.7	0	12.3
2	3.4	-22.8	1.4	6.2	9.8; 4.0	11.7	-	6.1
3	6.0	-21.2	2.4	9.6	12.3; 2.8	14.7	-	6.1
4	6.7	-20.8	2.6	10.4	12.8; 2.7	15.4	0	6.1
5	9.1	-21.9	3.5	12.1	12.8; 1.9	15.4	-	-

well within my total six day observed period of polynya growth (Table 4.2) from February 21-24 (3 days) and February 24-27 (3 days). These offshore extents, from the model and my observations (Table 4.2), are reasonably close to the range of offshore extent of 20-40km for such a polynya as suggested by Grebmeier and Cooper (1991).

4.2.2.2 ARCSyM Model (Lynch et al., 1997)-Simulated Polynya: Details of this model were presented in Chapter 2. To obtain an estimate of polynya size, I examined the ice concentration and temperature fields for 18Z February 24 and 18Z February 27 that resulted from my simulation run with a swamp ocean and from my run with an non-varying barotropic ocean circulation field. The dates of the simulated fields corresponded as closely as possible to the dates of the SAR/AVHRR and SSM/I data I had earlier acquired. SSM/I ice concentration fields and AVHRR temperature fields were used to further assess the model output, despite their low spatial resolution, because the model resolution was lower than that of the SAR imagery and the model domain was much greater than the SAR swath width.

Results from my "swamp" ocean model experiment indicate that a large polynya opening is evident by 1800Z February 24, with low concentration ice cover extending over 70km south of the island as shown (Figure 4.16a). SSM/I data, also shown in Figure 4.16, indicate a much smaller extension, ~25km, of ~80% ice concentration at 0000Z February 5. This is not overly surprising because much of the ice at the polynya is newly formed and thus is much thinner than the 30cm threshold defined in the model.

The simulated surface temperature corresponding to this date is shown in Figure 4.17. The distribution of the simulated surface temperatures agrees well with the AVHRR-based observations shown in Figure 4.6. However, the simulated surface temperatures are 3°K warmer than the AVHRR indicates within the polynya region, and the first-year ice is as much as 10°K colder than AVHRR indicates. This is shown in Figure 4.17 by the strong horizontal temperature gradient along the boundary of the simulated polynya region. The extensive maroon area (267°K; -5°C) depicted in the simulated temperature field for February 24 (Figure 4.17) is noticeably larger than that in the AVHRR mapping. As shown in Figure 4.17, the simulated ice surface temperatures undergo an abrupt decrease from polynya temperatures in excess of 267°K (-5°C) to first year pack ice temperatures colder than 249°K (-23°C). The "observed" ice temperature field associated with the polynya is predominantly in the -5 to -9°C range. As shown in Figure 4.6, AVHRR observations also suggest a more gradual decrease in ice surface temperatures, as indicated by the large

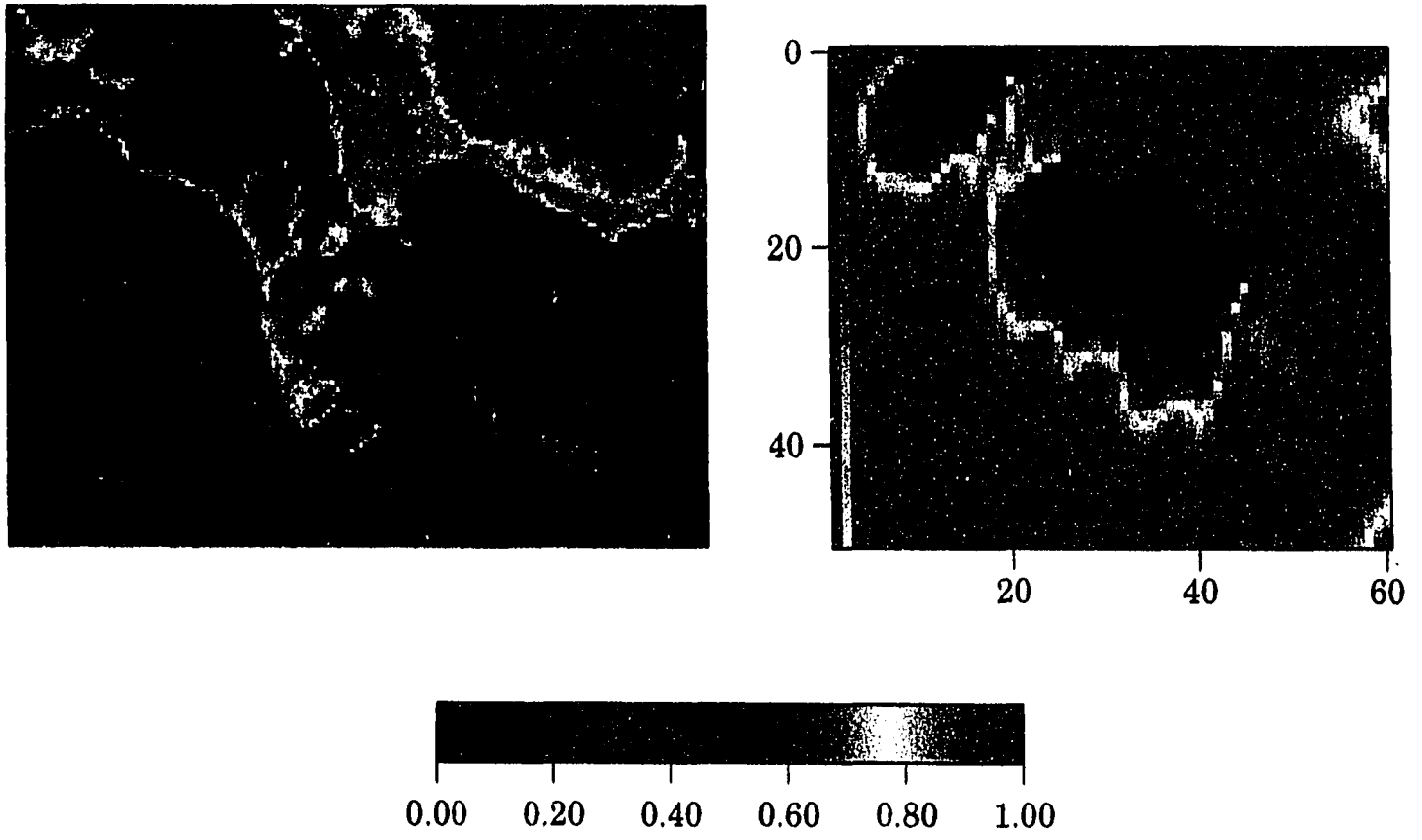

Figure 4.16(a): A Comparison of Observed and Simulated Ice Concentration -February 24/25, 1992. (left) Observed first-year ice concentration derived from SSM/I brightness temperatures for February 25, 1992; (right) "Swamp" ocean ARCSyM ice concentration for 00 Z February 24, 1992. ARCSyM pixel size is always 7 km x 7 km, unless specified otherwise. SSM/I pixel size is 25 km x 25 km. Concentration =1.0 indicates 100% ice cover. St. Lawrence Island is centered in each "image". The SLIP is indicated by the area of low ice concentration extending off the island's southern coast.

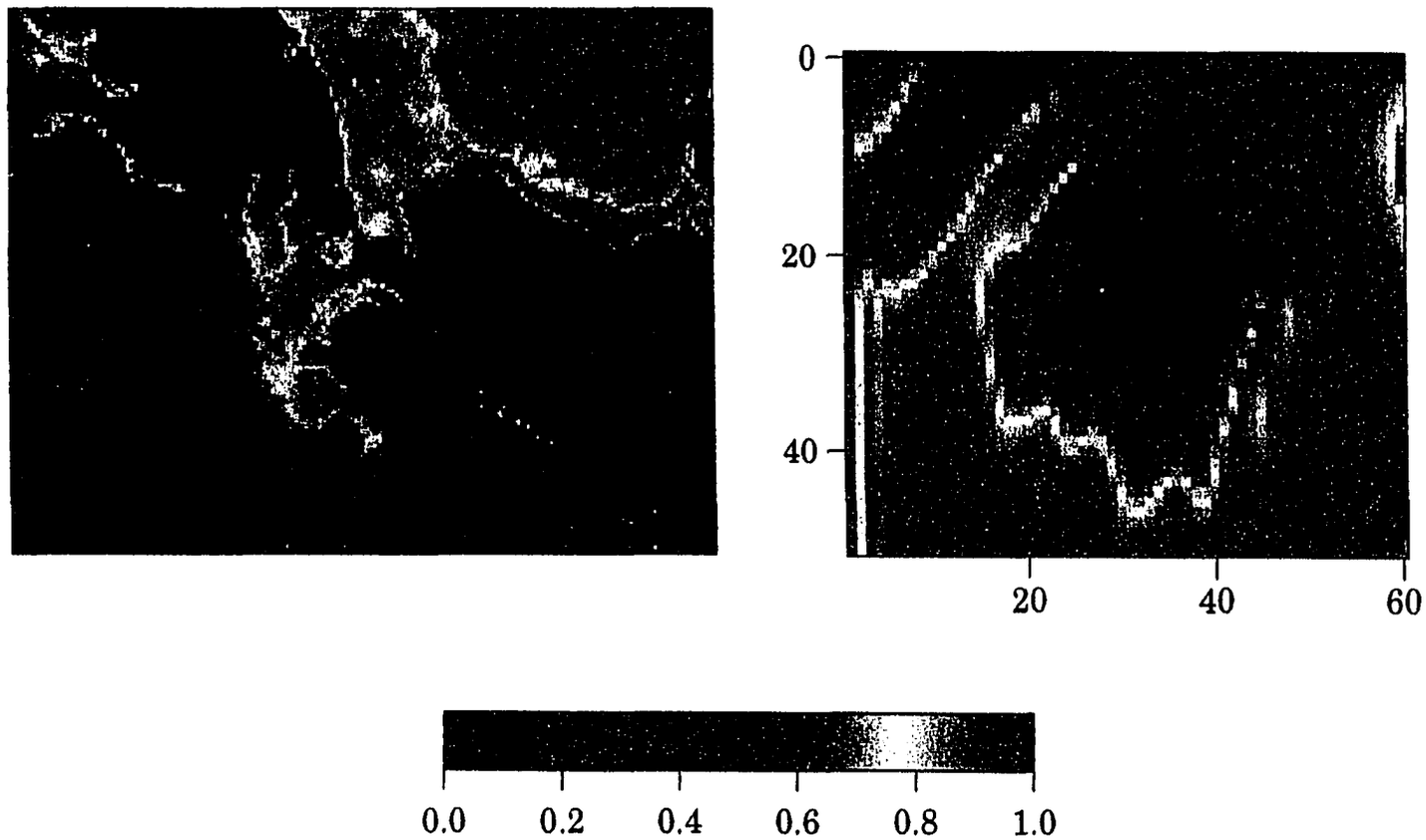

Figure 4.16(b): A Comparison of Observed and Simulated Ice Concentration -February 27/28, 1992. (left) Observed first-year ice concentration derived from SSM/I brightness temperatures for February 28, 1992; (right) "Swamp" ocean ARCSyM ice concentration for 00 Z February 27, 1992. ARCSyM pixel size is always 7 km x 7 km, unless specified otherwise. SSM/I pixel size is 25 km x 25 km. Concentration =1.0 indicates 100% ice cover. St. Lawrence Island is centered in each "image". The SLIP is indicated by the area of low ice concentration extending off the island's southern coast

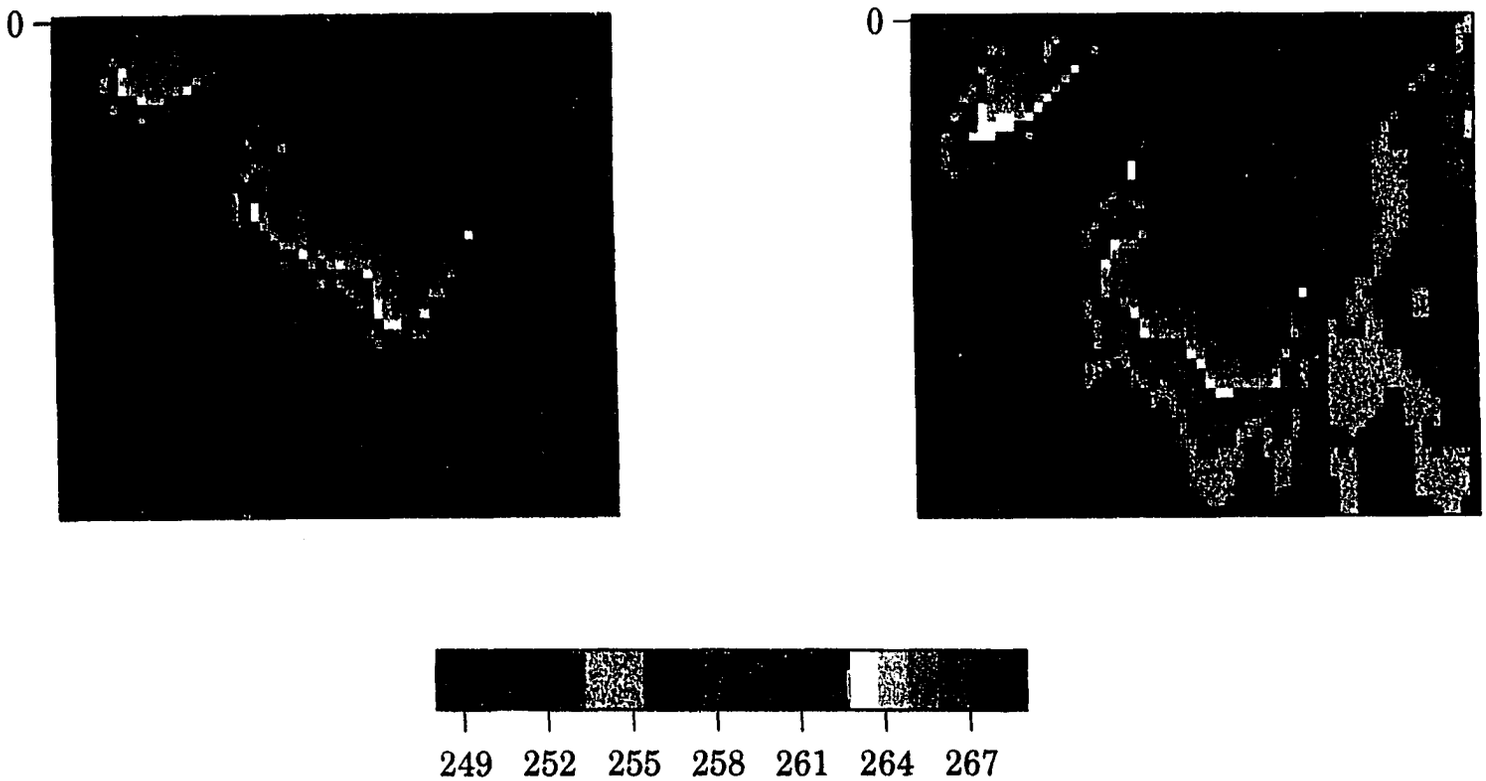

Figure 4.17: Simulated Surface Temperature-February 24 and February 27, 1992. "Swamp" ocean ARCSyM surface temperature (K) (weighted average of ice and ocean temperatures) for (left) February 24, 1992 and (right) February 27, 1992. ARCSyM pixel size is always 7 km x 7 km, unless specified otherwise. St. Lawrence Island is the black area just above the maroon to green banding of the polynya. Refer to Figures 4.6 and 4.11 for corresponding AVHRR imagery and Figures 4.5 and 4.9 for corresponding SAR/AVHRR imagery..

green (260-262°K; -12 to -10°C) and blue (256-259°K; -16 to -13°C) transitional ice zones. and a colder seasonal ice pack (<256°K; < -17°C).

By February 27, "swamp" ocean model simulated ice concentration (Figure 4.16) suggests a very large polynya region extending approximately 175km south of the island. 10km larger than that observed. The simulated polynya extends along the entire southern coast of the island similarly to the observed polynya. In addition, the simulated polynya also indicates ice "fingers" or "streamers" extending from the island southward, similar to groupings of frazil rows observed in the satellite imagery. Unlike the observed polynya, however, an extended lobe of low concentration ice is also present along the outer western coast of the island. A north-south gradient in simulated ice concentration is also evident. Ice concentration within the simulated SLIP region ranges from 0% to as much as 75% ice. with a large area of 0-20% ice extending 140km offshore. This offshore extent of simulated low ice concentration is up to five times as large as that observed in the SSM/I ice concentration field for 0000Z February 28 (Figure 4.16).

Unlike the polynya simulated in this "swamp" ocean-based experiment, the maximum observed polynya for February 27 (Figures 4.9-11) indicates a series of what seem to be older ice bands within the polynya region. The bands suggest a diurnal pulse-like expansion rather than a continuous southward expansion. There are approximately six of these bands, each having an average north-south extent of 30km, visible in the SAR imagery for this date. The band sizes, 19 to 40km, correspond somewhat closely to the observed ice displacements discussed earlier here and in Chapter 3. The banding does not imply 30km of open water every day, but rather serves as a measure or indicator of past net ice motion over a 24 hour period. Even so, there is no evidence of this banding in the simulated polynya region's ice concentration field.

The simulated surface temperature for February 27 indicates a large sector of warm temperatures extending from the southern island coast to 119 km offshore (Figure 4.17). The warmest observed area for the date is shown as the maroon (267°K; -5°C) section in the corresponding AVHRR image (Figure 4.11). A sharp horizontal gradient is evident in the simulated temperature field as indicated by the shift from red (266K; -6°C) to grey (<256°K; <-7°C). The AVHRR surface temperature field shown in Figure 4.11 indicates a more restricted area of warmest temperatures (267°K, -5°C) within the polynya region along the south-central coast, rather than along the southwestern coast as indicated in the simulation. The AVHRR field also shows somewhat broader horizontal bands of mid-range temperatures extending beyond the warmest areas of the polynya out

to the first-year ice pack (grey: <256°K; <-17°C). Overall the observed polynya is colder than on February 24 as is evidenced by the significant amount of green color-mapped ice (260-262°K; -10 to -12 °C). This is not surprising, though, as the grease ice within the actual polynya region becomes colder and more characteristic of the seasonal ice pack over time. It seems that the model severely overestimates the large area of warm surface temperatures associated with the polynya as defined by satellite imagery, but this can be readily traced to the ice thickness-open water threshold set (< 30cm ice = open water) in the model and, potentially, other thermodynamic-dynamic feedback issues beyond the scope of my research.

My "barotropic" simulation produced a polynya region with a much more detailed structure than that obtained in the "swamp" simulation. Smaller-scale characteristics such as narrow north-south "fingers" within the asymmetric lobes of low ice concentration were evident in the blue region of Figure 4.18a. As shown in Figure 4.18, simulation results from February 24 depict a large area of low ice concentration (blues: ~20% ice) and warm temperatures (red: 266°K; -6°C to yellow: 263°K; -9°C) extending westward from the western coast of St. Lawrence Island. The area is also evident in the simulated ice concentration field of February 27 shown in Figure 4.18a, although it is reduced in size from that of the "swamp" model and does not appear in this date's simulated surface temperature field. However, these areas of low ice concentration and warmer temperatures do not appear at all in the corresponding satellite data discussed earlier in this chapter.

Simulated ice surface temperatures within the polynya region are closer to observed temperatures than those obtained from the "swamp" ocean experiment, but they are still 2-3K warmer than those estimated from the AVHRR imagery (Figure 4.6 and 4.11). However, this difference is only noteworthy next to the island's southwestern coast (denoted by maroon (267°K; -5°C) and red (266°K; -6°C) in Figure 4.6) on February 24. The simulated temperature field for February 27 is quite similar to that observed in the corresponding AVHRR image in Figure 4.11, both in terms of distribution along the coast and southward extension from the coast. Simulated ice surface temperatures for February 24 and February 27 appear to decrease gradually from the active ice formation areas close to the island and then southward towards the southernmost boundary of the SLIP region,rather than abruptly as in the "swamp" ocean case.

The "barotropic" polynya region for February 27 extends 140km offshore (up to 75% ice concentration), with a sector of low concentration (0-20%) ice extending only 70km offshore. In general, the "barotropic" simulation produces a slightly less extensive area of

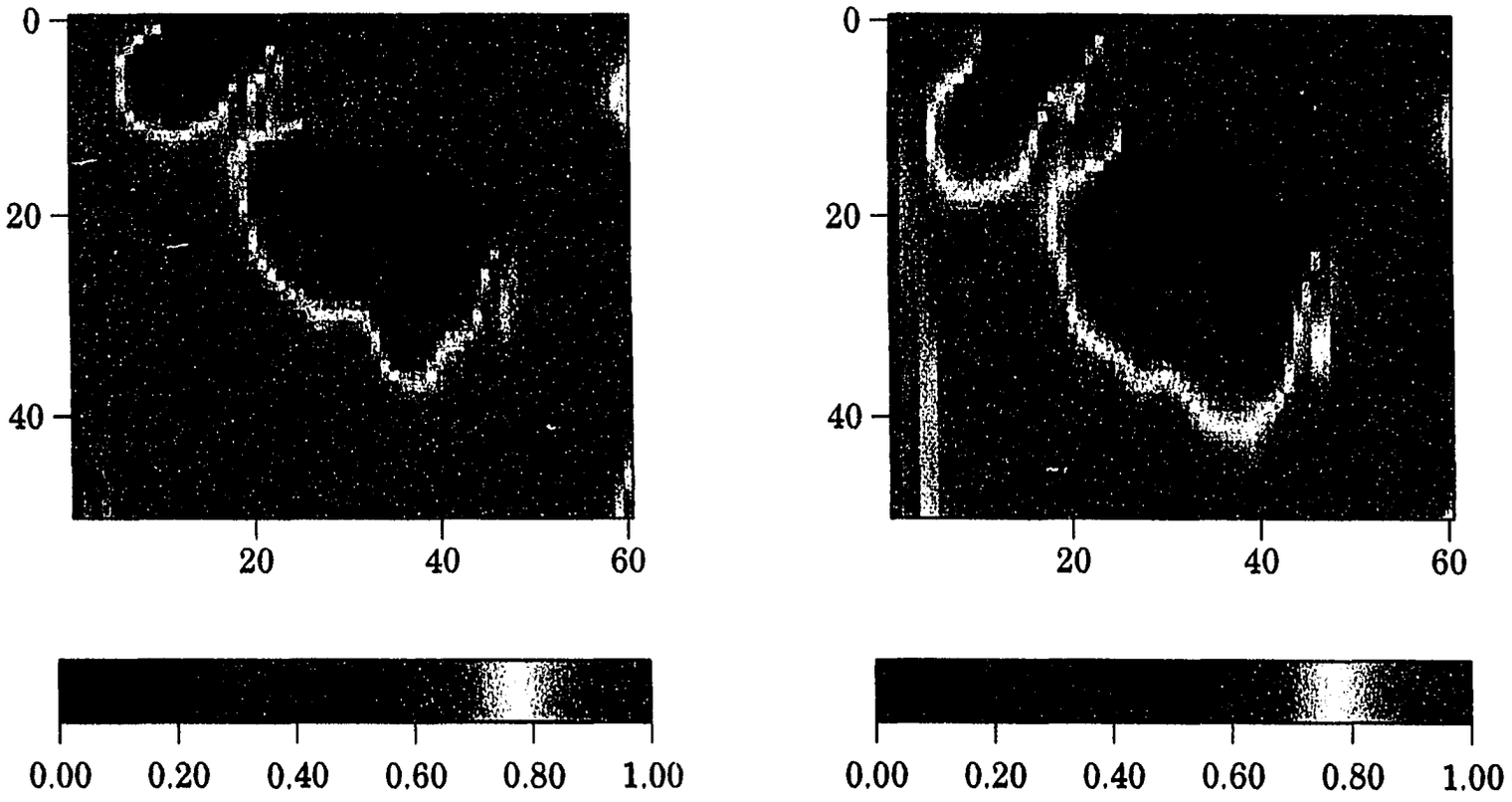

Figure 4.18(a): Simulated Ice Concentration-"Barotropic" Simulation. (left) ARCSyM (with ocean currents) ice concentration for 00 Z February 25, 1992. (right) ARCSyM (with ocean currents) ice concentration for 00 Z February 27, 1992. Note the differences in SLIP shape and the areal extent of the low ice concentration sectors here in comparison to the "swamp" ocean simulation results shown in Figure 4.16(a).

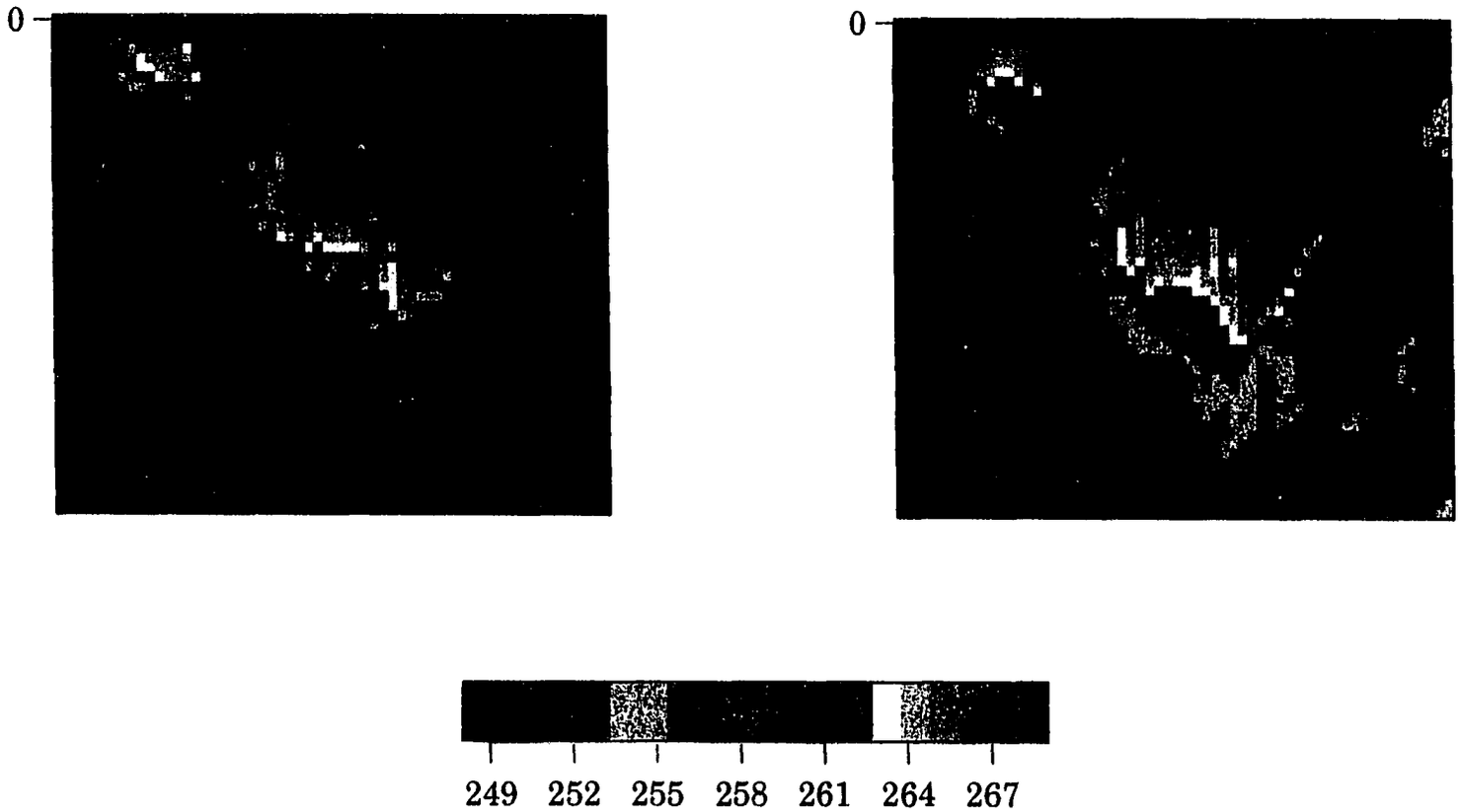

Figure 4.18(b): Simulated Surface Temperature-"Barotropic" Simulation. (left) ARCSyM surface temperature (K) (weighted average of ice and ocean temperatures) for 18 Z February 24, 1992; (right) ARCSyM surface temperature (K) (weighted average of ice and ocean temperatures) for 18 Z February 27, 1992. Note the differences in SLP shape and the areal extent of the warm low ice concentration sectors here in comparison to the "swamp" ocean simulation results shown in Figure 4.16(b). See Figures 4.5 and 4.9 for corresponding SAR/AVHRR imagery.

low ice concentration than does the "swamp" simulation for February 27 (Figure 4.17). The "barotropic" ocean reduces the size of the simulated polynya by 20% from that of the "swamp" case, making its lower ice concentration sector more similar to that observed in corresponding satellite imagery. However, the simulated areas of low concentration on February 24 and February 27 are still much larger than those observed in the corresponding SAR and SSM/I imagery (see Section 4.2.1; Figures 4.16 and 4.17). These erroneously large areas of low concentration in the simulated results can again be traced back to the model's open water-ice distinction parameterization.

The two-lobed shape of the simulated polynya (Figure 4.18) is similar to the shape of the polynya depicted in the corresponding AVHRR imagery (Figures 4.6 and 4.11). This shape reflects the island coastline geometry and has since been further described in an analytical study of coastline-polynya shape relationships by Darby et al. (1995). Overall, the actual shape of the barotropic ocean simulation SLIP region shown in Figure 4.18 corresponds better to the area visible in the SAR and AVHRR imagery (see Figures 4.5-4.11) than does that of the "swamp" ocean polynya.

4.3 Summary

Satellite observations and model simulation of the SLIP's development show that the February 1992 southern SLIP opened over a period of 2-3 days after the observed Gambell wind shifted to northerly. The most extensive period of polynya expansion or growth occurred from February 21-27, the period of most persistent northerly winds. At its largest extent in SAR imagery, this event's polynya region boundary was well-defined for over 165 km south of the island. Corresponding AVHRR imagery for March 1 indicates that the polynya boundary may, in fact, have extended nearly 235km south of the island, almost reaching St. Matthew Island.

A brief (24 hours) weakening of the wind between February 27 and March 1 dramatically slowed the polynya expansion and led to the narrowing of the existing plume. Weak winds and cold temperatures caused any existing open water within the plume to freeze, resulting in a negligible amount of open water in the polynya by March 1. From the ARCSyM simulations I was able to observe the potential influence of the ocean on the polynya's rate of expansion and its shape change under weak wind conditions. Although the oceans incorporated into the SLIP simulation were quite primitive in comparison with reality, they showed that the addition of even a constant barotropic ocean to the model created a more realistic polynya throughout the simulation period.

As shown in Tables 4.3 and 4.4, my measurements of polynya size from satellite imagery indicate that the Pease model and the ARCSyM were able to create a polynya within the observed time frame of development and that the offshore extents of the polynya region were fairly consistent between the model and observation. The Pease model numbers were somewhat similar to my sector "offshore extent" measurements although my "entire polynya" measurements were much larger. While the Pease model proved useful in that it allowed me to predict the offshore extent of the SLIP based simply on observed temperature and wind data, it fell short of my needs when used by itself. It could not give any indication of varying distributions of ice conditions (i.e., areas of open water or water-ice mix) within the developing polynya, nor could it be used to obtain a polynya area because the model is a 1-D model that treats a polynya as strictly open water. It also could not indicate the effects an ocean current might have on polynya development, as it does not include an ocean except as a constant heat source.

The ARCSyM's results proved more informative than those from the Pease model in terms of polynya area and ice concentration within the polynya, as well as atmosphere and ocean influences on polynya shape and rate of development. The "entire polynya region" N-S and E-W extent obtained from the "barotropic" model for February 24-27 was within a few km of my satellite-based measurements. Unfortunately, while the version of this climate system model (still under development) that I worked with was a dramatic improvement over earlier 1-D and 2-D models used for predicting the SLIP, the ARCSyM's ice concentration constraints led it to indicate a much larger area of low ice concentration or open water and thus a larger active polynya area than I observed in the imagery. Differences were also apparent between the observed and the ARCSyM "within polynya" ice-open water distribution gradients.

My results also point out the importance of: a) defining what a polynya is in a particular study; b) establishing a consistent cutoff point beyond which a polynya sector within the polynya region is no longer considered to contain open water; and c) being able to observe or parameterize that chosen definition of a polynya consistently. Improved classification algorithms and more lengthy time series of high resolution observational, remote or *in situ*, data will certainly help refine the determination of ice-water areas within the polynya region. In retrospect, my choice of an ice feature- temperature cutoff value of -9°C was probably too cold and so my "active area" measurements are probably slightly on the large side.

Table 4.3 February 1992 Southern SLIP Event-February 24-27. Summary of present study results and historical information for comparison with SLIP events in the past. References to historical and other data are given as the second line of information in the box. Reference Key: GC91-Grebmeier and Cooper (1991); CM94-Cavalieri and Martin (1994); CM95-Comiso and Massom (1995); W89-Walter (1989); S83-Schumacher et al. (1983).

	Ice Concentration (% ice)	Surface Temperature (°C)	Polynya Shape	Wind Speed ($m\ s^{-1}$)	Ice Motion ($m\ s^{-1}$)	SLIP Size (km offshore extent)
Historical	variable	-2 to -9 CM94; W89	bowl/plume	n/a	3% of wind	20 to 40 GC91
Present Study Observed	min. ~80% ice SSMI imagery	-5 to -9 SAR/AVHRR	bowl	~11	0.33 86 km/3 days	69
Analytical Model						
PM	n/a	n/a	n/a	n/a	n/a	16 to 21
Climate System Model						
ARCSyM "Swamp"	large area of low ice concentration	3 degrees > observed; sharp gradient	square	10.6	0.35 91 km/3 days	91
ARCSyM "Barotropic"	reduced area of low ice concentration	1-2 degrees> observed; "smoother" gradient	suggestion of two lobes at southern edge	10.6	0.29 75 km/3 days	70

Table 4.4 February 1992 Southern SLIP Event-February 27-March 1. As in Table 4.3, but for February 27-March 1, 1992.

	Ice Concentration (% ice)	Surface Temperature (°C)	Polynya Shape	Wind Speed ($m\ s^{-1}$)	Ice Motion ($m\ s^{-1}$)	SLIP Size (km offshore extent)
Historical	variable	-2 to –9 CM94; W89	bowl/plume 2 lobes	n/a	3% of wind	20 to 40 GC91
Present Study Observed	min. ~70-80% ice SSMI imagery	-5 to –12 SAR/AVHRR	bowl/plume 2 lobes	~6.8	0.22 56 km/3 days	165
Analytical Model						
PM	n/a	n/a	n/a	n/a	n/a	11 to 17
Climate System Model						
ARCSyM "Swamp"	0 to 75 % ice	distribution is 2-3 degrees too warm	bowl with 2 lobes at southern edge	weak	0.05 13 km/3 days	140 to 210
ARCSyM "Barotropic"	0 to 75 % ice	-5 to –12 improved distribution	elongated bowl/plume with 2 lobes	weak	0.27 70 km/3 days	70 to 140

Although all of my measurements and model simulations suffered to a certain extent from a lack of ground-truthing and lack of fine-tuned ice-water classification algorithms, the combination of AVHRR, SAR, SSM/I, and model data did allow me to obtain useful, meaningful measurements of polynya size. In the following chapter I will use my measurements of polynya size to explore heat fluxes, ice production, and dense water production associated with the February 1992 southern SLIP event.

CHAPTER 5: POLYNYA THERMODYNAMICS, ICE PRODUCTION, AND DENSE WATER PRODUCTION

Latent heat polynyas are notable for their large ocean to atmosphere energy fluxes, large ice production rates and correspondingly high dense water production rates due to the continual open water/ice formation cycle that takes place. If the water contains ice crystals, frazil ice formation will begin soon after the surface water reaches the freezing temperature. In this chapter, I have calculated energy fluxes, ice production and dense water production rates associated with the February 1992 SLIP. I chose to use four different vehicles for this: the PM model (Pease, 1987); the ice/dense water production model, the CMI/CMD model, formulated by Cavalieri and Martin (1994); the CW2 model (Wade, 1993); and the ARCSyM (Lynch et al., 1997). Daily meteorological data used as model input were those from Gambell on St. Lawrence Island.

5.1 Polynya Size Model (PM; Pease, 1987): Model Details and Ice Production

The analytical PM model uses a simplified Maykut thermodynamic energy balance (Maykut, 1978) to determine the freezing rate or ice growth rate over open water within a polynya. This model's freezing rate is formulated as:

$$(5.1) \qquad -\rho_i L \frac{dH}{dt} = (1-\alpha) Q_r + Q_{ld} - Q_{lu} + Q_s + Q_e$$

where L is latent heat of freezing for salt water; ρ_i is the ice density specified as 0.95×10^3 kg m^{-3}; and dH/dt is the local rate of change in ice thickness. $(1-\alpha)Q$ is the unreflected short-wave radiation and is neglected as its contribution to the freezing rate is considered to be small (Pease, 1987; Maykut, 1982) during winter months at high latitudes. Q_{lu} is the upward (outgoing) longwave radiation specified as 301W m^{-2} since T_w varies only slightly at a polynya. Q_{ld} is the downward (incoming) longwave radiation calculated from $Q_{ld} = \sigma \varepsilon_a T_a^4$ where T_a is the daily observed temperature at Gambell, σ is the Stefan-Boltzmann constant, and ε_a is the emissivity. Q_e and Q_s are combined based on Pease's (1987) assumption that cold air over the ice is moisture saturated with respect to ice before blowing over the polynya so that latent heat, Q_e, is much smaller than the sensible heat.

Q_s, and therefore can be accounted for by a slight adjustment in the sensible heat parameterization (i.e., creating a turbulent flux term, Q_s^*). Additional discussion of this assumption can be found in Pease (1987). The turbulent heat flux, Q_s^*, used in this model is then, $Q_s^* = \rho_a C_h C_p U_a (T_a - T_w)$ where U_a is the daily wind speed at Gambell. Outgoing longwave radiation was based on Gambell temperature data. Parameters such as air density, ice density, specific heat coefficient, and latent heat of freezing were taken from Pease (1987).

Model output consisted of daily net turbulent heat flux over open water, incoming longwave radiation, and daily ice freezing or production rate for the SLIP region. All flux calculations assume an open water initial state on each day of calculation. No attempt is made to allow fluxes to vary with increasing ice thickness. Each day's net energy flux is assumed to go directly into ice production and thus, determine the daily ice production rate. Unlike the polynya size part of the PM model discussed in Chapter 4, the energy balance part of the PM model does not include a term for ice motion. Instead, it assumes that each day's model run starts from a completely open water state. The ice that is produced on one day is assumed to be swept downwind completely by the start of the next day. Ice production rates were converted to ice volume using my SAR/AVHRR polynya area measurements for use in dense water production calculations discussed later.

I ran the PM model using a daily time step for the two week period of February 18 to March 2, 1992 to correspond to the southern SLIP event during that period. Results from this model experiment are shown in Table 5.1. Turbulent fluxes ranged from a high of -609.6W m^{-2} on February 28 to a low of -114W m^{-2} on February 20. The total net daily ocean to atmosphere heat flux, F_{net}, ranged from -153.0W m^{-2} on February 20 to -671.1 W m^{-2} on February 29. Although these numbers are lower than expected based on historical observations from the most active sites within the polynya, the more negative PM model heat fluxes were indeed obtained for the coldest and windiest periods, during the time of persistent northerly winds. The least negative heat fluxes occurred just prior to the observed development of the polynya, during the period of "transition" winds. Ice production rates reflect the differences in heat flux levels as the largest rates of ice production, 13.0-18.9m day^{-1}, occurred from February 26-28 and the lowest rates, 4.3-10.2 cm day^{-1}, occurred from February 19-21. To put these numbers in context with observations, the polynya was first observed to be open in the 2239Z February 21 SAR

Table 5.1: SLIP Ice Production-PM Model. Energy fluxes and ice production rates derived from the PM model are shown. F_{net} is the total net open water to atmospheric heat flux used to determine the ice production rates. Results are based on input daily average temperature and wind data at Gambell on St. Lawrence Island. Turbulent Flux is this model's representation of sensible and latent heat flux, combined into one term by the model (see text).

DATE 1992	AVERAGE DAILY AIR TEMPERATURE (°C)	AVERAGE DAILY WIND SPEED ($m\ s^{-1}$)	TURBULENT FLUX ($W\ m^{-2}$)	Fnet ($W\ m^{-2}$)	ICE PRODUCTION RATE ($cm\ day^{-1}$)
Feb 18	-10.9	15.9	-377.7	-420.7	11.5
19	-11.6	12.8	-327.4	-363.3	10.2
20	-10.2	5.2	-114.0	-153.0	4.3
21	-16.1	8.0	-298.6	-391.7	9.9
22	-17.9	8.9	-374.0	-435.6	12.2
23	-15.9	8.8	-323.9	-377.6	10.6
24	-14.5	10.1	-334.8	-381.2	10.7
25	-13.8	8.5	-266.3	-313.4	8.8
26	-15.9	11.2	-412.2	-463.7	13.0
27	-17.9	13.7	-575.8	-517.2	17.6
28	-21.1	12.1	-609.6	-671.1	18.9
29	-22.8	6.0	-328.9	-405.8	11.4
March 1	-21.2	5.9	-298.8	-368.9	10.4
MEAN	-16.1	9.8	-357.1	-404.9	11.5
STD DEV	3.9	3.1	126.7	117.1	3.7
RANGE	-10.2 to -22.8	5.2 to 15.9	-114.0 to -609.6	-153.0 to -671.1	4.3 to 18.9

imagery and it reached its largest observed extent by February 27. The high ice production rates reflect the large heat transfer between ocean and atmosphere thought to be typical of the continuous opening, re-opening, and expansion of the polynya region over the entire event.

5.2 CMI Model (Cavalieri and Martin, 1994): Model Details and Ice Production

This model is an analytical model that originally combined polynya areas specified as boxes derived from NIMBUS 7 scanning multi-channel microwave radiometer (SMMR)-derived ice concentration maps with local weather observations, and oceanographic data to calculate ice production and brine flux from polynyas. The SLIP area was originally represented by two SMMR pixels (25km resolution) rather than by area measurements due to difficulty in determining absolute ice-water boundaries at SMMR resolutions. In adapting this model to my efforts, I have substituted my higher resolution SAR/AVHRR measurements of SLIP polynya size in place of the SMMR-based boxes. For discussion purposes, I have split the original CM model into two parts, the CMI or ice production model, and the CMD or dense water production model (Section 5.5).

The CMI model does not include a stepwise ice growth term in its heat budget formulation. Instead, as did the PM, it converts the total net heat loss from the open water area to an ice quantity per unit area per day. This means that the model has no memory of the previous time increment's ice growth. The model further assumes that polynya ice growth is frazil ice under wind-driven conditions which correctly reflects the environment during the SLIP event in question. After ice forms, it is considered to be "swept" down to the southern edge of the polynya entirely so that the next day's production begins from an open water state only. As was true of the set of PM model energy balance equations, there is no ice motion term in the set of CMI model equations. While the CMI model is similar to the PM model in its basic structure, it differs in that it includes a consideration of cloud cover fraction in its flux parameterizations. The PM model considered only clear sky conditions. The CMI model has been previously applied in various stages of development to the Bering, Chukchi, Beaufort, and East Siberian Seas (Martin and Cavalieri, 1989, and Cavalieri and Martin, 1994).

As a first step towards an ice production determination at the SLIP, I calculated heat fluxes over open water based on my measurements of polynya area. In this case, unlike in the PM model, the emissivity is calculated after Maykut and Church (1973) as

$\varepsilon_a = 0.7829\left(1 + 0.2232CL^{2.75}\right)$ where ***CL*** represents the observed cloud cover in octas. F_s, the incoming short-wave radiation, is calculated as a combination of clear sky and cloud cover conditions (Cavalieri and Martin, 1994; Laevastu, 1960; and Zillman, 1972) using $F_s = (1-\alpha)\kappa Q$ where α is 0.1 for open water; κ is accounts for cloud cover (κ=1–0.6CL^3 where ***CL*** is the cloud fraction after Laevastu (1960)); and ***Q*** is the shortwave radiation. (See Cavalieri and Martin (1994) for specific equations used in determining ***Q***.) Fixed parameters such as air density (ρ_a), heat transfer coefficient (C_h), specific heat of air (C_p), and ocean temperature (T_w) were specified to be: 1.3kg m^{-2}; 2.0x10^{-3}; 1004J deg^{-1} kg^{-1}; and -1.8°C, respectively, based on values used in earlier work by Pease (1987) and Cavalieri and Martin (1994). Gambell data was used to calculate incoming longwave radiation and incoming shortwave radiation.

Following the CMI model algorithm, I determined the total daily ocean to atmosphere heat loss, H_{loss}; at the SLIP by

(5.2) $$H_{loss} = (8.64 \times 10^{-4}) \times \text{polynya area} \times F_{net}$$

My SAR/AVHRR-based polynya measurements described in Chapter 4 were used for polynya area. Next, I calculated the rate of freezing, or ice formation, R_f, as:

(5.3) $$R_f = \frac{dh}{dt} = \frac{F_{net}}{\rho_{ice} L}$$

where F_{net} is the net daily heat loss; ***L*** is latent heat of fusion=3.34x10^{5}J kg^{-1} ; ***h*** is ice thickness, and ice density, ρ_{ice}, is 0.92 x 10^{3}kg m^{-3}. Using the total daily heat loss, H_{loss}, and the rate of freezing, the volume of ice production in cubic meters within the polynya per day was calculated as:

(5.4) $$VOL_{ice} = \frac{H_{loss}}{\rho_{ice} L}.$$

My CMI model output consisted of daily net turbulent heat flux over open water, daily ice

freezing or production rate for the SLIP region, and ice production volume.

I ran the CMI model for the period of February 18-March 1, 1992 using a daily timestep as I did for my PM experiment. Results for my CMI model experiment are shown in Table 5.2. The largest negative flux values occur during period of low temperatures, high wind speeds, and greatest polynya expansion. The largest ice production rates correspond to the largest negative heat fluxes as they did in the PM model results. Turbulent fluxes ranged from -116.5W m^{-2} late in the early "transition" wind period (i.e., prior to observed polynya development) to -610W m^{-2} on February 28 (i.e., just after the observed peak of polynya development). F_{net} ranged from -149.5W m^{-2} to 589.4W m^{-2}. Ice production rates ranged from 4.2 to 16.2cm day^{-1}. The CMI's flux values and ice production rates were slightly lower than those obtained from the PM model. I attribute this to the different means of parameterizing the fluxes between the two models. Additionally, I think the CMI model is a slight improvement over the PM model in terms of estimating ice production because it attempts to account for cloud cover.

5.3 Cox, Weeks, Wade Model (CW2; Wade, 1993): Model Details and Ice Production

The CW2 ice growth model (Wade, 1993) that I used for calculating heat fluxes and ice growth/production rates is basically a five part analytical/numerical model that includes: 1) an initialization of the first layer of ice (~0.6 cm in my study) rather than starting from a open water state; 2) a calculation of the surface energy balance; 3) a determination of the properties of the ice at different levels in the ice sheet; 4) a treatment of the different aspects of the desalination process; and 5) a finite-difference routine to estimate changes in the temperature profile and growth rate. The surface energy balance employed in the model is based on the thermodynamic model of Maykut and Untersteiner (1971) and Maykut (1978) formulated as:

$$(1-\alpha)F_r - I_o + F_L - F_E - F_s + F_e - F_c = 0 \qquad (5.5)$$

where $(1-\alpha)F_r$ is the net short-wave radiation at the ice surface as determined by the model: F_r is the incoming shortwave radiation; αF_r is the reflected shortwave radiation; and α is the albedo whose variations as a function of ice thickness are estimated from field

Table 5.2: Ice Production-CMI Model. As in Table 5.1, but for CMI model. Turbulent Flux is this model's representation of sensible and latent heat flux combined into one term by the model (see text).

DATE 1992	AVERAGE DAILY AIR TEMPERATURE (°C)	AVERAGE DAILY WIND SPEED ($m\ s^{-1}$)	TURBULENT FLUX ($W\ m^{-2}$)	Fnet ($W\ m^{-2}$)	FREEZE RATE (ICE PRODUCTION) ($cm\ day^{-1}$)
February 18	-10.9	15.9	-375.8	-402.4	11.0
19	-11.6	12.8	-328.4	-345.5	9.7
20	-10.2	5.2	-116.5	-149.5	4.2
21	-16.1	8.0	-295.5	-316.5	8.9
22	-17.9	8.9	-371.6	-392.8	11.0
23	-15.9	8.8	-323.9	-356.3	10.0
24	-14.5	10.1	-335.3	-377.7	10.6
25	-13.8	8.5	-264.3	-295.6	8.3
26	-15.9	11.2	-416.0	-442.3	12.4
27	-17.9	13.7	-574.8	-476.1	16.2
28	-21.1	12.1	-610.7	-589.4	16.6
29	-22.8	6.0	-321.7	-352.4	9.9
March 1	-21.2	5.9	-301.5	-337.0	9.5
MEAN	-16.1	9.8	-356.6	-374.9	10.6
STD DEV	4.0	3.2	126.7	101.7	3.2
RANGE	-10.2 to -22.8	5.2 to 15.9	-116.5 to -610.7	-149.5 to 589.4	4.2 to 16.6

measurements of Weller (1972). I_o is net short-wave radiation transmitted through the surface of the ice (i.e., passes into the interior of the ice) determined by the model from $I_o = i_o(1-\alpha)F_r$ where i_o= 17%, as it was in Wade (1993), based on Maykut and Untersteiner's (1971) suggestion that I_o is approximately 17% of the net shortwave radiation (fraction of net shortwave radiation transmitted into the interior of the ice). F_L is the incoming longwave radiation obtained as in Wade (1993) through the use of values from Marshunova (1961) and application of a polynomial smoothing equation in a manner similar to that used for incoming shortwave radiation. While the values for F_L were Arctic-based, rather than Bering Sea-based, this was the best means available of obtaining incoming longwave radiation values for this study. F_E is the emitted longwave radiation or the outgoing (emitted) longwave radiation as calculated using the Stefan-Boltzmann Law, $F_E = \varepsilon\sigma\alpha T_o^4$, where T_o^4 is the ice surface temperature (K) as determined by model iteration; σ is 5.67 x 10^{-8}W m^{-2} K^{-4}; and ε is the emissivity. This sensible heat flux term, F_s, is calculated by the model from $Fs = \rho_a C_p C_s U(T_a - T_o)$ where ρ_a=1.3kg m^{-3}, the average air density; C_p= 1006J kg^{-1} K^{-1}, specific heat at constant pressure; C_s= 0.002, sensible heat transfer coefficient; U= Gambell observed daily wind speed in m s^{-1}; T_a= Gambell observed daily air temperature in K; and T_o= model determined ice surface temperature in K. F_e is latent heat flux calculated by the model from $F_e = \rho_a L C_e U(q_a - q_o)$ where ρ_a=1.3kg m^{-3}. the average air density: L= (2.5 x10^6 - 2.274 x 10^3 x (T_a -273.15)), the latent heat of vaporization (J kg^{-1}): T_a= Gambell daily air temperature in K; U= Gambell daily wind speed in m s^{-1}; and C_e= 0.00175, evaporation coefficient (Cox and Weeks, 1983). The difference in specific humidity, q_a-q_o , is derived by the model from a polynomial relationship based on observed air temperature at Gambell, model-derived ice surface temperature, and observed Gambell relative humidity following procedures of Wade (1993) and Maykut (1978). F_c is the conductive heat flux upward through the ice calculated by $F_c = \frac{\kappa}{H}(T_b - T_o)$ where T_o= model-derived ice surface temperature in K; T_b =-1.8°C. temperature of the water-ice interface, i.e. at bottom of ice layer; κ= thermal conductivity of ice layer (W m^{-1} K) calculated by the model based on relationships between conductivity of pure ice, thermal conductivity of brine, and brine volume determined by Ono (1975), Cox and Weeks (1983), and Wade (1993); and H= ice thickness (m) as determined by the model.

The temperature profile of the ice grown by the model, and the position of the

freezing interface for each layer of ice grown by the CW2 model is determined using a finite difference model developed by Goodrich (1974). The ice surface temperatures and thermal properties of each layer of ice were determined separately within the overall model scheme in my experiments based on observed Gambell meteorological data. The surface temperature of the first layer of ice is determined by balancing energy fluxes at the ice surface from the surface energy balance. Once the initial layer surface temperature was determined within the model, the thermal conductivity, latent heat, and heat capacitance (Yen, 1981) were calculated by the model. At each time step, the model checked ice thickness, determined ice surface temperature for the next time step and updated all ice properties. Long-wave emitted radiation, latent heat flux, sensible heat flux, and conducted heat flux were computed as a function of ice surface temperature until the surface energy equation is balanced for each time step. The model also calculates the thermal conductivity, latent heat, and heat capacitance associated with ice growth at each time step as part of the energy balance routine.

The growth rate for the initial layer of ice is determined by the freezing degree-day equivalent of one ½ hour time step for the first freezing day relative to -1.8°C. Initialization of the growth rate for this first ice layer is based on the empirically-derived ice growth relations of Bilello (1961). An empirical formula (Anderson, 1961) is then used to estimate the amount of ice that will grow in that time, thus establishing an initial estimated ice growth rate. After initialization is completed, ice is grown for a user-specified length of time. The initialization or first layer of ice is considered to be all sea ice while the remaining ice layers are assumed to be a mixture of ice and sea water in a 1:3 ratio at 1.8°C (Wade, 1993). The finite difference routine in the model locates the position of the freezing interface of each additional layer as it account for phase change by substituting the moving boundary condition of the phase change interface with an apparent latent heat source term added to the heat conduction equation (Wade, personal communication).

Before running the model, I adapted it to use meteorological data for St. Lawrence Island rather than the Arctic-based climatology built into it. My initial experiments involved a series of "one day" tuning runs to determine a suitable sensible heat coefficient, C_h, to use for the SLIP region. The initial Arctic value encoded in the model was C_h=0.003 but this seemed inappropriate in an area consisting of a mixture of ice types and open water. Previously, Pease (1987) had used C_h=0.002 in her Bering Sea polynya model. Andreas and Murphy (1986) suggested that a C_h value of 0.00149 was more appropriate for leads and polynyas. Walter's (1989) observations over white ice at the SLIP indicated that

a maximum value of C_h =0.0012 was representative of SLIP local conditions. I initially chose to test C_h= 0.002 and C_h= 0.00149 based on discussions in the related literature. In the end, I decided to use C_h =0.00149 for all following CW2 experiments because I was actually calculating sensible and latent heat rather than approximating a turbulent flux as in Pease (1987). Further, I was also working with an area that consisted of open water and various stages of new ice production and growth.

Incoming longwave radiation and incoming shortwave radiation were calculated using Gambell data prior to the model iterations. Oceanic heat flux, surface emissivity, ocean temperature, i_o (i.e., shortwave ice transmission coefficient), and sensible heat flux coefficient were also specified as model input. For simplicity in flux calculations, and because snow was such a variable unknown quantity, I chose to set snow accumulation equal to zero.

The CW2 model attempts to balance its energy equation (see above) to obtain ice growth as it iterates values of outgoing longwave radiation, latent heat flux, sensible heat flux, and conductive heat flux as a function of ice surface temperature (Wade, 1993). Once the equation is balanced, iteration is stopped. Output quantities include ice thickness, ice surface temperature, conductive heat flux, sensible heat flux, latent heat flux, outgoing longwave radiation, outgoing shortwave radiation, net shortwave radiation, and net longwave radiation. Finally, I used my SAR/AVHRR polynya area measurements to convert the "point" ice growth obtained as model output to a volume of ice for later use in dense water production calculations, by making a very generalized assumption that the ice growth rate is similar throughout the polynya area.

In addition to the C_h tuning experiments, I ran this CW2 model six times for the period of February 18-March 2, by breaking model runs into time periods of single days, two days (i.e. February 21-22,1992), three days (i.e. February 21-23, 1992), four days, six days, and seven days. This way I could potentially obtain a primitive relationship between ice age, ice thickness, and ice surface temperature to help guide my determination of "active ice formation" or "polynya sector" areas in the SLIP and to refine the energy balance/ice production results for the entire polynya region which is a mix of water, and ice of varying thicknesses. This CW2 model scheme has a distinct advantage over other energy budget ice growth models as it has a memory and so recalls ice growth from previous time steps as it "grows" new ice. In other words, if the model is run for three

Table 5.3: Ice Production-CW2 Model. Ice growth, ice temperature, sensible heat flux, and latent heat flux results are shown for "1st model time step (½ hour)", and after a "24 hour" time period. For example, on February 18, 0.7 cm of ice represented the first ½ hour ice growth (initial model ice growth) and 7.4 cm of ice was the thickness at the end of the day (24 hour ice growth). Changes in values reflect changes due to increasing thicknesses of ice "grown" over the 24 hour time period. Sensible heat flux and latent heat flux are added together to get the "CW2 turbulent flux" term referred to in the text for comparisons with PM and CMI results. Negative fluxes indicate ocean to atmosphere energy transfer.

DATE 1992	GAMBELL AIR TEMP (°C)	GAMBELL WIND SPEED ($m\ s^{-1}$)	SENSIBLE HEAT FLUX ($W\ m^{-2}$)	LATENT HEAT FLUX ($W\ m^{-2}$)	ICE SURFACE TEMP (°C)	ICE GROWTH 1st time step; 24 hour (cm)
Feb 18	-10.9	15.9	-228.5 -62.2	-166.0 -68.0	-3.6 -9.6	0.7 7.4
Feb 19	-11.6	12.8	-205.0 -53.5	-137.9 -58.9	-3.3 -8.1	0.7 6.7
Feb 20	-10.2	5.2	-83.2 -89.5	-58.3 -40.5	-2.1 -7.0	0.3 4.7
Feb 21	-16.1	8.0	-202.4 -97.7	-100.2 -35.8	-3.1 -11.6	0.6 7.3
Feb 22	-17.9	8.9	-248.3 -93.4	-114.6 -47.0	-3.5 -10.5	0.7 7.7
Feb 23	-15.9	8.8	-215.0 -71.8	-113.8 -43.7	-3.3 -10.3	0.6 7.2
Feb 24	-14.5	10.1	-219.8 -77.0	-123.7 -48.2	-3.3 -9.9	0.7 7.1
Feb 25	-13.8	8.5	-179.8 -101.4	-106.8 -49.1	-3.0 -9.7	0.6 6.9
Feb 26	-15.9	11.2	-266.0 -106.8	-137.7 -44.8	-3.7 -13.0	0.7 8.2
Feb 27	-17.9	13.7	-356.3 -120.0	-166.3 -42.1	-4.6 -16.6	0.9 9.2
Feb 28	-21.1	12.1	-386.1 -127.2	-154.6 -38.1	-4.8 -17.3	0.9 9.5
Feb 29	-22.8	6.0	-226.7 -112.3	-91.6 -38.0	-3.2 -11.6	0.6 7.7
Mar 1	-21.2	5.9	-208.5 -121.9	-89.6 -36.2	-3.1 -12.2	0.6 7.6
MEAN	-16.1	9.8	-232.7; -95.0	-120.1; -45.4	-3.4; -11.3	0.7; 7.5
STD DEV	4.0	3.2	75.3; 23.4	32.0; 9.3	0.7; 3.0	0.15; 1.2
RANGE	-10.9 to -22.8	5.2 to 15.9	-179.8 to -386.1 -53.5 to -127.2	-58.3 to -166.3 -36.2 to -68.0	-2.1 to -4.8 -7.0 to -17.3	0.3 to 0.7 4.7 to 9.5

days. the ice growth and energy fluxes reflect three days of growth rather than restarting with zero ice thickness each day of the model experiment as the CMI and PM models would have done.

Results from my "one day" CW2 model experiments are shown in Table 5.3. The two sets of numbers in the flux and ice growth columns reflect the nature of the CW2 model. I chose to show the initial time step results (first half hour) and results after 24 hours as this model is capable of giving results for fluxes and ice growth at each time step. The first step heat flux results are probably most comparable to the PM and CMI results as this time step is the closest the CW2 model gets to ice growth from an open water state. I suspect that these CW2 heat flux values are lower than the PM or CMI values because the CW2 values reflect fluxes associated with a very small layer of ice (0.6 to 0.9cm thick) due to model initialization, and because the CW2 uses what appears to be a more complete, more "realistic" flux parameterization scheme. Ideally, the CW2 model would be able to start iterating from zero ice thickness and in later developmental stages, it may yet achieve this. The 24 hour results are also important as they show the decrease in heat fluxes over time and will be used later in this chapter for CW2-based dense water calculation purposes as they correspond to a daily time period.

When reviewing this model in the context of its application to the SLIP, it is important to remember that the SLIP region is not completely open water at all times, rather the water is continually being covered and re-opened over time due to new ice production. This new ice produced blows downwind within the polynya region, but as it does, it continues to thicken and thus alter the thermodynamics of the polynya region through resultant changes in ocean to atmosphere heat transfer rates and surface albedo changes. With modifications to allow for inclusion of x-y space, and additional fine-tuning of flux parameterizations, this CW2 model has the potential to allow one to estimate changes in surface temperature, heat transfer and ice production rates within the polynya region over time and space.

Results from my CW2 model experiments for the 1992 February southern SLIP event (Table 5.3) suggested that ice of 0.6cm would have a surface temperature range of -3 to -5°C and 9.0cm of ice would have a surface temperature range of -16 to -17°C. Turbulent flux (sensible heat flux + latent heat flux) ranges from -522.6W m^{-2} to -141.5 W m^{-2} (initial time step) and from -165.3 to -112.4W m^{-2} (24 hours). Again as shown by the PM and CMI models, the largest heat losses and the highest rate of ice growth occurred at or after the period of extensive polynya expansion. From Table 5.3, it is also readily

apparent that the range of CW2 values for heat fluxes and ice growth drops substantially over the 24 hour period reflecting again the changes in surface heat flux transfer and lessening influence of atmospheric conditions on the ocean due to increased ice cover. Although the CW2 model likely provides an estimate of the lower limit of the fluxes due to dynamical constraints. it is an improvement over both the PM and CMI models primarily because of its ability to actually calculate all the fluxes in the energy balance scheme as well as reflect changes in heat fluxes and ice growth over time. This memory ability may also make it valuable for inclusion as an ice growth component in a more complex coupled air-sea-ice climate system model.

5.4 ARCSyM (Lynch et al., 1997): Thermodynamics and Heat Flux Fields:

The effects of the SLIP have the potential to be felt locally and regionally because the SLIP is one of several western Arctic polynyas thought to be major contributors of heat and dense water to the Arctic climate system (Cavalieri and Martin, 1994; Pease, 1980; Smith et al., 1993; Schumacher et al., 1983; Aagaard and Carmack, 1986). A main advantage of using a coupled model such as the ARCSyM for polynya simulation is the model's ability to simulate three-dimensional atmospheric fields at extremely fine resolution for a climate model. These model-derived surface fluxes depict one key mechanism by which the variability at the surface of ice covered seas influences the atmosphere. In theory. by converting these heat fluxes to ice production rates as with the other models discussed above. one could obtain another estimate of the polynya's potential rate of ice growth rate and then dense water production rates.

The thermodynamic components of turbulent heat and moisture fluxes are parameterized in the ice model of the ARCSyM using a standard form as in Lynch et al. (1995 and 1997):

(5.6) $$SH = \rho_a C_a C_t U_a (T_w - T_a)$$

(5.7) $$LH = \rho_a L_v C_t T_a U_a (Q_{sat}(T_w) - Q_a)$$

where SH is the sensible heat flux and LH is the latent heat flux. The turbulent transfer coefficient, C_t. used here is allowed to vary as a function of the near surface atmospheric stability (i.e.. C_t decreases as atmospheric stability increases; Lynch et al., 1995; Holton, 1979). Specifics of this model. model input, and my experimental scheme were discussed earlier in Chapter 2. To review briefly, the model was run for two primary experiments.

one with a "swamp ocean" component and one with a "barotropic ocean" component. These model experiments were run for the period of February 18-March 2, 1992. Model output discussed here include the sensible and the latent heat flux fields for February 25 and February 28, 1992, as well as representative atmospheric profiles of temperature and moisture associated with the simulated polynya/ice field.

5.4.1 Summary of Heat Flux Fields- "Swamp Ocean Experiment: Heat flux fields obtained from the "swamp ocean" simulation's two periods, February 24-27 and February 27-March 1, are represented by simulated SLIP heat flux fields from February 25 and February 28. The term "fluxes" or "turbulent heat flux" will be used interchangeably, hereafter unless specified otherwise, to represent sensible plus latent heat flux. As shown in Figure 5.1, sensible and latent heat flux fields obtained from the simulation indicate the presence of a polynya by an area of increased surface fluxes extending southward off the coast of St. Lawrence Island. The sensible and latent heat fluxes associated with the simulated polynya are larger than those over the simulated surrounding ice pack by 30 - 100W m^{-2} and 10 to 30W m^{-2}, respectively.

Development of the areas of largest ocean to atmosphere fluxes occur concurrently with expansion of the areas of warmest simulated temperatures and lowest simulated ice concentrations south of St. Lawrence Island. The simulated sensible and latent fluxes also reflect the errors in simulated ice concentration and the surface temperature discussed in Chapter 4. It is not surprising that the geographic extents of the highest fluxes shown offshore of the island in Figure 5.1 indicate too large a polynya region. Maximum simulated turbulent fluxes ranged from -110 to -130W m^{-2}, located in the areas of lowest ice concentration within the polynya. Based on my calculations presented earlier in this chapter, I found that "observed" turbulent fluxes over actual open water potentially ranged from -260 to -270W m^{-2} on February 25 and from –540 to 610W m^{-2} on February 28. The maximum simulated flux values on these days therefore underestimate open water conditions. Instead, the simulated fluxes reflect those that might be observed over at least 7-10cm of ice (i.e. -150.5 to -165.3W m^{-2} from CW2 results) rather than those over open water.

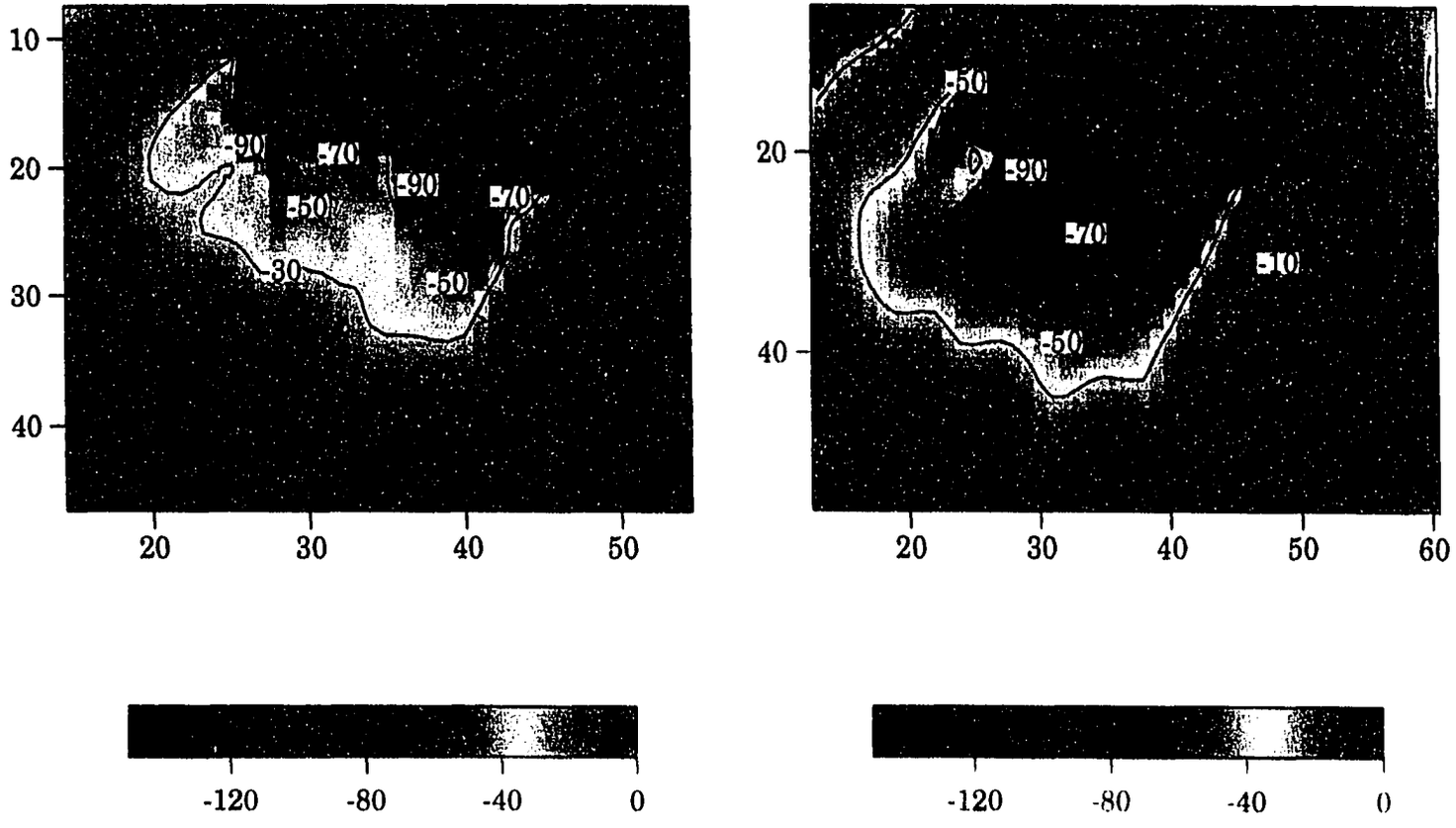

Figure 5.1(a): ARCSyM "Swamp" Ocean Heat Fluxes. Simulated sensible heat fluxes for (left) February 24, 1992 and (right) February 27, 1992. St. Lawrence Island has been masked black. The simulated SLIP is the large area of highly negative fluxes extending southward from St. Lawrence Island. Time is 12 Z. Units are W m^{-2}, with contours every 20 W m^{-2}. Axes scales indicate model grid cells (7 km grid spacing). Negative flux value indicates flux from ocean to atmosphere.

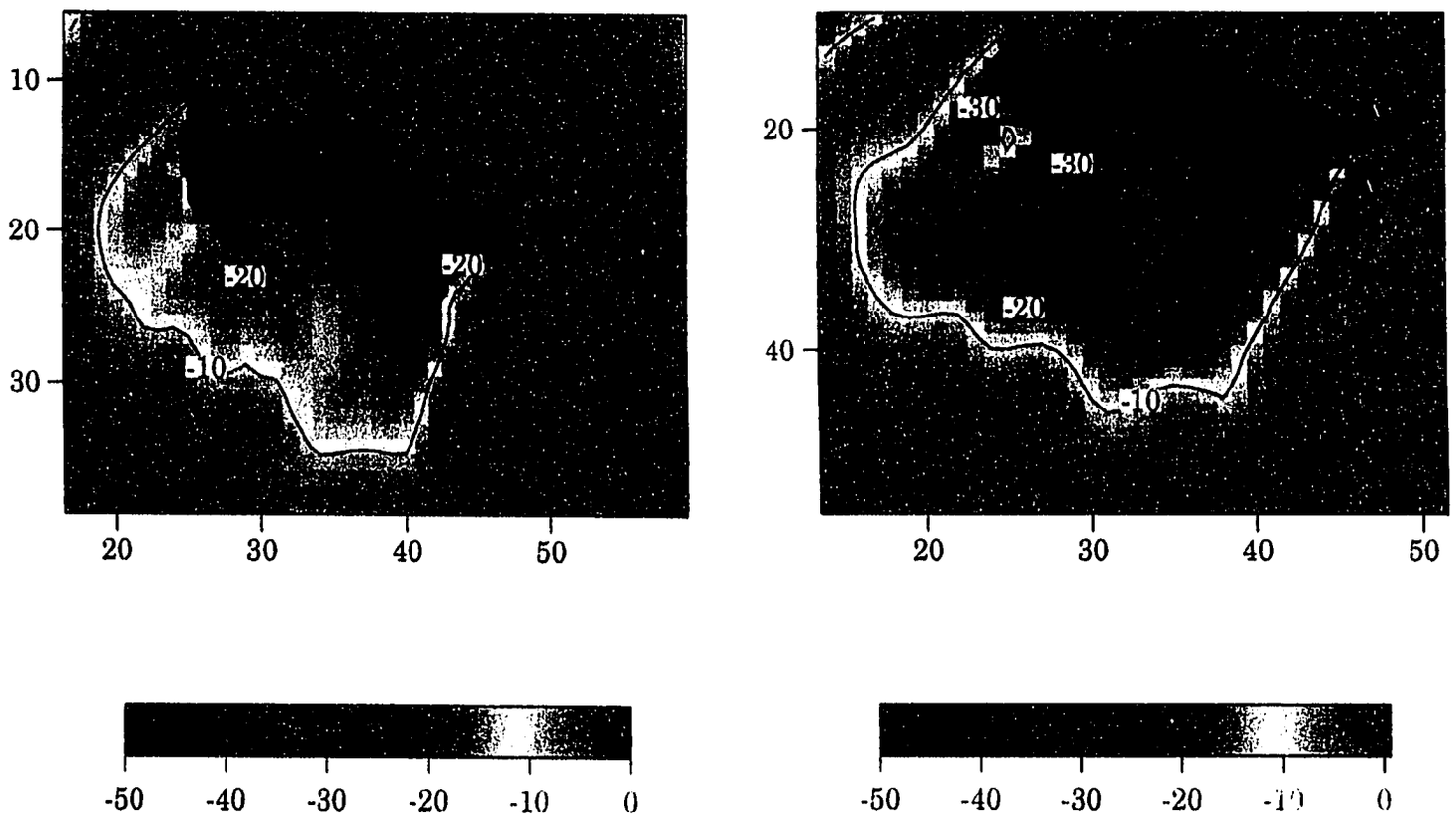

Figure 5.1(b): ARCSyM "Swamp" Ocean Heat Fluxes. Simulated latent heat fluxes for (left) February 24 1992 and (right) February 27, 1992. St. Lawrence Island has been masked black. The simulated SLIP is the large area of highly negative fluxes extending southward from St. Lawrence Island. Time is 12 Z. Units are W m^{-2}, with contours every 20 W m^{-2}. Axes scales indicate model grid cells (7 km grid spacing). Negative flux value indicates flux from ocean to atmosphere.

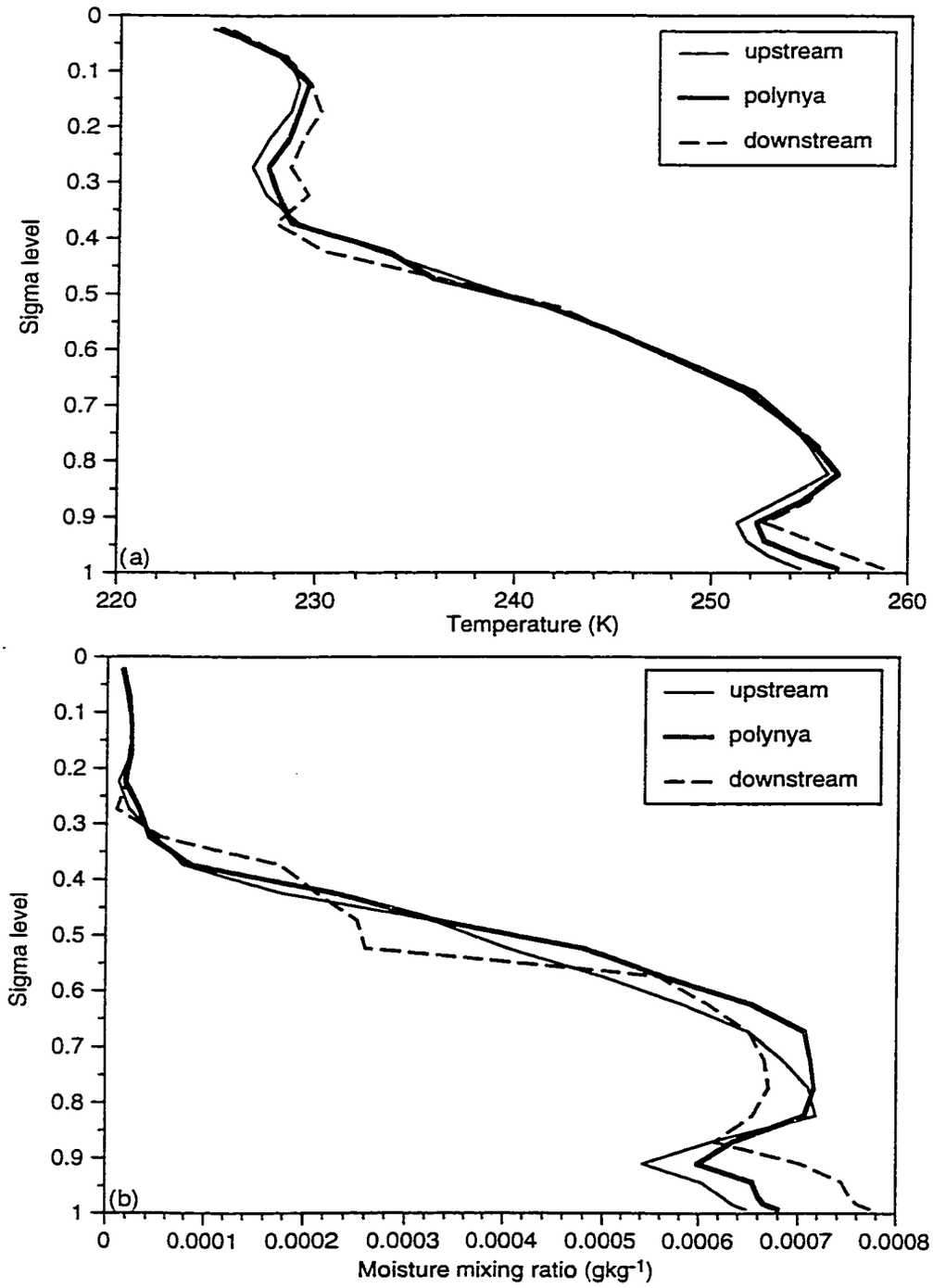

Figure 5.2: SLIP Atmospheric Impact. ARCSyM "swamp" ocean experiment results of (a) air temperature (K); (b) moisture mixing ratio (g kg^{-1}) profiles for three points situated approximately 50 km upwind of the polynya, directly over the polynya, and approximately 50 km downwind of the polynya. The profiles indicate the warming and moistening of the atmosphere attributable to the polynya by differences in vertical profiles upwind, downwind, and directly over the polynya.

Although the magnitudes of the simulated fluxes should be interpreted cautiously due to model limitations, the relative magnitudes of simulated fluxes across the simulated polynya region are reasonable. The highest sensible and latent heat values were found in the most active regions of the polynya and values decreased further away from the St. Lawrence Island coast. The spatial distribution of these simulated fluxes indicates that despite the inability of global climate models to resolve the SLIP, due to its relatively small size, the effect of the polynya's energy transfer can potentially extend over 50km downstream. Vertical profiles of "swamp" ocean experiment atmospheric temperature and moisture for a point 50km upstream, 50km downstream and directly over the polynya are shown in Figure 5.2. Despite the model's limitations, the simulated atmospheric warming above the polynya due to the presence of the polynya is well-defined as the profiles of simulated temperature in Figure 5.2 show this change is notable over the polynya to as high as the ~800mb or 0.8 sigma level. The vertical profiles of simulated temperature suggest that the presence of the SLIP increases the lower tropospheric air temperature locally over the polynya by ~2°C. The vertical extent of this influence is similar to that shown for the Arctic (e.g. Figure 5.3 shown here from Brown, 1989). The effect of heat fluxes from an ice edge has the potential to be noted in the atmosphere downwind for 100 km or more depending on flux magnitudes. Thus, the impact of polynyas on regional-scale climate may be large enough to require their consideration in larger-scale models.

5.4.2 Summary of Heat Flux Fields- "Barotropic" Ocean Experiment: The addition of a "barotropic" ocean circulation and an improved drag coefficient formulation to the ice model had the effect of changing the shape and distribution of regions of high turbulent fluxes (Figure 5.4) associated with the polynya. As shown in Figure 5.4, the maximum simulated turbulent fluxes for February 25, 1992 were -140W m^{-2} located just off the southwestern coast of St. Lawrence Island. Maximum "barotropic" ocean simulated turbulent flux values for the February 28 ranged between -180 to -200W m^{-2} (Figure 5.4). As mentioned earlier, the maximum simulated turbulent flux values obtained from the "swamp" ocean simulation (Figure 5.1) ranged from -110W m^{-2} on February 25 to -130W m^{-2} on February 28. The extent of "barotropic" ocean simulated fluxes associated with the polynya extended 49km off the southern coast of St. Lawrence Island on February 25 and 100-114km offshore on February 28. Overall, the "barotropic" ocean simulated flux values were closer to those representative of actual open water. However, they were still too small

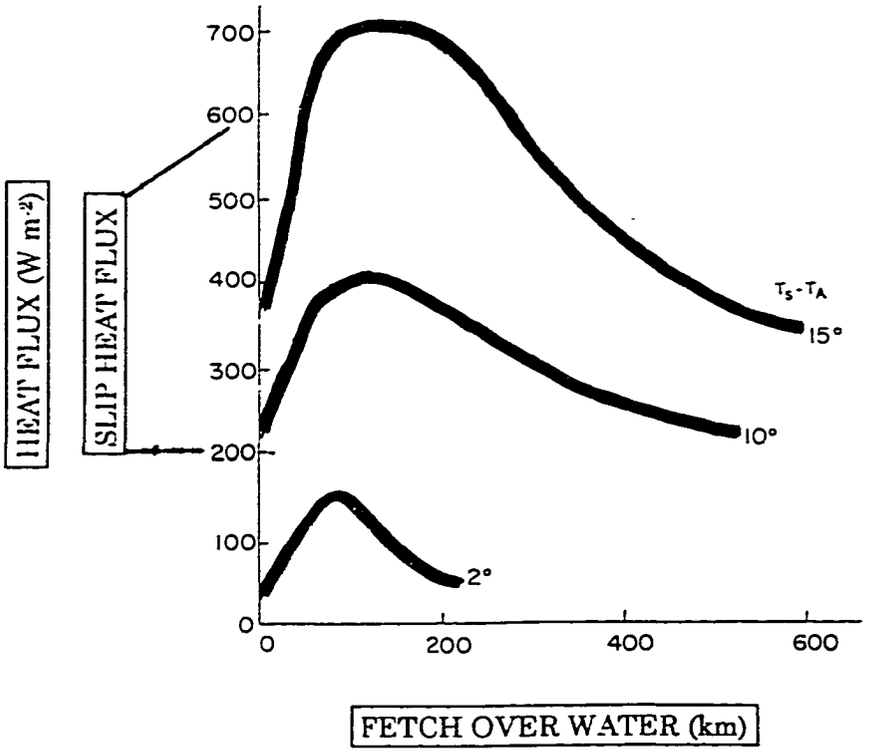

Figure 5.3 Energy Flux Impact on Atmosphere-Arctic Ice Edge. Diagram shows the potential downwind extent of the effect of ice edge air-sea-ice energy exchanges during a cold air outbreak period in the Arctic. Downstream or "fetch over water" distances are given for combinations of total heat flux (i.e., latent plus sensible) and resulting $T_{surface}$-T_{air} temperature differences. Turbulent flux values for the 1992 southern SLIP range from 200 to-600 W m^{-2} as denoted by the "SLIP HEAT FLUX" label on the y-axis (see also text and Tables 5.1-5.3). (After Brown, 1990.)

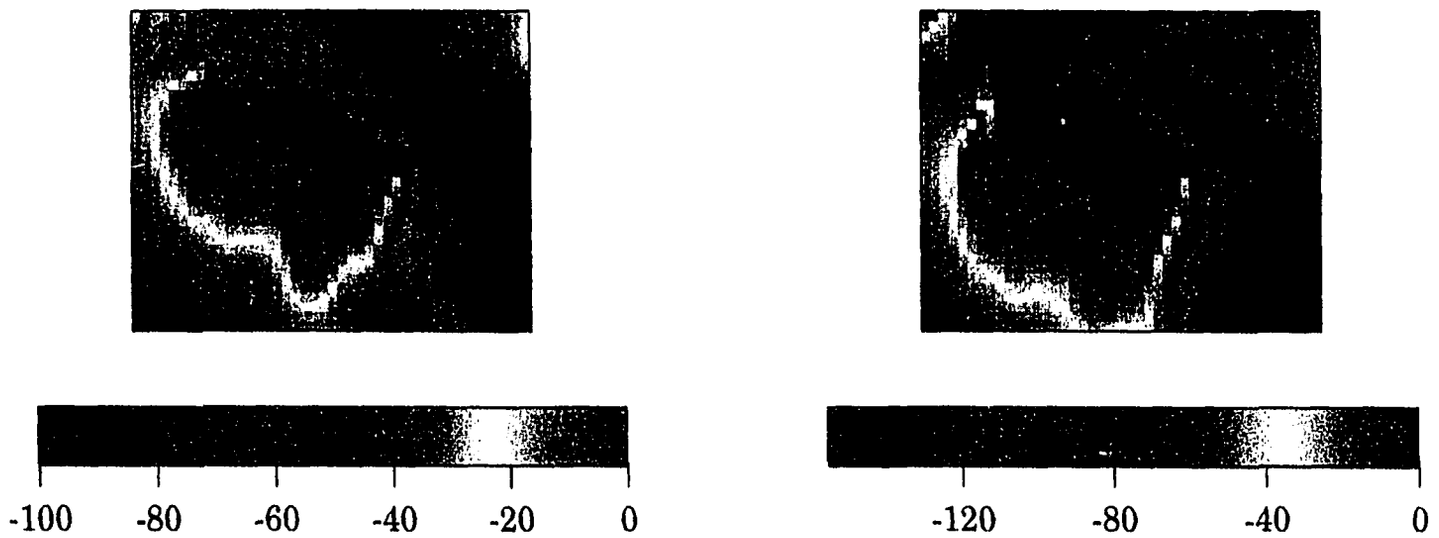

Figure 5.4(a): ARCSyM "Barotropic" Ocean Experiment Heat Fluxes: Simulated sensible heat fluxes for (left) February 24, 1992 and (right) February 27, 1992. St. Lawrence Island has been masked black. The simulated SLIP is the large area of highly negative fluxes extending southward from St. Lawrence Island. Time is 12 Z. Units are W m^{-2}. Axes scales indicate model grid cells (7 km grid spacing). Negative flux value indicates flux from ocean to atmosphere. Note the differences in SLIP depiction and the areal extent of the more negative fluxes here in comparison to the "swamp" ocean simulation results shown in Figure 5.1a.

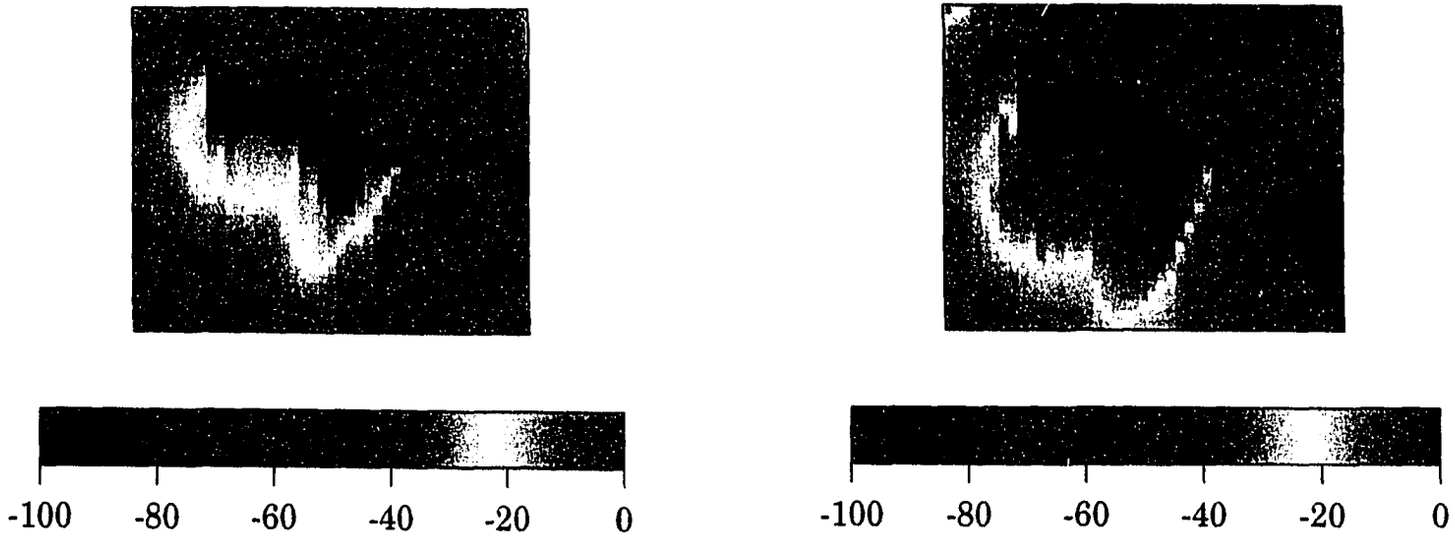

Figure 5.4(b): ARCSyM "Barotropic" Ocean Experiment Heat Fluxes: Simulated latent heat fluxes for (left) February 24, 1992 and (right) February 27, 1992. St. Lawrence Island has been masked black. The simulated SLIP is the large area of highly negative fluxes extending southward from St. Lawrence Island. Time is 12 Z. Units are W m^{-2}. Axes scales indicate model grid cells (7 km grid spacing). Negative flux value indicates flux from ocean to atmosphere. Note the differences in SLIP depiction and the areal extent of the more negative fluxes here in comparison with the "swamp" ocean simulation results shown in Figure 5.1b.

in magnitude in comparison with the previously calculated fluxes. Instead, the "barotropic" ocean case's simulated fluxes corresponded better to those expected for ice thicknesses of 7 cm based on my CW2 results, only a slight improvement over the "swamp" ocean case.

When judging the errors in simulated fluxes, it is again important to keep in mind that the ARCSyM model doesn't recognize an ice phase for ice less than 30cm thick, rather it treats this as open water. A calculated turbulent flux value of -60W m^{-2} on February 28 (CW2 method) would reflect 30cm ice thickness. Given that, simulated turbulent fluxes less than -60W m^{-2} represent the ARCSyM's open water range. Thus, the problem with the small simulated fluxes appears to lie in the ARCSyM's ice thickness-open water parameterization rather than solely in the flux calculations themselves. Due to this limitation in the ARCSyM at this stage of development, I did not calculate an ARCSyM ice production rate here. However, the most significant aspects of the ARCSyM results are that the model created a polynya at the appropriate time, as corroborated by the observed polynya, and that trends in the fluxes represent differences between open water and varying thicknesses of ice, i.e., gradients in fluxes outward towards the polynya boundary, and lower fluxes in areas where I observed thicker, colder ice.

5.5 Dense Water Production and Halocline Water Formation

After establishing ice production rates at the SLIP using the CW2, CMI, and PM models, I proceeded to calculate estimates of dense water production rates associated with this particular SLIP event. Typically 2/3 of the salt is rejected from the ice into the ocean as brine during ice formation in sea water. This increased salinity influences open water freezing temperatures and the local current structure through convection and horizontal salinity gradients (Gawarkiewicz and Chapman, 1995). I used flux results from my heat budget analyses, ice production rates, and Chapter 4's polynya area measurements to determine the dense water production during the February 1992 southern SLIP event.

The CMI has a companion box model (Cavalieri and Martin, 1994), the CMD, which takes ice production rates and sea water salinity estimates and then determines dense water and halocline water production rates for polynyas such as the SLIP. I chose to use this box model approach from Cavalieri and Martin (1994) because of its simplicity. Although the CW2 model also has a salt flux component, it was not developed enough nor sufficiently tested for my purposes (Wade, personal communication). The PM model did not have a salt flux component.

The CMD model is based on laboratory work, model results, and observations

(Maxworthy and Narimousa, 1994; Aagaard et al. 1981; Aagaard et al. 1985; Schumacher et al. 1983; Melling, 1993; Cavalieri and Martin, 1994; and Martin and Cavalieri, 1989). This model allowed me to calculate the salt flux generated at the SLIP, the salinity and density differences between the SLIP water and the ambient sea water, the potential dense water production, and finally the potential halocline water production attributable to this SLIP event. I used the results from my CW2, PM, and CMI experiments along with my SAR/AVHRR-derived polynya areas to drive the CMD box model in three separate experiments, each one driven individually by one of these ice production models.

There are several important assumptions inherent to this model as discussed in Cavalieri and Martin (1994) and in Martin and Cavalieri (1989). Those important to the SLIP are: a) frazil ice production in the polynyas generates salt enhanced water with salinities 1.5 to 2‰ above the ambient surface water; b) the enriched water from the polynya enters the Arctic Ocean to contribute to the cold halocline water; and c) the flux of water into the cold halocline layer, where the flux consists of water with a range of salinities, can be represented by a single salinity of 32.85‰. These assumptions and their implications appear to correspond well to the observations of Schumacher et al. (1983). Additional field data would certainly provide a better assessment of these assumptions. However, no new *in situ* collection of winter season data (i.e., moorings) for this region has been undertaken since Schumacher's efforts.

Following Cavalieri and Martin (1994), I started with the range of observed ambient salinities, not enhanced salinities, found to be characteristic of northeastern Bering Sea by Schumacher et al. (1983) as these are the most representative values for the region. As such, the eastern side of the southern polynya site is characterized by a range of background salinities of 30, 31, 32 ‰ and the corresponding western side is characterized by background salinities of 31, 32.75, 33‰. The differences in the salinity range for the east and west side of the polynya site location are based on observations of Schumacher et al. (1983) which suggested the salinity increases from east to west across the northeastern Bering Sea. By comparison, the average salinity of the Arctic Ocean halocline is 32.85‰. (Note: Halocline salinity ranges from 30.0‰ to 34.45‰, Aagaard et al., 1981).

The dense water/halocline water production model starts with calculation of salt production, S_{flux}, in kg per polynya area per day from ice volume and ice-water salinity differences using:

(5.8) $$S_{flux} = \rho_i \, VOL_i \, (S_w - S_i) \, x \, 10^{-3}$$

where the salinity of ice is determined by $S_i = 0.31 S_w$ where S_i is the salinity of the ice and S_w is the sea water salinity (Martin and Kaufman, 1981). Vol_i=ice production and ρ_i=density of ice.

Next, I calculated the potential enhanced salinities, S_e, within the polynya due to brine rejection during ice formation from:

(5.9) $$S_e = S_w + \Delta S$$

where S_w is the initial sea water salinity and δS is 1.5‰ or 2.0‰, typical salinity enhancements at such a polynya as discussed in Cavalieri and Martin (1995).

I, then, calculated the dense water production, ***DWVA***, by:

(5.10) $$DWVA = \frac{S_{flux}}{\rho_e S_e - \rho_w S_w}$$

where ***DWVA*** is the volume flux of dense water produced; ρ_e is the density of the salinity-enhanced polynya water; ρ_w is the density of the ambient sea water, S_w; and S_{flux} is the salt flux associated with the polynya.

Finally, as a means of estimating this particular SLIP event's potential dense water contribution to the Arctic Halocline waters, I calculated the volume flux of halocline water, ***HWV*** (salinity 32.85‰) potentially produced as a result of this event in two ways. First, for enhanced salinity, S_e, of less than 32.85‰ and dense water production, ***DWVA***, I used:

(5.11) $$HWVA = \frac{DWVA \, (S_e - 32)}{(32.85 - 32)}$$

as suggested by Cavalieri and Martin (1994) to calculate a volume flux "A" of halocline water. If, however, the enhanced salinity, S_e, turned out to be greater than 32.85‰, initially, I followed Cavalieri and Martin's (1994) assumption that the salt production itself generates a volume of water at 32.85‰, ***DWVB***, and that this enhanced salinity water

Table 5.4: CMD Dense Water and Halocline Water Production-February 21, 1992. Calculations were based on polynya areas obtained from SAR/AVHRR imagery, and daily average meteorological data from Gambell on St. Lawrence Island. Polynya sector areas are: West=525.8 km^2 and East=283.14 km^2. Ice production shown is output from the CMI model and serves as input for the CMD model. CMD model was run for five different salinities representing ranges of salinity observed in the vicinity of St. Lawrence Island by Schumacher et.al. (1983; see also Cavalieri and Martin, 1994). Each salinity was enhanced by (A) 1.5 ‰ and by (B) 2.0 ‰ to reflect potential salinity enhancement due to brine rejection from ice formation processes in the vicinity of the SLIP. Refer to text for equation details.

	MINIMUM EASTERN SALINITY 30 ‰	MINIMUM WESTERN SALINITY; INTERMEDIATE EASTERN SALINITY 31 ‰	MAXIMUM EASTERN SALINITY 32 ‰	INTERMEDIATE WESTERN SALINITY 32.75 ‰	MAXIMUM WESTERN SALINITY 33 ‰
Ice Production (km^3 day^{-1})	0.072	0.072	0.072	0.072	0.072
Salt Production (kg day^{-1})	4.8 E8	9.21 E8 4.96 E8	5.12 E8	9.73 E8	9.80 E8
Dense Water Production (A) (Sv)	0	0	0.0038	0.0071	0.0072
Halocline Water Production (A) (Sv)	0.0019	0.0055 0.0030	0.0066	0.0189	0.0211
Dense Water Production (B) (Sv)	0	0.0061 0.0027	0.0028	0.0053	0.0054
Halocline Water Production (B) (Sv)	0.0019	0.0060 0.0032	0.0066	0.0173	0.0190

Table 5.5: CMD Dense Water and Halocline Water Production-February 24, 1992. As in Table 5.4, but for February 24, 1992. Polynya sector areas are: West=745.16 km^2 and East=448.81 km^2.

	MINIMUM EASTERN SALINITY 30 ‰	MINIMUM WESTERN SALINITY; INTERMEDIATE EASTERN SALINITY 31 ‰	MAXIMUM EASTERN SALINITY 32 ‰	INTERMEDIATE WESTERN SALINITY 32.75 ‰	MAXIMUM WESTERN SALINITY 33 ‰
Ice Production (km^3 day^{-1})	0.12	0.12	0.12	0.12	0.12
Salt Production (kg day^{-1})	9.08 E8	1.55 E8 9.38 E8	9.68 E8	1.65 E9	1.66 E9
Dense Water Production (A) (Sv)	0	0	0.0071	0.0120	0.0121
Halocline Water Production (A) (Sv)	0.0035	0.0093 0.0056	0.0125	0.0318	0.0357
Dense Water Production (B) (Sv)	0	0.0086 0.0052	0.0053	0.0090	0.0091
Halocline Water Production (B) (Sv)	0.0035	0.0100 0.0061	0.0125	0.0292	0.0320

Table 5.6: CMD Dense Water and Halocline Water Production-February 27, 1992. As in Figure 5.4, but for February 27, 1992. Polynya sector areas: West=940.52 km^2 and East=774.20 km^2.

	MINIMUM EASTERN SALINITY 30 $^0/_{00}$	MINIMUM WESTERN SALINITY; INTERMEDIATE EASTERN SALINITY 31 $^0/_{00}$	MAXIMUM EASTERN SALINITY 32 $^0/_{00}$	INTERMEDIATE WESTERN SALINITY 32.75 $^0/_{00}$	MAXIMUM WESTERN SALINITY 33 $^0/_{00}$
Ice Production (km^3 day^{-1})	0.278	0.278	0.278	0.278	0.278
Salt Production (kg day^{-1})	1.30 E9	1.65 E9 1.36 E9	0.50 E9	3.00 E8	3.10 E8
Dense Water Production (A) (Sv)	0	0	0.0187	0.0232	0.0234
Halocline Water Production (A) (Sv)	0.0051	0.0098 0.0081	0.0329	0.0612	0.0686
Dense Water Production (B) (Sv)	0	0.0165 0.0136	0.0139	0.0174	0.0175
Halocline Water Production (B) (Sv)	0.0051	0.0194 0.0160	0.0329	0.0561	0.0616

Table 5.7: CMD Dense Water and Halocline Water Production-February 21-27, 1992. As in Table 5.4-6 but summarizing CMI and CMD results for the entire February 1992 southern SLIP event. Combined polynya sector areas (east plus west) are as follows: February 21=808.94 km^2; February 24=1,193.97 km^2; February 27=1,714.2 km^2. Table values are listed as (top) February 21, (mid) February 24, and (lower) February 27 in each data block. Results from each of the salinity categories shown in Tables 5.4-5.6 have been combined into the three basic categories shown here. Event mean values and standard deviations have been given in parentheses (i.e., mean; standard deviation) for ice production, salt production, dense water production, and halocline water production. Mean dense water production (Dense Water Production A and B combined) for the intermediate salinity region of the SLIP for this event is 0.159 Sv with a standard deviation of 0.003 Sv.

	MINIMUM SALINITY REGION	INTERMEDIATE SALINITY REGION	MAXIMUM SALINITY REGION
Ice Production (km^3 day^{-1})	0.072 0.120 0.278 (0.157; 0.11)	0.072 0.120 0.278 (0.157; 0.11)	0.072 0.120 0.278 (0.157; 0.11)
Salt Production (kg day^{-1})	1.30 E9 2.46 E9 2.95 E9 (2.24 E9; 0.9 E9)	1.47 E9 2.59 E9 4.36 E9 (2.81 E9;1.5 E9)	1.49 E9 2.63 E9 5.60 E9 (3.24 E9; 2.1 E9)
Dense Water Production (A) (Sv)	0	0.0071 0.0120 0.0232 (0.014; 0.008)	0.0110 0.0192 0.0421 (0.024; 0.016)
Halocline Water Production (A) (Sv)	0.0074 0.0128 0.0149 (0.012; 0.004)	0.0240 0.0374 0.0693 (0.044; 0.023)	0.0280 0.0482 0.1015 (0.059; 0.038)
Dense Water Production (B) (Sv)	0.0061 0.0086 0.0165 (0.010; 0.005)	0.0080 0.0142 0.0310 (0.018; 0.012)	0.0082 0.0144 0.0315 (0.018; 0.012)
Halocline Water Production (B) (Sv)	0.0079 0.0135 0.0245 (0.015; 0.008)	0.0205 0.0353 0.0721 (0.043; 0.027)	0.0256 0.0445 0.0945 (0.055; 0.036)

Table 5.8: Dense Water Production: PM/CMD, CW2/CMD, CMI/CMD Models. Summary of all dense water production experiments for the February 1992 southern SLIP event. Each "ice production" model was paired with the CMD dense water production box model of Cavalieri and Martin (1995) to obtain results shown. As in earlier tables, cells with three entries indicate values for February 21, 24, and 27, respectively, top to bottom. Salinity categories are as defined in Tables 5.4-5.7. "n/a" indicates that it was not possible to produce this dense water type given ice production, ambient salinity, and perhaps, current box model. "Event mean" refers to mean value of particular water type, DWVA or DWVB, resulting from each salinity category for the event. "Overall mean" combines model results for both DWVA and DWVB from all salinity categories into one event-wide value for each specific model. For comparison purposes, Cavalieri and Martin obtained a "overall mean" dense water production rate of 0.017 Sv +/- 0.01 Sv.

	PM/CMD MODEL			CW2/CMD MODEL			CMI/CMD MODEL		
Salinity	Min	Int	Max	Min	Int	Max	Min	Int	Max
Dense Water A (Sv)	n/a	0.0087 0.0127 0.0207	0.0135 0.0142 0.0377	n/a	0.0058 0.0084 0.0131	0.0090 0.0134 0.0239	n/a	0.0071 0.0120 0.0232	0.0110 0.0192 0.0421
Event Mean (Sv)	n/a	0.0140	0.0218	n/a	0.0091	0.0154	n/a	0.0140	0.0240
Std Dev (Sv)	n/a	0.0061	0.0138	n/a	0.0037	0.0076	n/a	0.0080	0.0160
Dense Water B (Sv)	0.0075 0.0091 0.0148	0.0099 0.0150 0.0278	0.0101 0.0152 0.0282	0.0049 0.0060 0.0094	0.0066 0.0099 0.0176	0.0067 0.0100 0.0179	0.0061 0.0086 0.0165	0.0080 0.0142 0.0310	0.0082 0.0144 0.0315
Event Mean (Sv)	0.0105	0.0175	0.0178	0.0068	0.0113	0.0116	0.0100	0.0180	0.0180
Std Dev (Sv)	0.0038	0.0092	0.0093	0.0023	0.0057	0.0057	0.0050	0.0120	0.0120
Overall Mean & Std Dev (Sv)	0.016 Sv +/- 0.009 Sv			0.011 Sv +/- 0.003 Sv			0.016 Sv +/- 0.005 Sv		

mixes with water at the halocline mean salinity resulting in a volume "B" of halocline water, ***HWVB***, produced being calculated as:

$$HWVB = \frac{S_{flux}}{\rho_{32.85}\ S_{32.85} - \rho_w\ S_w} \tag{5.12}$$

where ρ_w is the density of the original sea water; S_w is the original sea water salinity, and S_{flux} is the salt flux generated at the polynya.

Results from my ice production and dense water production calculations summarized in Tables 5.4-5.8 show that the dense water production rates range from 0.0058Sv to 0.0421Sv, depending on initial salinity level, salinity enhancement, area of polynya, and ice production converted to ice volume. The largest production rates were always obtained in the maximum salinity category. Tables 5.7 and 5.8 show that DWVB was larger than DWVA in the intermediate salinity category, but DWVB was smaller than DWVA in the maximum salinity category. However, this was not true of halocline water production rates where results shown in Table 5.7 indicate that HWVA is larger than HWVB in both the maximum and intermediate salinity categories. In general, the highest rates of dense water and halocline water production were obtained for February 27, 1992, again reflecting the large heat fluxes, high ice production rates, and large polynya sector area on that date. From Table 5.8, it is apparent that the PM/CMD model combination provided the largest dense water production rates and also, the largest halocline water production rates while the CW2/CMD rates were lowest. Despite the obvious shortcomings of all the models used to obtain dense water production and halocline production rates, I would suggest that the PM/CMD model is a good initial approach to obtaining estimates of these rates. It can, however, be improved upon by the CMI/CMD model, and the CW2/CMD model has the most potential for reasonable estimates of production rates.

5.6 Discussion

I used four different methods to estimate heat fluxes at the SLIP, and three methods to calculate the ice and dense water production rates associated with the February 1992 southern SLIP. My results indicate that polynya energy balance-based production calculations are highly dependent on model treatment of the ice production. In two of the models, PM and CMI, the ice production rate was determined entirely from the net daily flux, F_{net}, shown in Table 5.9. Average CMI and PM results show that open water F_{net}

Table 5.9: SLIP Heat Flux Summary. Compared here are heat flux results obtained for the SLIP from the PM (Pease, 1987), CMI (Cavalieri and Martin, 1994) using SAR/AVHRR imagery, and the CW2 (Wade, 1993) ice growth models. In all cases, negative flux indicates energy transfer from ocean to atmosphere. PM and CMI rates are based on open water flux calculations, while CW2 incorporates fluxes that vary in response to ice growth throughout the 24 hour period. Net heat flux is near or equal to zero for the CW2 energy balance due to the model's method of calculating the energy balance (Wade, 1993). CW2 values are shown as "first time step" and "after 24 hour" flux values. Bold date/data rows correspond to the time periods of the ARCSyM simulated flux fields discussed in the text.

DATE 1992	CW2 TURBULENT FLUXES ($W\ m^{-2}$) ½ hour	24 hour	CMI TURBULENT HEAT FLUX ($W\ m^{-2}$)	PM TURBULENT HEAT FLUX ($W\ m^{-2}$)	CMI NET HEAT FLUX ($W\ m^{-2}$)	PM NET HEAT FLUX ($W\ m^{-2}$)
February 18	-394.5	-130.2	-375.8	-377.7	-402.4	-420.7
19	-342.9	-112.4	-328.4	-327.4	-345.5	-363.3
20	-141.5	-130.0	-116.5	-114.0	-149.5	-153.0
21	-302.6	-133.5	-295.5	-298.6	-316.5	-391.7
22	-362.9	-140.4	-371.6	-374.0	-392.8	-435.6
23	-328.8	-115.5	-323.9	-323.9	-356.3	-377.6
24	**-343.5**	**-125.2**	**-335.3**	**-334.8**	**-377.7**	**-381.2**
25	**-286.6**	**-150.5**	**-264.3**	**-266.3**	**-295.6**	**-313.4**
26	-403.7	-151.6	-416.0	-412.2	-442.3	-463.7
27	**-522.6**	**-162.1**	**-574.8**	**-575.8**	**-476.1**	**-517.2**
28	**-540.7**	**-165.3**	**-610.7**	**-609.6**	**-589.4**	**-671.1**
29	-318.3	-150.3	-321.7	-328.9	-352.4	-405.8
March 1	-298.1	-158.1	-301.5	-298.8	-377.0	-368.9
MEAN	-352.8	-140.4	-356.6	-357.1	-374.9	-404.9
STD DEV	102.1	17.4	126.7	126.7	101.7	117.1
RANGE	-141.5 to-522.6	-112.4 to -165.3	-116.5 to -610.7	-114.0 to 609.6	-149.5 to -589.4	-153.0 to -671.1

Table 5.10: SLIP Ice Production Summary. Compared here are ice production results obtained for the SLIP from the PM (Pease, 1987), CM (Cavalieri and Martin, 1994) using SAR/AVHRR imagery, and the CW2 (Wade, 1993) ice growth models. PM and CM rates are based on open water flux calculations, while CW2 incorporates fluxes that vary in response to ice growth throughout the 24 hour period.

DATE 1992	PM ICE PRODUCTION (cm day^{-1})	CMI SAR/AVHRR ICE PRODUCTION (cm day^{-1})	CW2 ICE PRODUCTION (cm day^{-1})
February 18	11.5	11.0	7.4
19	10.2	9.7	6.7
20	4.3	4.2	4.7
21	9.9	8.9	7.3
22	12.2	11.0	7.7
23	10.6	10.0	7.2
24	10.7	10.6	7.1
25	8.8	8.3	6.9
26	13.0	12.4	8.2
27	17.6	16.2	9.2
28	18.9	16.6	9.5
29	11.4	9.9	7.7
March 1	10.4	9.5	7.6
MEAN	11.5	10.6	7.5
STD DEV	3.7	3.2	1.2
RANGE	4.3 to 18.9	4.2 to 16.6	4.7 to 9.5

values ranged from -398 to -405W m^{-2}. In general, as shown in Table 5.10, the PM model produced slightly larger ice production rates than CMI, averaging 12cm day^{-1} over the study period as compared to 11cm day^{-1} for the CMI. Both models showed a decrease in ice production rates from February 18-20, a large jump of ~2cm day^{-1} in production rate from February 21 to 22, and then a fairly stable period through February 24. After declining on February 25, the ice production rates climbed to maximums of 17cm day^{-1} to 19cm day^{-1} on February 28 (Table 5.10). While the higher ice production rates and fluxes on February 27 and February 28 rather than on February 24 may seem strange, in light of the polynya development observed in the SAR imagery during this event, it can be explained. February 27 and February 28 were much colder than February 24 and so more heat energy was lost to the atmosphere from the ocean on February 27 and February 28, assuming open water initial conditions.

To properly model the thermodynamic processes in a polynya region, an energy balance model must be able to account for the effect of mixed phase open water and ice situations as well as that of ice formation on heat transfer processes. In short, without *in situ* observations, models like the CW2 (Wade, 1993) which incorporate an "ice memory" become quite useful tools, even more so if a realistic dynamic component were to be added in future versions. All heat fluxes were calculated rather than specified in the CW2. Latent and sensible heat fluxes were determined separately, as part of the energy balance equation solution, rather than as a single representative term. For example, on February 24, 1992, the initial model ice growth was 0.7cm with associated latent and sensible heat fluxes of -124W m^{-2} and -220W m^{-2}, respectively. After 24 hours, this model had grown 7 cm of ice (Table 5.3). The latent and sensible heat fluxes associated with this thickness of ice were -48 and -77W m^{-2}, respectively, representing a drop of 35-40% in heat flux over 24 hours. This drop was not reflected in the PM or CMI models. The CW2 (Table 5.3, 5.9-10) produced lower ice production rates than the other two models as direct result of its "ice growth memory" and more complex flux parameterizations.

The only direct means of comparing heat fluxes between the three models is to look at the differences between the turbulent heat flux (e.g., turbulent for CM and PM vs. latent plus sensible for CW2) terms obtained from all three models (Table 5.9). In all cases, CW2 F_{sens} was lower than the turbulent flux, F_{turb}, from PM and CM. However, when CW2 F_{latent} is added to CW2 F_{sens}, the combined value falls between the other models' F_{turb} and F_{net} for the period of February 18-24. After February 24, the combined CW2 value is less than F_{turb} of the other models. These differences suggest that perhaps the latent heat magnitude is

not insignificant with respect to sensible heat in the case of the SLIP, and also, that the characterization of the sensible heat transfer coefficient in all three models needs further consideration.

My average CW2 latent and sensible heat estimates from the initial time step of -120W m^{-2} and -232.7W m^{-2}, and my average PM (CM) turbulent heat flux estimate of 357.7W m^{-2}, compare fairly well with previously observed heat fluxes measured during aircraft flights over the SLIP (Pease, 1987; Walter, 1989). In 1983, sensible heat was measured to be -334W m^{-2} over the SLIP while latent heat was -78 to -85W m^{-2} (net=-419 W m^{-2}; Walter, 1989). In 1985, sensible heat was -150W m^{-2} while latent heat was -42 W m^{-2} (net=-192W m^{-2}; Walter, 1989). Based on observation and calculation, Schumacher et al. (1983) estimated that the net heat loss to the atmosphere over active ice formation areas at St. Lawrence Island in Winter 1981 was about -535W m^{-2}. Walter (1989) observed that heat fluxes can become much higher in areas such as the lee of the hills along the southwestern coast of St. Lawrence Island, where ice is forming rapidly, yet being swept away from the coast almost immediately. Sensible heat fluxes may reach -1000W m^{-2} or more in these warm pockets (Walter, 1989). Maykut (1978) suggested that sensible and latent heat fluxes over open water in a high arctic environment may be -575 and -147 W m^{-2}, or greater, respectively. My CW2 sensible heat values fall within the previously-observed range at the SLIP, but my CW2 latent heat values are more representative of the high Arctic environment. My PM and CMI F_{turb} are slightly high based on the 1983 and 1985 SLIP observations. However, they are well below the "warm pocket" value of up to -1000W m^{-2} suggested by Walter (1989). As net heat loss to the atmosphere becomes balanced by the ice formation rate at the polynya, observed heat fluxes can become greatly reduced (e.g., ~5cm of ice cover leads to ~ 50% flux reduction, Maykut, 1978; see also Table 5.3). My CW2 results do show this reduction as the model heat fluxes are reduced 35-40% in magnitude after formation of 7cm of ice. Again, the PM and CMI models are not capable of accounting for this reduction. The differences in heat flux magnitude between the previously observed SLIP events and my CW2 results, for the February 1992 southern SLIP discussed here, are attributable to differences in ice thickness and ice concentration in the various events, as well as to the CW2 model's flux parameterizations.

Results from Schumacher et al. (1983) indicate that ice growth rates associated with new ice formation at the February 1983 SLIP were 0.17m day^{-1} leading to a total winter growth of 5m per unit area. Cavalieri and Martin (1994) calculated a total winter growth of 6.2m of ice at the SLIP in 1988. My CW2, PM, and CMI results indicate the

potential for 2.7m, 4.2m, and 3.9m of ice per unit area, respectively, if one extends the rates over the same period of time as in Schumacher et al. (1983) and Cavalieri and Martin (1994). Overall, my CW2 ice production rates (Table 5.10) did not show as wide a range of ice production values as the other two models (Table 5.10) but all three models showed the largest rates on February 27 and February 28, a period of somewhat lower wind speeds and extremely cold air temperatures. Given the observations discussed above and taking into account the limitations of the models, my calculated fluxes and ice production rates appear reasonable.

The SLIP and other polynyas observed around the perimeter of the Arctic Ocean have been suggested to be important sites for production of the dense (cold, high salinity) water required for the maintenance of the Arctic Ocean halocline. Cavalieri and Martin's (1994) calculations estimated that arctic polynyas produced dense water at a rate of 0.9Sv with a range of 0.7-1.2Sv. In applying the CMI/CMD dense water/halocline water production model to my SAR/AVHRR derived polynya areas, instead of using SMMR-based "polynya boxes", I obtained an average dense water production of 0.016Sv, based on intermediate ambient salinity and my ice production rates for the February 1992 southern SLIP event (Table 5.11).

The range of dense water production rates resulting from my SAR/AVHRR version is 0.006 to 0.042Sv (see Tables 5.4 -5.8; 5.11). Results using my PM ice production rates in the CMD dense water algorithm were only slightly larger (i.e., the difference is in the fourth decimal place) than those obtained using my CMI ice production rates (Table 5.11). This is not surprising as the PM ice production rates were 7% larger than the CMI's rates. Using an average turbulent heat flux term of F_{latent} plus F_{sens} from the CW2 first time step and my ice production rates obtained from the CW2 as input for the CMD dense water algorithm, I obtained a somewhat smaller dense water production of 0.011Sv (Table 5.11). This decrease in dense water production rate is reflective of the lower ice production rates obtained from the CW2.

As mentioned above, Cavalieri and Martin (1994) estimated that the average annual dense water flux from the western Arctic polynyas is 0.51Sv +/- .2Sv. Of this amount, the Bering Sea polynyas' contribution was estimated to be 0.059Sv or just over 11%. Cavalieri and Martin (1994) also estimated that the SLIP's dense water production

Table 5.11 (a): SLIP Dense Water Production. Shown here is a comparison of SLIP dense water production results obtained in this current study (CM ice production and dense water production model with ERS-1 SAR and AVHRR polynya measurements) and those obtained in a similar earlier study (CM model with SMMR-based polynya boxes; Cavalieri and Martin, 1994) of the SLIP's dense water production. See text and Tables 5.4-5.7 for salinity category details.

SALINITY CATEGORY	CAVALIERI AND MARTIN (1994) DENSE WATER PRODUCTION (Nine Year Average:1981-1988)	FEBRUARY 1992 SOUTHERN SLIP EVENT CMI/CMD DENSE WATER PRODUCTION (Nine Day Event: February 21-March 1, 1992)
Minimum Salinity	0.0078 Sv	0.0104 +/- 0.005 Sv
Intermediate Salinity	0.0155	0.0159 +/- 0.003
Maximum Salinity	0.0278	0.0210 +/- 0.004
AVERAGE	**0.0170 Sv +/-0.01**	**0.0157 +/- 0.005 Sv**

Table 5.11(b): Potential SLIP Dense Water Contribution to Arctic Halocline. Ice production rates and dense water production are summarized for the February 1992 southern SLIP event. The dense water production model of CM (Cavalieri and Martin, 1994) was applied to ice production rates obtained from the PM, CM, and CW2 models to determined dense water production for this SLIP event. CM Historical is the results of Cavalieri and Martin's (1994) efforts using SMMR polynya boxes and a SLIP event from an earlier year. "Percent of Bering Sea Contribution" is the percentage of the Bering Sea polynyas' dense water contribution to the Arctic halocline attributable to this SLIP event. "Percent of Western Arctic Contribution" is the percentage of the western Arctic region's dense water contribution to the Arctic halocline attributable to the SLIP, based on estimates presented in this chapter. "Percent of Entire Arctic Contribution" is SLIP's % of the entire Arctic contribution. CM dense water production breakdown by salinity category for the February 1992 southern SLIP is shown above in Table 5.10a.

MODEL	AVERAGE ICE PRODUCTION ($cm\ day^{-1}$)	AVERAGE DENSE WATER PRODUCTION (Sv)	PERCENT OF BERING SEA CONTRIBUTION (%)	PERCENT OF WESTERN ARCTIC CONTRIBUTION (%)	PERCENT OF ENTIRE ARCTIC CONTRIBUTION (%)
PM	11.5	0.016 +/- 0.009	~27	~3.0	**~1.6**
CMI/CMD	10.6	0.016 +/- 0.005	~27	~3.0	**~1.6**
CW2	7.5	0.011 +/- 0.003	~19	~2.1	**~1.1**
CM Historical	-	0.017 +/- 0.01	~29	~3.3	**~1.7**

rate was 0.017Sv ± 0.01Sv. or 29% of the Bering Sea's total. My CMI/CMD dense water production rate of 0.016Sv ± 0.005Sv (±0.009Sv for PM/CMD model). obtained based on SAR/AVHRR areas for one particular SLIP event, turned out to be nearly identical to that of Cavalieri and Martin (1994), while my CW2/CMD result of 0.011Sv ± 0.003Sv was smaller. It is, however. important to note several points:

a) The CM data (1994) are a set of nine year means (1978-1987) based on a period of winter days when open water was observed. while my SAR/AVHRR data cover a period of nine days in late February 1992. Thus, my individual event is not necessarily fully representative of all polynya events, even those within the same season.

b) The variability in my dense water production rates during this SLIP event shows that more consideration should be given to "within event" production variability when estimating the event total dense water production.

c) My polynya areas were obtained from relatively high resolution imagery spaced three days apart in time. while the SMMR boxes reflected coarser spatial resolution (100m SAR pixel size vs. 25 km SMMR pixel size) and daily coverage of the SLIP.

d) The CMI model is very simplistic in its heat budget to ice production calculation. A model similar to the CW2, or an improved ARCSyM. run over the entire event period should produce more realistic results.

Despite these limitations, I think that my calculations provide estimates of the correct magnitude. My results (Table 5.11) suggest that the February 1992 southern SLIP event had the potential to produce dense water at a rate that might account for ~2-3% of the western Arctic's annual contribution to maintenance of the Arctic Ocean halocline, and therefore, ~1-2% of the entire Arctic's annual contribution. The implications of my results and potential impacts of variations in the SLIP, itself, are explored in broad terms in the next chapter.

CHAPTER 6: DISCUSSION

In this dissertation, I have used a combination of satellite imagery, meteorological observations, and models to investigate the ice circulation, heat fluxes, ice production and brine production rates associated with the SLIP. I have also used observations in combination with a high-resolution climate system model simulation of the SLIP to investigate the polynya's regional effects, and the potential impact of incorporating the effects of polynyas into larger scale climate system models. In this final chapter, I revisit my hypotheses in the context of my results summarized in Table 6.1 as a means of discussing what I consider to be the contributions and implications of my research. I close the chapter with suggestions for future work.

6.1 Ice Circulation: The SLIP is a wind-driven event, but the ocean also plays an important role in determining the ice circulation associated with the SLIP. Bering Sea pack ice moves generally southward during the winter but its extent is limited by warm Pacific Ocean waters. However, there are periods such as during early February 1992 and late February-early March 1992 when the southward drift of ice is slowed or even reversed locally.

I have shown the effects of local wind directions, ocean circulation, and island topography for three separate SLIP events along St. Lawrence Island's southern coast and for one northern coast polynya. Using SAR imagery and ice motion products, I found that ice circulation in the SLIP does not always follow the free drift theory for ice. Ice motion along the SLIP's outer boundary was variable in speed and direction unless north/ northeasterly or southerly winds prevailed for an extended period of time. Ice features associated with polynya development moved nearly parallel to the wind at 3-4% of the wind speed for wind >7m s^{-1}, contrary to the "free drift" concept. For northerly-northeasterly wind of <7m s^{-1}, ice moved at 2-4% of the wind speed with a drift angle ranging from 48° to the left of the wind to 53° to the right of the wind. The "rightward" deflection is consistent with the "free-drift" concept but the "leftward" deflection is not. Ice speeds for areas surrounding the SLIP were large (34+cm s^{-1}) and were a principal reason why the February southern SLIP expanded to its large extent in such a short period of time. Unfortunately, even during periods of persistent north/northeasterly winds, ice motion vectors products

Table 6.1 February 1992 Southern SLIP Event. A summary of all of present study results is compared with historical information. References to historical and other data are given as the second line of information in the box. Reference Key: GC91-Grebmeier and Cooper (1991); CM94-Cavalieri and Martin (1994); CM95-Comiso and Massom (1995); W89-Walter (1989); S83-Schumacher et al. (1983). Note: Prior research has indicated that turbulent fluxes over open water can be in excess of -1000 W m^{-2}. In this table, I have used actual field data from SLIP events in the early 1980's to represent a range of turbulent fluxes previously observed at the SLIP. Split cell columns are used when giving information specifically for the February 24-27 and 27-March 1 periods. All other numbers reflect event ranges or averages. CW2/CMD turbulent flux is for 1st time step and also for 24 hours. The PM and CW2 fluxes were incorporated into the CMD to obtain dense water production estimates for PM and CW2 models. (Note: Dense water production range for the entire February 1992 SLIP event is presented in Tables 5.10 & 11).

	SLIP Size (km offshore)	Ice Concentration (% ice)	Surface Temperature (°C)	Polynya Shape	Wind Speed ($m\ s^{-1}$)	Ice Motion ($m\ s^{-1}$)	Turbulent Flux ($W\ m^{-2}$)	Ice Growth ($cm\ day^{-1}$)	Dense Water Production (Sv)
Historical	20 to 40 GC91	variable	-2 to -9 CM95; W89	bowl/plume	n/a	2-3% of wind	-150 to -419 W89	~17 S83	0.017+/-0.01 CM94
Present Study Observed	69	~70-80% ice SSMI imagery	-5 to -9 SAR/AVHRR	bowl | 2 lobe	11 | 6.8	0.33 3% | 0.22 3.2%	n/a	n/a	n/a
Analytical Model									
PM/CMD	16 to 21	n/a	n/a	n/a	n/a	n/a	-114 to -610	4.3 to 18.9	0.017+/-.009
CM/CMD	n/a	n/a	n/a	n/a	n/a	n/a	-117 to -611	4.2 to 16.6	0.016+/-.005
Numerical Model									
CW2/CMD	n/a	n/a	n/a	n/a	n/a	n/a	-142 to -523 -112 to -165	4.7 to 9.5	0.011+/-.003
Climate System Model									
ARCSyM "Swamp"	91 to 140 to 210	large area of low ice concentration 0 to 75 % ice	2-3 warmer than observed; sharp gradient	square | bowl w/ 2 lobes	10.6 | weak	0.35 3.3% | 0.05	-110 to -130	n/a	n/a
ARCSyM "Barotropic"	70 to 70 to 140	reduced area of low ice concentration	1-2 > obs. "smoother" gradient	long bowl | plume w/ 2 lobes	10.6 | weak	0.29 2.7% | 0.27 2.6%	-80 to -200	n/a	n/a

within the polynya were scarce due to the highly dynamic, short-lived nature of the ice and the subgrid (vector grid=5km x 5km) scale of the ice features.

Combined, SAR and AVHRR imagery allowed me to track polynya development with detail that could not normally be achieved using the individual forms of remotely-sensed data because of the lack of image resolution, narrow swath width, and inherent winter darkness or cloudiness. In short, I was able to observe a polynya's life cycle through ice motion vectors and corresponding imagery. My observations indicate that the recurrent polynya boundaries are very sensitive to short-lived variations in atmospheric forcing. Local wind fluctuations affecting polynya development are, in turn, dependent on the position, intensity, and track of individual storm systems as the March southern event showed. In the early February case, the southern polynya closed completely as winds became southerly, and a northern polynya opened within a period of ~3-6 days. I also showed that the February southern SLIP polynya development began within 3 days of the onset of prevailing northerly winds. My satellite-based measurement of SLIP development showed a polynya region expansion of 165km over ~ 6 days. In contrast, brief periods of southerly winds during the period of February 27-March 1 caused the southern polynya to slow its expansion considerably. Additional observations indicated that the pack ice pushed inward on the polynya boundary from the west when winds weakened rapidly for a day or more. This inward motion during periods of weak winds is most likely due to ocean forcing associated with the northeastward flow in Anadyr Strait. I suspect that the polynya region's thinner ice and low ice concentration is what made it possible for the pack ice along the polynya's western boundary to easily compress the polynya inward under the given wind conditions.

SAR and AVHRR observations revealed that the shape and extent of the polynya reflected the island topography, especially the widest area of the polynya located adjacent to the coast. The east-west orientation of the coastline allows wind to blow offshore over a broad area in the preferred direction of ice flow (away from a fixed boundary) for polynya formation. A long single (or double-tailed) lobe-shaped polynya was observed to develop over time. The shape was due, at least in part, to the ice's response to variations in wind intensity resulting from the island's channeling effect on the surface level wind field. Although I was unaware of his concurrent modeling efforts, Darby (1996) also notes a polynya shape-island geography relationship. The ice pattern within the polynya, especially the banding visible on February 27, also seemed to indicate a response to wind pulses and/or diurnal tides as the ice velocity observed and the size of the bands seem to fit

what would be expected for a diurnal cycling. In successfully using the ARCSyM regional-scale climate model to simulate the SLIP, I also showed that the addition of ocean current, although primitive in my experiments, improved the shape and extent of the polynya. Therefore, I suggest that the polynya is ocean-driven as well as wind-driven, and that polynya shape cannot be considered independent of the shape and orientation of its bounding coastline.

6.2 Heat Fluxes: The SLIP is a source of sensible and latent heat flux that affects the local atmosphere and the surrounding area. Identification of open water and thin ice areas in the SLIP is crucial for the measurement of the polynya's size, as well as for determination of ice and dense water production, because heat fluxes from open water to the atmosphere differ dramatically from those through an ice cover. SAR and AVHRR, together, allowed me to define areas of the polynya that were most likely to contain open water so that I could use these areas in heat flux calculations (PM, CMI/CMD, CW2 models). Prior to this, heat flux calculations were based on coarse resolution satellite imagery or extremely limited aircraft reconnaissance. My refinement is another step towards actually being able to distinguish between polynya area's ice-open water sectors for heat flux calculation purposes. Even so, despite the high speed of ice moving offshore during polynya development, little open water was actually observed within the polynya region. This ice-water distinction is obviously critical for realistic calculation results. For example, my CW2 results show that heat flux dropped 40% by the time that 7cm of ice had grown, indicating the large effect of just a small thickness of ice.

My SAR/AVHRR graphical combination did allow me to observe broad boundaries between ice and ice-water mix areas within the polynya so that I could then estimate the areas of the ice and open water sectors. For instance, I was able to detect a distinctly warm region off Southwest Cape on the southern side of St. Lawrence Island during the February 1992 southern event. Walter (1989) had also observed large heat fluxes in this area in the early 1980's. My point-based calculations of energy fluxes at the SLIP and the few earlier results found in the literature confirm that conditions at the SLIP were conducive to large energy fluxes being observed. Despite shortcomings in simulation of open water area, my ARCSyM fields also indicate that the SLIP is a site of extensive sensible and latent heat flux affecting the local atmosphere. Simulated fields of ice concentration and ice temperature concur with observational results in that the area of the simulated SLIP

having the lowest ice concentration and the highest temperatures was located off Southwest Cape.

Overall, my calculated heat flux values at the SLIP were lower than I had expected based on the open water heat fluxes observed by Walter (1989) in the 1980's and suggested by Maykut (date) for the Arctic. This was probably primarily due to the treatment and parameterizations of fluxes in the various models, although my selection of site data and choice of heat transfer coefficients also lead to uncertainty. In retrospect, I note that a possible shortcoming in my flux calculations could have been the use of Gambell meteorological data as my sole source of wind and temperature data as Gambell is located on the on the north side of the island, away from the southern polynya. As such, it might have been better to use a combination of Gambell data and gridpoint values over the SLIP to interpolate data for the southern coast of the island. Nevertheless, Gambell was within the 50km range shown to be impacted by the ARCSyM simulated polynya and it was the only available meteorological station data for the island. Magnitudes shown in the simulated flux fields are also suspect, due to the model's problem with excess open water, but the trends exhibited in the simulation fields are in agreement with those expected during polynya development.

6.3 Dense Water Production: The polynyas of the Bering Sea are thought to be responsible for most of the ice and dense water produced in the Bering Sea. The SLIP is the second largest polynya in the Bering Sea region and is considered to be a site of significant brine production. Based on my work, the February 1992 southern SLIP had the potential to produce 7-17cm day^{-1} of ice when calculations started from an open water or near open water (0.7cm thickness) situation. Based on my calculated ice production rates from SLIP area measurements, this SLIP was capable of producing a volume of ice of 0.1-0.157km^3 day^{-1} over the 9 day event period or an event total of nearly 1.5km^3 of ice. By comparison, the Anadyr polynya, the largest Bering Sea polynya, is capable of producing 11 km^3 of ice in an event (Cavalieri and Martin, 1994). The range of ice production and dense water production I obtained exceeds that of Cavalieri and Martin (1994), in part, because I also used the CW2 model to obtain fluxes and ice production rates. This CW2 model is more sophisticated than the CMI/CMD combination in the way it handles variations in the fluxes and ice growth, although, the CW2 also has shortcomings as were discussed in Chapters 4 and 5. As ice and dense water production are derived directly from heat fluxes in all of my chosen methods, the method of calculating day to day fluxes is extremely

critical to determining realistic ice and dense water production rates. It is difficult to assess the relative production contributions of the polynyas to the overall "picture" without heat fluxes that reflect at least day to day changes in the ice growth.

According to Cavalieri and Martin (1994), the polynyas of the Western Arctic account for over half of the dense water production that enters the Arctic Ocean halocline. The vast size of the Anadyr polynya makes it difficult for other Bering Sea polynyas to be recognized as significant dense water production sites, regardless of their initial ambient salinities or ice production and dense water production rates. However, of the overall western Arctic's contribution of dense water to the Arctic Halocline, the Bering Sea accounts for ~11%. According to my calculations, I find that the February 1992 southern SLIP had the potential to account for 19-27% percent of the Bering Sea's contribution. Based on my single event study. I found that this SLIP was capable of producing dense water at a rate that would lead to 2-3% of the Western Arctic's total contribution and about 1-2% of the total Arctic contribution.

6.4 Implications

Would the Arctic halocline be affected if the SLIP did not exist ? Possibly so, because models and observations show that the halocline requires ~1.2 Sv (Bjork, 1989) to maintain its present state. The SLIP does influence the density of the Bering Sea water that enters the Arctic Ocean. This water is also nutrient rich and therefore could also affect biogeochemical budgets of the Arctic Ocean.

On a regional basis, an important issue would be the geographic and temporal extent of the factor that caused the SLIP not to exist. For instance, a change in Aleutian Low structure and the Siberian high-Aleutian Low relationship certainly affected the atmospheric circulation over the Bering Sea several times during the 1991/1992 winter. January and March were characterized by a single Aleutian Low and southern SLIP events in the middle of the month. February's large southern SLIP event occurred late in the month after a dramatic switch in the atmospheric circulation. However, the only period in the 1992 winter to have strong enough "non-northerly" winds to completely close the large southern polynya and open a small northern SLIP also occurred during February, the only month with a split Aleutian Low mean pattern. As my work only deals with one season's events, it is difficult to speculate just how typical the observed response of polynya development (i.e., extent. shape. lifespan) to atmospheric circulation really is. Ocean-

atmosphere cause and effect relationships are still not well understood for the Bering Sea region and therefore, present a topic for additional in-depth research.

What would happen to the ice field of the Bering Sea if St. Lawrence Island didn't exist or if all of the Bering Sea polynyas were gone? The SLIP is driven by the local and large-scale atmospheric circulation as well as by the ocean circulation, and thus, the question is not easily answered. One might generalize these driving mechanisms to say that most latent heat polynyas are the direct result of these interactions and are part of a system of polynyas existing within the overall regional climate. My ARCSyM results show that the vertical extent of atmospheric warming and moistening due to the polynya's presence is at least to the 800mb level, over and downwind of the polynya to a distance of 50km. Based on my heat flux values and a chart of flux distribution downwind (Figure 5.3), the polynya's potential effect on the atmosphere could extend out to 600km, although the major effect would be within 150km of the polynya. Larger polynyas and areas with a concentration of large open leads will undoubtedly have a greater overall areal impact. This flux of heat and moisture is part of what makes the Bering Sea a transitional climate region, especially in winter, as it is not as extreme as the Arctic region nor as temperate as the North Pacific Ocean region. If the cause of the SLIP shutdown was a basin-wide phenomenon that also reduced the Anadyr polynya significantly, then in addition to decreased atmosphere and ocean energy fluxes, the Bering Sea dense water contribution to the Arctic would be much less.

Modeling details of a polynya such as the SLIP is a challenging task due to the spatial and temporal scale of the polynya event, and the scales of interactions between the polynya and the rest of the regional climate system components. However, obtaining basic information about a polynya is not so daunting. In my work I have shown and confirmed that simple models employing temperature and wind can give informative results about the SLIP that can be verified by satellite imagery. Both models and satellite observations are useful for creating long-term time series of polynya activity. For instance, all that is really required to run the PM model to obtain an estimate of potential polynya size is air temperature and wind speed. All three ice production models, the PM, CMI, and CW2 proved to be useful in determining local energy fluxes and ice production rates with a minimum of input information. The CW2 was able to take this idea further and give insight into the *changes* in fluxes and growth rates over time based on conditions associated with ice that had already "grown". Had a lengthy record of Gambell data been readily available for input to these models, I would have been able to calculate a lengthy time

series of "proxy" polynya offshore extent and broad estimates of ice and dense water production rates. Area, though, cannot be calculated unless one uses the length of the island coast as one dimension.

The more complex model that I used in my work, the ARCSyM, is certainly a step in the right direction as it provides a 3-dimensional look at polynya development and associated feedbacks over time. The complexity of the polynya's interactions is best simulated through the use of such a model, capable of incorporating all components of the physical climate system in an interactive or coupled manner. Models like this can derive more realistic results as the fields are interdependent. Despite the limitations of the early developmental version of the ARCSyM model I used, the model was capable of providing information that was verifiable to a certain extent. The valuable information showed how the polynya "fit into" the surrounding region in terms of the changes in 3-dimensional energy fluxes, ice circulation variability, simple ocean circulation influence, and polynya development (shape and extent) associated with model-derived changes in forcing over time. If my SLIP results hold true for other similar polynyas in the Bering Sea, the impact of polynyas, in general, on regional scale climate may indeed be large enough to warrant consideration of the combined effect of all polynyas in larger-scale models.

6.5 Future Work and Concluding Statements

While *in situ* data always have the greatest appeal, the ability to gain useful information remotely or by simulation is important for those whose resources limit fieldwork, or for those studying phenomena at inhospitable places such as the SLIP region. Creation of the experimental GPS ice motion products and my analyses of these products showed the potential for remote monitoring of ice circulation in the Bering Sea at high resolution. GPS processing has met with great success in the Arctic where the ice motion is not as extensive or as variable as ice motion in the Bering Sea. Maps of Arctic ice circulation have already been created for the Beaufort Sea by Thorndike and Kwok (personal communication). Despite this, the first generation ERS-1 GPS system I worked with is no longer operating. It has been replaced by the newly-commissioned Radarsat GPS which has drawn from the lessons learned with the first generation GPS's and has the potential to produce much higher quality ice motion fields. As of my writing, RADARSAT ice circulation data have yet to be formally released for the Bering Sea or the Arctic. It is possible that GPS ice motion product representation of the complex motions associated with polynya development and the seasonal pack as a whole may never be attained for the

Bering Sea region. However, perhaps maps of the entire Bering Sea's ice circulation can be produced in the future. As the Arctic maps have, Bering Sea maps could potentially provide new information about ice transport, ocean surface circulation, and atmospheric circulation on a basin-wide scale.

All three of the analytical models used here would greatly benefit from expansion into two spatial (i.e., east-west and north-south extents) dimensions, in addition to the existing dimensions of time and ice growth rate, so that computations could more realistically reflect the distribution of differing ice growth rates over the polynya area. For example, by simply combining the PM polynya size model and the CW2 model, one might be able to account for multiple ice growth rates and changes in energy fluxes as the polynya expands and ice forms and then thickens over time downstream. To do this, one might use the PM model to make a polynya of size A in t hours. The CW2 model would be used to grow ice at some average rate for the same t hours. The PM model would move this new ice offshore as the polynya expands. The CW2 would concurrently grow new ice in the newly expanded area, but continue to grow the older ice and reflect its energy fluxes as well. The PM/CW2 process would be stopped once the polynya reaches it maximum extent as determined from the PM model. Addition of wind directional data could guide the polynya development by indicating the time of wind shift occurrences that would affect polynya expansion. Additional satellite observations from SAR, or a combination of several types of satellite data, could refine these models to include the polynya area, as well as timing of the observed polynya opening and closing. This type of experiment would undoubtedly provide a more refined view of the fluxes and ice production associated with the SLIP. With the refined results in hand, the CMD model could then be applied to the situation to obtain a more representative estimate of the dense water production at the SLIP. In addition, if the CW2 brine rejection model was fully-developed, it, too, could provide an estimate of brine rejection as ice was formed and aged within the polynya. CW2 results could then also be converted to dense water and halocline water production estimates for the SLIP using a CMD-type model.

Future efforts should also focus on refining ice/open water classification, heat flux and brine flux calculation techniques, and determining dense water transport paths based on field and remote observation. Surface albedo changes due to increased ice cover and the addition of snow to that ice cover have great impact on the energy balance of a region. Although extremely difficult to obtain without *in situ* observations, a proper parameterization of snow for use in polynya simulation experiments would certainly be

advantageous for future energy budget work. Ice thickness and areal coverage changes driven by ice-ocean-atmosphere interaction are also extremely important factors to consider in energy balance approaches.

Current techniques for computing dense water production at polynyas (Cavalieri and Martin, 1994; Gawarkiewicz and Chapman, 1995; and Chapman and Gawarkiewicz, 1997) still need to be verified by *in situ* observation. Should the entire polynya region be taken into account in dense water production calculations or just the most active sector ? What effect does the depth of the shelf have on dense water production ? What is the time frame for dense water production and what is the transport mechanism for getting the brine from the newly-forming ice in the polynyas into the Arctic Halocline layer ? Polynya observing or modeling techniques should also be continually updated as new data are acquired, and the updated techniques should also be applied to existing data in retrospective analyses.

A primary goal of any future work should be to create a comprehensive database of proxy and observed time series to further enhance our understanding of polynya processes. Advances in model development should draw from the advances in the observational record so that model validation, prediction, and assessment of the overall climate system becomes more reliable. The best combination of tools for studying the SLIP and other such polynyas would be: a multi-year time series of high resolution satellite imagery with ice typing and motion; an updated multi-year field data set for initial ground-truthing; and a regional climate system model combining a "realistic" baroclinic ocean, multi-phase, multi-type ice, and a regionally-representative atmosphere. Finally, to best study and predict the effects of the SLIP and other Bering Sea polynyas on the entire western Arctic, it would be most helpful to be able to nest these regional-scale components into a larger scale climate system model of the Arctic.

This dissertation has shown aspects of what can be learned about the SLIP today with *combinations* of the tools and techniques available now. Even more importantly, it provides additional insight into the polynya's characteristics, *i.e.*, ice circulation, polynya life cycle, heat fluxes, and dense water production potential. This work takes another step towards future prediction of polynya activity and the assessment of polynyas' effects on the regional climate system.

REFERENCES

Aagaard, K., J. H. Swift, and E. Carmack, Thermohaline circulation in the Arctic mediterranean seas, *J. Geophys. Res.*, 90, 4833-4846, 1985.

Aagaard, K., L. K. Coachman, and E. Carmack, On the halocline of the Arctic Ocean, *Deep Sea Research*, 28, 529-545, 1981.

Anderson, D. L., Growth rate of sea ice, *J. Glaciol.*, 3,1170-1172, 1961.

Anderson, D. L., Physical properties of snow and sea ice, *USAF Cambridge Center, GRD Research Notes*, 29, December 1959, 136-140, 1959.

Andreas, E. L. and B. Murphy, Bulk transfer coefficients for heat and momentum over leads and polynyas, *J. Phys. Oceanogr.*, 16(11), 1875-1883, 1986.

Anthes, R. A., E. Y. Hsie and Y. H. Kuo, Description of the Penn State/NCAR Mesoscale Model Version 4 (MM4). *NCAR Tech Note, NCAR/TN-282+STR*, 1987.

Bilello, M. A., Formation, growth, and decay of sea ice in the Canadian Arctic Archipelago. *Arctic*, 14(1), 3-24. 1961.

Bjork, G., A one dimensional time-dependent model for the vertical stratification of the upper Arctic Ocean, *J. Phys. Oceanog.*, 19, 52-67, 1989.

Bonbright, D. I., PODS SSM/I Functional Requirements (Version 1.0). *JPL Document 715-63 August 3, 1984*, NASA Jet Propulsion Lab, Pasadena, CA, 1984.

Briegleb, B. P., Delta-Eddington approximation for solar radiation in the NCAR Community Climate Model. *J.Geophys. Res.*, 97, 7603-7612, 1992a.

Briegleb, B. P., Longwave Band Model for Thermal Radiation in Climate Studies. *J.Geophys. Res.*, 97, 11,475-11,485, 1992b.

Brown, R. A., Ch. 1 Meteorology, in *Polar Oceanography, Part A: Physical Science*, ed. W. O. Smith, Academic Press, San Diego, 40, 1990.

Carmack, E. C., Ch. 4 Large-scale physical oceanography of polar oceans, in *Polar Oceanography, Part A: Physical Science*, ed. W. O. Smith, Academic Press, San Diego, 171-222, 1990.

Carsey, F. D., R. G. Barry, and W. F. Weeks, Chapter 1: Introduction, in *Microwave Remote Sensing of Sea Ice*, ed. F. D. Carsey, Geophysical Monograph 68, American Geophysical Union, Washington D.C., 1-7, 1992.

Carsey, F. D. and H. J. Zwally, Chapter 16 Remote Sensing as a research tool, in *Geophysics of Sea Ice*, ed. N. Untersteiner, Plenum Press,1021-1098, 1986.

Carsey, F. D. (ed.), *Microwave Remote Sensing of Sea Ice*, Geophysical Monograph 68.

American Geophysical Union. Washington D.C., 1992.

Cavalieri D. J. and S. Martin. The contribution of Alaskan, Siberian, and Canadian coastal polynyas to the cold halocline layer of the Arctic Ocean, *J. Geophys. Res.*, 18,342-18,362. 1994.

Cavalieri, D. J. and R. G. Onstott, Arctic coastal polynya observations with ERS-1 SAR and DMSP SSM/I. *in Proc. First ERS-1 Symposium: Space at the Service of our Environment, Cannes, France, 4-6 November 1992*, 295-299, 1992.

Cavalieri. D. J.. P. Gloersen. W. J. Campbell, Determination of sea ice parameters with the Nimbus 7 SMMR, *J. Geophys. Res.*, 89, 5355-5369, 1984.

Cavalieri. D. J., J. P. Crawford, M. R. Drinkwater, D. T. Eppler, L. D. Farmer, R. R. Jentz. and C. C. Wackerman. Aircraft active and passive microwave validation of sea ice concentration from the Defense Meteorological Satellite Program Special Sensor Microwave Imager, *J. Geophys. Res.*, 96. 21,989-22,008, 1991.

Chapman, D. C. and G. Gawarkiewicz, Shallow convection and buoyancy equilibration in an idealized coastal polynya, *J. Phys. Oceanog.*, 27, 555-566, 1997.

Coachman, L. K. and C. A. Barnes, The contribution of Bering Sea water to the Arctic Ocean. *Arctic*, 14, 147-161, 1961.

Colony, R. and A. S. Thorndike, Sea ice motion as a drunkard's walk, *J. Geophys. Res.*, 90. 965-974, 1985.

Cox, G. F. N. and W. F. Weeks. Equations for determining the gas and brine volumes in sea ice samples, *J. Glaciol.*. 29, 306-316, 1983.

Curlander, J. C.. B. Holt. K. J. Hussen, Determination of sea ice motion using digital SAR imagery. *IEEE J. Ocean. Eng.*, OE-10(4). 358-367. 1985.

Curry. J. A. and E. E. Ebert. Annual Cycle of Radiation Fluxes over the Arctic Ocean: Sensitivity to Cloud Optical Properties, *J. Climate*, 5, 1267-1280,1992.

DeSoto. Y., H. Tippens. T. Kotlarek, I. Hsu, *User's Guide, Alaska SAR Facility Archive and Catalog Subsystem JPL D-5496*, NASA Jet Propulsion Lab , Pasadena, CA. 1991.

Dickinson. R. E.. A. Henderson-Sellers and P. J. Kennedy. Biosphere-Atmosphere Transfer Scheme (BATS) version 1E as coupled to the NCAR Community Climate Model, *NCAR Tech. Note, NCAR/TN-387+STR*, 1993.

Darby, M. S., A. J. Willmott, and T. A. Somerville, On the influence of coastline orientation on the steady state width of a latent heat polynya. *J. Geophys. Res.*, 100 (C7), 13.625-13.633. 1995.

Ebert, E.. A pattern recognition technique for distinguishing surface and cloud types in

polar regions, *J. Appl. Meteor. Climatol.*, 26, 1412-1427, 1987.

European Space Agency (ESA), SAR Ice phase acquisition daily plots 27/12/1992-0/03/1992 North American Stations, prepared by ERS-1 Team, 12 March 1992, Issue 1.0, in *ERS-1 Phase B (Ice Phase) Catalogue and GAP Display 10 March 1992, Document ER-TN-EPO-GU-1015-1.0 Issue 1.0, Rev 1.0*, European Space Agency (contact Alaska SAR Facility, Fairbanks, Alaska 99775), 1992.

Flato, G. M., and W. D. Hibler III, Modeling pack ice as a cavitating fluid, *J. Phys. Oceanogr.*, 22, 626-651, 1992.

Gawarkiewicz, G. and D. C. Chapman, A numerical study of dense water formation and transport on a shallow, sloping continental shelf, *J. Geophys. Res.*, 100 (C3), 4489-4507, 1995.

Giorgi, F., M. R. Marinucci, and G. T. Bates, Development of a Second Generation Regional Climate Model (RegCM2), Part I: Boundary layer and radiative transfer processes, *Mon. Wea. Rev.*, 121, 2794-2813, 1993a.

Gloersen, P. and D. J. Cavalieri, Reduction of weather effects in the calculation of sea ice concentration from microwave radiance, *J. Geophys. Res.*, 91, 3913-3919, 1986.

Glueck, M. F., and J. E. Groves, Use of the HLS color model as a technique for combining AVHRR and ERS-1 SAR imagery to evaluate near-shore ice processes in the St. Lawrence Island polynya, *in Proceedings of the 3rd Circumpolar Symposium on Remote Sensing of the Arctic Environments, University of Alaska Fairbanks, May 16-20, 1994*, 25, 1994.

Goodrich, L. E., A one-dimensional numerical model for geothermal problems, *Technical Report 421*, National Research Council of Canada, Division of Building Research, 1974.

Haefliger, M., K. Steffen, and C. Fowler, AVHRR surface temperature and narrow-band albedo comparison with ground measurements for the Greenland ice sheet, *Ann. Glaciol.*, 17, 49-54, 1993.

Hansen, J., G. Russell, D. Rind, P. Stone, A. Lacis, S. Lebedeff, R. Ruedy, and L. Travis, Efficient three-dimensional global models for climate studies: models I and II, *Mon. Wea. Rev.*, 111, 609-662, 1983.

Hibler, W. D., III, A dynamic thermodynamic sea ice model, *J. Phys. Oceanog.*, 9, 815-846, 1979.

Hilland, J. E., T. Bicknell, C. L. Miller, Alaska synthetic aperture radar (SAR) facility data processing architecture IAF-91-155, presented at *the 42nd Congress of the International Astronautical Federation, October 5-11, 1991, Montreal, Canada*, 1991.

Holt, B., D.A. Rothrock, and R. Kwok, Determination of sea ice motion from satellite images, in *Microwave Remote Sensing of Sea Ice*, ed. F. D. Carsey, Geophysical Monograph 68, American Geophysical Union, Washington DC, 1-7, 1992.

Holton, J. R., *An introduction to dynamic meteorology*, 2nd Edition, Academic Press, New York, 1979.

Key, J. and M. Haefliger, Arctic ice surface temperature retrieval from AVHRR thermal channels, *J. Geophys. Res.*, 97(D5), 5885-5893, 1992.

Key, J., Cloud cover analysis with Arctic Advanced Very High Resolution Radiometer data 2. Classification with spectral and textural measures, *J. Geophys. Res.*, 95(D6), 7661-7675, 1990.

Kidwell, K., *NOAA Polar Orbiter data user's guide*, NOAA Natl. Satellite Data and Inf. Serv., Washington, D. C., 1991

Kim, Y. S., R. K. Moore, R. G. Onstott, and S. Gogineni, Towards identification of optimum radar parameters for sea ice monitoring, *J. Glaciol.*, 31 (109), 214-219, 1985.

Kozo, T. L., L. D. Farmer, J. P. Welsh, Wind-generated polynyas off the coasts of the Bering Sea islands, in *Sea Ice Properties and Processes, Proceedings of the W.F. Weeks Sea Ice Symposium, February 1990*, eds. S.F. Ackley and W.F. Weeks, CRREL Monograph 90-1, Hanover, New Hampshire, 126-132, 1990.

Kwok, R., D. A. Rothrock, H. L. Stern, and G. F. Cunningham, Determination of the age distribution of sea ice from langrangian observations of ice motion, *IEEE Trans. on Geosc. and Rem. Sens.*, 33(2), 392-400, 1995.

Kwok, R. and G. Cunningham, *Alaska SAR Facility Geophysical Processor System data user's handbook, version 2.0, JPL D-9526*, NASA Jet Propulsion Lab, Pasadena, CA, 1993.

Kwok, R., E. Rignot, B. Holt, and R. Onstott, An overview of the geophysical sea ice products generated at the Alaska SAR Facility, *J. Geophys. Res.*, 97 (C2), 2391-2402, 1991.

Kwok, R., J. C. Curlander, R. McConnell, and S. S. Pang, An ice-motion tracking system at the Alaska SAR Facility, *IEEE J. Ocean Eng.*, 15(1), 44-54, 1990.

Laevastu, T., Factors affecting the temperature of the surface layer of the sea, *Commentat. Phys. Math.*, 25, 1-36, 1960.

Lynch, A. H., M. F. Glueck, W. L. Chapman, D. A. Bailey, and J. E. Walsh, Remote sensing and climate modelling of the St. Lawrence Island polynya, *Tellus, 49A*, 277-297, 1997.

Lynch, A. H., W. Chapman, J. E. Walsh, and G. Weller, Development of a regional climate model of the western Arctic, *J. Climate*, 8, 1555-1570, 1995.

Manabe, S. and R. T. Wetherald, Large-scale changes of soil wetness enduced by an increase in atmospheric carbon dioxide, *J. Atmos. Sci.*, 44, 1211-1235, 1987.

Manabe, S. and R. T. Wetherald, The effects of doubling the CO2 concentration on the climate of a general circulation model, *J. Atmos. Sci.*, 32, 3-5, 1975.

Martin, S. and D. J. Cavalieri, Contributions of the Siberian shelf polynyas to the Arctic Ocean intermediate and deep water, J. Geophys. Res., 94, 12,725-12,738, 1989.

Martin, S. and P. Kaufman, A field laboratory study of wave damping by grease ice, *J. Glaciol.*, 27, 283-314, 1981.

Maslanik, J. and J. Key, Comparison and integration of ice-pack temperatures derived from AVHRR and passive microwave imagery, *Ann. of Glaciol.*, 17, 372-378, 1993.

Massom, R. A. and J. C. Comiso, The characterization of new sea ice formation and the determination of surface temperature using Advanced Very Resolution Radiometer data, *J. Geophys. Res.*, 99 (C3), 5201-5218, 1994.

Massom, R. A., Satellite Remote Sensing of Polar Regions, Applications, Limitations and Data Availability, (Belhaven Press, London), Lewis Publishers CRC Press, Florida, 1991.

Maxworthy, T. and S. Narimousa, Unsteady, turbulent convection into a homogeneous, rotating fluid with oceanographic applications, *J. Phys. Oceanog.*, 24(5), 865-887, 994.

Maykut, G., Energy exchange over young sea ice in the central Arctic, *J. Geophys. Res.*, 83, 3646-3658, 1978.

Maykut, G. A. and P. E. Church, Radiation climate of Barrow, Alaska, 1962-1966, *J. Appl. Meteorol.*, 12, 620-628, 1973.

Maykut, G. A. and N. Untersteiner, Some results from a time dependent thermodynamic model of sea ice, *J. Geophys. Res.*, 76(6), 1550-1575, 1971

McCandless, S. W., Jr. and S. A. Mango, The theory, design and application of space-based synthetic aperture radar, Volumes 1 and 2, *unpublished lecture notes from short course given at the Alaska SAR Facility, Geophysical Institute, University of Alaska Fairbanks, Alaska, November 1990*, 1990.

McMillan, L. M. and D. B. Crosby, Theory and validation of the multiple window sea surface temperature technique, *J. Geophys. Res.*, 89, 3655-3661, 1984.

McNutt, S. L., Ice conditions in the eastern Bering Sea from NOAA and LANDSAT

imagery: Winter conditions 1974, 1976, 1977, 1979, *NOAA Tech. Memo. ERL PMEL 24*, NOAA, Boulder, CO, 1981a.

Melling, H., The formation of a halocline shelf front in wintertime in an ice-covered Arctic Sea, *Cont. Shelf Res.*, 13, 1123-1147, 1993.

Muench, R. D., J. D. Schumacher, and S. A. Salo, Winter currents and hydrographic conditions on the northern central Bering Sea shelf, *J. Geophys. Res.*, 93, 516-526, 1988.

Muench, R. D., The sea ice margins: A summary of physical phenomena, *NOAA Tech. Memo. ERL PMEL-88*, Pacific Marine Environmental Lab, NOAA, DOC, Seattle, WA, 1989.

NASA, *SAR: Synthetic Aperture Radar: Earth Observing System Instrument Panel Report Volume II*, NASA, Washington DC, 1987.

NSIDC, DMSP SSM/I brightness temperature grids for the polar regions on CD-ROM: user's guide, *NSIDC, Special Report-1*, Boulder, January 1992, 1992.

Niebauer, H. J. and D. M. Schell, Physical environment of the Bering Sea population, Chapter 2 in *The Bowhead Whale, Special Publication Number 2*, eds. J. J. Burns, J. J. Montague, and C. J. Cowles, The Society for Marine Mammology, Lawrence, Kansas, 23-43, 1993.

Niebauer, H. J., Sea ice and temperature variability in the eastern Bering Sea and the relation to atmospheric fluctuations, *J. Geophys. Res.*, 85, 7507-7516, 1980.

Ono, N., Thermal properties of seaice IV, *Technical Report, CRREL*, Cold Regions Research and Engineering Lab, Hanover, NH, 1975.

Overland, J. E. and A. T. Roach, Northward flow in the Bering and Chukchi Seas, *J. Geophys. Res.*, 92, 7097-7105, 1987.

Overland, J. E. and C. H. Pease, Cyclone climatology of the Bering Sea and its relation to sea ice extent, *Mon. Wea. Rev.*, 110, 5-13, 1982.

Parkinson, C. L., and W. M. Washington, A large-scale numerical model of sea ice, *J. Geophys. Res.*, 84, 311-337, 1979.

Pease, C. H., Eastern Bering Sea ice processes, *Mon. Wea. Rev.*, 108, 2015-2023, 1980.

Pease, C. H., The size of wind-driven coastal polynyas, *J. Geophys. Res.*, 92, 7049-7059, 1987.

Proshutinsky, A. Yu., Modeling seasonal fluctuations of the level of the Arctic Ocean, *Soviet Meteorology and Hydrology*, 2, 39-46, 1988.

Rind, D., R. Suozzo, N. K. Balachandran, A. Lacis, and G. Russell, The GISS global

climate/middle atmosphere model, Part I Model structure and climatology. *J. Atmos. Sci.*, 45, 329-370, 1988.

Rothrock, D. A. and H. L. Stern, Sea ice deformation observed with ERS-1 SAR. in *Proceedings of the First ERS-1 Symposium: Space at the Service of our Environment, 4-6 November 1992, Cannes, France*, 1992.

Salo, S., L. K. Coachman, and J. D. Schumacher, Winter currents on the eastern Bering Sea shelf (abstract), *EOS Trans. AGU*, 63(3), 100, 1982.

Schumacher, J. D., K. Aagaard, C. H. Pease, and R. B. Tripp, Effects of a shelf polynya on flow and water properties in the northern Bering Sea, *J. Geophys. Res.*, 88, 2723-2732, 1983.

Shuchman, R. A. and R. G. Onstott, Ch. 3 Remote sensing of the polar oceans. in *Polar Oceanography, Part A: Physical Science*, ed. W. O. Smith, Academic Press, San Diego, 123-170, 1990.

Shea, D. J., K. E. Trenberth, and R. W. Reynolds, A global monthly sea surface temperature climatology, *J. Climate*, 5, 987-1001, 1992.

Smith, S. D., R. D. Muench, C. H. Pease, Polynyas and leads: An overview of physical processes and environment, *J. Geophys. Res.*, 95, 9461-9479, 1990.

Stern, H., R. Kwok, S. Li, and M. Milkovich, J.1 Ice Motion Validation Team Report May 3, 1993. in Kwok, R. and G. Cunningham, *Alaska SAR Facility Geophysical Processor System data user's handbook, version 2.0, JPL D-9526*, NASA Jet Propulsion Lab, Pasadena, CA, 101-108, 1993.

Stringer, W. J. and J. E. Groves, Location and areal extent of polynyas in the Bering and Chukchi Seas. *Arctic*, 44:164-171, 1991.

Stringer, W. J., J. Zender-Romick, and J. E. Groves, Width and persistence of the Chukchi Polynya, *unpublished report, National Oceanic and Atmospheric Administration, Outer Continental Shelf Environmental Assessment Program, Research Unit 267*. (available from NOAA, Ocean Assessments Division, Alaska Office, 222 West Eighth Avenue, Anchorage, AK 99513-9543), 22 pp., 1982.

Svensson, U. and A. Omsted, Simulation of supercooling and size distribution in frazil ice dynamics. *Cold Reg. Sci. and Technol.*, 22, 221-233, 1994.

Thorndike, A. S. and R. Colony, Sea ice motion in response to geostrophic winds, *J. Geophys. Res.*, 87(C8), 5845-5852, 1982.

Trenberth, K. E., Global analyses from ECMWF and atlas of 1000mb to 10mb circulation statistics. *NCAR Tech Note, NCAR/TN-373+STR*, 1992.

Ulaby, F. T., R. K. Moore, and A. K. Fung, Microwave Remote Sensing: Active and Passive, Volume I. Artech House, Norwood, MA, 1981.

Ulaby, F. T., R. K. Moore, and A. K. Fung, Microwave Remote Sensing: Active and Passive, Volume II. Artech House, Norwood, MA, 1982.

Ulaby, F.T., R .K. Moore, and A. K. Fung, Microwave Remote Sensing: Active and Passive, Volume III, Artech House, Norwood, MA, 1986.

Vant, M. R., R. O. Ramseier, and V. Makios, The complex dielectric constant of sea ice at frequencies in the range 0.1 - 40 GHz, *J. of Appl. Phys.*, 43(3), 1264-1280, 1978.

Vasecky, J. F., R. Samadini, M. P. Smith, J. M. Daida, and R. N. Bracewell, Observations of sea ice dynamics using synthetic aperture radar images: Automated analysis, *IEEE Trans. Geosci. Rem. Sens.*, 26, 38-48, 1988.

Wade, R. H., Studies of the geophysics of sea ice, *Ph.D. Dissertation, University of Alaska Fairbanks*, Geophysical Institute, Fairbanks, Alaska, 1993.

Walter, B. A., A study of the planetary boundary layer over the polynya downwind of St. Lawrence Island in the Bering Sea using aircraft data, *Boundary-Layer Meteorol.*, 48, 255-282, 1989.

Weeks, W. F. and S. F. Ackley, The growth, structure, and properties of sea ice, in *Geophysics of Sea Ice*, ed. N. Untersteiner, Plenum Press, 9-164, 1986.

Welch, R. M., S. K. Sengupta, A. K. Goroch, P. Rabindra, N. Rangaraj, and M. S. Navar, Polar cloud and surface classification using AVHRR imagery: An intercomparison of methods, *J. Appl. Meteorol.*, 31, 405-420, 1992.

Weller, G., Radiation flux investigation, Technical Report 14, *AIDJEX Bull.*, 1972.

Wetherald, R. T. and S. Manabe, Cloud feedback processes in a general circulation model, *J. Atmos. Sci.*, 45(8), 1397-1415, 1988.

Yu, Y., D. A. Rothrock, and R. W. Lindsay, Accuracy of sea ice temperature derived from the advanced very high resolution radiometer, *J. Geophys. Res.*, 100 (C3), 4525-4532, 1995.

Zillman, J. W., A study of some aspects of the radiation and heat budget of the southern hemisphere ocean, *Meteorol. Stud.*, 26, Bureau of Meteorology, Department of Interior, Canberra, Australia, 1972.

Zubov, N. N., *Arctic Ice*, Izd. Glavsevmorputi, Moscow, 1943.